Using extraterrestrial ^{3}He concentration to examine changing sedimentation rates over climate cycles and climatic disturbances: evidence from the Cenomanian-Turonian of the Umbria–Marche Basin, Italy

James R. Lucas

Thesis submitted to the University of Oxford for the degree of Doctor of Philosophy

Department of Earth Sciences

Linacre College

April 2021





Supervised by

Dr Stuart Robinson, Prof. Hugh Jenkyns and Prof. Chris Ballentine

Abstract

Using extraterrestrial ^{3}He concentration to examine changing sedimentation rates over climate cycles and climatic disturbances: evidence from the Cenomanian-Turonian of the Umbria–Marche Basin, Italy

James Lucas

Linacre College, Oxford

April 2021

The concentration of extraterrestrial ^{3}He ($^3He_{ET}$) measured in pelagic sediments may be used as a proxy for sedimentation rate, allowing the construction of high-resolution timescales over "short" geological intervals (100s kyr), with temporal resolution in theory limited only by sampling resolution. The construction of a $^3He_{ET}$ timescale through the Bonarelli Level, a ~1 m thick interval of interbedded black and grey shales and radiolarian sands which is the sedimentary expression of Oceanic Anoxic Event 2 (~94 Ma) in Umbria–Marche, Italy, provides not only a novel method for estimating the duration of this record (478±160 kyr), but also allows rates and durations to be attached to the environmental shifts recorded in changing styles of sedimentation and/or changing geochemical records. Slow-downs in sedimentation rates are associated with the intervals of biotic turnover represented by the lithological shift from limestone to black shale at the base of the Bonarelli Level, and from black shale to limestone at its top. A transient increase in the accumulation rate of carbonates above the Bonarelli Level likely reflects enhanced biogenic calcite preservation due to build-up of excess alkalinity during OAE 2.

Precession cycles within the rhythmically bedded Scaglia Bianca Formation, a sequence of pelagic limestones well characterised by cyclostratigraphy that underlie the Bonarelli Level, were also investigated using $^3He_{ET}$ timescales. Exploration of the timings and possible drivers of lithological change within these Scaglia Bianca precession cycles provides insight into how local palaeoclimatic and Earth System processes reacted to 'base level' orbital forcing in the Cenomanian prior to the perturbation associated with OAE 2. Precession cycles deposited under eccentricity maxima (expressed as limestone-black shale-black chert sequences) and minima (expressed as limestone-laminated limestone-grey chert) were selected for comparison. Calculation of the proportion of time per cycle represented by silica- and organic-rich facies indicates that, when the amplitude of precessional insolation forcing was greatest (at eccentricity maxima), the palaeoenvironmental system spent longer in the more nutrient-rich environment under which silica- and organic-rich sediments were deposited, reflecting increased time spent above a 'threshold' insolation level.

This work expands the use of extraterrestrial timescales to stratigraphic sections with heterogeneous lithologies, including organic-rich black shales and cherts. $^3He_{ET}$ is shown not to be liberated during the diagenetic process of chert formation. Various methods of calculating $^3He_{ET}$ background flux in sections with heterogeneous lithology were also evaluated, and a best-practice method proposed.

Extended Abstract

Using extraterrestrial ^{3}He concentration to examine changing sedimentation rates over climate cycles and climatic disturbances: evidence from the Cenomanian–Turonian of the Umbria–Marche Basin, Italy

James Lucas

Linacre College, Oxford

April 2021

Oceanic Anoxic Event 2 (OAE 2), a globally recognised carbon-cycle perturbation originally recognised by the widespread synchronous deposition of organic-carbon rich pelagic sediments (Schlanger and Jenkyns, 1976), was a period of climate change ~94 Ma during which rapid warming was accompanied by an accelerated hydrological cycle, enhanced continental weathering, increased nutrient input to the oceans, intensified upwelling, increased organic productivity and expansion of marine anoxia/euxinia. Changes in these Earth System processes have been tracked through extensive study of geochemical proxies expressed in sediments deposited during OAE 2 (e.g. Jenkyns, 2010, review; Owens et al., 2012, 2013; Pogge von Strandmann et al., 2013; Helmond et al., 2014; O'Brien et al., 2017; O'Connor et al., 2020). Determining the rates of change of key geochemical species across OAE 2 records can illuminate both the forcing mechanisms behind observed palaeoenvironmental changes, and the timescale of the Earth system response to that forcing. This thesis presents a high-resolution timescale across the Bonarelli Level, the sedimentary expression of Oceanic Anoxic Event 2 in Umbria–Marche, Italy, using the concentration of extraterrestrial ^{3}He ($^{3}He_{ET}$) as a relatively novel proxy for sedimentation rate.

Over “short” geological intervals (100s kyr), the assumed constant background flux of extraterrestrial ^{3}He to sediments means that instantaneous sedimentation rates may be calculated on a bed-by-bed basis using the relationship: $[^3He_{ET}] = F / \alpha$, where $[^3He_{ET}]$ represents the concentration of extraterrestrial ^{3}He, ccSTP/g, F the background flux of $^3He_{ET}$ into sediments, ccSTP/cm^2/yr, and α the accumulation rate of sediment, g/cm^2/yr (Takayanagi and Ozima, 1987). These parameters, in theory, mean that the resolution of age models constructed using $^3He_{ET}$ is limited only by sampling resolution, although in practice resolution is also limited by the smearing effects of bioturbation. $^3He_{ET}$ timescales are particularly suited for construction over rapid intervals of dramatic climate perturbation such as OAE 2, during which changes may have occurred more rapidly than the smallest resolvable cyclostratigraphic time interval (the duration of a short precession cycle) and dramatic lithological changes may make periodic variations needed to apply a cyclostratigraphic timescale difficult to identify.

The initial work of this thesis was concerned with the development of a standard methodology for liberating helium from powdered samples in the Oxford Noble Gas Laboratory, using a Fusions Diode .970 Laser Stepped Heating System, in addition to developing a suitable ‘clean-up’ process to permit measurements to be made in organic carbon- and sulphur-rich black shale sediments (expanding the range of lithologies in which $^3He_{ET}$ has been measured). The reproducibility of $^3He_{ET}$ measurements was characterised; the statistically small number of helium-bearing interplanetary dust particles (IDPs) expected in measured aliquots of sediment results in a lower reproducibility than would be expected solely from analytical uncertainty (Farley and Patterson, 1995), with the observed spread of measured replicates in this thesis approximated using a Gaussian distribution with 1σ ~20%. The feasibility of constructing $^3He_{ET}$ timescales through sections containing chert was also confirmed; transects through chert nodules from the Cenomanian Scaglia Bianca Formation of Furlo, Italy, and the Lower Campanian Newhaven Chalk Formation of Peacehaven, UK, demonstrated no correlation between concentration of helium and the ‘degree of chertification’, indicating that helium is not preferentially liberated from sediments that have diagenetically evolved into cherts. Measurements

of neon gas released from samples detected radiogenic and extraterrestrial Ne components, though with an overwhelming contribution from atmospheric neon.

As part of the development of the $^{3}He_{ET}$ timescale technique for use in a wider array of sedimentary sections, a 'best practice' method for determining the background flux of extraterrestrial ^{3}He through lithologically heterogeneous sections was developed. Uncertainty on background flux is the largest contributor to error in $^{3}He_{ET}$ timescales, and incorrect determination of background flux introduces a systematic error in calculations of sedimentation rate from $^{3}He_{ET}$. Through lithologically heterogeneous sections in which sedimentation rate varies, 'spot sampling' for background flux may lead to systematic oversampling of certain lithologies and hence an inaccurate background flux estimate. To mitigate this effect, background flux through the cyclically bedded Cenomanian sediments below the Bonarelli Level was calculated using the homogenised mixture of the expression of a complete orbital cycle as a base sampling 'unit', a method suggested as 'best practice' in any lithologically heterogeneous section. Variability in the incoming flux of extraterrestrial ^{3}He over Cenomanian/Turonian boundary time was characterised from multiple 'homogenised cycle' measurements made across this interval; this variability led to a large error on the calculated $^{3}He_{ET}$ background flux over the interval spanning the Bonarelli Level: $1.14\pm0.38 \times 10^{-13}$ ccSTP/cm^2/kyr.

High-resolution timescales over expressions of eccentricity-modulated precession in the Scaglia Bianca (a Cenomanian rhythmically bedded formation of deep-marine pelagic limestones, cherts and local black shales that underlie the Bonarelli Level) in the Furlo and Contessa sections, Umbria–Marche, Italy, were constructed to provide context for the palaeoenvironmental changes observed over OAE 2 by investigating the palaeoenvironmental response to 'background' orbital forcing in the Umbria–Marche Basin. $^{3}He_{ET}$ timescales provide a novel method for determining the division of time within a precession cycle, something not possible using cyclostratigraphy.

Within the Scaglia Bianca, eccentricity is known to have modulated the amplitude of precessional forcing: a phenomenon clearly visible in the lithological expression of precession, with cycles deposited during eccentricity maxima containing black cherts (and in some localities black shales) and cycles deposited during eccentricity minima containing only grey cherts with a much lower organic-carbon content (Batenburg et al., 2016). Lithological variations through these precession cycles were conceptualised using a 'threshold model' under which extremes of precessional forcing nudged the local palaeoceanographic system from a depositional regime favouring carbonate deposition, to one favouring the deposition of organic-rich black shales and (proto-)cherts (following Batenburg et al., 2016). In palaeoenvironmental terms, this 'threshold' is proposed to reflect an increase in nutrients to a level at which an ecological change occurred from assemblages dominated by k-strategist calcareous plankton to those dominated by r-strategist non-mineralising phytoplankton, with an associated increase in zootrophic radiolaria (e.g. Margalef, 1978). A greater proportion of the precession cycle by time was spent 'below' this threshold in cycles deposited under eccentricity minima (limestone accounts for ~90% of the cycle 'by time') than in those deposited under eccentricity maxima (where limestone only accounts for ~65% of the cycle 'by time'). An order of magnitude increase in flux of terrestrially derived ^{4}He is measured in some black chert beds, perhaps suggesting that these nutrients were sourced from exposed landmasses.

Within cycles deposited at eccentricity maxima, sedimentation rates were found to vary by an order of magnitude in cycles containing black shale beds (those deposited at Furlo), with typical sedimentation rates ~0.1 cm/kyr in black shales, and >1 cm/kyr in cherts and limestones. A marked increase in organic-carbon mass accumulation rate (OC MAR) in black shale beds of up to ~0.025 $g/cm^2/kyr$ was ascribed to both enhanced preservation of organic carbon, and an increase in primary productivity, estimated during black shale deposition as 30–59 $gC/m^2/yr$, almost double that estimated during limestone deposition, 15–27 $gC/m^2/yr$ (though it should be noted that both these productivity estimates are within the range of 'low productivity regions' in modern oceans (Demaison and Moore, 1980)). A lack of significant intra-cycle variation in sedimentation rates

measured in limestone beds implies that, below the proposed insolation 'threshold', environmental conditions impacting carbonate production and preservation did not change significantly. Duration estimates (from $^{3}He_{ET}$) for the radiolarian-rich chert beds expressed in these precession cycles were combined with sedimentological evidence to suggest both that the deposition of their primarily lithology, radiolarian sand, did not occur in a single 'wash-in' event (chert beds in these cycles span 0.6–2.4 kyr), and that the distinction between black chert and black shale beds (where they occur) reflects differences in primary lithology rather than solely diagenetic separation.

Creation of a high-resolution $^{3}He_{ET}$ timescale through the Bonarelli Level, a ~1.3 m thick interval of organic-carbon-rich black shales and radiolarian sands, allowed not only the calculation of a new duration estimate, but also, through the calculation of an instantaneous sedimentation rate for each measured bed, provided the opportunity to estimate the rates and durations of changes in palaeoenvironment recorded in the rapidly shifting lithology over this record of OAE 2. The calculated duration of deposition of the Bonarelli Level, 478±160 kyr, is consistent with recent estimates from cyclostratigraphy (~490 kyr; Mitchell et al., 2008; Lanci et al., 2010; Batenburg et al., 2016). The initial 'build up' phase of the globally recognised carbon-isotope excursion spans 174±58 kyr at Furlo, comparable to cyclostratigraphic duration estimates from the Western Interior Seaway (~149–240 kyr; Sageman et al., 2006; Ma et al., 2014).

The overall organic-carbon mass accumulation rate over the span of the Bonarelli Level, 0.044±0.011 g/cm^2/kyr, is fairly typical of average OC MARs in pelagic marginal settings over OAE 2 (Owens et al., 2018). However, within the Bonarelli Level, accumulation rates of both bulk sediment and organic carbon were highly heterogeneous, reflecting rapid changes in depositional conditions (driven by rapid palaeoenvironmental change) during OAE 2. Sedimentation rates measured through the Bonarelli Level varied by almost two orders of magnitude (0.04–1.13 cm/kyr), whilst OC MARs range from values below the limit of detection to peak values in black mudstone/shale beds of 0.22±0.09 g/cm^2/kyr. High OC MARs in Bonarelli Level sediments were ascribed to the effects of both increased

primary productivity, and enhanced preservation of organic matter. Organic-carbon primary productivity estimated during the deposition of beds with high OC MARs, 60–110 gC/m^2/yr, are elevated compared to modern open-ocean productivity rates (~30 gC/m^2/yr; Demaison and Moore, 1980; Falkowski et al., 1998), though still lower than productivity rates from modern 'high productivity' upwelling settings (at least ~300–400 gC/m^2/yr; Falkowski et al., 1998; Behrenfeld et al., 2005). Four 'high OC MAR' intervals were identified within the Bonarelli Level, linked to the transient establishment of more dysoxic/euxinic conditions over spans of 12–64 kyr; within some 'high OC MAR' intervals sub-10 kyr alternation of OC-rich and OC-poor beds suggest that different bottom-water conditions (with differing organic-carbon preservation potential) were rapidly established and replaced.

$^3He_{ET}$ timescales have the potential to recognise hiatal surfaces in the sedimentary record in cases where sediment has not been removed during periods of non-deposition. Although no $^3He_{ET}$ evidence was identified for the proposed ~400 kyr hiatus between the Bonarelli Level and the overlying limestones at Furlo (see Voigt et al., 2007; Gambacorta et al., 2015; Batenburg et al., 2016) this is inconclusive evidence for its absence, as erosion at the putative hiatal surface may have served to remove $^3He_{ET}$-bearing particles, resulting in unquantifiable 'missing' time. A condensation interval recognisable as a 'spike' in $^3He_{ET}$ concentration was, however, identified within the Bonarelli Level, ~40 cm above its base. This interval may represent a prolonged period of low primary productivity and low biotic silica production, within which 5 cm of black shale and radiolarian sand are thought to have been deposited over a span of ~50 kyr.

Slowdowns in sedimentation rate were also observed at the base and top of the Bonarelli Level, likely associated with biotic turnover. At the base of the Bonarelli Level a ~30 kyr slowdown, spanning ~3.5 cm of shales and mudstones coincident with a dramatic drop in carbonate content, may represent the interval between an effective cessation of carbonate accumulation and a ramp-up in biogenic silica as carbonate-producing plankton were out-competed under higher nutrient

conditions (see Erba, 2004). At the top of the Bonarelli Level ~85 kyr of slowly accumulating sediment coincident with the final decline in total organic-carbon content may represent the time between re-establishment of oxygenated marine conditions (limiting TOC preservation) and the completion of the biotic turnover that restored carbonate deposition.

Above the Bonarelli Level a carbonate overshoot similar to those observed following other major periods of environmental perturbation (such as the Paleocene-Eocene Thermal Maximum, e.g. Luo et al., 2016) was observed. Carbonate accumulation rates of ~2× typical pre- and post-event values were measured over a ~3.5 kyr interval beginning ~20 kyr after the deposition of the stratigraphically lowest bed containing significant carbonate content above the Bonarelli Level. Enhanced carbonate accumulation is suggested to have been a response to the build-up of excess alkalinity over OAE 2 due to low carbonate productivity and sedimentation through this interval.

Acknowledgements

I'd like to thank my supervisors Stuart Robinson, Hugh Jenkyns and Chris Ballentine for conceiving of this project, and for their valuable guidance throughout. I also thank Sietske Batenburg for foundational discussions about cyclostratigraphy as I began this project, and for showing me around the Umbria–Marche Basin. I thank the Oxford Environmental Research DPT for funding me, and Linacre College for their pastoral support.

Darren Hillegonds and Jennifer Mabry, the Laboratory Managers for the Oxford Noble Gas Lab over the course of my thesis, have my warmest thanks for not only teaching me to use the mass spectrometers and keeping the lights (and the machines) on in the lab, but also for being an insightful, patient, and all-around invaluable resource during technique development.

I'd like to thank the Noble Gas Group, Oxford, particularly Rebecca Tyne, Anran Cheng and Rosie Jones for discussions in group meetings, in the lab, and on the side-lines of conferences. Likewise, I would like to thank the 'Mesozoic Mayhem' Group, Oxford, particularly Ritwika Sengupta and Lauren O'Connor.

I thank Simona Nicoara, of the Open University, for measuring stable carbon isotopes in my samples. Thanks to Stephen Wyatt for teaching me how to use the Rock Eval machine and showing me around the Chemistry Lab, to Owen Jones for the use of the Rock Crushing facilities as well as pointers on microfossil ID, to Jonathon Wells for preparing my thin sections, and to Jamie Long and the Earth Sciences Workshop for machining custom sample cells for me.

Finally, of course, I'd like thank my family for always having my back.

Contents

Abstract.....i

Extended Abstract.....iii

Acknowledgements.....xi

Contents.....xiii

Chapter 1 – Introduction.....1

1.1 Specific research aims.....7

2.1 Thesis outline.....10

Chapter 2 – Literature Review.....12

2.1 Extraterrestrial helium, IDPs (interplanetary dust particles) and $^{3}He_{ET}$ age models.....13

2.1.1 Interplanetary dust particles.....13

2.1.2 IPDs in sediments.....19

2.1.3 Theory of $^{3}He_{ET}$ age models.....26

2.1.4 Previous use of $^{3}He_{ET}$ age models.....40

2.2 Geological setting of the Umbria–Marche Basin.....42

2.2.1 Sampling locations.....43

2.2.2 Late Cretaceous palaeogeography.....44

2.2.3 The Scaglia Bianca Formation.....46

2.2.4 Post-depositional history.....52

2.3 Climate cycles and climatic disturbances.....52

2.3.1 Cyclicity through the Cenomanian-Turonian.....53

2.3.2 Oceanic Anoxic Event 2.....65

Chapter 3 – Method development: analytical approach for He isotopes, an exploration of Ne-isotopes, and measurement of He-isotopes in diverse pelagic lithologies.....78

Abstract.....78

3.1 Methodology: analytical approach.....80

3.1.1 Sample preparation.....80

3.1.2 Mass Spectrometer.....84

3.1.3 Post-collection data processing.....94

3.1.4 Deconvolution of sources of helium.....97

3.1.5 Sample reproducibility and sources of error.....100

3.2 An exploration of Neon isotopes in Cretaceous pelagic sediments from the Scaglia Bianca.....105

3.3 Application of the analytical approach to diverse pelagic lithologies.....113

3.3.1 He-isotopes in pelagic carbonates and black shales.....113

3.3.2 He-isotopes in pelagic cherts within pelagic carbonate sequences.....115

3.4 Conclusion.....122

Chapter 4 – High-resolution timescales through precession cycles.....124

Abstract.....124

4.1 Introduction.....125

4.2 Geological Setting.....126

4.3 Methodology.....127

4.4 Results.....133

4.4.1 Sedimentology of Scaglia Bianca precession cycles.....133

4.4.2 Helium concentration.....144

4.5 Discussion.....148

4.5.1 Background Flux.....148

4.5.2 $^{3}He_{ET}$ age models.....159

4.5.3 Orbitally forced changes in climate.....165

4.6 Conclusion.....191

Chapter 5 – A high-resolution timescale through the Bonarelli Level.....194

Abstract.....194

5.1 Introduction.....195

5.2 Methodology.....196

5.2 Results.....198

5.3.1 Total Organic Carbon content, carbonate content and Hydrogen Index.....201

5.3.2 Helium concentration.....204

5.3.3 Sedimentation rates.....204

5.3.4 Organic-carbon mass-accumulation rates.....205

5.4 Discussion.....208

5.4.1 Duration of the Bonarelli Level.....208

5.4.2 Sedimentation rates through the Bonarelli Level.....215

5.4.3 Carbon cycle through the Bonarelli Level.....224

5.4.4 Condensed horizons.....229

5.4.5 Above the Bonarelli Level.....235

5.5 Conclusion.....240

Chapter 6 – Conclusions and Future Work.....243

6.1 Conclusions.....243

6.2 Future Work.....252

6.2.1 Redistribution of IDPs.....252

6.2.2 Timings within orbital cycles.....254

6.2.3 Duration and pacing of CIEs and other proxy records over Mesozoic hyperthermals.....255

6.2.4 Carbonate overshoot.....257

References.....258

Appendix: Noble Gas data

List of Figures

Chapter 2 – Literature Review

Figure 2.1: Fraction of extraterrestrial ^{3}He in a sample against observed ^{3}He/^{4}He ratio.....32

Figure 2.2: Location of the Umbria–Marche Basin.....43

Figure 2.3: Generalised palaeogeographic maps showing the setting of the study area at the Cenomanian-Turonian boundary.....45

Figure 2.4: Summary of Cretaceous lithostratigraphic units in the Umbria–Marche Basin.....47

Figure 2.5: Cartoon showing the deposition of a limestone-black chert cycle as proposed under 'anti-monsoonal' and 'monsoonal' models.....58

Figure 2.6: Overview cartoon of processes active over Oceanic Anoxic Event 2.....67

Chapter 3 – Method development: analytical approach for He isotopes, an exploration of Ne-isotopes, and measurement of He-isotopes in diverse pelagic lithologies

Figure 3.1: ^{3}He (cc) measured in different masses of a limestone, shale, and chert sample.....83

Figure 3.2: Approximate area-time products of samples from Contessa and Furlo.....84

Figure 3.3: Schematic diagrams of mass spectrometer preparatory line and sample holders.....85

Figure 3.4: Comparison of average blank values associated with different sample packing.....87

Figure 3.5: Glassy residue of melted silver foil-wrapped sample following heating.....87

Figure 3.6: Helium measured during trials of sample packing techniques.....88

Figure 3.7: Replicates of a pelagic limestone sample measured both with and without baking of the sample cell during pumping to vacuum.....93

Figure 3.8: Observed reproducibility of ^{3}He concentration between all sample replicates measured in this study.....102

Figure 3.9: ^{20}Ne/^{22}Ne ratios versus ^{21}Ne/^{22}Ne ratios, and ^{20}Ne/^{22}Ne ratios versus ^{3}He/^{4}He ratios of Furlo samples.....109

Figure 3.10: Estimated proportions of ^{22}Ne from atmospheric, extraterrestrial and nucleogenic endmembers.....112

Figure 3.11: Comparison of extraterrestrial ^{3}He measurements made on samples from the same section by Farley et al. (2012) and on the Oxford system.....114

Figure 3.12: Helium content across two chert nodules from the Cenomanian Scaglia Bianca, Furlo, and Campanian Newhaven Chalk Formation, Peacehaven.....119

Chapter 4 – High-resolution timescales through precession cycles

Figure 4.1: Position of studied cycles within overall Furlo section.....129

Figure 4.2: Annotated outcrop photograph of Furlo section, showing position of studied precession cycles……130

Figure 4.3: Summary of the three trialled methods for determining background flux through intervals with heterogenous lithology.....132

Figure 4.4: Lithology, total organic carbon content, carbonate content and Hydrogen Index values for the four studied cycles.....134

Figure 4.5: Precession cycle outcrop photographs.....138

Figure 4.6: Thin section images of precession cycle lithologies.....139

Figure 4.7: Thin section images of precession cycle lithologies.....141

Figure 4.8: Van Krevelen-type plot showing the variation of organic matter types with lithology in the studied Scaglia Bianca precession cycles.....144

Figure 4.9: Extraterrestrial ^{3}He and terrestrial ^{4}He concentration through the studied precession cycles.....146

Figure 4.10: Comparison of background flux determined through different means.....149

Figure 4.11: Linear sedimentation rate, organic-carbon mass-accumulation rate and flux of terrestrial ^{4}He through the studied precession cycles.....160

Figure 4.12: Precession cycle logs against time.....164

Figure 4.13: Summary of postulated methods of chert formation in the Scaglia Bianca.....168

Figure 4.14: Percentage of C_{org} deposited on the seafloor that is then preserved against bulk mass accumulation rate of the sediment in differing environments of deposition.....177

Figure 4.15: Summary of 'threshold model' linking insolation forcing and the drivers of palaeoceanographic change.....186

Chapter 5 – A high-resolution timescale through the Bonarelli Level

Figure 5.1: High-resolution sedimentary log of the Bonarelli Level with outcrop photograph…….197

Figure 5.2: High-resolution log of the Bonarelli Level presented alongside total organic carbon content, carbonate content, Hydrogen Index of organic matter (HI), $\delta^{13}C_{TOC}$, extraterrestrial ^{3}He and terrestrial ^{4}He concentration, linear sedimentation rate and organic-carbon mass-accumulation rate measured in each bed.....199

Figure 5.3: Rock Eval results for the Bonarelli Level succession.....202

Figure 5.4: Porcellanite bed from the top of the Bonarelli Level.....203

Figure 5.5: Sedimentation rates and organic-carbon mass accumulation rates of lithologies within the Bonarelli Level.....206

Figure 5.6: Log of the Bonarelli Level plotted against depth and time.....209

Figure 5.7: Comparison of $\delta^{13}C_{TOC}$ and $\delta^{13}C_{carb}$ profiles through global sections spanning OAE 2…….211

Figure 5.8: $\delta^{13}C_{TOC}$ curve through the Bonarelli Level at Furlo.....213

Figure 5.9: Productivity-associated OC MAR elevation……..217

Figure 5.10: Samples in which OC MAR rates are thought to be elevated by enhanced preservation compared to records of pyrite abundance and redox-sensitive trace element enrichment.....221

Figure 5.11: Detail of a 'high OC MAR' interval, presented against a scaled-time log.....222

Figure 5.12: Lithological change over suspected condensed intervals.....230

List of Tables

Chapter 2 – Literature Review

Table 2.1: Review of recorded noble gas concentration and ratios in IDPs separated from marine sediments.....15

Table 2.2: Review of end-member values used in the deconvolution of helium in marine sediments..33

Chapter 3 – Method development: analytical approach for He isotopes, an exploration of Ne-isotopes, and measurement of He-isotopes in diverse pelagic lithologies

Table 3.1: Average decarbonated sample weight and original bulk sample weight for the three primary lithology types investigated in this thesis.....83

Chapter 4 – High-resolution timescales through precession cycles

Table 4.1: Background flux values through the Scaglia Bianca and associated standard error, as calculated using three different methods.....156

Table 4.2: Proportion of time occupied by each lithology within the studied precession cycles, presented as time occupied within a 21 kyr precession cycle.....165

Table 4.3: Estimated primary productivity from Furlo precession cycles.....179

Chapter 5 – A high-resolution timescale through the Bonarelli Level

Table 5.1: Linear sedimentation rate ranges and averages in different lithologies from the Bonarelli Level.....207

Table 5.a2: Organic-carbon mass-accumulation rate ranges and averages in different lithologies from the Bonarelli Level and enclosing sediments.....207

Table 5.2: Primary productivity values estimated for all samples with organic-carbon mass-accumulation rates higher than 0.15 gC/cm^2/kyr.....228

1. Introduction

The sedimentary record contains the only evidence of climatological changes in the distant past, with the lithology and geochemistry of a section reflecting the palaeoenvironmental conditions when the rock was laid down. Of great interest are the rates of change in palaeoenvironmental/palaeoclimatic conditions; knowing the speed of palaeoenvironmental changes can illuminate the nature of the processes forcing them and the mechanisms by which the Earth System responds to that forcing which may, where the rock record preserves a response to, for example, rapid greenhouse gas input to the atmosphere, contextualise the comparative rates of anthropogenic change (e.g. Jenkyns, 2010; Zeebe and Zachos, 2013). Crucial to the interpretation of any sedimentary record, however, is the understanding that it does not provide a direct record of palaeoclimatological change: rather, a sedimentary section records palaeoenvironmental conditions as encoded in rock, and is impacted by both the nature of the sedimentary processes during deposition and by diagenetic changes. It is not possible to directly measure time spanned by a sedimentary record, only thickness. Therefore, in order to calculate rates of change from the geological record, the relationship between 'rock' and 'time' must first be clarified. One method of doing so, as explored in this thesis, is developing some geochemical proxy for sedimentation rate.

This thesis uses a relatively novel proxy for sedimentation rate, extraterrestrial ^{3}He ($^{3}He_{ET}$), to unpick the geological record of palaeoenvironmental response to cyclical orbital forcing and a major climatic perturbation. Extraterrestrial ^{3}He is used to construct high-resolution timescales for orbitally-forced precession cycles in the Cenomanian Scaglia Bianca Formation, central Italy, and for the associated Bonarelli Level, a ~1m thick unit of interbedded black shales and radiolarian sands that is the local expression of Oceanic Anoxic Event 2 (a dramatic climatic perturbation of global significance).

$^{3}He_{ET}$ timescales are based on a simple principle: extraterrestrial helium, hosted in interplanetary dust particles (IDPs), is delivered to sediments at what is assumed to be a constant rate over time (the theory underpinning the use of $^{3}He_{ET}$ timescales is presented briefly below and is explored, along with its underlying assumptions, in more depth in Section 2.1). The extraterrestrial and terrestrial helium component of sediments can be deconvolved as these two endmembers have markedly different isotopic compositions ($^{3}He/^{4}He$ ratios are often given as ~2.4×10^{-4} and 2–4×10^{-8}, respectively, e.g. Farley (2001); see Section 2.1.3 for further discussion). The delivery of $^{3}He_{ET}$ at a constant rate means that the concentration of $^{3}He_{ET}$ measured in the sediment is proportional to the background flux of $^{3}He_{ET}$ and inversely proportional to sedimentation rate, as sedimentation acts to dilute the IDPs:

$$[^{3}He_{ET}] = F / \alpha \qquad \text{Equation 1.1}$$

where $[^{3}He_{ET}]$ is the concentration of extraterrestrial ^{3}He (ccSTP/g), F is the background flux of extraterrestrial ^{3}He into sediments (ccSTP/cm^2/yr) and α is the accumulation rate of sediment (g/cm^2/yr) (Takayanagi and Ozima, 1987). The equation above can, in principle, be used to calculate instantaneous sedimentation rate for every packet of sediment measured, making $^{3}He_{ET}$ timescales a very powerful tool as theoretically the resolution of the age model is limited only by sampling density.

The novelty of the $^{3}He_{ET}$ technique means that it has only been used in a fraction of the sections to which it might usefully be applied. The Bonarelli Level, the expression of Oceanic Anoxic Event 2 in Marche-Umbria, Italy (see Schlanger and Jenkyns (1976)), is one such section. Oceanic Anoxic Event 2 (OAE 2) was a period of dramatic climatic perturbation at the Cenomanian-Turonian boundary (~94 Ma), one of a number of Mesozoic hyperthermals (Jenkyns, 2010). A substantial disturbance to the global carbon cycle over OAE 2 is evident from the positive carbon-isotope ($\delta^{13}C$) excursion over this interval; a wealth of studies utilising various geochemical proxies have demonstrated that during OAE 2 a rapid rise in temperature was accompanied by an accelerated hydrological cycle, enhanced

continental and oceanic weathering, increased nutrient input to the oceans, intensified upwelling, biotic turnover, increased organic productivity and expansion of marine anoxia/euxinia (see review of Jenkyns (2010) and the literature review contained in Chapter 2, Section 2.3.2).

$^{3}He_{ET}$ timescales are most usefully applied where more 'conventional' chronological tools such as cyclostratigraphy are more difficult to use (Murphy et al., 2010; see further discussion in Section 2.1.3), and this is certainly true of the Bonarelli Level. The Bonarelli Level was one of the first sedimentary expressions of OAE 2 to be recognised due to its high organic-carbon content (up to 30% in some beds); its base represents a dramatic lithological shift from the rhythmically bedded limestones and cherts of the surrounding Scaglia Bianca Formation to a ~1.3 m thick succession of interbedded black and grey mudstones and shales, radiolarian sands and local thin black cherts, essentially carbonate-free (Schlanger and Jenkyns, 1976; Arthur and Premoli Silva, 1982; Farrimond et al., 1990), with the reverse lithological shift taking place at its top. The potential for condensation horizons associated with these lithological shifts (as proposed by Tsikos et al., 2004; Jenkyns et al., 2007; Voigt et al., 2007; Gambacorta et al., 2015) heightens the likelihood of the periodic signals necessary for cyclostratigraphic analysis being missed or misinterpreted - as does the presence of intervals of non-deposition associated with lithological shifts within the Bonarelli Level itself. $^{3}He_{ET}$ age models may theoretically be used to explore hiatuses under circumstances in which periods of non-deposition were not accompanied by erosion, as a cessation of background sedimentation would lead to a high concentration of $^{3}He_{ET}$ on a bed-top, allowing these intervals to be identified and providing an estimate of their duration (Mukhopadhyay et al., 2001b).

$^{3}He_{ET}$ age models, therefore, provide a novel method of estimating the duration of Oceanic Anoxic Event 2, but perhaps even more interesting is their ability to investigate the division of time within the lithological expression of the event, providing timescales for the environmental shifts indicated by changing styles of sedimentation or geochemical records. It is hoped that the application of $^{3}He_{ET}$ timescales to changes through the Bonarelli Level will enhance the understanding of the timescales

on which Earth system processes important during OAE 2 react to perturbation and return to equilibrium (e.g. change in the dominant planktonic communities, changes in terrigenous input, etc.). Previous studies utilising $^{3}He_{ET}$ timescales to explore the Palaeocene–Eocene Thermal Maximum (PETM), another dramatic climatic perturbation, have uncovered more nuance in the speed of recovery from this event than was captured in cyclostratigraphic studies; though the same overall span of the PETM was derived from both $^{3}He_{ET}$ age-models and cyclostratigraphy, $^{3}He_{ET}$ age-models measure significantly higher sedimentation rates in post-event carbonates, indicating oceanographic conditions very favourable to carbonate production and/or preservation post-event, and shortening the estimated span of time for the recovery of the carbon-cycle perturbation (cf. Murphy et al., 2010; Westerhold et al., 2018).

$^{3}He_{ET}$ age models have also never before been applied to the lithological expression of a precession cycle, though they are one of the very few tools that allow the division of time within one of these cycles, so commonly used as a cyclostratigraphic yardstick, to be investigated. In the Scaglia Bianca, precession cycles have been linked to the ~20 cm thick rhythmic alternations of limestone and chert, clearly visible by eye (de Boer, 1982, 1991; Mitchell et al., 2008; Lanci et al., 2010; Batenburg et al., 2016; see further discussion in Section 2.2.3). Variation in the lithological expression of these cycles – most obvious in the nature of the ~5 cm thick chert beds which may be either grey or black (in certain localities these black cherts are accompanied by ~1 cm of black shale) – has been linked to amplitude modulation of precession cycles by short and long eccentricity (Mitchell et al., 2008; Lanci et al., 2010; Sprovieri et al., 2013; Batenburg et al., 2016). In this study, application of $^{3}He_{ET}$ age models to four cycles deposited under different amplitudes of precessional forcing allows the palaeoenvironmental response under these differing conditions to be examined in detail.

The initiation of OAE 2 has been robustly linked to the eruption of various Large Igneous Provinces (Sinton and Duncan, 1997; Kerr, 1998; Erba, 2004; Snow et al., 2005; Kuroda et al., 2007; Turgeon and Creaser, 2008; Zheng et al., 2013; Du Vivier et al., 2014); however, it has been suggested that

some control on the exact timing of the carbon cycle perturbation was exerted by orbital configuration (Mitchell et al., 2008; Batenburg et al., 2016; Laurin et al., 2016). This hypothesis has often been linked, in the Scaglia Bianca Formation, to the observation of the similarity between the black cherts (and local black shales) which occur rhythmically interbedded with limestone in the Scaglia Bianca and the black shale and chert of the Bonarelli Level (Mitchell et al., 2008; Batenburg et al., 2016). A paired study of $^{3}He_{ET}$ timescales through both the Bonarelli Level and through Scaglia Bianca precession cycles serves therefore to put the Bonarelli Level into context, as exploration of the timings and possible drivers of lithological change within precession cycles provides insight into how local palaeoclimate and Earth System processes responded to 'base level' orbital forcing in the Cenomanian prior to the perturbation associated with OAE 2.

The sections of interest to this study are well suited for construction of $^{3}He_{ET}$ age models. $^{3}He_{ET}$ is most useful as a proxy for sedimentation rate when it can be applied to former deep-marine pelagic sediments. The background flux of $^{3}He_{ET}$ is low: the modern $^{3}He_{ET}$ flux is estimated at ~1×10^{-12} ccSTP/cm^{2}/kyr (Marcantonio et al., 1996, 1998), so for concentrations of $^{3}He_{ET}$ to be measurable in 'handleable' sample sizes of a few grams of sediment it must be sought out in settings, such as the deep ocean, where background sedimentation rate is also relatively low. In addition, there is no way to estimate the size of 'gaps' in a $^{3}He_{ET}$ age model caused by the removal of sediment (and its constituent IDPs) by erosion. Although such gaps may be present in records even from pelagic settings (Trabucho-Alexandre, 2014), making detailed sedimentary logs accompanying $^{3}He_{ET}$ measurements essential to record any sedimentological evidence of erosional processes, less erosion is likely to have taken place in the deep ocean than in more turbulent-water terrestrial, shallow and near-shore settings. In this respect, the subject of this study, the Scaglia Bianca Formation, comprising pelagic limestones and cherts believed to have been deposited under 1500–3000 m water depth (see Arthur and Premoli Silva, 1982; Kuhnt, 1990; Bernoulli and Jenkyns, 2009), is a prime candidate for the application of a $^{3}He_{ET}$ timescale.

$^{3}He_{ET}$ age models are also most suitable for use over geologically short timescales, on the order of 10^{5} years (Farley, 2001). This limitation is largely due to the long-term (in)stability of $^{3}He_{ET}$ background flux, which must be assumed to have been constant over the studied interval if sedimentation rate is to be calculated using Equation 1. However, background $^{3}He_{ET}$ flux is known to vary over Myr timescales, and long-term background flux records display rare but dramatic spikes in the influx of interplanetary dust particles, thought to be the result of asteroid break-ups or comet showers, with $^{3}He_{ET}$ flux very variable within these intervals (Farley, 2001; Mukhopadhyay et al., 2001; Farley et al., 2012). For this reason, the '$^{3}He_{ET}$ technique' is not used to construct long-term age models over epochs; in addition, timescales of this length may often be adequately investigated using other dating tools including cyclostratigraphy, biostratigraphy, and magnetostratigraphy. The power of $^{3}He_{ET}$ timescales lies, rather, in investigating stretches of time with which these methods struggle: brief, interesting events such as the Palaeocene-Eocene Thermal Maximum (Farley and Eltgroth, 2003; Murphy et al., 2010), the Cretaceous-Tertiary boundary event (Mukhopadhyay et al., 2001b; Lowery et al., 2018), or OAE 2 (this study) where rapid and dramatic lithological shifts may make methods such as cyclostratigraphy difficult to use.

The application of the $^{3}He_{ET}$ technique to the Scaglia Bianca and Bonarelli Level, however, still requires some expansion to the existing methodological procedure (which follows Patterson and Farley, 1998). Measurements of $^{3}He_{ET}$ have, thus far, been made primarily in carbonate successions, with some measurements in pelagic clays (e.g. Patterson and Farley, 1998; Farley and Eltgroth, 2003; Mukhopadhyay and Farley, 2006; Marcantonio et al., 2009; Torfstein, 2012; Chavrit et al., 2016). In this thesis, the use of $^{3}He_{ET}$ timescales is expanded into sections containing cherts and organic-carbon (and pyrite)-rich anoxic black shales (necessitating a rigorous clean up protocol of sample gases before mass spectrometry). Prior to this study, the effect of chert formation (from biogenic opal) on extraterrestrial helium preservation was unknown, though informally it was anticipated that this process was likely to lead to helium loss. Cherts are a significant lithological component within both the Scaglia Bianca and, to an extent, the Bonarelli Level, so understanding the impact of chert

formation to the $^3He_{ET}$ record is essential to interpret $^3He_{ET}$ concentrations measured in this lithology. It is hoped that the expansion of the $^3He_{ET}$ technique to include measurements in organic-carbon-rich sediments and in cherts will increase the range of sections considered viable targets for study.

Furthermore, existing methods for the calculation of background $^3He_{ET}$ flux (see Farley and Eltgroth, 2003; Murphy et al., 2010) are deemed to be unsuitable for use in sections, such as the Scaglia Bianca, with drastically changing lithology. It is feared that current methods of 'spot sampling' for background flux may lead to skewed results in sections comprising varying lithologies with different sedimentation rates; in this study, two alternate methods for the calculation of background flux through the Scaglia Bianca are compared with the 'spot sampling' method. The presented record of changing background flux through the Scaglia Bianca also allows investigation of short-term variations in background flux (building on the work of Mukhopadhyay et al., 2001a; Farley et al., 2012); these variations in the flux of $^3He_{ET}$ on timescales of ~10^4 years must be understood and quantified to be accounted for in presented errors on $^3He_{ET}$ timescales.

1.1 Specific research aims

The specific aims of this project were threefold.

1. To develop and test an analytical methodology to allow the creation of $^3He_{ET}$ timescales through the lithologically variable Scaglia Bianca Formation and Bonarelli Level. This required three questions to be addressed:
    a. Could an analytical protocol be developed for extracting helium from lithologically-diverse powdered samples (including cherts, black shales and limestones) using a laser heating system in the Oxford laboratory (such an analytical protocol did not exist prior to this thesis)? Thus far, helium has typically been liberated from such

samples by heating in a vacuum furnace (after Patterson and Farley, 1998); it was hoped that heating using a laser heating system would yield lower blanks.

b. Is extraterrestrial helium lost during silica diagenesis and chert formation?

c. In lithologically diverse sections, what is the most appropriate way to calculate the background flux of $^{3}He_{ET}$?

2. To construct high-resolution $^{3}He_{ET}$ timescales through the limestone-(black shale)-chert cycles of the Scaglia Bianca. These Scaglia Bianca cycles are thought to have been driven by precession cycles, with varying sedimentary expression depending on the amplitude modulation of precessional forcing by short and long eccentricity: alternations of limestone and grey chert are generally thought to correspond to low-amplitude precession cycles, whilst limestone and black chert cycles (containing black shale in some localities) correspond to high-amplitude cycles (Mitchell et al., 2008; Batenburg et al., 2016; Laurin et al., 2016). Questions explored were:

   a. How do sedimentation rates vary through a cycle? Do sedimentation rates measured in the same lithology differ between precession cycles?

   b. How do organic-carbon mass-accumulation rate (OC MAR) and primary productivity vary, both intra- and inter-cycle? How does the primary productivity estimated from organic-carbon rich beds compare to modern high-productivity settings, and does this help distinguish between different models of black shale deposition (as discussed in Herbert and Fischer, 1986; Mitchell et al., 2008; Lanci et al., 2010; Batenburg et al., 2016)?

   c. Do sedimentation rates measured in chert beds provide insight into the deposition method of their pre-diagenesis lithology (thought to be radiolarian sand, e.g. Gambacorta et al., 2014)?

d. Does the flux of terrestrial ^{4}He (which may be used as a proxy for terrigenous input, e.g. Patterson et al., 1999) vary over a cycle and between different cycles?
e. How much time within a cycle is represented by each lithology? Does the distribution of time between different palaeoenvironments differ in cycles deposited under different amplitudes of forcing?

3. To create a $^{3}He_{ET}$ timescale over the Bonarelli Level, the sedimentary expression of Oceanic Anoxic Event 2 in central Italy. Creation of a high-resolution timescale through this record of dramatic climate perturbation, as is possible using $^{3}He_{ET}$ concentrations, provides the relatively rare opportunity to estimate the rates and durations of changes in palaeoenvironment that are recorded in the rapidly shifting lithology over the Bonarelli Level. Multiple questions were explored:
    a. How do sedimentation rates vary through the Bonarelli Level, and are sedimentation rates measured in Bonarelli Level lithologies similar to their pre-Bonarelli counterparts?
    b. What was the magnitude of primary productivity during the deposition of Bonarelli Level black shales? What were the varying contributions of productivity and preservation to the high total organic-carbon contents measured in Bonarelli Level sediments?
    c. What was the total duration of the Bonarelli Level?
    d. Can condensed horizons within the Bonarelli Level be identified? Is there evidence for the hiatuses at its top and base proposed by Tsikos et al. (2004), Jenkyns et al. (2007), Voigt et al. (2007), and Gambacorta et al. (2015)?
    e. Is there evidence for elevated sedimentation rates in the carbonates overlying the Bonarelli Level (similar to those observed after the Palaeocene–Eocene Thermal

Maximum and Cretaceous–Paleogene boundary event by other $^3He_{ET}$ studies (e.g. Mukhopadhyay et al., 2001b; Farley and Eltgroth, 2003; Murphy et al., 2010)?

1.2 Thesis outline

Following the introduction (Chapter 1), this thesis contains a three-part literature review (Chapter 2). The first section of Chapter 2 covers the origin and composition of interplanetary dust particles and their preservation in geological sediments, and the theory behind, and previous use of, $^3He_{ET}$ age models. The second section provides an overview of the Scaglia Bianca Formation (the Late Cretaceous palaeogeography in which it was deposited, its sedimentological description, and its post-depositional history) in order to provide both an understanding of the processes, both syn- and post-depositional, that may have affected the preserved $^3He_{ET}$ record, and to provide context for palaeoenvironmental interpretations presented in later chapters. The final section gives a brief summary of previous palaeoclimatological work on cyclicity in the Cenomanian–Turonian interval and on Oceanic Anoxic Event 2, with an emphasis on their central Italian expressions: the rhythmically bedded Scaglia Bianca and the Bonarelli Level, respectively.

Three data chapters follow. The first (Chapter 3), on 'method development', details the use of the Oxford laboratory's laser heating system in releasing helium from powdered sedimentary samples. The protocol for extracting and measuring extraterrestrial helium is presented, including discussion of sample volumes, packaging and heating methods, as is the clean-up protocol on the mass-spectrometer preparatory line (this clean-up must be sufficient to remove the CO_2, organic compounds and sulphur from organic-carbon and sulphur-rich black shales). The isotopic composition of neon measured in all samples from this study is investigated in order to determine the contribution from different sources of neon to these sediments. Results of $^3He_{ET}$ concentration measured along transects through chert nodules are presented to resolve the question of whether chert formation leads to the loss of extraterrestrial helium.

The second chapter (Chapter 4), on 'high-resolution timescales through precession cycles', presents four high-resolution $^{3}He_{ET}$ timescales constructed through Scaglia Bianca precession cycles. Precession cycles deposited under eccentricity maxima and minima are compared, with changes in lithology, sedimentation rate, organic-carbon mass-accumulation rate and flux of terrestrially sourced helium evaluated. Various methods of constructing background flux through sections with heterogeneous lithology are presented, and a best-practice method proposed.

The third chapter (Chapter 5), on 'a high-resolution timescale through the Bonarelli Level', presents changes in helium concentration, sedimentation rate, and organic-carbon mass accumulation rate through the Bonarelli Level, along with a high-resolution timescale over the section. This exercise allows the determination of a new estimate for the time represented by the Bonarelli Level, along with investigation of condensed horizons, primary productivity changes in black shales, and the sedimentation pattern of post-event carbonates.

The thesis concludes with a brief discussion and synthesis of the results from the data chapters, along with directions for future work (Chapter 6).

2. Literature Review

This thesis deals with the application of the novel $^{3}He_{ET}$ age-model technique to the expression of Oceanic Anoxic Event 2 (OAE 2) in the Umbria–Marche Basin, Italy, and the preceding record of eccentricity-modulated precession cycles, necessitating a three-part review of relevant literature. First, the theory behind the $^{3}He_{ET}$ age-model approach is discussed, including the origin and composition of the extraterrestrial helium-bearing component in marine sediments, and a summary of the previous use of $^{3}He_{ET}$ age-models.

Understanding the context of the studied sections is vital to both interpreting the palaeoenvironmental implications of $^{3}He_{ET}$ results and anticipating processes that may have acted both syn- and post-depositionally to affect the $^{3}He_{ET}$ preserved in sediments. The second part of this review, therefore, gives an overview of the geological setting of the studied sections.

Finally, the interest of this study in creating high-resolution timescales over the rapid palaeoenvironmental changes observed within both Scaglia Bianca precession cycles and over the climatic perturbation OAE 2 requires a summary of previous sedimentological and geochemical work on these sections. Records of orbital cyclicity preserved in the rhythmically bedded Scaglia Bianca are presented in detail, along with hypothesised palaeoclimatic drivers for the observed lithological change. To exhaustively summarise all research on Oceanic Anoxic Event 2 is beyond the scope of this review; a brief overview of global palaeoclimatic change is provided with a focus on the Bonarelli Level, the organic-rich expression of OAE 2 in the Umbria–Marche Basin.

2.1 Extraterrestrial helium, IDPs (interplanetary dust particles) and $^3He_{ET}$ age models

2.1.1 Interplanetary dust particles

The $^3He_{ET}$ age-models constructed in this study are predicated on a supply of helium with an extraterrestrial source and high $^3He/^4He$ ratio carried in interplanetary dust particles (IDPs). Extraterrestrial helium is recognisable in sediments, as the elevated $^3He/^4He$ ratios of IDPs (~2.4×10^{-4} (Nier and Schlutter, 1990, 1992)) contrast sharply with the low $^3He/^4He$ ratios typical of the Earth's crust, which are dominated by the ratio of ^3He to ^4He production (~1.1×10^{-8} (Ballentine and Burnard, 2002)). These distinct endmembers allow the extraterrestrial component of helium in sediments to be deconvolved. The following section presents a brief overview of the origin and composition of the IDPs that carry this extraterrestrial helium component, and their noble gas signatures.

Origin and composition of IDPs

Interplanetary dust particles (IDPs) in our Solar System have a range of origins, from fragmentation of asteroid families to collisions in the Kuiper Belt (Dermott et al., 1994; Flynn, 1996; Liou et al., 1996; Bradley, 2007). Once produced, dust is drawn towards the inner Solar System by Poynting-Robertson drag (a combination of light pressure and radiation drag) and into Earth-crossing orbits (Dohnanyi, 1978; Dermott et al., 2001). Prior to atmospheric entry, IDPs are estimated to have spent 10^4–10^5 years as small particles orbiting the sun: their relatively brief residence time in the Solar System makes the flux of interplanetary dust to the Earth very sensitive to dust production rate on timescales longer than 10^4–10^5 years (Bradley et al., 1984; Farley, 2001).

Measurements from satellites indicate that most IDPs in the vicinity of Earth have diameters on the order of 100 µm (Love and Brownlee, 1993), although those collected in the stratosphere show a size range of 1–50 µm, with most between 5 and 15 µm (Bradley, 2007). The bulk composition of an IDP is typically chondritic, with three principal mineralogical classes based on their most abundant

silicate minerals: ‘pyroxene’, ‘olivine’ and ‘layer silicate’, the latter further divided into ‘smectite’ and ‘serpentine’ classes (Sandford and Walker, 1985; Bradley, 1988). Morphologically, these chondritic IDPs are divided into two types: olivine and pyroxene IDPs are generally ‘porous’, resembling “a bunch of grapes” with high porosity and low density, whilst layer silicate IDPs are ‘smooth’, solid objects with platy or fibrous surface textures (Bradley, 2007). Not all IDPs are chondritic: some are composed of refractory phases and others are single mineral grains of olivine, pyroxene or iron-rich sulphides with adhering chondritic material (Zolensky, 1987; Bradley, 2007).

Noble gas signatures of IDPs

An overview of measurements of helium concentration and isotopic ratio in IDPs separated from marine sediments and captured in the stratosphere is presented in Table 2.1. The abundances and isotopic compositions of noble gases in most IDPs are comparable to lunar fines, and consistent with an implanted solar wind origin (Rajan et al., 1977; Nier and Schlutter, 1990, 1992). Although an alternate solar flare origin has been suggested for the noble gases in IDPs (Amari and Ozima, 1988), a solar wind origin is favoured by most today (Patterson and Farley, 1998; Farley, 2001, 2012; Murphy et al., 2010; Torfstein, 2012). The source of noble gases to IDPs affects not only their isotopic composition, but also the ease with which they may be released: ions implanted by solar wind seldom penetrate more than 0.05 μm (500 Å; Rajan et al., 1977).

Rare IDPs with exceedingly high $^{3}He/^{4}He$ ratios have been investigated; this ‘excess’ ^{3}He (elevated relative to average IDP $^{3}He/^{4}He$ ratios) indicates a much longer exposure to cosmic ray irradiation than most IDPs and these rare particles are thought to have been shed from outer solar system cometary bodies, which have accreted from small particles exposed to intense ^{3}He rich radiation either in the early solar system or in a pre-solar molecular cloud (Pepin et al., 2000).

The helium content of IDPs on Earth may be depleted by diffusive loss during frictional heating in the atmosphere, an effect more pronounced the larger the IDP and the faster its entry velocity.

	sample	^{4}He (cc STP g^{-1})	^{3}He (cc STP g^{-1})	^{3}He/^{4}He
Merrihue, 1964	magnetic separates from marine sediments	1.548×10^{-5}	6.1×10^{-9}	3.94×10^{-4}
Amari and Ozima, 1988	High-temperature fraction of magnetic separates from marine sediments	$5–18 \times 10^{-6}$	$8–40 \times 10^{-10}$	$1.8±0.4 \times 10^{-4}$
Nier et al., 1990	'picked IDPs' from marine sediments	$3.1±0.5 \times 10^{-4}$		$3.1±0.5 \times 10^{-4}$
Rajan et al., 1977	stratospheric IDPs	$2–25 \times 10^{-3}$		
Hudson et al., 1981	stratospheric IDPs			
Nier and Schlutter, 1990	stratospheric IDPs	$5.4±2.0 \times 10^{-2}$		$2.4±0.3 \times 10^{-4}$
Nier and Schlutter, 1992	stratospheric IDPs	$7.6±2.0 \times 10^{-2}$		$3.0±0.3 \times 10^{-4}$
Pepin et al., 2000	stratospheric IDPs			$2.23±0.12 \times 10^{-4}$

Table 2.1: Review of recorded noble gas concentration and ratios in IDPs separated from marine sediments (Merrihue, 1964; Amari and Ozima, 1988; Nier et al., 1990) and captured in the stratosphere (Rajan et al., 1977; Nier and Schlutter, 1990, 1992; Pepin et al., 2000).

Correlation between helium and zinc abundances (zinc depletion is a heating indicator in IDPs) in stratospheric IDPs indicate that, whilst isotopic compositions are consistent with fractionated solar wind, helium is lost through frictional heating during atmospheric entry (Kehm et al., 2002). It is worth noting that as larger IDPs are more likely to lose helium on entry to the atmosphere, and as sampling of stratospheric IDPs is biased towards larger particles (>10 μm), measurements of stratospheric IDPs may underestimate the concentration of helium (and ^{3}He/^{22}Ne) in the 'bulk' of IDPs (Chavrit et al., 2016).

Carrier phase of noble gases in IDPs

The carrier phase of helium in IDPs is important to understand as it is likely to affect the retentivity of extraterrestrial helium in sediments under varying environmental (i.e. redox) conditions. Unfortunately, a definitive identification of the carrier phase of noble gases in IDPs has not yet been reached, though leaching experiments suggest that the host phase(s) of helium in IDPs preserved in

geologically old sediments are consistent with extraterrestrial silicates, Fe-Ni sulphides and possibly magnetite (Mukhopadhyay and Farley, 2006).

Magnetite has long been thought important as a carrier phase, as the high $^{3}He/^{4}He$ ratios indicative of extraterrestrial material are concentrated in the magnetic fraction of pelagic sediments (Amari and Ozima, 1985). Magnetite is attacked by strong HCl; multiple studies have found significant ^{3}He loss in bulk pelagic sediments leached with 3M and 6M HCl, consistent with magnetite as a carrier phase (Fukumoto et al., 1986; Matsuda et al., 1990; Mukhopadhyay and Farley, 2006). IDPs are estimated to contain around 8 wt% primary magnetite, though the thermal shock of atmospheric entry produces secondary magnetite in most IDPs by the decomposition of amorphous silicates. Whether or not appreciable quantities of helium would be lost during this secondary magnetite formation is debated, and it may be that the extraterrestrial carrier phase is simply associated with magnetite (Amari and Ozima, 1985; Mukhopadhyay and Farley, 2006).

However, chemical leaching of sediments with HNO_3 indicate that the dominant carrier of extraterrestrial helium may be different in recent and geologically old sediments. Fukumoto et al. (1986) observed that the extraterrestrial ^{3}He concentration in the magnetic fraction of Quaternary sediments is resistant to HNO_3, consistent with magnetite as the carrier phase, but in Mukhopadhyay and Farley's (2006) HNO_3 leach of 90 Myr old pelagic clay almost 90% of extraterrestrial ^{3}He was lost. This result may indicate that either magnetite is not the dominant carrier phase in geologically old sediment or perhaps that after tens of millions of years on the ocean floor magnetite becomes more susceptible to attack by HNO_3 (Mukhopadhyay and Farley, 2006).

Extraterrestrial silicates are strong candidates for carriers of IDP noble gases in geologically old sediment. Fukumoto et al. (1986) suggested extraterrestrial silicates as an additional carrier phase to magnetite after the observation that approximately 50% of the ^{3}He in Quaternary sediments was contained in the non-magnetic fraction. This finding was reproduced in geologically old sediments by Mukhopadhyay and Farley (2006), who found that approximately 50% of the ^{3}He in 90-Myr-old

pelagic clay was also in the non-magnetic fraction. Both magnetic and non-magnetic components lost close to 90% of their extraterrestrial ^{3}He when leached with 6M HCl, implying that either both magnetic and non-magnetic carriers exist and are both strongly attacked by 6M HCl, or that the carrier is magnetic or associated with a magnetic phase and that the magnetic separation only removed 50% of magnetic grains from the sediment (Fukumoto et al., 1986; Mukhopadhyay and Farley, 2006).

Casting doubt on the viability of extraterrestrial silicates (dominantly olivine, pyroxene and layer silicates) as a carrier phase over geological time is their high potential for diagenetic alteration. Terrestrial layer silicates are stable on the seafloor for millions of years, but even 'layer silicate' IDPs contain significant proportions of anhydrous phases (Thomas et al., 1990). Olivine and pyroxene crystals on the ocean floor, such as those in Mid Ocean Ridge Basalts, undergo alteration within a few million years, and extraterrestrial olivine and pyroxene are likely to behave similarly (Mukhopadhyay and Farley, 2006). For example, Brownlee (1985) described 50-Myr-old cosmic spherules collected from the ocean floor which have been altered to the extent that only magnetite and the iron-rich rims of olivine remain. This finding does, however, demonstrate the long-term stability of magnetite on the ocean floor, and it has been suggested that magnetite rims, formed around olivine and pyroxene crystals during heating on atmospheric entry (Germani et al., 1990; Bradley, 2007) might act as a barrier to protect silicate phases from chemical alteration (Mukhopadhyay and Farley, 2006). This process could also explain the association between the He carrier phase and magnetite in IDPs, suggested to take the form of composite grains, inclusions, or magnetite rims (Mukhopadhyay and Farley, 2006).

Other significant compositional components of IDPs are refractory phases (such as chromite, diamond, SiC, graphite, amorphous carbon, Al_2O_3, and organic material) and Fe-Ni sulphides. Refractory phases are not thought to be a major carrier phase of extraterrestrial ^{3}He, as HF-HCl leaching (to which these phases are resistant) of both recent and 90-Myr-old sediments removed

significant quantities of ^{3}He (Fukumoto et al., 1986; Huss and Lewis, 1995; Mukhopadhyay and Farley, 2006). Although chemical leaches did not remove all ^{3}He, and therefore refractory phases could account for up to 10% of the total, Mukhopadhyay and Farley (2006) favoured incomplete dissolution of the carrier phase as an explanation for this result. By contrast, leaching experiments indicate that Fe-Ni sulphides also have properties consistent with a possible carrier phase of helium in IDPs (Mukhopadhyay and Farley, 2006). If either Fe-Ni sulphides or magnetite are principal carrier phases of extraterrestrial noble gases the long-term retention of these substances in the sedimentary record is likely to be affected by redox conditions (Mukhopadhyay and Farley, 2006).

The question of whether extraterrestrial noble gases have a single major carrier phase or several has been investigated through stepped heating. ^{3}He release-profiles as a function of time from step-heating are the same for both the magnetic and non-magnetic fraction of pelagic clays; this result has been interpreted to suggest a single magnetic, or magnetic-associated, carrier phase incompletely separated between the two fractions (Amari and Ozima, 1985; Mukhopadhyay and Farley, 2006).

A bimodal release of ^{3}He was observed during stepped heating of 90-Myr-old pelagic clays, with around 15% released between 300 and 400°C and around 75% between 450 and 800°C (Mukhopadhyay and Farley, 2006). High $^{3}He/^{4}He$ ratio in both releases is interpreted to suggest that grains contain two reservoirs of extraterrestrial helium: a weakly bound fraction that is released by 400°C and a high-temperature reservoir. Mukhopadhyay and Farley (2006) suggested two possible processes to account for the weakly bound helium fraction. The first follows the work of Ducati et al. (1973): low-temperature release of helium may be from an amorphous layer created on the outer tens of nm of crystals by damage to the lattice from irradiation of IDPs by solar wind and solar flare ions. Solar wind ions implanted at depths of >30 nm would reside in the relatively undamaged crystal lattice and therefore would be lost less readily by diffusion. The second suggestion harks back in some ways to the discussion on the origin of noble gases in IDPs. Solar wind ions may in fact be

responsible only for the 15% of ^{3}He in the low-temperature release, with the high-temperature fraction representing He from solar energetic particles, which are more vigorous and therefore more deeply implanted into minerals. Solar energetic particles are much rarer than solar wind particles: for this hypothesis to be correct over 99% of the solar wind He in IDPs now in sediments must be lost, perhaps by atmospheric entry heating, or by diffusional loss on the seafloor.

2.1.2 IPDs in sediments

The deposition and preservation of $^{3}He_{ET}$-bearing IDPs in sediments is a prerequisite for the construction of $^{3}He_{ET}$ timescales. An overview of previous studies of IDPs in sediment is presented below, along with a summary of processes that impact the deposition and preservation of these particles.

Discovery of IDP contribution to pelagic sediments

Merrihue (1964) was the first to identify extraterrestrial noble gases in a magnetic separate from Pacific red clay. The identification of an extraterrestrial component in pelagic sediments was based on both an elevated concentration of ^{3}He, a common indicator of extraterrestrial material, and on $^{40}Ar/^{36}Ar$, $^{4}He/^{20}Ne$ and $^{20}Ne/^{36}Ar$ ratios. Krylov et al. (1973) found that $^{3}He/^{4}He$ ratios were higher where sedimentation rates were lower in a study comparing Pacific and Atlantic pelagic clays with silty and sandy oozes from the coastal Atlantic. High-temperature heating steps returned the most elevated $^{3}He/^{4}He$ ratios; this result was used to infer that ^{3}He was bound inside minerals of extraterrestrial origin, rather than diffusion of mantle ^{3}He through pelagic oozes. Both Merrihue (1964) and Krylov et al. (1973) estimated that up to 1% of pelagic red clays could be composed of cosmic dust. Ozima et al. (1984) confirmed these results, observing elevated $^{3}He/^{4}He$ and an inverse relationship between ^{3}He concentration and sedimentation rate in a range of pelagic samples from the Pacific and Atlantic oceans. Following this, interest in the extraterrestrial noble gas content of

sediments has taken off, with studies focusing both on long-term records of extraterrestrial dust input (e.g. Takayanagi and Ozima, 1987; Farley, 1995; Farley and Patterson, 1995; Marcantonio et al., 1996; Farley et al., 1998; Patterson and Farley, 1998; Mukhopadhyay et al., 2001a; Farley et al., 2006a; Farley et al., 2012; Chavrit et al., 2016) and on using the relationship between ^{3}He concentration and sedimentation rate to construct age models (e.g. Mukhopadhyay et al., 2001b; Farley and Eltgroth, 2003; Marcantonio et al., 2009; Murphy et al., 2010; Lowery et al., 2018).

In the studies referenced above, extraterrestrial noble gas content was measured from bulk sediment. It is possible to extract individual extraterrestrial particles from both recent and geologically old sediments (e.g. Brownlee, 1985; Grachev et al., 2008; Reshma et al., 2013; Boschi et al., 2017; Schmitz et al., 2017) but, although useful for studying the mineralogy of extraterrestrial particles in pelagic sediments, individual particles have little use in noble gas studies. Their scarcity even in slowly accumulating sediments means that huge volumes of sediment are required to find an appreciable number: extraterrestrial spinels are currently extracted only from carbonates, which may be dissolved in bulk to allow picking of extraterrestrial spinals from a much less voluminous non-carbonate fraction (Boschi et al., 2017; Schmitz et al., 2017), and studies of microspherules focus only on the magnetic fraction (Grachev et al., 2008; Reshma et al., 2013). From these extracts, extraterrestrial particles are then identified visually, which introduces a further collection bias towards larger particles (Brownlee, 1985; Grachev et al., 2008). For this reason, studies of extraterrestrial noble gases are performed on bulk sediment.

Size distribution of helium-bearing IDPs

Understanding the size distribution of helium-bearing IDPs that reach Earth is critical to understanding their distribution in pelagic sediments. If helium-bearing IDPs are significantly smaller or larger, and/or less or more dense, than the surrounding bulk sediment they are more likely to be concentrated or depleted by processes such as winnowing. In addition, whilst small IDPs are fairly

ubiquitous in sediments, large particles are rare (Farley, 2001). If a significant proportion of extraterrestrial helium is carried by rare, large IDPs, the probability of any given sample containing such a grain is low and a typical sediment aliquot is likely to statistically under sample the overall ^{3}He flux, the so-called “nugget effect” (Farley, 2001).

Measurements from satellites indicate that IDPs in the vicinity of Earth have a range of sizes from 1–500 μm, though the mass flux to Earth is dominated by 200 μm particles (Love and Brownlee, 1993). However, as the degree of helium loss during atmospheric entry is partially dependent on particle size, most of the extraterrestrial helium on the seafloor is expected to be carried by very small IDPs (Ozima et al., 1984; Farley et al., 1997). Helium is lost during entry heating either by melting of the grain or by diffusive loss (Farley, 2001). The degree of heating of an IDP during atmospheric entry depends on its size, density, velocity and entry angle (Love and Brownlee, 1991). Mild heating is associated with small particle size, low entry velocity and low entry angle (though not so low that the particle ‘skips’ back out of the atmosphere).

The size distribution of helium-bearing IDPs in sediment has been estimated by two complementary methods: quantitative modelling of atmospheric entry heating of IDPs (characterising the size distribution of IDPs that do not experience significant helium loss and hence carry extraterrestrial He to the sea floor), and measuring helium release from different size fractions of ocean sediment (Farley et al., 1997; Mukhopadhyay and Farley, 2006; McGee et al., 2010; Torfstein, 2012).

The modelling work of Farley et al. (1997) calculated that only a very small fraction of the infalling dust passes through the atmosphere without being heated to temperatures greater than that required for He release (~600°C). The size distribution of these ‘He-retaining’ particles is much smaller than that of the parent population. Around 0.5% of the mass of total incident dust is predicted to transit the atmosphere without substantial helium loss; most of the mass is carried by particles between 10 and 100 μm in diameter. However, as extraterrestrial helium is thought to have an implanted solar-wind origin, the most important consideration may in fact be surface area

delivery. Smaller particles account for a larger proportion of surface area by mass, and in this model around 4% of the surface area of the incident dust transits the atmosphere, with most ^{3}He (70%) carried by particles of 3–35 μm diameter (Farley et al., 1997).

Examination of the heating patterns of Antarctic micrometeorites has indicated that it is theoretically possible for extraterrestrial ^{3}He to be preserved in larger particles than models would indicate: a proportion of 50–100 μm micrometeorites examined by Stuart et al. (1999) were found to have un-melted cores, incompatible with typical heating-model assumption of isothermal heating of such particles (Love and Brownlee, 1991). As larger particles, particularly those with melt rims, may be more resistant to alteration, Stuart et al. (1999) theorised that 50–100 μm micrometeorites may be the primary extraterrestrial ^{3}He carrier in geologically old sediments. However, more recent sieving experiments on Oligocene pelagic clays demonstrate that at most 20% of ^{3}He is carried by particles greater than 50 μm in diameter (Mukhopadhyay and Farley, 2006), consistent with the larger body of sieving experiments suggesting that most extraterrestrial ^{3}He is found in the small size fraction (Brook et al., 2009; McGee et al., 2010; Torfstein, 2012; Chavrit et al., 2016).

In fact, there is growing evidence that extraterrestrial ^{3}He may be more concentrated in fine-grained particles than models have predicted. Whilst Farley et al. (1997) predicted that the majority of the ^{3}He flux would be delivered by particles in the 5–10 μm size range, McGee et al. (2010) estimated that the majority of ^{3}He-bearing grains had diameters <4 μm, and Torfstein (2012) estimated that around half of extraterrestrial ^{3}He was found in <2 μm particles. This concentration of extraterrestrial ^{3}He in very fine-grained particles means that the under-sampling of $^{3}He_{ET}$ predicted by Farley (2001) is less significant, as clay-sized particles are distributed more homogeneously; reproducibility of extraterrestrial ^{3}He as measured in sediments is indeed found to be better than model predictions (Torfstein, 2012).

Sedimentary re-distribution of IDPs

Before it is possible to use extraterrestrial ^{3}He measured in sediments as a proxy for sedimentation rate, or to estimate IDP flux to Earth, the possible focusing and redistribution effects that act on IDPs must be understood.

IDPs are not thought to be significantly redistributed in transport through the atmosphere. Particles in the size range 3–35 μm (the size range of ^{3}He bearing IDPs predicted by Farley et al. (1997)) are not transported far in the stratosphere and are removed rapidly from the troposphere by rain-out events (Farley et al., 1997, after Sigurdsson, 1990).

However, the question of whether IDPs are redistributed during transport in the ocean is more open-ended, as the settling time of particles through the water column is highly dependent on their size, density, and tendency to flocculate. Individual IDPs with diameters of around 10 μm are estimated to settle through a 5 km water column in less than 10 years, based on both experimental results and settling equations (Raudkivi, 1990; McCave and Gross, 1991; Zhiyao et al., 2008). This timescale is rapid compared to horizontal ocean circulation rates, so redistribution effects are unlikely to be large (Farley et al., 1997). By contrast, if IDPs with 2 μm diameters remain solitary in the water column they would be expected to settle much more slowly: estimates of the time taken to settle through 5 km vary from tens of years (McCave and Gross, 1991; Stokes Law) to thousands of years (Zhiyao et al., 2008, a settling equation for 'natural' conditions). Over these longer timescales redistribution through transport during ocean circulation becomes more likely. However, flocculation of IDPs with other small particles as marine snow is expected to greatly decrease settling time; variations in shape and density are not thought to significantly affect settling velocity, so flocculated particles with a larger effective diameter would be expected to settle faster (Fowler and Knauer, 1986; McCave and Gross, 1991).

Once deposited, IDPs may later be reworked, raising the possibility that they may be concentrated or depleted in certain regions. Whether the action of currents produces a relative depletion or

concentration effect depends partly on the size of $^{3}He_{ET}$-bearing grains compared to the surrounding sediment, and partly on their relative density. ^{3}He-bearing IDPs with diameters of around 10 µm are slightly smaller than the bulk of carbonate sediments but larger than pelagic clays. The expected densities of IDPs vary: around 50% are composed primarily of layer silicates, so would be expected to have a similar density to clays, whilst the other ~50% are dominated by denser pyroxene and olivine (Bradley, 1988). Overall, winnowing is expected to increase local $^{3}He_{ET}$ concentration in clays and decrease it in carbonates, though this effect is thought to be small (Farley et al., 1997; Farley, 2001). The smaller size estimate for ^{3}He-bearing IDPs indicates that these particles are clay-sized and would therefore behave during redistribution like pelagic clays (Torfstein, 2012).

Evidence for the effects of sedimentary focusing on local $^{3}He_{ET}$ burial rate is debated. Although it has been argued that focusing effects acted to vary the local $^{3}He_{ET}$ burial rate by a factor of five through the Quaternary, with a cyclical temporal pattern reflecting climate driven reorganisation of bottom currents (Farley and Patterson, 1995; Marcantonio et al., 1995, 1996), a more recent study evaluating the consistency of both $^{3}He_{ET}$- and $^{230}Th_{xs}$-derived mass accumulation rates through glacial–interglacial cycles indicates, by contrast, that lateral advection did not substantially bias $^{3}He_{ET}$-based mass accumulation estimates (McGee et al., 2010). Although $^{3}He_{ET}$ is concentrated in fine particles which might be expected to be winnowed, the cohesiveness of these fine-grained sediments is thought to limit their fractionation relative to a coarser grain size (McGee et al., 2010). The potential extent and effects of sedimentary redistribution must be carefully considered in any study. Preferential migration of IDPs relative to the surrounding sediment is judged unlikely in deep sea sections, as IDPs are not significantly different in size from most marine sediments (Farley, 2001).

Post-depositional redistribution of helium is possible through physical mixing processes such as bioturbation (Farley, 2001). The effect of bioturbation on a $^{3}He_{ET}$ record in a sedimentary section is to smear the $^{3}He_{ET}$ signal across the depth of bioturbation: in modern oxygenated continental slope

and basin settings the bioturbation-induced mixed layer has been estimated ~3–12 cm on the basis of ^{210}Pb profiles (Stordal et al., 1985; Henderson et al., 1999; Smith et al., 2000). This smearing is a factor that must be considered when choosing sampling resolution. Post-depositional chemical redistribution is unlikely. Once helium is liberated from its carrier it is likely to escape through the sedimentary pore space to the atmosphere, and from there to space, and is unlikely to be reincorporated into the sedimentary solids that are measured in studies of sedimentary helium (Farley, 2001).

IDP preservation in geological sediments

Extraterrestrial He has the potential to be preserved in the sedimentary record over geological timescales (e.g. Farley and Patterson, 1995; Mukhopadhyay et al., 2001a; Farley et al., 2012), with the oldest extraterrestrial ^{3}He yet identified from 450 Ma Ordovician sediments (Patterson et al., 1998). Nevertheless, post-depositional loss of extraterrestrial He is a process that must be considered.

If, as suggested by Mukhopadhyay and Farley (2006), Fe-Ni sulphides and magnetite are possible carrier phases of extraterrestrial helium (see Section 2.1.1), the long-term retention of extraterrestrial helium may depend on the redox conditions within sediment pore waters. Fe sulphides in particular are stable only in a relatively narrow range of Eh and pH conditions, though their ability to retain extraterrestrial helium over geological time is still not well understood (Mukhopadhyay and Farley, 2006).

The most significant cause of post-depositional helium loss is thought to be heating-induced diffusive loss. The absolute value of ^{3}He loss by diffusion will depend on the size and shape of the IDPs in the sediment, along with the chemistry and mineral structure of the carrier phase, and the $^{3}He_{ET}$ concentration profile within the mineral (Mukhopadhyay and Farley, 2006). Extrapolating back from a high-temperature (450–800°C) ^{3}He diffusion profile created using stepped heating

experiments, Mukhopadhyay and Farley (2006) suggested helium diffusivity in IDPs of $2x10^{-17}$ cm^2/s at a modern 'seafloor temperature' of 2°C. However, this value must be considered with extreme caution as diffusivity is extrapolated over many orders of magnitude (Mukhopadhyay and Farley, 2006); quantitative estimations of the fraction of extraterrestrial helium loss based on a section's history are therefore judged to be too inaccurate to be useful. Despite this, it is still qualitatively evident that different stratigraphic sections from the same time period may have experienced differing degrees of helium loss depending on their thermal and exposure history. Heating associated with extended deep burial in sedimentary basins is, for example, likely to result in a significant loss of ^{3}He (Hiyagon, 1994; Mukhopadhyay and Farley, 2006). $^3He_{ET}$ loss has also been suggested to occur due to decomposition of ^{3}He-bearing magnetic grains under subaerial exposure, with surviving helium is held in a second, more resistant carrier (Mukhopadhyay et al., 2001a). Evidence of differing degrees of $^3He_{ET}$ loss in different stratigraphic sections comes from comparison between an extraterrestrial ^{3}He flux record of Cretaceous and Cenozoic age from a terrestrial section in the Italian Apennines and a record of the same age from a pelagic clay core, in which, although the ^{3}He flux pattern was the same, the absolute values in the terrestrial section were a factor of four lower (Mukhopadhyay et al., 2001a).

2.1.3 Theory of $^3He_{ET}$ age models

Creating $^3He_{ET}$ age models

The concentration of extraterrestrial ^{3}He in sediments has long been recognised as inversely proportional to sedimentation rate (Krylov et al., 1973; Ozima et al., 1984). The concentration of $^3He_{ET}$ in sediments reflects the dilution of helium-bearing IDPs by other types of sedimentation. This relationship was codified by Takayanagi and Ozima (1987) as follows:

$$[^3He_{ET}] = F / \alpha \qquad \text{Equation 2.1}$$

where [$^3He_{ET}$] is the concentration of extraterrestrial ^3He (ccSTP/g), F is the background flux of extraterrestrial ^3He into sediments (ccSTP/cm^2/yr) and α is the mass accumulation rate of sediment (g/cm^2/yr). This simple equation can be used both to determine sedimentation rate in sections with known and constant background flux, and to examine long-term changes in $^3He_{ET}$ background flux in sections where sedimentation rate is known (Farley, 2001).

As $^3He_{ET}$ age models provide an instantaneous sedimentation rate for each sample measured, they are most suitable for use in sections with rapid changes in sedimentation rate (Murphy et al., 2010). $^3He_{ET}$ age models are a powerful tool for examining the pacing of rapid climate perturbations, such as Oceanic Anoxic Events, whose sedimentary record shows dramatic lithological changes. Cyclostratigraphy, an alternate method of constructing age models, is often difficult to use in sections containing dramatic lithological changes, as these sudden shifts may make periodic variations (in, for example, concentrations of sedimentary components) difficult to identify, meaning that they may be missed or misinterpreted. As the resolution of $^3He_{ET}$ age models is, in theory, limited only by sampling resolution, they also have the potential to be used to unpick the changing sedimentation rates within precession cycles (~20 kyrs), the smallest unit of cyclostratigraphic measurement. Although, in reality, the smearing effect of bioturbation means that depth of burrowing limits the maximum resolution, $^3He_{ET}$ age-models remain a powerful tool when combined with other sedimentological observations.

As expanded upon later in this section, when constructing a $^3He_{ET}$ age model, it is first necessary to deconvolve the extraterrestrial helium component from the overall helium measured in the sediment. Then, background flux is calculated from a section with known sedimentation rate close, both spatially and temporally, to the section of interest (Murphy et al., 2010). An age model is constructed by integrating $^3He_{ET}$-based sedimentation rates (calculated using Equation 2.1) through the section.

Deconvolving the extraterrestrial component of helium in sediments

Potential sources of helium to marine sediments include extraterrestrial helium from IDPs, atmospheric (air-derived) helium, helium derived from cosmic ray spallation, mantle-derived helium delivered to the seabed from rocks in both continental and oceanic settings, and radiogenic ^{4}He and nucleogenic ^{3}He carried in terrigenous detrital material.

Most studies consider that the only significant sources of helium to sediments are IDPs carrying extraterrestrial helium, and detrital terrestrial material carrying helium with a crustal signature (Merrihue, 1964; Ozima et al., 1984; Fukumoto et al., 1986; Takayanagi and Ozima, 1987; Amari and Ozima, 1988; Farley and Patterson, 1995; Marcantonio et al., 1995, 2009; Patterson and Farley, 1998; Farley, 2001; Mukhopadhyay et al., 2001a, 2001b; Farley and Eltgroth, 2003; McGee et al., 2010; Farley et al., 2012; Torfstein, 2012; Chavrit et al., 2016), but all potential sources of helium will be considered in turn below.

The low concentration of helium in air makes the atmosphere unlikely to be a significant source of helium to marine sediments (Farley, 2001). The likelihood of a significant contribution to ^{3}He is even lower, due to air's low isotopic ratio. (Atmospheric helium concentrations are $5.24\pm0.05 \times10^{-6}$ ppv and $7.34\pm0.07 \times10^{-15}$ ppv for ^{4}He and ^{3}He, respectively (Porcelli et al., 2002)). Estimations of air-derived helium in marine sediments, calculated using the abundance of Ne and the assumed He/Ne ration of the air-derived component, indicate that only around 1% of the total ^{3}He is air-derived, making this a negligible source of ^{3}He to marine sediments (Farley, 2001; Mukhopadhyay et al., 2001a).

Spallogenic helium produced by cosmic rays at the Earth's surface, and transported to the deep ocean in detrital minerals, is another potential source of ^{3}He in marine sediments (Farley, 2001). However, detrital material carried to the deep sea tends to be derived from a small fraction of the Earth's surface, so the delivery of spallogenic ^{3}He to the sea floor is a small fraction of the mean global production rate (Farley, 2001). In addition, common detrital minerals such as clays are not

thought to retain much cosmic-ray helium, suggesting that the spallogenic ^{3}He component of deep-marine sediments is negligibly small (Farley and Patterson, 1995; Farley, 2001; Mukhopadhyay et al., 2001a).

Mantle-derived ^{3}He may be delivered to the seabed in detrital material, trapped in fluid intrusions and vesicles of some igneous and metamorphic rocks (Farley, 2001). Despite one dissenting study (Marcantonio et al., 1998), mantle helium is not thought to be a significant contributor to ^{3}He in deep-marine sediments, largely because even if the source rocks have high mantle helium contents, the process of chemical alteration and weathering to the fine grain sizes delivered to the ocean is likely to break open fluid inclusions and vesicles and allow trapped helium to escape (Kurz et al., 1996; Farley, 2001).

Radiogenic ^{4}He, on the other hand, is thought to be a significant contributor to the helium content of deep-sea sediments. It is held mostly in detrital minerals of terrestrial origin as, although carbonate contains fairly high U contents, it hosts little to no helium, perhaps because energetic alpha particles are ejected from high surface-area carbonate grains after production (Patterson and Farley, 1998; Farley, 2001). The radiogenic detrital component of deep-sea sediments is often considered to have a $^{3}He/^{4}He$ ratio between 1–4 $\times 10^{-8}$, a typical crustal value (Takayanagi and Ozima, 1987; Amari and Ozima, 1988; Farley and Patterson, 1995; Marcantonio et al., 1995; Patterson and Farley, 1998; Farley, 2001; Farley and Eltgroth, 2003; Farley et al., 2012), though some studies have instead calculated a site-specific terrestrial end-member (McGee et al., 2010; Torfstein, 2012; Chavrit et al., 2016).

The source of terrigenous helium-bearing material to the pelagic sites examined in the studies above is widely considered to be wind-blown dust, though river-borne and ice-rafted sediment may be locally important (Farley and Patterson, 1995; Marcantonio et al., 1998). In places where the specific source region of the terrigenous material reaching a section is known, its $^{3}He/^{4}He$ may be used as a site-specific terrestrial end-member; McGee et al. (2010), for example, used the helium composition

of North Atlantic glacial detrital sediments as the terrestrial end-member for Holocene and Last Glacial Maximum sediments in that region. Over many (primarily European and North Atlantic) sections, however, the composition of terrestrial end-member is more generally assumed to be based on the average ratio of the upper continental crust, ~2×10^{-8}, noting that the helium composition of Chinese loess samples reflect this average crustal value (Farley and Patterson, 1995; Patterson and Farley, 1998; Farley, 2001; Mukhopadhyay et al., 2001a, 2001b; Murphy et al., 2010; Farley et al., 2012).

The contribution of radiogenic helium produced post-depositionally is thought to be minimal. Though there is no reason for the radiogenic production of ^{4}He from uranium hosted in zircon, apatite or rutile within the terrigenous fraction to cease during the erosion of these minerals to transportable dust, or their burial in pelagic sediments, most if not all radiogenic ^{4}He is likely to be lost after production as the grain size of the host phase is typically smaller than the recoil distance of high-energy alpha particles, allowing ^{4}He to escape (see Ballentine and Burnard, 2002; Torfstein, 2012).

In sediments with a substantial amount of radiogenic ^{4}He, nucleogenic ^{3}He from the reaction $^{6}Li(n,\alpha)\rightarrow{}^{3}H\rightarrow{}^{\beta3}He$ is also likely to be present (Farley, 2001; Mukhopadhyay et al., 2001a). The overall $^{3}He/^{4}He$ ratio of the radiogenic detrital component is therefore highly dependent on the concentration of Li in the sediments (Andrews, 1985). Nucleogenic $^{3}He/^{4}He$ ratios in typical sedimentary lithologies vary: with ratios of 0.23×10^{-8} in limestones with Li contents of 5 µg/g, and 1.97×10^{-8} in clays and shales with Li contents of 60 µg/g (Andrews, 1985). Farley (2001) suggests quantifying the nucleogenic ^{3}He component by assuming a production ratio of radiogenic ^{4}He and nucleogenic ^{3}He, though the value of this production ratio is uncertain. The best way of assessing the nucleogenic ^{3}He contribution to sediment is likely to be by measuring the Li concentration and calculating the expected $^{3}He/^{4}He$ production ratio (Mukhopadhyay et al., 2001a).

The actual deconvolution of the various components of He in marine sediments is typically carried out using a two-component mixing model (Patterson and Farley, 1998). This model assumes that the only major contributors of helium to the sediment are IDPs with an extraterrestrial signature and terrestrial detrital material with a radiogenic signature. The concentration of extraterrestrial ^{3}He ($[^3He_{ET}]$) is calculated from the total observed ^{3}He concentration ($[^3He_{observed}]$) and observed $^3He/^4He$ ratio, provided that the $^3He/^4He$ ratios of the terrestrial and extraterrestrial end-members are known:

$$[^3He_{ET}] = [^3He_{observed}] \times (^4He/^3He_{observed} - {}^4He/^3He_{terrestrial})/(^4He/^3He_{ET} - {}^4He/^3He_{terrestrial})$$

Equation 2.2

Table 2.2 presents a summary of the end-member values used in various studies. The $^3He/^4He$ ratio of the extraterrestrial end-member is typically taken as 2.4×10^{-4}, the average of measurements of individual IDPs by Nier and Schlutter (1990, 1992), though a different 'average IDP' value 3.6×10^{-4} has also been used (c.f. Farley, 1995; Marcantonio et al., 1995, 2009; McGee et al., 2010; Farley et al., 2012; Chavrit et al., 2016). The $^3He/^4He$ ratios of chosen terrestrial endmembers typically lie between $1\text{-}4\times10^{-8}$.

As shown in Figure 2.1, the $^3He_{ET}$ fraction estimated from observed $^3He/^4He$ is relatively insensitive to the choice of extraterrestrial end-member, but very sensitive to the choice of terrestrial end-member in samples with a higher fraction of terrestrial ^{3}He and lower measured $^3He/^4He$ ratios. For this reason, it is preferable to work on sections with $^3He/^4He$ ratios indicative of little contribution of terrestrial ^{3}He, as these are less sensitive to errors in estimated $^3He_{ET}$ fraction caused by incorrect end-member values (Patterson and Farley, 1998; Farley, 2001; Farley and Eltgroth, 2003; Farley et al., 2012).

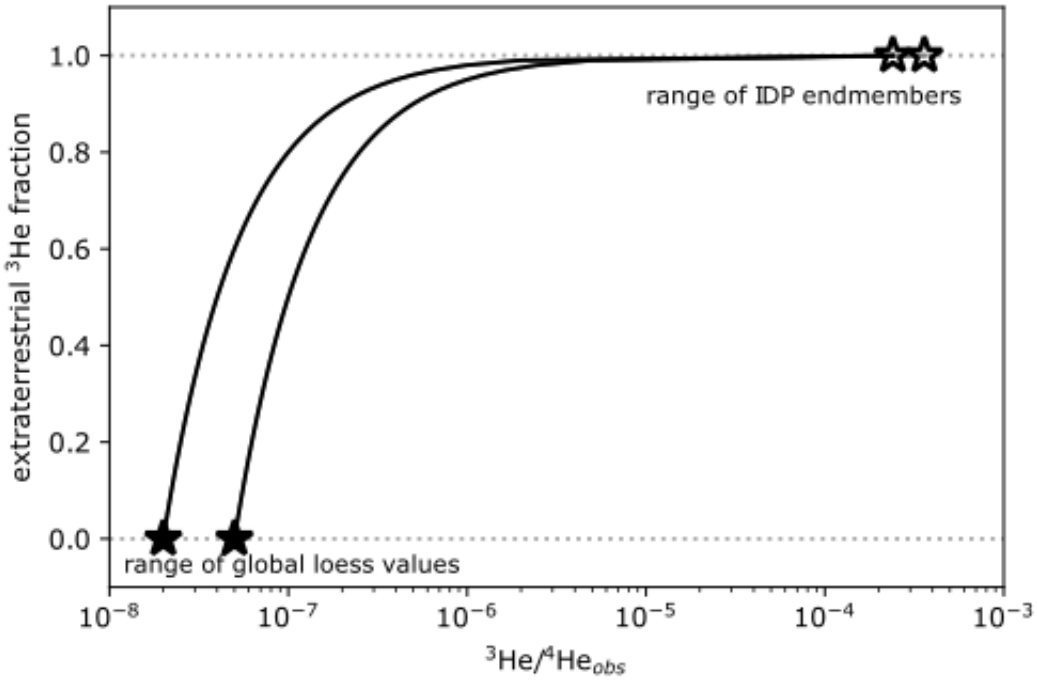

Figure 2.1: Fraction of extraterrestrial ^{3}He in a sample against observed $^3He/^4He$ ratio (after Farley, 2001), showing mixing lines between a range of different endmembers. Extraterrestrial end-members from the literature are represented by open stars, terrestrial end-members by filled stars. As can be seen from shape of this graph, the $^3He_{ET}$ fraction estimated from observed $^3He/^4He$ is relatively insensitive to the choice of extraterrestrial end-member, but very sensitive to the choice of terrestrial end-member in samples with a higher fraction of terrestrial ^{3}He. Mixing lines originating from either end of the plotted range of extraterrestrial end-members cannot be distinguished from this graph, as they plot on top of one another.

It has been suggested that the helium contributed by each end-member may be separated through stepped heating (Farley, 2001). A bimodal release of ^{3}He at ~400°C and ~900°C is observed across stepped heating studies, with the helium released in the high-temperature peak having a distinctly extraterrestrial signature (Amari and Ozima, 1988; Matsuda et al., 1990; Hiyagon, 1994; Farley, 2001; Mukhopadhyay and Farley, 2006). However, though Farley (2001) proposed that the helium released in the lower temperature peak was entirely nucleogenic/radiogenic and cosmogenic in origin, Mukhopadhyay and Farley (2006) concluded that extraterrestrial helium is also liberated at these lower temperatures. For this reason, stepped heating is not typically used to separate the extraterrestrial component of ^{3}He.

Study	$^3He/^4He$ of Terrestrial Endmember	Comments	$^3He/^4He$ of Extraterrestrial Endmember	Comments
Ozima et al., 1984	*not given*		4×10^{-4}	value of implanted solar wind
Takayanagi and Ozima, 1987	1×10^{-8}	deep-ocean sediment value from Ozima and Podosek (1983)	2×10^{-4}	solar flare ratio
Farley, 1995	2×10^{-8}	'crustal helium' from Andrews (1985)	2×10^{-4}	IDP value of Nier and Schlutter (1990)
Farley and Patterson, 1995	2×10^{-8}	average crustal ratio observed in Chinese loess	*not given*	
Marcantonio et al., 1995	1×10^{-8}	from Ozima and Podosek (1983)	2.4×10^{-4}	from individual IDPs measured in the atmosphere by Nier and Schlutter (1990, 1992)
Patterson and Farley, 1998	2.09×10^{-8}	average value from Chinese loess from Farley and Patterson (1995)	4×10^{-4}	similar to ratio observed in the solar wind (Geiss et al., 1972) and in bulk lunar fines (Nier and Schlutter, 1990)
Farley, 2001	4×10^{-8}	average of Chinese loess samples	1.40×10^{-4}	maximum ratio measured in sediments
Mukhopadhyay et al., 2001a	4.17×10^{-8}	average value from Chinese loess from Farley and Patterson (1995)	1.39×10^{-4}	from solar wind (Geiss et al., 1972) and bulk lunar fines (Nier and Schlutter, 1990)
Mukhopadhyay et al., 2001b	4.14×10^{-8}	average of Chinese loess samples from Farley (2001)	4×10^{-4}	bulk lunar fines value of Nier and Schlutter (1990)
Farley and Eltgroth, 2003	4×10^{-8}	results compared assuming a range of end-member values between 2×10^{-8} and 6×10^{-8}	*not given*	
Marcantonio et al., 2009	10^{-6}–10^{-8}	values from a range of terrestrial sources from Marcantonio et al. (1998)	2.41×10^{-4}	endmember value calculated from data, agrees with IDP value of Nier and Schlutter (1992)
McGee et al., 2010	1×10^{-8}	chosen as an average of previous measurements of North Atlantic sediments	2.4×10^{-4}	IDP value of Nier and Schlutter (1990, 1992)
Murphy et al., 2010	2.1×10^{-8}	after Farley (2001)	4×10^{-4}	after Farley (2001)

Farley et al., 2012	$2–4\times10^{-8}$	'average terrestrial crust' after Marcantonio et al. (1998); Farley (2001)	2.4×10^{-4}	IDP value of Nier and Schlutter (1990, 1992)
Torfstein, 2012	2.93×10^{-7}	site specific dust end member: 'South East Asia <4 mm loess fraction' from <4 mm fraction of a mud crust sample, Taklimakan Desert, China (McGee, 2010)	3.82×10^{-4}	calculated from a regression curve
Chavrit et al., 2016	9×10^{-8}	composition of the study's most radiogenic sample	3.64×10^{-4}	average IDP value – equal to composition of implanted solar wind from Eberhardt et al. (1972)

Table 2.2: Review of end-member values used in the deconvolution of helium in marine sediments. The ratios used in deconvolution calculations in each study are presented, along with a comment as to their origin. The terrestrial end-member $^{3}He/^{4}He$ ratio of 2.93×10^{-7} used by Torfstein (2012) is significantly higher than typical crustal values, which are less than ~5×10^{-8} in tectonically stable areas (e.g. Mamyrin and Tolstikhin, 1984; Andrews, 1985; Oxburgh and O'nions, 1987). Torfstein (2012)'s choice of terrestrial end-member ratio should, perhaps, be regarded as anomalous; it originated from measurements of the <4 mm fraction of a single mud crust sample, and was an order of magnitude higher than other Chinese loess samples measured in the same study (McGee, 2010).

Determining background flux

If using Equation 2.1 ($[^3He_{ET}] = F/\alpha$) to calculate the sedimentation rate (α) from the concentration of extraterrestrial ^3He ($[^3He_{ET}]$), the section of interest must have a known, stable background flux (F). This proviso limits the use of $^3He_{ET}$ age models to geologically short time periods over which the background flux is not thought to have changed dramatically. An incorrect determination of background flux will affect the entire age model; errors in sedimentation rates from $^3He_{ET}$ models are often propagated solely from uncertainty in background flux, reflecting its status as the most significant source of error (Farley and Eltgroth, 2003; Murphy et al., 2010).

When determining the background flux for use in Equation 2.1, what is actually being calculated is the 'apparent' background flux. As explored in Section 2.1.2, many factors can lead to geographically separated locations having a distinct 'local' apparent background flux, even if sediments were deposited over the same time period. For example, 'local' background flux over the PETM interval was found to vary by about a factor of 3 between sites in the North Atlantic and Pacific: between 2.2 and 6.9×10^{-17} ccSTP/cm^2/yr (Murphy et al., 2010). This range of values may be due to regional focusing effects or different diagenetic histories which systematically affect the concentration of extraterrestrial helium deposited and/or preserved in each section. That these effects have a systematic, rather than random, effect on the concentration of extraterrestrial helium in these sections is confirmed by long-term studies of background flux at different sites, which show the same patterns of variation in $^3He_{ET}$ flux over time (Farley et al., 2006a, Chavrit et al., 2016). Another factor which systematically impacts 'apparent' background flux is diffusive helium loss in geologically old sections, in which the 'apparent' background flux measured is likely to be much lower than the actual contemporary flux from space (Farley, 2001). In addition, due to the rarity of helium-bearing IDPs and their uneven distribution in the sediment, measurements of typical aliquots of sediment (2–3 g) systematically underestimate the $^3He_{ET}$ flux (Farley et al., 1997; Mukhopadhyay et al., 2001a). It is key to the accuracy of $^3He_{ET}$ age models that any proportional depletion of measured $[^3He_{ET}]$ from its original 'true' value is the same in the measurements used for both the background flux and

the age model. This circumstance is generally held to be true if the background flux is calculated from a section close both spatially and temporally to the section of interest (i.e. from the same location in sediments that are stratigraphically adjacent to the main interval of interest), and means that the systematic error in [$^3He_{ET}$] and F cancel out on either side of Equation 2.1, allowing the calculation of an absolute sedimentation rate (Mukhopadhyay et al., 2001a; Murphy et al., 2010).

Background flux is calculated over an interval where sedimentation rate is known using Equation 2.1. This method of calculating background flux places another limitation on the use of $^3He_{ET}$ age models: target sections must be close, spatially and temporally, to a section with a known sedimentation rate. This is usually a section that is rhythmically bedded and suitable for cyclostratigraphy, but sedimentation rates can also be calculated from magnetostratigraphic chron boundaries or, conceivably, from biostratigraphy (Farley and Eltgroth, 2003; Murphy et al., 2010).

In published studies, background flux has been calculated from instantaneous flux measurements from samples evenly spaced through an interval before the section of interest (e.g. 15 samples over 120 kyr, Murphy et al., 2010; 15 samples over ~3 Myr, Farley and Eltgroth, 2003). These samples may be combined and analysed in replicate, with average flux over the interval calculated using an average mass accumulation rate (Farley and Eltgroth, 2003; Murphy et al., 2010). Alternatively, background flux can be calculated from each point sample using the average sedimentation rate, and these values averaged; this methodology has the benefit of showing whether there are any trends through the section (Murphy et al., 2010). When applied to the same section, both these methods return a very similar value for background flux (Murphy et al., 2010). However, when calculating 'point' background flux it is necessary to assume that there was no variation in sedimentation rates at a resolution below that at which the average sedimentation rate was calculated, e.g., no sub-precessional variation in section where sediment rates are calculated using cyclostratigraphy (Murphy et al., 2010).

Another important consideration is how much background flux varied over the time interval of interest. Variation of background $^3He_{ET}$ flux over time has itself been the subject of several studies (Farley, 1995, 2001; Farley et al., 1998, 2012; Patterson and Farley, 1998; Mukhopadhyay et al., 2001b). Over the Cretaceous, background flux varied by about an order of magnitude, from 0.5–6 $\times 10^{-15}$ ccSTP/cm^2/yr, with 'spikes' in background $^3He_{ET}$ flux associated with comet showers or asteroid collisions (Farley et al., 2012). Even over the shorter timescales (100s of kyr) for which $^3He_{ET}$ age models are judged to be most appropriate, apparent background flux may vary. Although periodic 100 kyr variations in background flux, once proposed through the Quaternary by Farley and Patterson (1995), have been rejected as explained by the effect of sediment focussing and local burial rates (Marcantonio et al., 1996), Farley et al. (2012) observed variation with 1σ = 35% in the apparent background flux over the 400 kyr prior to deposition of the Bonarelli Level.

Reproducibility

Reproducibility of [^{3}He] measurements is lower than would be expected from analytical uncertainty; this effect is thought to be due to the statistically small number of helium-bearing IDPs in aliquots of sediment measured (Farley and Patterson, 1995). Although very small IDPs are abundant enough to be statistically well represented, large particles are sufficiently rare to be seldom measured at all. IDPs of intermediate size may or may not be present in a given sample (Farley et al., 1997).

Predicted reproducibility depends, in part, on the size distribution of extraterrestrial helium-bearing particles. It may be the case that most $^3He_{ET}$ is carried by IDPs ~20 µm; a 'typical' sample aliquot of 2–3 g contains on average only one such particle (Farley et al., 1997; Patterson and Farley, 1998). Smaller IDPs are more common; it has been suggested that the significant size-fraction for $^3He_{ET}$-bearing IDPs is ~2 µm, with a 'typical' sample expected to contain tens of IDPs of this size (Torfstein, 2012).

An observation common to studies of $^{3}He_{ET}$ in marine sediments is also that a small number of samples contain significantly higher ^{3}He concentrations and $^{3}He/^{4}He$ ratios, indicative of a significantly elevated $^{3}He_{ET}$ content (Farley et al., 1997; Patterson and Farley, 1998; Mukhopadhyay et al., 2001a; Torfstein, 2012). These samples are thought to contain rare 'helium-rich particles'. Initially assumed to be large particles carrying a correspondingly large volume of $^{3}He_{ET}$, recent sieving experiments suggest that they may instead be smaller particles with a higher than usual concentration of extraterrestrial helium (Patterson and Farley, 1998; Mukhopadhyay et al., 2001a; Torfstein, 2012). Measurements containing helium-rich particles are often regarded as outliers for the purposes of $^{3}He_{ET}$ age models; this has the effect of systematically underestimating the 'true' $^{3}He_{ET}$ concentration in samples, but as a systematic error also present in the estimation of background flux it is usually judged to cancel out in Equation 2.1 (Farley et al., 1997).

The larger the sample size, the better represented helium-bearing IDPs are likely to be, improving reproducibility of [^{3}He] measurements. The number of IDPs in a sample is proportional to its 'area-time product', calculated by dividing the mass of sample analysed by the sediment mass accumulation rate (Farley et al., 1997). The area-time products of aliquots of sediments with higher sedimentation rates (such as carbonates) are smaller than those with low sedimentation rates (such as clays). The area-time product of sample aliquots must always be borne in mind as, if samples used to calculate background flux represent significantly different area-time products (e.g. an order of magnitude) to samples used in the $^{3}He_{ET}$ age model, the systematic 'undersampling' error mentioned above may not cancel out on either side of Equation 2.1 (Farley et al., 1997).

The 1σ uncertainty in [^{3}He] measurements due to this poor reproducibility is often judged to be 20% for 'typical' samples of 2–3 g of carbonate sediment, based on the atmospheric entry heating model of Farley et al. (1997) and Patterson and Farley (1998), and the observed distribution of replicate values (Farley et al., 1997; Patterson and Farley, 1998; Farley, 2001; Mukhopadhyay et al., 2001a; Farley and Eltgroth, 2003; Murphy et al., 2010). By contrast, [^{4}He] measurements in these sample

aliquots are much more reproducible, with a population standard deviation of around 8.5% (Patterson et al., 1999; Mukhopadhyay et al., 2001a). The observed variability in measured ^{4}He concentrations has been ascribed to variability in extraterrestrial ^{4}He; terrestrial particles carrying radiogenic ^{4}He, responsible for most of the ^{4}He in marine sediments, are clearly sampled more representatively than IDPs (Patterson et al., 1999; Mukhopadhyay et al., 2001a) .

Implications of $^4He_{terr}$ flux record

The terrestrial component of ^{4}He ($^4He_{terr}$) can be deconvolved using a very similar equation to Equation 2.2 (Patterson et al., 1999):

$$[^4He_{terrestrial}] = [^4He_{observed}] \times (^3He/^4He_{observed} - ^3He/^4He_{ET})/(^3He/^4He_{terrestrial} - ^3He/^4He_{ET})$$

Equation 2.3

The terrestrial ^{4}He concentration in sediments can be used as a tracer of the flux or composition of detrital matter to the ocean. For example, over the past 700 kyr the flux of $^4He_{terr}$ has varied cyclically, recording changing aridity in dust source regions over 100 kyr glacial–interglacial cycles (Patterson et al., 1999), and over the last 4 Myr of the Cretaceous Period a significant rise in the concentration of $^4He_{terr}$ in the detrital material tracks a strong increase in the seawater $^{87}Sr/^{86}Sr$, interpreted as a change in the source of detrital material, possibly due to increased continental weathering (Mukhopadhyay et al., 2001b).

Patterson et al. (1999) suggested that the dominant carrier phase of terrestrial ^{4}He is zircon, possibly accompanied by apatite and sphene. U and Th (and hence radiogenic ^{4}He) are concentrated in trace mineral phases, and zircons, unlike clay minerals, are expected to have comparatively high ^{4}He retentivity (Patterson et al., 1999). Calculations by Patterson et al. (1999) indicate that all of the observed ^{4}He content of Asian loess could reasonably be attributed to zircon.

Further radiogenic decay of U and Th in such grains post-deposition is not thought to affect the helium record of pelagic sediments, even over geological timescales (Patterson et al., 1999). In order to be transported to deep-marine settings, terrigenous grains have likely been eroded and fragmented down to sizes smaller than the typical alpha particle recoil length; ^{4}He produced post-depositionally is therefore likely to be ejected into surrounding sedimentary particles (such as quartz or clays) with lower helium retentivities, meaning that the post-depositional ^{4}He is not retained over geological timescales (Patterson et al., 1999).

2.1.4 Previous use of $^{3}He_{ET}$ age models

$^{3}He_{ET}$ age models have so far only been used to investigate two periods of rapid climate change in the pre-Quaternary record: the Cretaceous–Paleogene boundary event and the Palaeocene–Eocene Thermal Maximum (PETM) (Mukhopadhyay et al., 2001b; Farley and Eltgroth, 2003; Murphy et al., 2010; Lowery et al., 2018). In both cases, features of the $^{3}He_{ET}$ method have allowed facets of these events to be explored in ways that would not be possible with age models produced by other methods.

Over the K–Pg boundary, a $^{3}He_{ET}$ age model was used to search for hiatal surfaces and investigate the hypothesis that the K–Pg mass extinction only appeared catastrophic because of long duration hiatuses at the boundary (Mukhopadhyay et al., 2001b). An instantaneous sedimentation rate for the K–Pg boundary clay at several different sites could be determined, returning a short duration of around 10 kyr and implying that the K–Pg extinction was indeed catastrophic (Mukhopadhyay et al., 2001b). A $^{3}He_{ET}$ age model has also been used to put an upper limit on the timescale of biotic recovery at the impact site (Lowery et al., 2018).

$^{3}He_{ET}$ age models have been used in conjunction with cyclostratigraphy over the PETM to provide a more detailed examination of how time is allocated within the event (Farley and Eltgroth, 2003; Murphy et al., 2010). Interestingly, although recent cyclostratigraphic work has concluded that

estimates of the duration of the PETM provided by both $^{3}He_{ET}$ and cyclostratigraphic age models are the same, these models still disagree somewhat on the allocation of time within the event (see Murphy et al., 2010; Westerhold et al., 2018). $^{3}He_{ET}$ age models indicate a ~40 kyr longer duration of the event clay layer, and therefore a correspondingly shorter duration of the recovery interval (Murphy et al., 2010; Westerhold et al., 2018), with elevated sedimentation rate in the post-event 'recovery' carbonate compared to the 'normal' background (Farley and Eltgroth, 2003; Murphy et al., 2010). Notably, these discrepancies coincide with periods where low variability in the concentrations of minor elements Ba and Fe used to construct cyclostratigraphic age models at the studied sites (see Röhl et al., 2007) makes identification of significant cyclical variations difficult, highlighting the usefulness of $^{3}He_{ET}$ age modes in sections where cyclostratigraphy may be prone to error (Farley and Eltgroth, 2003; Murphy et al., 2010).

A seemingly common feature of both the K–Pg and PETM events, picked up by $^{3}He_{ET}$ age models, is an elevated sedimentation rate of post-event carbonates compared to carbonate sedimentation rates determined for levels higher in the section (Mukhopadhyay et al., 2001b; Farley and Eltgroth, 2003; Murphy et al., 2010). Over the K–Pg boundary this phenomenon is suggested to be due to post-extinction repopulation by a planktonic 'rebound fauna' characterised by high turnover rates (Mukhopadhyay et al., 2001b). Over the PETM, this sedimentation rate increase is thought to be consistent with both an acceleration of carbonate deposition due to enhanced terrestrial weathering and runoff during PETM recovery, and an increase in carbonate preservation due to an oversaturated water column following the dissolution of deep-sea carbonates during the PETM (Murphy et al., 2010).

Limitations of $^{3}He_{ET}$ age models are also explored in these studies, a key take-away message being that comparison between different sites allows more certainty that local effects such as sediment focusing have not affected calculated age models (Farley and Eltgroth, 2003; Murphy et al., 2010). It is also noted that, whilst the presence of eroded 'missing time' can be identified by comparing both

cyclostratigraphic and $^{3}He_{ET}$ age models from different sites (along with sedimentological evidence such as scour marks), neither method is better than the other at quantifying the exact amount of time lost (Farley and Eltgroth, 2003).

2.2 Geological setting of the Umbria–Marche Basin

The sedimentary sections examined in this study originate from the Umbria–Marche region of central Italy, which contains a continuous sedimentary record from the Jurassic to the Oligocene (Lowrie and Alvarez, 1981; Cresta et al., 1989). The geological history of the Umbria–Marche Basin is important for putting the studied sections into context. Understanding of the basin's Late Cretaceous palaeogeography informs the interpretation of processes driving observed changes in sedimentation rate, and processes by which $^{3}He_{ET}$ bearing IDPs might have been redistributed. The basin's later geological history (including further sedimentation in the Cenozoic, followed by uplift to form the Apennines) determined the thermal history experienced by the formations of interest, and hence the amount of helium lost through diffusive heating. The Scaglia Bianca Formation, from which the samples in this study were collected and which includes the Bonarelli Level, the sedimentary expression of Oceanic Anoxic Event 2, has been well studied; results of previous sedimentary and geochemical study are presented below.

2.2.1 Sampling locations

Sampled sections are taken from Furlo and Contessa (Figure 2.2). The Contessa section (GPS co-ordinates: 43°22'32"N; 12°33'389"E) is a quarried exposure located near the active Vispi Quarry, about 2km north of the village of Gubbio close to the Contessa highway (Cresta et al., 1989; Coccioni and Galeotti, 2003; Tsikos et al., 2004; Monaco et al., 2012; Gambacorta et al., 2016). The Furlo

section (GPS co-ordinates: 43°38'42"N; 12°42'40"E) is another quarried exposure in the upper part of an abandoned quarry on the flanks of Monte Pietralata, above the village of Furlo in the Furlo Gorge (Beaudoin et al., 1996; Turgeon and Brumsack, 2006; Mort et al., 2007; Turgeon and Creaser, 2008; Lanci et al., 2010; Gambacorta et al., 2015, 2016; Batenburg et al., 2016). Unlike the Contessa section, the Furlo section contains cm-thick black shale beds associated with the black cherts characteristic of the upper part of the Scaglia Bianca formation below the Bonarelli Level (Gambacorta et al., 2015).

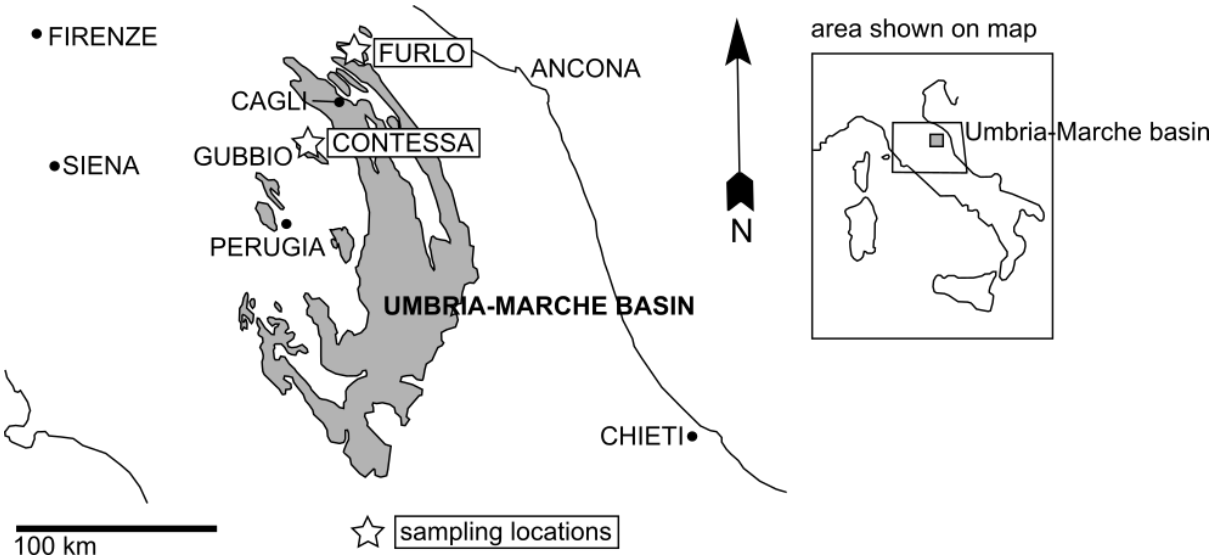

Figure 2.2: Location of the Umbria–Marche Basin in central Italy showing sampling locations. Shaded outcrop area represents Triassic–Eocene age basin fill (after Arthur and Premoli Silva, 1982).

2.2.2 Late Cretaceous palaeogeography

Late Cretaceous sediments of the Umbria–Marche Basin were deposited in a pelagic environment beneath the Neotethys, on the rifted northern margin of the Adria microplate (Dewey et al., 1973; Channell et al., 1979; Stampfli, 2005). At the time of deposition of the Late Cretaceous Scaglia Bianca Formation this region was located around 20–30°N (Vandenberg et al., 1978; Stampfli, 2005). A generalised palaeogeographic map (after Gambacorta et al. (2016)) showing the location of the Umbria–Marche Basin at the Cenomanian-Turonian boundary is presented in Figure 2.3.

Rifting in this region began in the Middle Triassic, and continued through the Jurassic and Early Cretaceous (Channell et al., 1979), with subsidence continuing to the early Paleogene (D'Argenio and Alvarez, 1980). Submarine topography was controlled by normal faulting, creating a 'basin and swells' topography of fault-bounded seamounts with intervening deeper water (Bernoulli and Jenkyns, 1974; Channell et al., 1979; Alvarez, 1990). This topography was, however, smoothed through the Cretaceous as the margin continued to subside (Bernoulli and Jenkyns, 1974).

Upper Cretaceous sediments are therefore part of a deepening succession, from Triassic shallow water carbonate platforms to pelagic limestones, cherts and marls in the Mesozoic and Paleogene (Bernoulli and Jenkyns, 1974, 2009; Alvarez, 1990; Gambacorta et al., 2015). The depth of deposition of Upper Cretaceous sediments has been variously estimated to have been between 1500 and 3000 m, though is always thought to have been above the CCD (Arthur and Premoli Silva, 1982; Kuhnt, 1990; Bernoulli and Jenkyns, 2009). Coincident with this deepening succession was an oceanographic change in the latest Jurassic, reflected in the deposition of deep-water coccolith-rich limestone overlying radiolarian chert. This lithological shift has been ascribed to either tectonic drift through the Late Jurassic into higher latitudes and away from an equatorial region of high siliceous productivity (Muttoni et al., 2005), or to a depression of the CCD below the sea floor as a result of an increase in calcareous planktonic production at this time (Bosellini and Winterer, 1975; Bernoulli and Jenkyns, 2009).

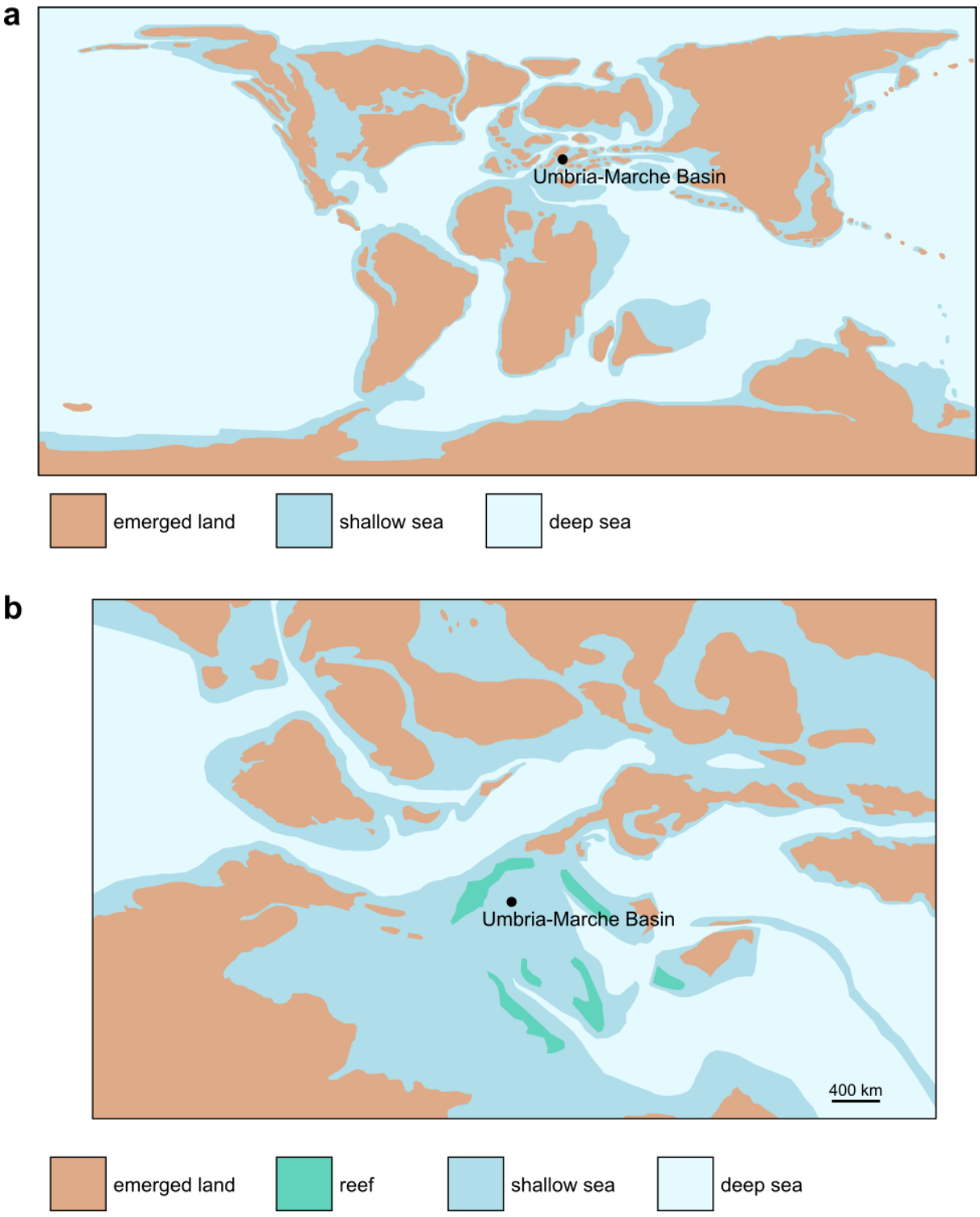

Figure 2.3: Generalised palaeogeographic maps showing the setting of the study area at the Cenomanian-Turonian boundary. ***(a)*** *Generalised global palaeogeographic map showing assumed land and marine areas at the Cenomanian-Turonian boundary (from Gambacorta et al., 2016; reconstruction based on R. C. Blakey, NAU Geology);* ***(b)*** *Regional palaeogeographic map (from reconstruction of R. C. Blakey, 2020, https://deeptimemaps.com/europe/).*

Upper Cretaceous sediments contain little terrigenous detritus (Bernoulli and Jenkyns, 1974; Channell et al., 1979). This lack of clastic admixture is suggested to be due to palaeogeography; during this period there may have been only a few or ephemeral rivers on the southern Tethyan margin, and nearshore carbonate platforms may have also acted to shield deeper basins from terrigenous input (Bernoulli and Jenkyns, 1974).

2.2.3 The Scaglia Bianca Formation

The Upper Cretaceous formation from which this study's samples are drawn, the Scaglia Bianca, was first described in a paper on the geology of the Gubbio region, Central Apennines, by Guido Bonarelli in 1891 (discussed in Bernoulli and Jenkyns, 2009). The Scaglia Bianca Formation (uppermost Albian to lower Turonian) consists mostly of off-white pelagic limestones and lies stratigraphically between the varicoloured marls of the Marne a Fucoidi Formation (lower Aptian to upper Albian) and the pinkish limestones of the Scaglia Rossa Formation (lower Turonian to middle Eocene) (Arthur and Premoli Silva, 1982; Cresta et al., 1989; Coccioni and Galeotti, 2003; Gambacorta et al., 2015, 2016). Contacts between these formations are gradational (Coccioni and Galeotti, 2003). Cretaceous lithostratigraphic units of the Umbria–Marche Basin are summarised in Figure 2.4.

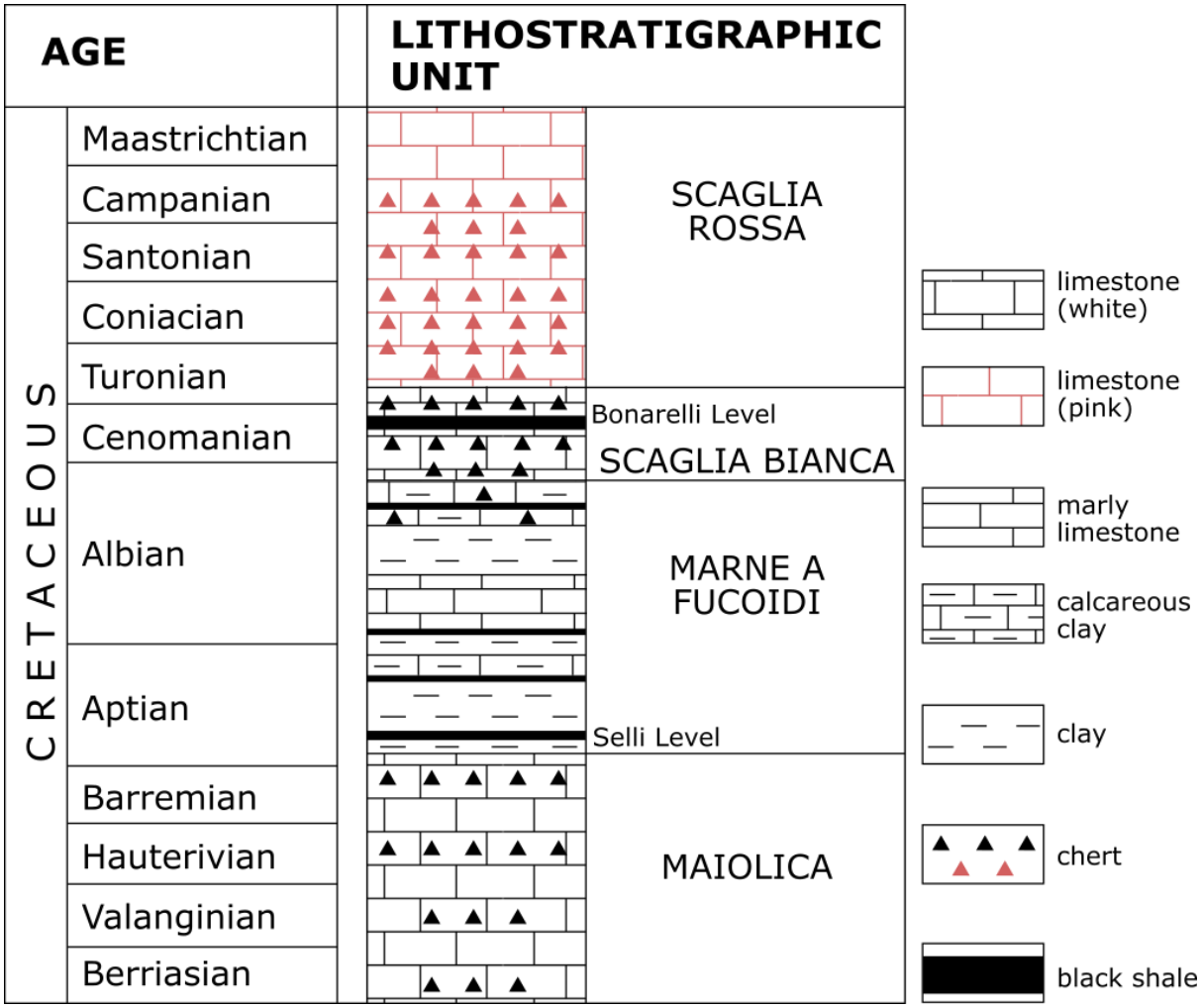

Figure 2.4: Summary of Cretaceous lithostratigraphic units in the Umbria–Marche Basin after Cresta et al. (1989).

The white biomicrites of the Scaglia Bianca Formation are formed from lithification of nannofossil-foraminiferal oozes, with coccoliths and calcitic microparticles the main carbonate sedimentary components (Bernoulli and Jenkyns, 1974; Coccioni and Galeotti, 2003; Turpin et al., 2012; Gambacorta et al., 2014). Evidence of bioturbation is common in limestone beds (Coccioni and Galeotti, 2003; Gambacorta et al., 2014). Minor lithologies include grey to black marlstones and shales, grey to black cherts and radiolarian layers (Cresta et al., 1989; Coccioni and Galeotti, 2003; Gambacorta et al., 2014, 2015). These lithologies are rhythmically interbedded, with chert-limestone cycles thought to correspond to precession cycles (Batenburg et al., 2016). Detailed sedimentary

facies analysis by Gambacorta et al. (2014) suggest that oxygenation and sea-floor current intensity were the major controlling factors of lithological variation.

The Scaglia Bianca has been subdivided by some workers into four members (Coccioni and Galeotti, 2003): from bottom to top these are the 'Lower Yellowish-Grey Member', 'Reddish Member', 'Upper Yellowish-Grey Member' and the 'Greyish Member'. This study is concerned with the top part of the Scaglia Bianca, all samples deriving from the 'Greyish Member' which begins after the mid-Cenomanian $\delta^{13}C$ excursion and is described as "light-grey to grey limestone with common nodules and lenses of dark-grey to black chert throughout" (Coccioni and Galeotti, 2003). The appearance of black shales, which occur in the upper portion of some exposures through the ~2 Myr interval between the mid-Cenomanian Event and the Bonarelli Level, are interpreted by Coccioni and Galeotti (2003) as reflecting the enhanced sensitivity of the sedimentary regime at this time to changes in the hydrological cycle under warmer conditions. The organic carbon in these shale layers is thought to be almost entirely of marine origin; this identification is based on its identification as "type II" organic matter using Hydrogen Index values (Arthur and Premoli Silva, 1982; Gambacorta et al., 2015).

The Bonarelli Level

At the top of the Scaglia Bianca is a regional marker bed: a distinctive ~1 m thick black shale-dominated interval known as the Bonarelli Level, first described by Guido Bonarelli (1891). The Bonarelli Level was identified by Schlanger and Jenkyns (1976) as being the central Italian expression of a global anoxic event (the Cenomanian-Turonian Oceanic Anoxic Event, or Oceanic Anoxic Event 2). In this interval, carbonate content drops to zero or near zero and total organic carbon (TOC) content rises to a maximum of ~30% (Arthur and Premoli Silva, 1982; Farrimond et al., 1990). OAE 2 is marked by a major shift to relatively heavy $\delta^{13}C$ values in organic carbon through the Bonarelli Level – with heavy $\delta^{13}C$ values in coeval bulk carbonate measured in other sections – (e.g., Tsikos et

al., 2004), along with major faunal turnover (e.g. Premoli Silva et al., 1999; Coccioni and Luciani, 2005; Musavu-Moussavou et al., 2007). Further information on oceanic anoxic events and geochemical climate proxies measured through the Bonarelli Level is given in Section 2.3.

The Bonarelli Level is lithologically heterogeneous, comprising interbedded black and grey mudstones and shales, radiolarian sands, local thin cherts and, at the top of the interval, grey marls. Some black shale or mudstone horizons are rich in fish debris and/or pyrite nodules (Arthur and Premoli Silva, 1982). This interval was subdivided into three parts by Arthur and Premoli Silva (1982), based on the outcrop at Gubbio, a division echoed by Cresta et al. (1989) and Kuroda et al. (2005) in the Bottaccione Gorge and Gorgo Cerbara respectively, and held broadly true over many different Bonarelli Level exposures.

A basal ~30 cm is primarily made up of unlaminated radiolarian sands/silts containing faint burrow mottles, interbedded with rare organic carbon-rich mudstones rich in pyrite and calcium phosphate. The middle ~30–35 cm has the highest organic-carbon content (Arthur and Premoli Silva, 1982; Kuroda et al., 2005) and is made up almost entirely of thinly laminated, unbioturbated dark mudstone. These organic carbon-rich intervals commonly contain increased FeS_2 concentrations (up to 7% calculated in the Gorgo Cerbara outcrop by Kuroda et al. (2005) using iron abundance after subtracting aluminosilicate iron). The organic matter in this subdivision is found as compressed amorphous streaks disseminated in the mudstone matrix, or as part of thin laminae couplets with phosphatic and siliceous material. The final ~40 cm, below a bed of cream coloured silicified limestone and chert that caps the Bonarelli Level, is composed of radiolarian mudstone and radiolarian sandy silt layers. Carbonate content increases gradually through this interval, and the organic-carbon content is relatively low (1–4% TOC), though pyrite remains a noticeable component.

Some studies have identified “couplets” through the Bonarelli Level, described either as alternating light (radiolarian-rich) and dark (organic carbon-rich) layers (Kuroda et al., 2005; Scopelliti et al., 2006) or, correspondingly, as alternating silica- and clay-rich layers (de Boer, 1982). The total

number of “couplets” has been estimated between 23–33 (de Boer, 1982) and the scale of these alternating layers varies from 1.5–50 mm, with organic carbon and biogenic silica content of beds inversely correlated (Kuroda et al., 2005). These alternations have been linked to precession cycles (de Boer, 1982; Kuroda et al., 2005; Scopelliti et al., 2006), and are discussed in more detail in Section 3.3.2.

Planolites, *Chondrites* and *Thalassinoides* trace fossils have been identified in rare bioturbated beds, largely light-coloured silts and mudstones occurring in the upper and lower parts of the Bonarelli Level (Monaco et al., 2012). However, individual trace fossils are rarely clearly preserved, with bioturbation typically appearing as mottling. This mottled appearance is interpreted by Monaco et al. (2012) as the result of bioturbation only taking place in the top “soupground” layers of sediment under dysaerobic conditions. The external mould of a single ammonite has been found in one Bonarelli Level outcrop (Donatelli et al., 2010).

The concentration of aluminosilicate minerals (measured using Al_2O_3 content as a proxy) varies very little through the Bonarelli Level; typically, Al_2O_3 content ranges between 2–5% (Kuroda et al., 2005). However, several bedded ‘microlaminae’ with elevated values of Al_2O_3 concentration up to 10% have been observed, which could represent either a sudden decrease in the supply of other sedimentary components (i.e. organic carbon and biogenic silica), or a sudden increase in aluminosilicate supply (Kuroda et al., 2005). This latter explanation is favoured by Kuroda et al. (2005), who interpret these intervals as gravity-flow sediments. Average sedimentation rate through the Bonarelli Level has been estimated by assuming a constant flux of Al_2O_3 through the Bonarelli Level and the limestones stratigraphically above it (with the sediment rate in these Turonian limestones determined using biostratigraphic timescales); using this method average sedimentation rates of 0.13–0.26 cm/kyr have been estimated (Arthur and Premoli Silva, 1982; Ohkouchi et al., 1999; Kuroda et al., 2005). An independent method of determining sedimentation rate through the

Bonarelli Level, matching the wavelengths of observed cycles in Rb/Al, Si/Al, and Cr/Al to periods of orbital cycles, obtained a similar average sedimentation rate of 0.25 cm/kyr (Scopelliti et al., 2006).

Further work investigating the source of detrital silicate materials suggests a decrease in the aeolian source strength (represented by a decrease in Ti/Al values) in the Bonarelli Level compared to the surrounding limestones; this has been interpreted as a dilution of wind-transported material by increased run-off rate through this interval (Scopelliti et al., 2006). Dramatic fluctuations in Rb/Al ratio through the Bonarelli Level have also been interpreted as representing repeated episodes of enhanced fluvial discharge (Scopelliti et al., 2006).

Pyrite in the Bonarelli Level typically occurs as micrometre-scale framboids, suggesting that the main source of pyrite was syngenetic formation in a euxinic water column (Kuroda et al., 2005). Evidence of diagenetic formation of pyrite within sediments is sporadically observed, though this process is thought to be less significant (Kuroda et al., 2005). Pyrite tends to be more abundant in organic carbon-rich intervals, though the correlation between organic carbon and FeS_2 concentrations is weak, suggesting that different factors (e.g. the availability of reactive iron rather than the deposition of organic matter) controlled the flux of these components to the sediment (Kuroda et al., 2005).

The organic carbon in the Bonarelli Level, perhaps its most distinguishing feature, is thought to be dominated by marine sources; the source of the organic carbon has been identified using biomarkers, Hydrogen Index values and microscopic analysis of amorphous organic carbon (Arthur and Premoli Silva, 1982; van Graas et al., 1983; Farrimond et al., 1990; Gambacorta et al., 2015). Terrestrial higher plants form a minor contribution, which varies with location across the Umbria–Marche Basin (Farrimond et al., 1990).

2.2.4 Post-depositional history

Prior to the uplift of the section during the Apennine orogeny, sedimentation in the Umbria–Marche Basin continued into the Miocene (Bortolotti et al., 1970; Arthur and Fischer, 1977; Arthur and Premoli Silva, 1982), beginning with the Turonian Scaglia Rossa, another rhythmically bedded unit comprising limestones, marls and pink cherts (see description in Trabucho-Alexandre et al., 2011). The Cretaceous Albian–Turonian succession was buried across the basin to a depth of 1–2 km, depending on palaeogeography (Arthur and Fischer, 1977; Trabucho-Alexandre et al., 2011).

Following the formation of the Apennine range (a fold and thrust belt) through the Neogene (Boccaletti et al., 1971; Tavarnelli, 1997), orogenic processes left the Mesozoic sediments folded, and the mudstones in the Bonarelli Level compacted by at least 40% (Arthur and Premoli Silva, 1982). Although $\delta^{18}O$ values of Cretaceous limestones show evidence of heating during diagenesis (e.g. Sprovieri et al., 2013), the degree of heating and burial that these sediments underwent was sufficiently limited that the black shales of the Bonarelli Level remain thermally immature (based on temperatures of maximum pyrolytic hydrocarbon yield, and hopane and sterane maturity parameters), though a greater degree of organic matter maturity in the south of the basin suggests deeper burial in that region (van Graas et al., 1983; Farrimond et al., 1990; Mort et al., 2007).

2.3 Climate cycles and climatic disturbances

The major focus of Chapters 4 and 5 in this thesis is the application of $^{3}He_{ET}$ timescales to the intricacies of the record of orbitally forced palaeoenvironmental change in the Scaglia Bianca and to intervals of dramatic climatic disturbance (OAE 2). These timescales are particularly useful when combined with other (geochemical or sedimentological) insights into palaeoenvironmental change, as they provide a method to gauge the rate of these changes.

A summary of the identification of orbital cycles within the Scaglia Bianca is, therefore, presented below, along with a review of the geochemical and sedimentological records that have been used to provide insight into the accompanying changes in palaeoenvironment. Likewise, a brief overview is provided of the global palaeoclimatic changes associated with OAE 2, along with global estimates of its duration. Following this, the duration of, hiatuses and cyclicity within, and sedimentation patterns after the Bonarelli Level (the expression of OAE 2 for which this study provides a $^{3}He_{ET}$ timescale) are discussed in detail.

2.3.1 Cyclicity through the Cenomanian-Turonian

The expected periods of Milankovitch orbital forcing through the Late Cretaceous are 18.5–23 kyr (precession), 41–54 kyr (obliquity), 95–123 kyr (short eccentricity) and 405 kyr (long eccentricity) (Berger et al., 1992; Berger and Loutre, 1994; Laskar et al., 2004, 2011a; Waltham, 2015; Laskar, 2020). The Milankovitch calculator of Waltham (2015) estimates an obliquity period of 39.1±1.2 kyr and precessional periods of 23.03±0.37 kyr, 21.79±0.34 kyr, 18.53±0.29 kyr and 18.68±0.30 kyr at 94 Ma; errors on these estimates result from uncertainties on the details of past Earth-Moon separation. Different precession frequencies may dominate at different points in the 405 kyr eccentricity cycle (Zeeden et al., 2015).

Cycles in the Scaglia Bianca

Multiple studies, exploiting a range of proxies and carried out at a handful of locations across the Umbria–Marche Basin, have concluded that orbitally influenced cyclicity occurs through the Scaglia Bianca. The earliest studies tended to focus on identifying cyclic patterns in the thickness of beds: de Boer (1982) detected the influence of eccentricity-precession interaction influencing the thickness of the carbonate-rich beds and, in a similar vein, both 100 kyr and 400 kyr eccentricity cycles were detected in the “thickness index” of Schwarzacher (1994) along with, perhaps, a 41 kyr obliquity

signal. Spectral analysis of the pattern of bed thickness (and carbonate content) through the Scaglia Bianca by Claps and Masetti (1994) also identified 100 kyr eccentricity cycles, along with 43–41 kyr obliquity and 23–17 kyr precession cycles. Beaudoin et al. (1996) identified ~20 kyr precession cycles through the Scaglia Bianca by noting that "black levels" (black cherts) were separated by intervals of carbonate lithology with thicknesses 20 cm, or multiples of this 'unit' (40 cm, 60 cm, etc.).

Cycles have also been detected in the variation of colour through the Scaglia Bianca. Mitchell et al. (2008) coded lithologies according to their greyscale pixel value, the variation between dark and light used as a proxy for organic-carbon content. Using this method, the dominant cycles identified were a ~95 kyr short eccentricity cycle and the ~23 kyr precession cycle, though other strong cycles were identified and correlated to predicted cycles derived from the combination of eccentricity, obliquity and precession in this time period. These cycles included ~21.5 kyr precession and two weaker cycles at ~18 kyr and ~16 kyr. Batenburg et al. (2016) measured colour reflectance, also hoping to capture the alternation of varicoloured lithologies, identifying in their record a ~21 kyr precession cycle, along with ~100 kyr and ~405 kyr eccentricity. In both these studies, the amplitude of the precession signal was found to be modulated by both short and long eccentricity (Mitchell et al., 2008; Batenburg et al., 2016).

The ratio of Anhysteretic to Isothermal Remanent Magnetism in Scaglia Bianca limestones was used by Lanci et al. (2010) as a proxy of magnetite grain size and hence bottom-water oxygen levels. This signal seems to have been most strongly influenced by eccentricity, recording strong peaks interpreted to correspond to ~400 kyr, ~125 kyr and ~100 kyr eccentricity.

Lanci et al. (2010) also examined the variation in carbonate content, detecting in this record two strong peaks thought to correspond to precessional periods of ~20 kyr and ~25 kyr, along with some weaker evidence for a ~100 kyr eccentricity signal modulating the amplitude of precession. In the Scaglia Bianca carbonate content record examined by Gambacorta et al. (2019) peaks corresponding

to ~400 kyr and ~100 kyr eccentricity, and ~40 ky obliquity were identified, along with precessional periods of ~22 kyr, ~21 kyr , and ~18k yr.

Batenburg et al. (2016) identified ~21 kyr (precession) and ~100 kyr and ~405 kyr (eccentricity) cycles in the stable isotope records of carbon ($\delta^{13}C$) and oxygen ($\delta^{18}O$), in addition to the influence of obliquity. A study of carbon and oxygen isotopes that focused on longer term orbital periods (Sprovieri et al., 2013) also identified the ~405 kyr eccentricity cycle, along with much longer cycles at periods of ~8.0, 4.7, 3.4 and 2.4 Myr.

Relatively few cyclostratigraphic studies of the Scaglia Bianca were able to deconvolve short eccentricity and precession into their various components (e.g. Mitchell et al. 2008) and most studies used average durations for these cycles (i.e. 100 kyrs and 21 kyrs, respectively). This limitation may be partly due to sampling resolution and partly due to the inconstancy of sedimentation rates through the interval (de Boer, 1986; Herbert et al., 1986), which are perhaps varying on a shorter frequency than can be captured using the evolutionary average spectral-misfit method.

In summary, a wide range of proxies record a strong precession and eccentricity signal through the Scaglia Bianca, with an increasing recognition that obliquity forcing may be important during this interval. The interpretation of these results, and how they reflect on changing climatic conditions during the deposition of the Scaglia Bianca, are discussed further below.

Precession and eccentricity cycles, climate and sedimentology

The most obvious “cycles” that can be observed by eye in the Scaglia Bianca are the rhythmic alternations of limestone and chert, which have been linked to precession cycles (de Boer, 1982, 1991; Mitchell et al., 2008; Lanci et al., 2010; Batenburg et al., 2016). Modulation of the lithological expression of these cycles can again be seen in outcrop: “bundles” of cycles containing black cherts

(and, at Furlo, thin black shales) alternate with intervals where cycles contain only less organic carbon-rich grey cherts. These lithological changes are suggested to be the effect of both short and long eccentricity modulation of the precession signal (Mitchell et al., 2008; Lanci et al., 2010; Sprovieri et al., 2013; Batenburg et al., 2016).

The primary cause of this lithological switch to 'black beds' (black chert and black shale) deposition has been debated (a summary of the two competing models is presented in Figure 2.5). In the 'anti-monsoonal' model changes in ocean ventilation are linked to driving orbital forcing; it has been proposed that bundles of cycles containing black beds were deposited during eccentricity minima, when the amplitude of precession forcing and seasonal contrast were low (Herbert and Fischer, 1986; Lanci et al., 2010). Li et al. (2017) also correlated the onset of Oceanic Anoxic Event 2 to an eccentricity minimum. Under this model, anoxia developed (and preservation of organic matter was enhanced) when reduced seasonal contrast led to a decrease in deep-water formation and so a decreased ventilation of the sea floor and of deep-intermediate water masses. Limestones in cycles containing black beds were found to be relatively magnetite-poor compared to the limestones in cycles where these black beds are not strongly expressed, and this finding was interpreted as indicating their deposition under poorly oxygenated conditions, which promote magnetite dissolution (Lanci et al., 2010). This difference is worth highlighting, as it indicates that the limestones themselves differ between different cycles; it isn't the case that all limestones represent the same environment with the only variation being the presence or absence of black beds.

The association of black shale deposition with times of decreased ocean ventilation in the 'anti-monsoonal' model echoes older work which considered the 'limestone-marl couplets' seen in the Cenomanian and the Aptian-Albian Marne al Fucoidi (also called the Scisti al Fucoidi, or Fucoid Marls, which lie stratigraphically below the Scaglia Bianca in the Umbria–Marche Basin) as influenced solely by carbonate productivity: representing fluctuating carbonate deposition on top of a continuous background deposition of non-carbonate sediment (de Boer, 1982, 1991; Herbert and Fischer, 1986;

Premoli Silva et al., 1989). Limestones were thought by these workers to have been deposited under cooler intervals with decreased continental runoff where a well-ventilated ocean promoted high carbonate productivity (Herbert and Fischer, 1986; de Boer, 1991), suggested specifically to be carbonate nannofossil blooms (Premoli Silva et al., 1989). 'Carbonate-poor' intervals were thought to represent warmer periods and/or those with increased continental runoff where decreased upwelling strength in a 'sluggishly' circulating ocean led to poor nutrient supply and low productivity, with anoxia (promoting the preservation of organic matter) linked to low overturning rates (Herbert and Fischer, 1986; de Boer, 1991). Evidence is not conclusive that carbonate productivity was greater in cycles that do not contain black beds: a study of calcareous nannofossil fertility indicators through the Marne al Fucoidi concluded that the relationship between carbonate fertility and black shales changed over the Albian: although in the late Albian anoxic (black) intervals were associated with warmer and less fertile waters, as hypothesized above, there was no significant change in the early to mid-Aptian in temperature or carbonate fertility between the cycles with and without black beds (Tiraboschi et al., 2009).

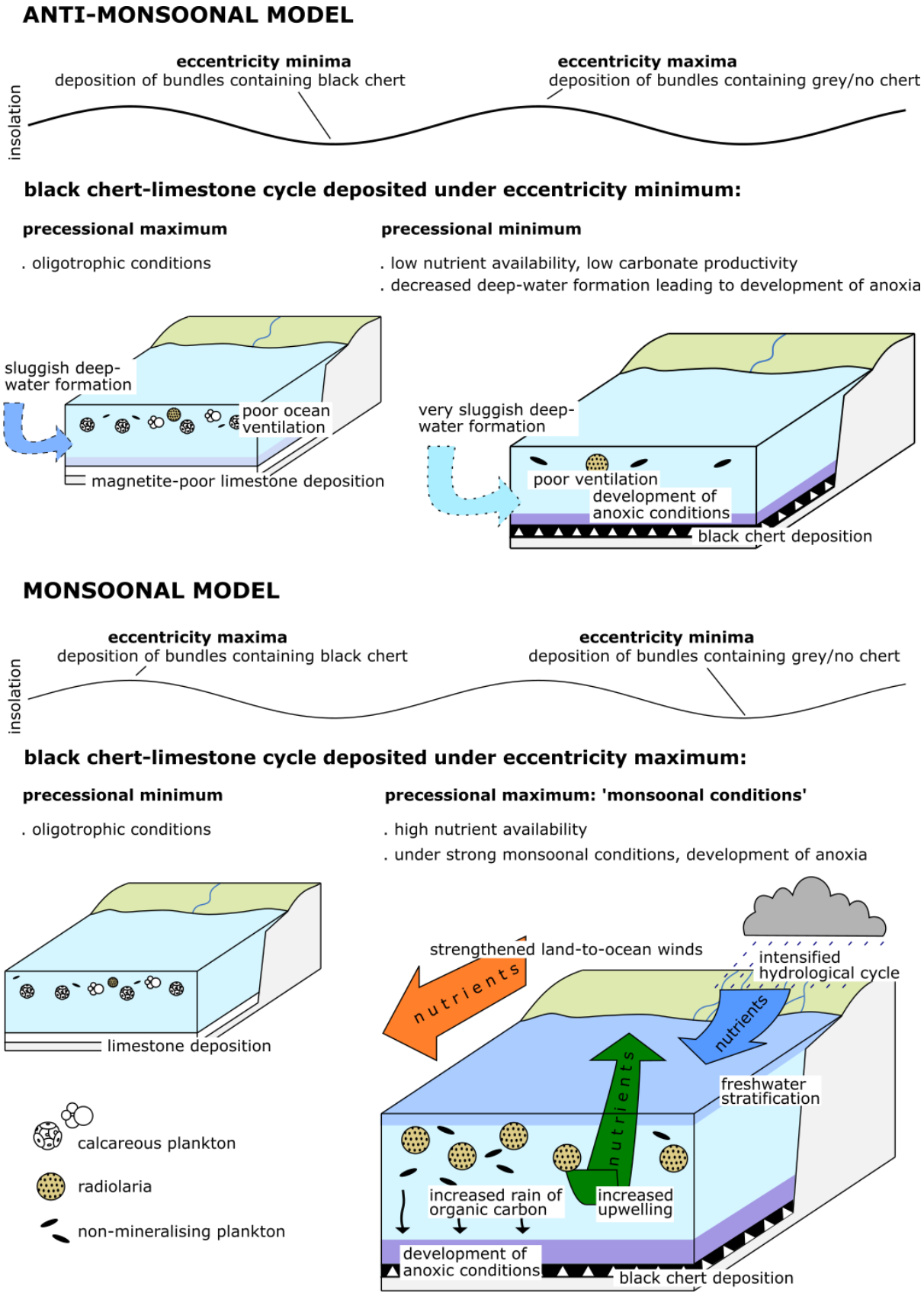

Figure 2.5: Cartoon showing the deposition of a limestone-black chert cycle as proposed under 'anti-monsoonal' (Herbert and Fischer, 1986; Lanci et al., 2010) and 'monsoonal' models (Mitchell et al., 2008; Batenburg et al., 2016).

By contrast, in the 'monsoonal' model (Mitchell et al., 2008; Batenburg et al., 2016; Gambacorta et al., 2016; Gambacorta et al., 2019) bundles of black cherts are proposed to have been deposited during periods of strong orbital forcing and increased Northern Hemisphere seasonal contrast. In this model, limestone was deposited under oxic, oligotrophic conditions. Cherts (grey and black) were deposited under 'monsoonal' conditions: periods in which nutrient availability was increased, either due to increased run-off or upwelling (Mitchell et al., 2008; Batenburg et al., 2016), or due to strengthened land-to-ocean winds and an increase in wind-blown nutrients (Gambacorta et al., 2019). The lithological shift from carbonate to chert is linked to nutrient availability as, in the Mesozoic, carbonate phytoplankton (coccolithophores) tended to dominate under oligotrophic conditions, but were outcompeted by non-mineralising phytoplankton under meso- to eutrophic conditions (Margalef, 1978; Premoli Silva et al., 1999; Leckie et al., 2002; Erba, 2004; Erba and Tremolada, 2004). The dominant source of biogenic silica to the Cretaceous cherts of Umbria–Marche were radiolaria (Coccioni et al., 1992; Erbacher et al., 1996; Leckie et al., 2002; Erba, 2004; Erba and Tremolada, 2004); their increase in abundance under nutrient-rich conditions may have been a response to changes in their food source. An increased supply of organic matter might also have had the effect of raising the CCD, further reducing the deposition of carbonate sediments (Trabucho-Alexandre et al., 2011).

Under the 'monsoon model', where black cherts are present they represent very high productivity, organic-rich events, deposited under strong 'monsoonal' conditions (Mitchell et al., 2008; Batenburg et al., 2016; Gambacorta et al., 2019). Preservation of organic carbon was promoted under these strong monsoonal regimes: both because increased productivity meant a greater export of organic carbon to the sea floor, and hence greater preservation potential, and because bottom-water stratification, due to increased freshwater input under monsoonal regimes, allowed the development of anoxia (Mitchell et al., 2008).

Similarly, elevated Ba content in the siliceous lithologies of the precessional chert, limestone, marl alternations of the Scaglia Rossa (the unit overlying the Scaglia Bianca) has been taken to imply that, in these cycles, cherts and marls corresponded to intervals of enhanced primary productivity (Trabucho-Alexandre et al., 2011). Here, however, nutrient supply is hypothesised to have been controlled by variations in upwelling intensity, itself driven by orbitally forced changes in the intensity of surface winds or the intensity of tides (Trabucho-Alexandre et al., 2011).

Existing evidence from cyclostratigraphic analysis largely favours the link between black shales and chert deposition and times of strong orbital forcing (times of eccentricity maxima that allowed the amplitude of the precession signal to increase). Although Lanci et al. (2010) concluded that black chert/shale was deposited at eccentricity minima, re-examination of the same record by Laurin et al. (2016) ascribed the opposite phase relationship on the basis of eccentricity interference patterns. A recent study of the amplitude modulation of precession-controlled stable isotope records ($\delta^{13}C$ and $\delta^{18}O$) by Batenburg et al. (2016) concluded that black shale/chert deposition corresponded to intervals of maximum variation in these signals.

A related question is whether the elevated organic-carbon content in the sub-Bonarelli 'black beds' was a result solely of enhanced OC preservation during these intervals, or whether an increase in organic-carbon primary productivity played a role. On the basis of TOC contents alone, it is difficult to differentiate. Studies of the Marne al Fucoidi (an Aptian-Albian unit of the Umbria–Marche Basin which, like the Scaglia Bianca, contains rhythmically deposited black shales) have investigated this question using nannofossil fertility indicators, biomarkers and palynology. Carbonate nannofossil fertility indicators through the Albian were examined by Tiraboschi et al. (2009) and largely pointed to conditions of low fertility during the deposition of black levels. However, as noted by the authors, as the fertility index is based on calcareous organisms, it is possible that the low abundance of certain taxa during black shale intervals represents not 'low fertility', but actually nutrient excess above the nannoplankton threshold.

Worth considering also are the distinctions between black shales. Another study of the Marne al Fucoidi divided black shales into two distinct types, containing different types of organic matter and deposited under slightly different conditions (Pratt and King, 1986). One group, the majority of black shales measured, had TOC contents of ~1.5%. Biomarkers in these shales, along with their low hydrogen indices, were judged to be indicative of a major non-marine source of organic matter; this terrestrial organic matter was thought to have been delivered through aeolian deposition on the basis of the rarity of woody matter and the thin-walled nature of spore and pollen grains (Pratt and King, 1986; Tiraboschi et al., 2009). In this group of black shales, organic-carbon accumulation rates are estimated at 5.5×10^{-3}–2.2×10^{-2} g/cm^2/kyr, and primary productivity at 2–10 gC/m^2/yr, a value that is 1–2 orders of magnitude lower than modern upwelling settings (Herbert et al., 1986; Pratt and King, 1986, Falkowski et al., 1998).

However, the second group, 'organic carbon-rich' black shales (TOC ~4%), appear to have a distinctive marine source of organic carbon. In these beds a shift to heavier $\delta^{13}C$ values is interpreted as reflecting brief periods of stimulated marine productivity (Pratt and King, 1986). These black shales have higher Hydrogen Indices than their more organic-carbon-poor counterparts, and a population of biomarkers consistent with marine organic matter: on the basis of biomarker evidence, the proportion of marine organic matter was judged to be proportional to TOC (Pratt and King, 1986). That said, it remains rather difficult to tell whether there was a shift in the source of organic carbon between black shales and the limestones that enclose them because, after deposition under oxidative conditions and partial degradation by bioturbation, the proportion of residual marine or aeolian organic matter in the limestones cannot be judged (Pratt and King, 1986).

Thus far no distinctions have been made between 'types' of black shale in the Scaglia Bianca, and, indeed, implied palaeoenvironmental conditions during the deposition of the Aptian-Albian Marne al Fucoidi black shales should not be taken as exact analogues of those during the deposition of the Cenomanian-Turonian Scaglia Bianca, as the two units were deposited in slightly different

palaeogeographic settings. The black shales of the Marne al Fucoidi alternate with much darker, marlier limestones than the white limestones of the Scaglia Bianca, clearly indicating a somewhat different overarching palaeoenvironmental regime (Bernoulli and Jenkyns, 1974).

It is worth noting also that the exact composition of coincident Scaglia-Bianca 'black beds' across the Umbria–Marche Basin differs with location: across most of the basin only black cherts are expressed, but in Furlo these are accompanied by thin black shales. The presence or absence of these black shales has been suggested to be controlled by palaeogeography (Gambacorta et al., 2016). Black shales have been suggested to have been preserved only in settings that favour 'ponding' of clays, implying that fine-grained sediment was prevented from being deposited by bottom currents in other locations (Gambacorta et al., 2016). Black shales have also been posited to have been deposited in locations at the furthest expansion freshwater deltaic plumes, with a corresponding detrital input (Gambacorta et al., 2016), though all the mechanisms above remain highly speculative as, crucially, very little knowledge of this level of palaeogeographic detail exists. An entirely different interpretation of these black shales is that the distinction between black shale and accompanying black chert is a result solely of diagenetic separation (Salmon et al., 2003).

In summary, broadly speaking, one school of thought proposes that black shales reflect enhanced organic-matter preservation during periods of oxygen depletion, with no increase in organic-carbon productivity at this time (Herbert and Fischer, 1986; de Boer, 1991; Tiraboschi et al., 2009) and the other that black shales reflect times of enhanced organic-carbon productivity (in addition to enhanced preservation), often linked to strong 'monsoonal' conditions at eccentricity maxima (Mitchell et al., 2008; Batenburg et al., 2016; Gambacorta et al., 2016; Laurin et al., 2016). Some studies have highlighted differences in geochemistry and potential driving mechanisms between different black-shale intervals (Pratt and King, 1986; Tiraboschi et al., 2009). Tiraboschi et al. (2009), in particular, posited different mechanisms for the formation of rhythmic black shales, like those seen in the Marne al Fucoidi and Scaglia Bianca, which they ascribed to regional stratification, to

those involved in the deposition of the thick black shales of Oceanic Anoxic Events, which were likely caused by ocean fertilisation and increased primary productivity leading to an expansion of anoxia.

Sensitivity to orbital forcing

It has been suggested that the reason orbital forcing was able to provoke such a strong and obvious response through the Scaglia Bianca is that the oceanographic conditions in the Umbria–Marche Basin at that time were specifically 'poised' in a state easily disrupted by small insolation changes (de Boer, 1986, 1991; Herbert and Fischer, 1986; Mitchell et al., 2008). A suggested contributing factor was the specific palaeolocation of the Umbria–Marche Basin on the southern Tethys margin, in the subtropics at the zone of convergence of subtropical winds (Intertropical Convergence Zone). This made the Umbria–Marche Basin sensitive to recording orbitally driven changes in the exact position of this convergence zone, which could prompt changes to ventilation of deep water and nutrient supply (Barron et al., 1985; de Boer, 1991). In addition, the warm shallow seas typical of the Cretaceous may have been more sensitive to changes in rainfall/evaporation and the production of warm, saline water bodies, an effect heightened at times by marine transgression and high sea level (Barron et al., 1985; de Boer, 1991). It has also been posited that the Umbria–Marche Basin may have tipped easily into a state promoting organic-matter preservation as it was already poised at relatively low oxygen levels (de Boer, 1986).

Other significant periodicities

Along with eccentricity and precession, obliquity forcing may have be important during deposition of the Scaglia Bianca (Mitchell et al., 2008; Batenburg et al., 2016) as, perhaps, was a longer ~2.4 Myr cycle (Mitchell et al., 2008; Sprovieri et al., 2013).

Despite obliquity forcing mainly affecting high-latitude insolation, its imprint has been observed in the Scaglia Bianca $\delta^{13}C$ and organic-carbon records (Mitchell et al., 2008; Batenburg et al., 2016). If small ice sheets did exist at the Cretaceous poles (as, for instance, suggested by Stoll and Schrag, 2000; Miller et al., 2005; Ray et al., 2019), ice-albedo feedback may have amplified and spread the obliquity signal to the subtropics (Mitchell et al., 2008). Alternatively, it has been argued that, even without necessarily invoking ice sheets, obliquity has an important control on the greenhouse carbon cycle by impacting the transient storage of organic carbon and/or methane in relatively unstable reservoirs such as peats, soils, lakes and permafrost in the terrestrial realm, as well as marginal marine euxinic sediments, intermediate carbonate deposits and deep-marine clathrates (Laurin et al., 2015). A configuration of ocean circulation in which high-latitude watermasses were transported to lower latitudes may also have allowed the propagation of a 'high-latitude' obliquity signal to more equatorial settings (Meyers et al., 2012).

A 2.4 Myr periodicity was identified by Sprovieri et al. (2013) as a modulator of an extended $\delta^{13}C$ record through an Umbria–Marche section of Albian–Campanian age. The La2010 solar system model contains a 2.4 Myr modulation of eccentricity related to the precession of the orbital perihelia of Mars and Earth (Laskar et al., 2011a). Mitchell et al. (2008) link this 2.4 Myr cycle to the pacing of Oceanic Anoxic Events through the Cretaceous, noting that the mid-Cenomanian Event (characterised under this theory as a 'weak OAE') occurred 2.4 Myr before OAE 2, as well as speculatively linking the timing of the Pialli Event (OAE 1d) to this cycle. Mitchell et al. (2008) hypothesised that OAEs coincided with the decreased seasonality of 2.4 Myr minima, though a more recent study has, in fact, linked OAE 2 with increased seasonality (a 405 kyr maximum) following the extended period of low seasonal variability induced by 2.4 Myr minimum (Batenburg et al., 2016), an interpretation followed in this thesis. Li et al. (2017) affirmed the significance of a shift to increased seasonality following a 2.4 Myr cycle minimum but, in their orbital timescale, linked this change in forcing with the termination of OAE 2 rather than its initiation.

2.3.2 Oceanic Anoxic Event 2

Overview

Oceanic Anoxic Event 2 (OAE 2 or the Cenomanian–Turonian Oceanic Anoxic Event), first recognised by Schlanger and Jenkyns (1976), was one of a number of Mesozoic hyperthermals (see overview of Jenkyns, 2010). Initially this event was identified by its expression in many records as an interval of organic carbon-rich sediments (Schlanger and Jenkyns, 1976), though it is now defined within a chemostratigraphic framework by its characteristic positive $\delta^{13}C$ excursion (see Tsikos et al., 2004; Jarvis et al., 2006, 2011) which has been recorded in marine carbonates, and both marine and terrestrial organic carbon (e.g. Scholle and Arthur, 1980; Schlanger et al., 1987; Arthur et al., 1988; Jenkyns et al., 1994; Hasegawa, 1997; Hasegawa et al., 2003; Tsikos et al., 2004; Uramoto et al., 2009; Jarvis et al., 2011; Nemoto and Hasegawa, 2011; Lenniger et al., 2014).

The Cenomanian–Turonian boundary $\delta^{13}C$ excursion demonstrates a substantial upset to the global carbon cycle during this interval. The initiation of OAE 2 has been linked to the eruption of the Caribbean, Ontong-Java, Madagascar and High Arctic Large Igneous Provinces which both outgassed CO_2 and, in the case of submarine eruptions, delivered nutrients to the oceans (Sinton and Duncan, 1997; Kerr, 1998; Erba, 2004; Snow et al., 2005; Kuroda et al., 2007; Turgeon and Creaser, 2008; Zheng et al., 2013; Du Vivier et al., 2014; Holmden et al., 2016; Jenkyns et al., 2017; Percival et al., 2020). Though not considered a primary driver, orbital configurations have also been suggested to have exerted some control on the exact timing of carbon-cycle perturbation (Mitchell et al., 2008; Batenburg et al., 2016; Laurin et al., 2016). A major transgression may also have contributed to the development of anoxia (Uličný et al., 1997; Jones and Jenkyns, 2001; Voigt et al., 2006; Du Vivier et al., 2014).

Extensive study of geochemical proxies through OAE 2 have demonstrated that a multitude of environmental processes were changing over this interval, summarised in Figure 2.6 (after Jenkyns,

2010). Global temperatures peaked during OAE 2 – though a brief cooling, the Plenus Event, occurred early in OAE 2 in some places (Jenkyns et al., 1994; Huber et al., 2002; Voigt et al., 2004, 2006; Forster et al., 2007a, 2007b; Sinninghe Damsté et al., 2010; Jarvis et al., 2011; Friedrich et al., 2012; van Helmond et al., 2014; O'Brien et al., 2017; Robinson et al., 2019; O'Connor et al., 2020). The hydrological cycle was intensified, with intensified weathering and greater fluvial run-off leading to an increase in delivery of terrestrially sourced nutrients to the ocean (Premoli Silva et al., 1999; Jenkyns, 2003; Negri et al., 2003; Frijia and Parente, 2008; Blättler et al., 2011; Pogge von Strandmann et al., 2013; van Helmond et al., 2014, 2015; Poulton et al., 2015; Jenkyns et al., 2017). Change in climatic conditions was accompanied by a turnover in planktonic communities (Jarvis et al., 1988; Premoli Silva et al., 1999; Erba, 2004; Coccioni and Luciani, 2005; Musavu-Moussavou et al., 2007; Keller et al., 2008; Parente et al., 2008). Particularly during the initiation of OAE 2, some parts of the ocean may have become more undersaturated in carbonate (Du Vivier et al., 2015).

Though the exact interpretations of the geochemical records differ, changes in ocean circulation over OAE 2 are suggested to have occurred across the proto-Atlantic, Western Interior Seaway and European shelf sea (MacLeod et al., 2008; Martin et al., 2012; Zheng et al., 2013, 2016; Batenburg et al., 2014). In places these may have contributed to nutrient-trapping and the development of black shales (Pucéat, 2008; Jiménez Berrocoso et al., 2010; Trabucho-Alexandre et al., 2010; Martin et al., 2012). A change in ocean circulation is thought to have occurred synchronous with the aforementioned interval of transient cooling shortly after the onset of OAE 2 (where cold water fauna are found in Northern European sections, dubbed the 'Plenus Cold Event' after Gale and Christensen, 1996), during which time transient ocean mixing and re-oxygenation may have occurred in a number of globally distributed ocean basins (Jenkyns et al., 1994, 2017; Leckie et al., 1998; Friedrich et al., 2006; Forster et al., 2007; van Bentum et al., 2009; Zheng et al., 2013; Gale et al., 2019; O' Connor et al., 2020). This cooling episode, during which sea-surface temperatures fell by 2–11 °C across the Northern Hemisphere (Forster et al., 2007; Pearce et al., 2009; Sinninghe Damsté et al., 2010; van Helmond et al., 2014, 2015), may have been driven by the drawdown of CO_2 by

organic-carbon burial and/or silicate weathering (Kuypers et al., 1999; Barclay et al., 2010; Blättler et al., 2011; Jarvis et al., 2011; van Bentum et al., 2012; Percival et al., 2020). The Plenus Cold Event is recognisable in some $\delta^{13}C$ records (Jenkyns et al., 1994, 2017; Tsikos et al., 2004; Erbacher et al., 2005; Voigt et al., 2008; Jarvis et al., 2011; Gale et al., 2019; O'Connor et al., 2020), and is thought to have lasted ~60 kyr (Jarvis et al., 2011).

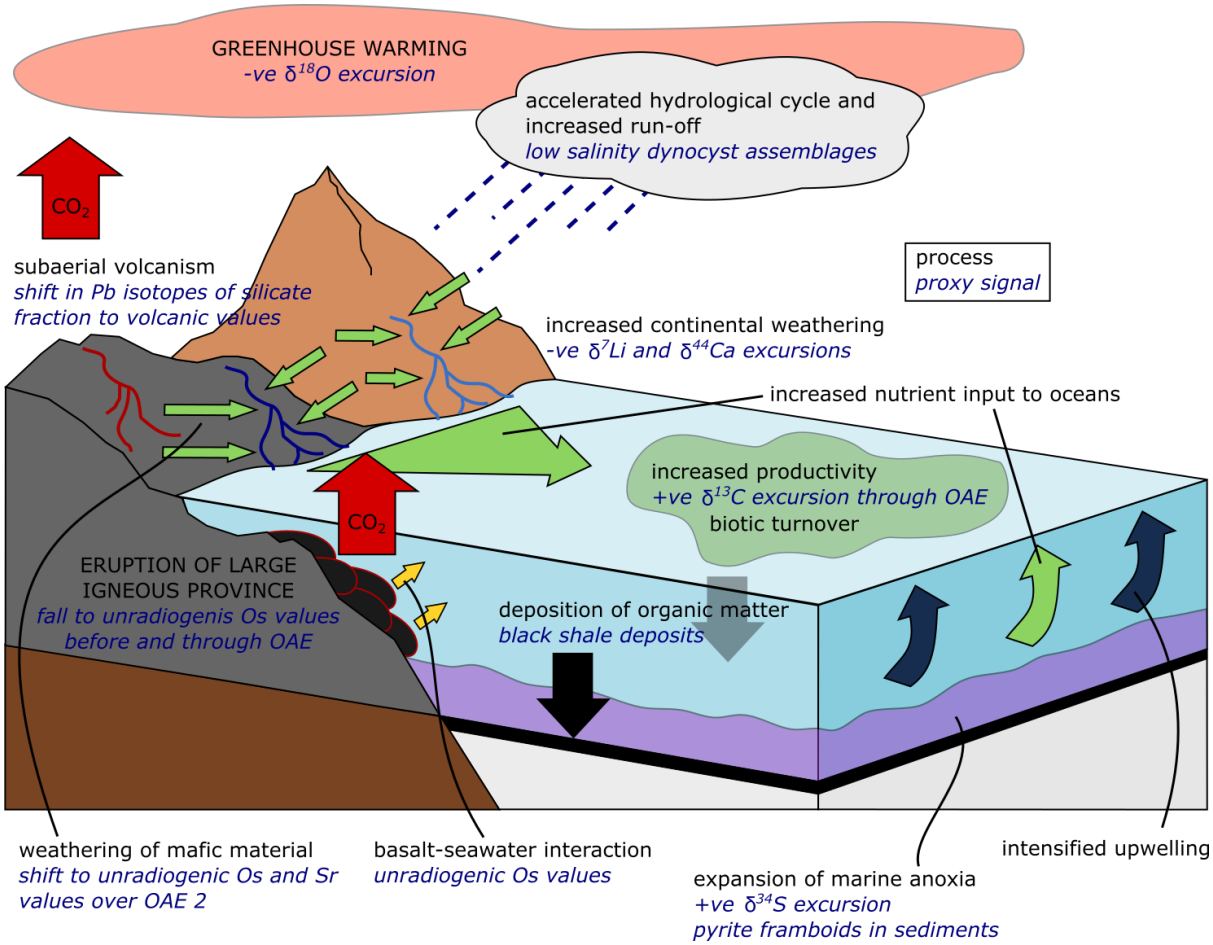

Figure 2.6: Overview cartoon of processes active over Oceanic Anoxic Event 2, along with the diagnostic proxy evidence, after Jenkyns (2010). Geochemical evidence is drawn from a wealth of studies: see body of text for full references.

There is widespread evidence for anoxia in at least part of the water column in certain locations during OAE 2 (Kuypers et al., 2002; Kolonic et al., 2005; Kuroda et al., 2005; Brumsack, 2006; Scopelliti et al., 2006; Turgeon and Brumsack, 2006; Jenkyns et al., 2007; Forster et al., 2008; Hetzel et al., 2009; van Bentum et al., 2009; Owens et al., 2013), with evidence of some photic-zone euxinia, particularly in the proto-Atlantic area (Sinninghe Damsté and Köster, 1998; Kuypers et al., 2002; Pancost et al., 2004; Kolonic et al., 2005; van Bentum et al., 2009). Reduced burial efficiency of phosphorus in anoxic bottom waters may have allowed this nutrient to be recycled from bottom waters, further fuelling productivity (Nederbragt et al., 2004; Mort et al., 2007, 2008). The contribution of enhanced productivity versus enhanced preservation to the high organic-carbon accumulation seen over OAE 2 has been debated, as has whether anoxic conditions were due to the expansion of oxygen minimum zones (sometimes called the 'bathtub ring model') or due to a totally anoxic water column following ocean stratification (the 'Black Sea model') (e.g. Schlanger and Jenkyns, 1976; Demaison and Moore, 1980; Bralower and Thierstein, 1984; Arthur et al., 1987; Jarvis et al., 1988; Pedersen and Calvert, 1990; Arthur and Sageman, 1994; Sinninghe Damsté and Köster, 1998; Kuypers et al., 2002; Pancost et al., 2004; Scopelliti et al., 2004; Meyers, 2006; Mort et al., 2007; Lanci et al., 2010; Trabucho-Alexandre et al., 2010).

The termination of OAE 2 has traditionally been associated with the reduction of CO_2 in the atmosphere through burial of organic carbon over the event and subsequent global cooling (e.g. Arthur et al., 1988). However, elevated temperatures continued into the Turonian following the termination of OAE 2 (see O'Brien et al., 2017), sustained, perhaps by a muted silicate-weathering carbon sink as decreasing Large Igneous Province volcanism towards the end of OAE 2 ceased to provide young and easily weatherable basalts (Percival et al., 2020). This suggests that factors other than a reduction in pCO_2 controlled the burial of organic matter (Robinson et al., 2019). The cessation of anoxic conditions and decreased burial of organic matter have, instead, been linked by Robinson et al. (2019) to reduced nutrient availability – which itself may have resulted from a combination of factors. Increased organic-matter burial under anoxic conditions during OAE 2 would

have led to an accompanying sequestration of nutrients (see Owens et al., 2016; Dickson et al., 2017), and weathering intensity appears to have declined prior to OAE 2's termination, this reduction perhaps in part associated with a sea-level rise, which may also have led to a reduced nutrient supply (Blättler et al., 2011; Jarvis et al., 2011; Pogge von Strandmann et al., 2013; Du Vivier et al., 2014; Holmden et al., 2016; Robinson et al., 2019). The termination of OAE 2 has also been linked by some to a change in orbital configuration (Li et al., 2017). Specifically, the increase in insolation variability following a node in insolation (these low insolation nodes occur with a period of ~2.4 Myr) is, in this interpretation, thought to have driven enhanced ocean circulation under increased seasonal contrast, resulting in better ocean ventilation and the cessation of anoxic conditions (Li et al., 2017); this interpretation does, however, depend on an inferred link between low insolation variability and the deposition of black shales, which is not a consensus view (see discussion in Section 2.3.1).

OAE 2 is an exceedingly well studied interval (see overview by Jenkyns (2010), and references above); the rest of this chapter focuses solely on the Bonarelli Level, the expression of OAE 2 in the Umbria–Marche region explored in this study.

Duration of deposition of the Bonarelli Level

Within the Umbria–Marche Basin, the depositional duration of the Bonarelli Level at Gorgo Cerbara was estimated as ~800 kyr by Ohkouchi et al. (1999), based on a sedimentation rate of ~0.13 cm/kyr. This figure was calculated using Al_2O_3 concentration as a proxy for accumulation rate and comparing the average Al_2O_3 concentration within the Bonarelli Level to that of the overlying Turonian limestones, estimated to have an accumulation rate of 0.53 cm/kyr on the basis of age-calibrated biostratigraphy (Premoli Silva et al., 1977). Using the same method at Gubbio, however, Turgeon and Brumsack (2006) calculated a duration of ~375 kyr for deposition of the Bonarelli Level. By correlating the biostratigraphy and carbon-isotope curve of Furlo to the Pueblo, USA, section, which

has been dated using $^{40}Ar/^{39}Ar$ of bentonites, Mort et al. (2007) estimated a Bonarelli Level duration of ~490 kyr.

Trabucho-Alexandre et al. (2011) counted 28 'couplets' within the Bonarelli Level at Moria; by relating these to precession cycles they estimated a duration of ~540 kyr. Scopelliti et al. (2006) estimated a much shorter duration for the Bonarelli Level at Bottaccione Gorge of only ~320 kyr, based on a sedimentation rate of ~0.25 cm/kyr calculated by the conversions of the wavelengths of identified orbital cycles in the space domain to the time domain. Using the same method, Batenburg et al. (2016) calculated a sedimentation rate of ~0.21 cm/kyr at Bottacione and ~0.28 cm/kyr at Furlo, giving durations of ~410 kyr and ~413 kyr for the Bonarelli Level at each location (see also 'Cyclicity within the Bonarelli Level').

As defined chemostratigraphically, the Cenomanian-Turonian OAE 2 extends from an initial sharp rise in $\delta^{13}C$ values, through a plateau of high $\delta^{13}C$, to the point where these values begin to decrease again (Tsikos et al., 2004). The termination of OAE 2 is now suggested to have occurred in the early Turonian (see Jenkyns et al., 2017). Carbon-isotope records at Gubbio (a composite of $\delta^{13}C$ bulk carbonate, TOC and phytane records) indicate that OAE 2 begins at the base of the Bonarelli Level (Tsikos et al., 2004) but the end is much harder to define. Following an earlier definition of the termination of OAE 2, which placed it at the Cenomanian-Turonian boundary, the end of OAE 2 in the Umbria-Marche basin has been placed ~1m above the uppermost radiolarian sand of the Bonarelli Level (Tsikos et al., 2004; Trabucho-Alexandre et al., 2011; Batenburg et al., 2016). Using this interpretation of the position of OAE 2 within the stratigraphic record, its full duration is a little longer than that of the Bonarelli Level: Batenburg et al. (2016) estimated ~490 kyr from the base of the Bonarelli Level to the Cenomanian-Turonian boundary.

However, this placement of the Cenomanian-Turonian boundary ~1m above the Bonarelli Level has been challenged by Voigt et al. (2007) and Gambacorta et al. (2015). On the basis of Turonian-like (~3‰) carbonate carbon isotope values in the limestones overlying the Bonarelli Level, a competing

interpretation of the carbon isotope record through the Umbria–Marche Basin is that the plateau phase of the OAE 2 carbon isotope excursion and the Cenomanian-Turonian boundary are completely missing, implying a significant hiatus above the Bonarelli Level (Voigt et al., 2007; Gambacorta et al., 2015). The interpretation and age of the post-Bonarelli Level limestones will be discussed further in a following section ('After the Bonarelli Level'); at this point it suffices to say that a large hiatus above the Bonarelli Level is likely to make any estimates of the duration of the black shale interval significant underestimates of the duration of OAE 2.

These estimates of Bonarelli Level and OAE 2 duration in the Umbria–Marche Basin lie within the range of durations (~320–800 kyr) estimated for the various expressions of OAE 2 from other geographic locations (Arthur et al., 1987; Meyers et al., 2001, 2012; Prokoph et al., 2001; Kuhnt et al., 2005; Sageman et al., 2006; Voigt et al., 2008; Ma et al., 2014; Eldrett et al., 2015; Li et al., 2017). These timescales are tied to points on the global chemostratigraphic $\delta^{13}C$ curve (the start of the $\delta^{13}C$ rise and the more ambiguously defined end of the plateau of high values) so should theoretically all calculate the same duration for OAE 2. The fact that they don't reflects that orbital cycles are not always easy to identify, particularly if a section is condensed or contains hiatuses.

In some sections, durations of each stage of the carbonate isotope curve have been calculated. The initial rise in $\delta^{13}C$ values is thought to take place over ~150–280 kyr, and the plateau of elevated $\delta^{13}C$ lasts 350–500 kyr (Sageman et al., 2006; Ma et al., 2014; Li et al., 2017). The decline of $\delta^{13}C$ values post-plateau is estimated as having taken place over an additional ~170–270 kyr (Sageman et al., 2006; Li et al., 2017).

Hiatuses in the Bonarelli Level

Sharp shifts in lithology as seen at the top and base of the Bonarelli Level may have been accompanied by hiatuses. Erosive surfaces have been noted at the top of the Bonarelli Level, and the rapid tapering of the upper part of the $\delta^{13}C$ signal at Furlo has been interpreted as, potentially, a

result of hiatuses (Tsikos et al., 2004; Voigt et al., 2007; Trabucho-Alexandre et al., 2011), with the limestones overlying the Bonarelli Level identified as Turonian based on their carbon isotopic values (Voigt et al., 2007; Gambacorta et al., 2015). High-resolution $\delta^{13}C$ records from across the Umbria–Marche Basin suggest hiatuses of differing lengths in different localities (Gambacorta et al., 2015). Using the timescale of Voigt et al. (2008) for comparison, these hiatuses are estimated to have lasted between 160–510 kyr; at Furlo, the hiatus between the top of the black shale interval and the subsequent limestones is estimated to span ~470 kyr (Gambacorta et al., 2015). These hiatuses are attributed to both erosion by bottom currents and/or a significant reduction in sedimentation rates associated with the changeover from biogenic silica and organic-matter deposition to biogenic carbonate deposition and changes in the calcite compensation depth (Gambacorta et al., 2014, 2015).

It is worth noting, however, that other studies have considered the presence of such an extensive hiatus at the top of the Bonarelli Level to be unlikely based on sedimentological and biostratigraphic evidence, and their own timescales through the event (Batenburg et al., 2016). The interpretation of some of this evidence remains debated: Batenburg et al. (2016) noted the first appearance of the calcareous nannofossil *Quadrum gartneri* ~1m above the top of the Bonarelli Level in the Bottaccione Gorge, taking this as evidence that the limestones stratigraphically below this level are Cenomanian in age; however, less significance is placed on the delayed appearance of *Quadrum gartneri* by, for example, Gambacorta et al. (2015) given the context of carbonate dissolution surrounding the Bonarelli Level and issues with *Q. gartneri* taxonomy.

At the base of the Bonarelli Level, a hiatus arising from the change in oceanographic conditions seems, conceptually, especially likely. A considerable amount of time might be expected to have elapsed between the cessation of carbonate deposition as the calcite compensation depth shoaled and the development of conditions sufficiently anoxic enough to allow the preservation of black shales (Gambacorta et al., 2015). A hiatus at the base of the Bonarelli Level has been posited to

explain the abrupt jump in a number of isotopic records ($\delta^{13}C_{org}$, $\delta^{15}N$, $\delta^{57}Fe$) at this horizon (Jenkyns, 2010), though Gambacorta et al. (2015) concluded from their high-resolution $\delta^{13}C$ records that there was no compelling evidence for a hiatus at the base of the Bonarelli Level in any of their studied sections.

Cyclicity within the Bonarelli Level

A feature noted by many workers on the Bonarelli Level is the apparent alternation of light (radiolarian-rich) and dark (organic-carbon-rich) layers – though the pattern of alternations varies through the level (Arthur and Premoli Silva, 1982; de Boer, 1982; Kuroda et al., 2005; Scopelliti et al., 2006).

The variation between organic-carbon- and biogenic silica-rich layers in the Bonarelli Level could be explained partly by dilution of C_{org} by biogenic silica or, in the upper parts of the Bonarelli Level, calcium carbonate: an inverse correlation between the concentrations of C_{org} and biogenic silica is observed (Kuroda et al., 2005). Although dilution of C_{org} by biogenic silica is thought to have contributed to observed lithological differences, Al_2O_3 content (representing the terrigenous fraction, which is assumed to be constant) is much less sensitive to changes in biogenic silica concentration than is C_{org}, indicating that the changes in C_{org} concentration cannot be explained solely by dilution (Kuroda et al., 2005).

These contrasting lithologies are therefore thought to represent the presence of two distinct palaeoenvironmental settings (Kuroda et al., 2005; Scopelliti et al., 2006). Previous environmental interpretations have suggested that the dark layers corresponded to periods of anoxia, whilst the light layers were deposited when the bottom water was oxic (de Boer, 1982); however, fine undisturbed laminations identified in many light layers suggests that during their deposition the bottom water was also largely anaerobic (Kuroda et al., 2005).

The light/dark distinction is instead suggested by Kuroda et al. (2005) to be due to deposition under distinct palaeoenvironments dominated either by biogenic silica deposition or by the deposition of organic carbon, partly induced by thickness of the anoxic water column and partly by changes in surface water ecology. Organic-carbon-rich intervals make up ~39% of the Bonarelli Level at Gorgo Cerbara by thickness, with silica-rich intervals comprising ~31% (Kuroda et al., 2005). The remainder of the section is made up of intervals characterised by a mixture of these two components (~24%). Sedimentation rate is thought to have varied between the two layers: Kuroda et al. (2005), using Al_2O_3 concentration as a proxy for accumulation rate, arrived at average sedimentation rates of 0.16 cm/kyr for silica-rich intervals, and 0.13 cm/kyr for silica-poor ones. It is worth noting that the lithological expression of this cyclicity varied through the event: the oxic/anoxic couplets described above are more characteristic of only the lower and upper parts of the Bonarelli Level (Kuroda et al., 2005). During the middle stage of the Bonarelli Level, the relatively few C_{org} poor layers have actually been suggested to be records of gravity-flow events (Kuroda et al., 2005).

Potential gravity-flows aside, these lithological (and by extension environmental) alternations may well have been orbitally forced, with C_{org}/biogenic silica-rich couplets deposited over the span of an orbital cycle (Kuroda et al., 2005; Scopelliti et al., 2006). Scopelliti et al. (2006) linked light-dark lithological variations through the Bonarelli Level to the ~21 kyr precession cycle on the basis of spectral analysis of cyclicity observed in geochemical records. Kuroda et al. (2005) zeroed in on the lower part of the Bonarelli Level where the alternation of these lithologies is clear (see the discussion of sub-division of the Bonarelli Level in Section 2.2.2), and also determined that C_{org}/biogenic silica-rich couplets in this section corresponded roughly to 19 and 23 kyr precession cycles. It is worth noting, however, that couplet thickness varies greatly and the durations for each couplet (calculated using Al_2O_3 concentration as a proxy for accumulation rate) varied between 5–39 kyr, interpreted as either destructive/constructive interference from other cycles such as obliquity and eccentricity, or as omission/amalgamation of cycles by hiatuses (Kuroda et al., 2005).

Spectral analyses of SiO_2 and Al_2O_3 through the Bonarelli Level, which reflect variations in detrital input (Al_2O_3 is thought to indicate riverine input, and SiO_2 may have either a biogenic or a detrital origin), yield dominant periodicities corresponding to both the precession and short eccentricity cycle; cyclicity with a period of 110 kyr was also observed in Rb/Al, Si/Al and Cr/Al ratios (Scopelliti et al., 2006; Batenburg et al., 2016). Intervals with high Rb/Al (assumed to reflect fine detrital supply) and Cr/Al (reflecting development of oxygen-deficient bottom waters and non-oxidised organic matter) are suggested to represent periodic increases of riverine influxes as a result of increased humidity, leading to sluggish circulation and reduced bottom-water circulation (Scopelliti et al., 2004, 2006). Conversely, Si/Al highs, which occur in antiphase during Rb/Al and Cr/Al lows, are suggested to represent periods of re-established circulation, during which the availability of nutrients from deep water masses resulted in enhanced biogenic silica production (Scopelliti et al., 2006).

There is growing evidence for an obliquity signal through the Bonarelli Level, on the face of it a surprising result given the low paleolatitude. Obliquity cycles have been identified in SiO_2, Al_2O_3, TiO_2 and organic-matter content; it is suggested that obliquity-driven changes in seasonality and ventilation caused co-incident increases in terrestrially derived components and siliceous plankton blooms (Batenburg et al., 2016). Obliquity signals have also been recognised in OAE 2 records from the Western Interior Basin, USA, and the North Atlantic; in fact, in some sections, obliquity is the dominant signal by the end of the event (Meyers et al., 2001, 2012; Kuypers et al., 2004). The strength of this obliquity signal may be because, at the time of OAE 2, the orbital configuration was such as to promote the influence of obliquity: deposition of the Bonarelli Level has been suggested to have coincided with a 2.4 Myr eccentricity minimum (Mitchell et al., 2008; Meyers et al., 2012; Batenburg et al., 2016). Changes in oceanography at this time may have also favoured the propagation of high-latitude signals to mid- and low latitudes (such as the Umbria–Marche Basin): sea-level rise at this time may have driven the formation of a new intermediate/deep-water source

at high latitudes, its movement allowing a high-latitude signal to propagate towards the Equator (Meyers et al., 2012).

Finally, cyclicity with an even shorter period than precession cycles has been observed in records of pyrite enrichment, particularly in the lower part of the Bonarelli Level (Kuroda et al., 2005). Variations on the order of 1000 yr have been interpreted as reflecting changes in the supply rate of reactive iron, thought to be supplied to the basin by advection along the chemocline from marginal seas (Kuroda et al., 2005). This all goes to show that, even within an extreme climatic event such as OAE 2, cyclical drivers of varying periods continue to affect the local oceanographic system; cyclicity attributed to eccentricity and precession cycles through OAE 2 is not unique to the Bonarelli Level, but has been observed through OAE 2 at other sites globally (Meyers et al., 2001; Kuypers et al., 2004; Scopelliti et al., 2004; Voigt et al., 2008).

After the Bonarelli Level

Two differing interpretations exist of the age of the limestones deposited immediately above the Bonarelli Level, as discussed above in the context of the proposed hiatus above the Bonarelli Level. The age of these limestones impacts the context in which their geochemical signatures are viewed. If, for example, they are Cenomanian in age (as proposed by Batenburg et al., 2016), detailed studies of the clay mineralogy of sediments above the Bonarelli Level would provide insight into local conditions during the exit from OAE 2. If, on the other hand, they are Turonian in age (Voigt et al., 2007; Gambacorta et al., 2015), no record of conditions during the termination of OAE 2 and in its immediate aftermath exists for study, as this time is 'missing' within a significant hiatus.

The record as it stands indicates more terrigenous material in the limestones immediately above the Bonarelli Level than in the underlying Scaglia Bianca limestones, or the Scaglia Rossa limestones further up-section (Trabucho-Alexandre et al., 2011). The composition of this post-Bonarelli terrigenous material is similar to that within the Bonarelli Level itself, and different to that within the

limestones deposited below the Bonarelli Level and further up-section. Trabucho-Alexandre et al. (2011) interpreted this observation as recording a shift in the provenance of terrigenous material coincident with the depositional onset of the Bonarelli Level due to some change in environmental conditions, with the signature of this provenance shift persisting until around a metre above the top of the Bonarelli Level (a horizon interpreted by Trabucho-Alexandre et al. (2011) as representing the Cenomanian-Turonian boundary).

Up section and unambiguously in the Turonian, the characteristic 'red' beds of the Scaglia Rossa Formation demonstrate the substantial change in depositional environment following the end of OAE 2; authigenic haematite in these beds reflects the improved seawater oxygenation and the reduced demand for oxygen in the sediments associated with decreased productivity (Trabucho-Alexandre et al., 2011).

Final Remarks

The low-resolution of timescales applied to palaeoenvironmental change over Mesozoic OAEs (and over pre-Cenozoic rapid climatic perturbations generally) has been identified as an issue hampering the comparison of records of organic-rich sediments in the Mesozoic and Palaeozoic, such as the Bonarelli Level, with Cenozoic OC-rich sediments, such as sapropels (Negri et al., 2009). If such a comparison were possible it might allow identification of common drivers or environmental responses within these records of climatic and environmental perturbation. High-resolution $^{3}He_{ET}$ timescales, which have been proved useful from the Cretaceous to the Holocene (e.g. Patterson and Farley, 1998; Mukhopadhyay et al., 2001b), seem likely to be a great aid in bridging this gap in our understanding of the genesis of organic-carbon-rich sediments.

3. Method development: analytical approach for He isotopes, an exploration of Ne-isotopes, and measurement of He-isotopes in diverse pelagic lithologies.

Abstract

Methodological development was carried out in the Oxford Noble Gas Laboratory to lay the groundwork for the application of $^3He_{ET}$ timescales to stratigraphic sections with heterogeneous lithologies, including organic-rich black shales and cherts. This lithological variety marks an expansion of the $^3He_{ET}$ technique's previous use; previous measurements of helium from seafloor sediments have been made only in limestones, marls and pelagic clays, which typically have low concentrations of C_{org} and S (Amari and Ozima, 1988; Fukumoto et al., 1986; Takayanagi and Ozima, 1987; Farley, 1995; Farley and Patterson, 1995; Marcantonio et al., 1995, 1996, 2009; Patterson et al., 1998; Patterson and Farley, 1998; Farley and Eltgroth, 2003; Murphy et al., 2010; Farley et al., 2012; Torfstein, 2012; Chavrit et al., 2016).

A laser ablation system was set up to release helium from sedimentary samples; powdered, decarbonated samples were heated using a Fusions Diode .970 Laser Stepped Heating System. Following trials of packaging and heating methods, samples of 100–400 mg (sample size dependent on lithology) were ultimately placed unwrapped into a sample cell; packaging samples in silver foil was also trialled. The exposure of sample gas to an activated charcoal trap at liquid nitrogen temperature to remove CO_2 and organic compounds (following e.g. Patterson and Farley, 1998; Chavrit et al., 2016) was found to be sufficient to deal with the gases released not only from pelagic limestones but also from black shale samples, such as those from the Bonarelli Level, that were both extremely rich in organic-carbon (up to 31% total organic carbon content) and known to contain high

concentrations of sulphur (Arthur and Premoli Silva, 1982; Farrimond et al., 1990; Kuroda et al., 2005).

Following the deconvolution of extraterrestrial ^{3}He, ~95% of ^{3}He in samples was found to be of extraterrestrial origin. The reproducibility of ^{3}He measurements was worse than analytical precision due to the 'nugget effect' of a statistically small number of helium-bearing interplanetary dust particles in each sample aliquot (Patterson and Farley, 1998; Farley, 2001), with the observed spread of measured replicates approximated using a Gaussian distribution with 1σ ~20%. Outliers, including those thought to be a result of the inclusion of rare 'helium-rich particles' (see Patterson and Farley, 1998; Mukhopadhyay et al., 2001a; McGee et al., 2010; Murphy et al., 2010; Torfstein, 2012), were identified and excluded on the basis of non-matching replicates. Over the sections studied in this thesis, 6–13% of measurements were identified as 'outliers' in this manner. Neon released from samples during the extraction process for helium was also measured, though was not the prime focus of this study. A significant extraterrestrial component of neon was present in these samples, though the majority appeared to be of atmospheric origin.

As chert is a diagenetic product, the hitherto unexplored question of whether chert formation during diagenesis results in the loss of extraterrestrial helium was explored using two bedding-parallel 'chert nodule to host carbonate' transects. No correlation between the concentration of helium and the 'degree of chertification' was identified; chert diagenesis appears to have no effect on the concentration of helium hosted in sediments, allowing the use of $^{3}He_{ET}$ timescales to be expanded into sections containing this lithology.

3.1 Methodology: analytical approach

Most prior studies of extraterrestrial helium in sediments followed the methodology of Patterson and Farley (1998), in which noble gases were liberated from decarbonated sediment samples by heating to 1200–1400 ^{o}C in a radiative vacuum furnace (e.g. Patterson and Farley, 1998; Mukhopadhyay et al., 2001a; McGee et al., 2010; Chavrit et al., 2016). Following release, gases were purified through exposure to an activated charcoal trap at liquid nitrogen temperatures and to getters, before being separated on a cryogenic trap (e.g. Patterson and Farley, 1998; Chavrit et al., 2016). Fundamentally, the same overall approach was followed in this study, but with the key difference of heating with a laser ablation system to release helium from the samples instead of with a radiative vacuum furnace. Initial testing and development of sample preparation and mass spectrometer protocol was carried out using a suite of Scaglia Bianca samples collected in the Bottaccione Gorge, Italy (GPS co-ordinates: 43°21'42"N; 12°34'54"E, ~2 km east of the Contessa section described in Section 2.2.1) by Jenkyns (Jenkyns et al., 1994). These Bottaccione Gorge samples were only used for method development and comparison of the Oxford system with other labs (Section 3.3.1); separate sample suites were used in the construction of age models in Chapters 4 and 5.

3.1.1 Sample preparation

Decarbonating samples

The carbonate fraction of pelagic sediments contains little to no helium, so decarbonation of powdered samples allows larger aliquots of sample to be analysed (Patterson and Farley, 1998). Samples were powdered manually using an agate pestle and mortar, following Patterson and Farley, (1998); Torfstein (2012); and Chavrit et al. (2016). Approximately 5 g was decarbonated in 10% acetic acid (in excess) for six hours at room temperature under gentle agitation to remove the

carbonate fraction (Patterson and Farley, 1998). Samples were then rinsed in deionised water until neutrality and oven dried at 40 ^{o}C (following Patterson and Farley, 1998; Chavrit et al., 2016).

Decarbonation with stronger or more concentrated acids than 10% acetic (for example, 12M HF – 3M HCl, or 6M HCl) has been shown to remove between 70–90% of the ^{3}He (Mukhopadhyay and Farley, 2006). Following Patterson and Farley (1998) most studies of extraterrestrial ^{3}He use 10% acetic acid for decarbonation, though some use concentrations as low as 0.5N (McGee et al., 2010; Torfstein, 2012). Comparison between leached and unleached aliquots of the same sample has been typically held to show that helium content is unaffected by 10% acetic acid leaching (Patterson and Farley, 1998; Mukhopadhyay et al., 2001a); however work by Torfstein (2012) indicated that even mild acetic acid leaching may, in fact, slightly deplete a sample's helium. For the sake of consistency, therefore, all samples were subject to the decarbonation process, even those with little to no carbonate content, so that any depletion effect would be applied consistently across all samples.

Sample Size

The primary concern when choosing sample size is to obtain enough ^{3}He for analysis. The (post-decarbonation) mass of sample required to provide a ^{3}He signal significantly above blank levels varied with lithology (as concentration of extraterrestrial ^{3}He, the main contributor to ^{3}He in samples, is inversely proportional to sedimentation rate (Farley, 2001)). Replicates of different masses of a limestone, shale and chert sample were made to determine the most appropriate (decarbonated) sample weight: ~150–200 mg for limestones, ~100–150 mg for He-rich shales and ~300–400 mg for He-poor cherts (Figure 3.1, Table 3.1). Previous studies have measured ~200–500 mg of sample in each heating run (Patterson and Farley, 1998; McGee et al., 2010; Chavrit et al., 2016).

The full range of approximate 'area-time products' (mass of sample analysed/sediment mass accumulation rate) of samples measured in this study is 0.002–0.19 m^{2} yr (Figure 3.2). Most samples, however, have area-time products between 0.003–0.07 m^{2} yr, with an average of 0.034 m^{2} yr,

comparable to the area-time products of carbonate sediments from other studies (Farley and Eltgroth, 2003; Murphy et al., 2010; Farley et al., 2012). Since the majority of ^{3}He in pelagic sediments is hosted in discreet interplanetary dust particles (IDPs) (see e.g. Farley, 2001), it is thought that this size of sample aliquot is likely to underestimate the ^{3}He content of the sediments as a whole; in fact, it has been estimated that an area-time product of 100 m^2 yr would be necessary for a good statistical representation of all helium-bearing interplanetary dust particles (Farley et al., 1997; Patterson and Farley, 1998; Farley, 2001; Torfstein, 2012). This problem is thought to be the reason that reproducibility of ^{3}He-concentration measurements is lower than would be expected from analytical uncertainty (for more details, see 'Reproducibility' in Chapter 2, Section 2.1.3). In line with other studies (e.g. Farley et al., 1997; Patterson and Farley, 1998), it is assumed that by keeping the area-time product (and hence degree of under-sampling) reasonably consistent through a stratigraphic section, the effect of systematic under-sampling cancels out in calculation of sedimentation rates, as it affects both the apparent concentration of ^{3}He in sediments and the apparent ^{3}He background flux. There is the potential for systematic error to be introduced to $^{3}He_{ET}$ age-models if different samples measured have very different area-time products. In this study, estimated area-time products in samples used for background flux ranged between 0.02–0.05 m^2 yr. The estimated area-time products of most samples used to construct age models were broadly similar to those of background flux samples, however, ~10% of age-model samples had estimated area-time products of around an order of magnitude lower than this, an unfortunate side-effect of sampling in sections containing varying lithologies that accumulated at different rates. Following the simulated distributions of Farley et al. (1997) this order of magnitude decrease in area-time product may result in systematic relative under-sampling of extraterrestrial ^{3}He of up to ~12%. This is about half the size of the 1σ 'random error' in $^{3}He_{ET}$ concentration measurements (20%) which arises from the inconsistent distribution of IDPs in the sediment. The origin of this 20% value is described in Section 3.1.5.

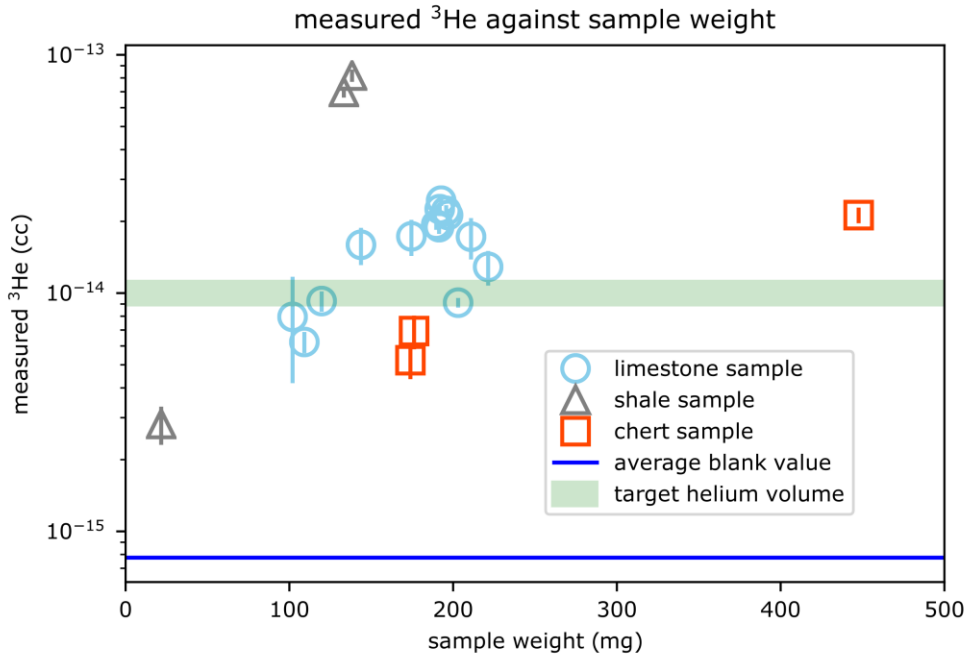

Figure 3.1: ^{3}He (cc) measured in different masses of a limestone, shale, and chert sample, with an indication of the target minimum volume of helium release in sample measurements (>10× blank values). Error bars represent the analytical error on the measurement of ^{3}He (cc).

	decarb sample weight (mg)	bulk sample weight (g)	^{4}He yield (ccSTP)	^{3}He yield (ccSTP)
limestones (avg.)	149	2.15	4.14×10^{-8}	4.15×10^{-14}
shales (avg.)	135	0.15	2.74×10^{-8}	3.71×10^{-14}
cherts (avg.)	302	0.38	3.71×10^{-8}	1.99×10^{-14}
hot blank (avg.)			0.08×10^{-8}	0.08×10^{-14}

Table 3.1: Average decarbonated sample weight and original bulk sample weight for the three primary lithology types investigated in this thesis, along with the average yield of ^{4}He and ^{3}He. The average helium yield from hot blanks is presented for comparison.

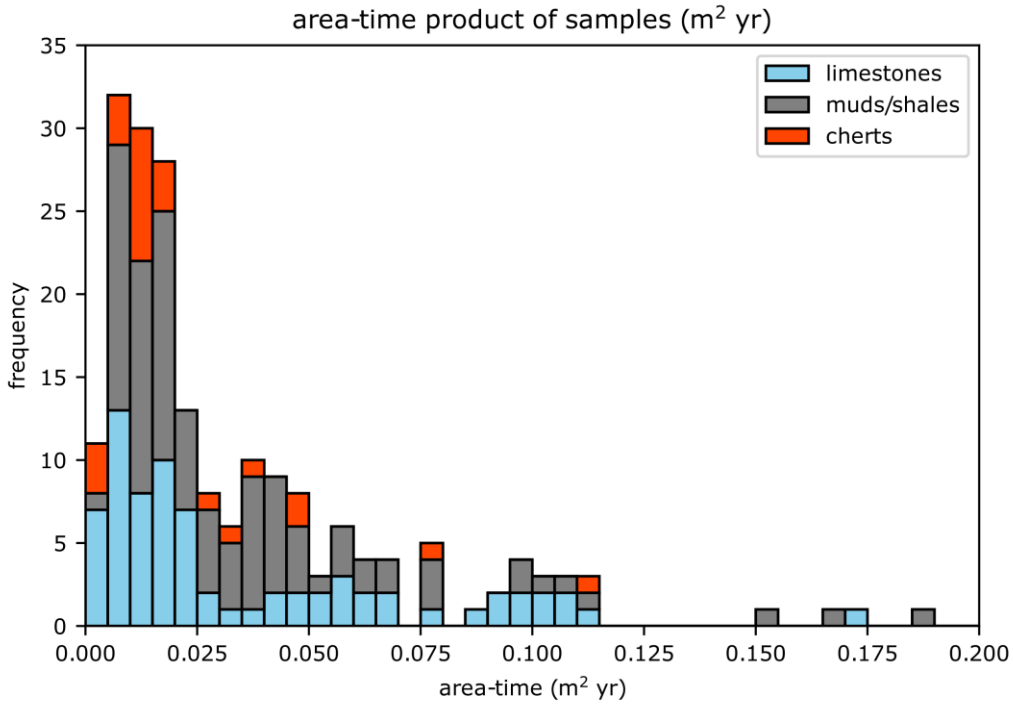

Figure 3.2: Approximate area-time products of samples from Contessa and Furlo (from which age-models were constructed in Chapters 4 and 5), separated by lithology.

3.1.2 Mass Spectrometer

Laser heating system

Sample powders were heated using a Fusions Diode .970 Laser Stepped Heating System. Figure 3.3a includes a schematic of the sample cell construction. The outer window of the sample cell is sapphire glass, impermeable to helium, but quartz glass was used for the smaller, thinner window directly above the sample holder (see Figure 3.3a), as exposure to the laser running at high power was found to crack small sapphire glass windows. The thinner, replaceable, second window acts primarily to protect the outer sapphire window from damage or staining as the contents of the sample cell are heated, as well as, when laid flush with the top of the sample holder, limiting the movement of powdered samples during evacuation and heating.

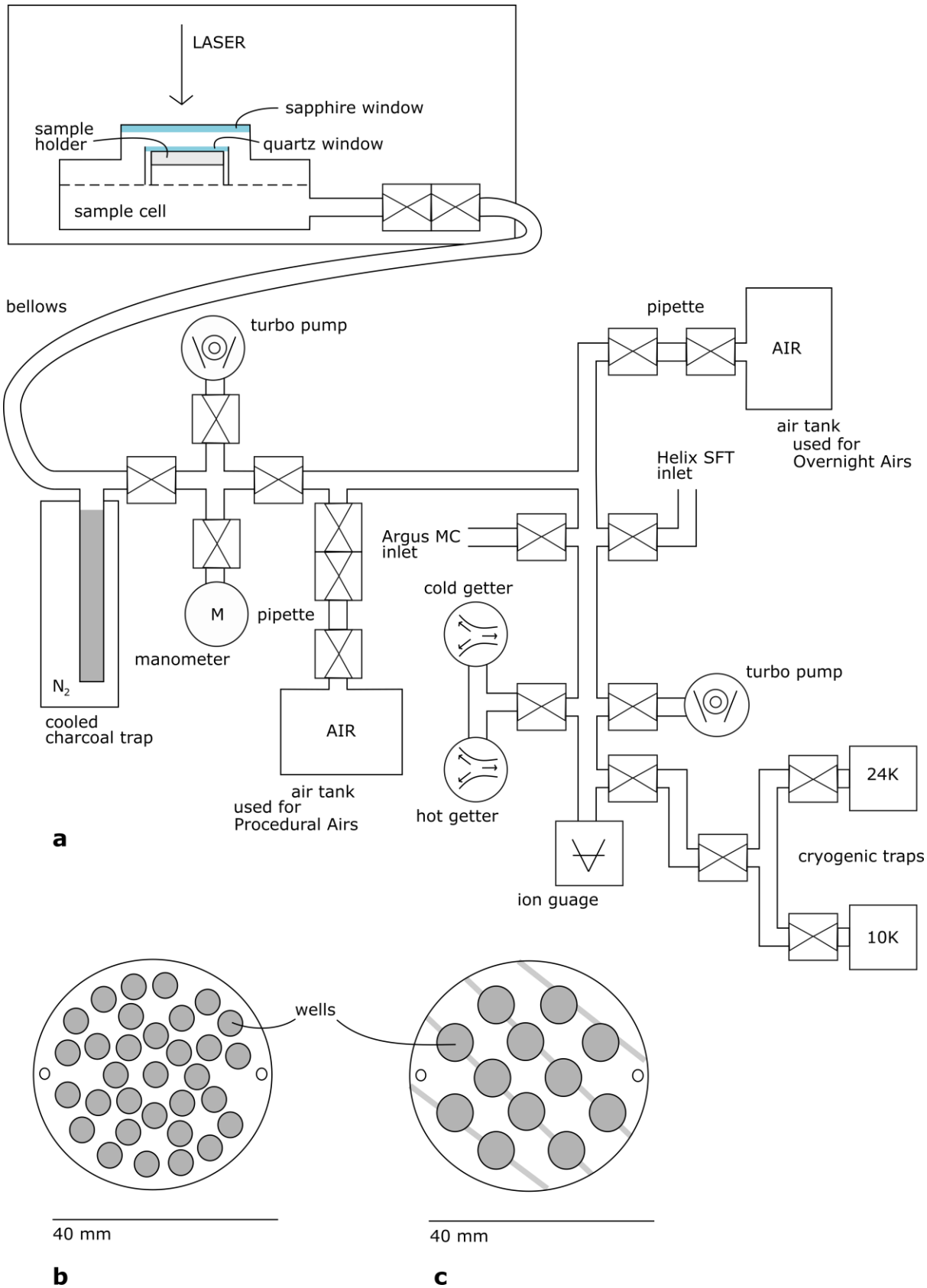

Figure 3.3: Schematic diagrams of mass spectrometer preparatory line and sample holders. ***(a)*** *schematic diagram of mass spectrometer preparatory line, including details of sample cell;* ***(b)*** *schematic of the sample holder used with small silver-lined packets (see body text);* ***(c)*** *schematic of the sample holder used with large silver-lined packets and powders (see body text).*

Two sample packaging techniques were trialled: wrapping sample powders in metal packets, and filling wells in the sample cell with unwrapped powder. Wrapping sample powders was intended to both make the process of loading powders into the sample holder easier and to reduce the likelihood of ejection of material from sample cell wells during heating. Different metal packets and styles of wrapping were trialled, with the aim of maximising helium release from the samples whilst minimising the contribution to blanks.

Silver (Ag), tin (Sn) and tantalum (Ta) foil packets were trialled – previous $^{3}He_{ET}$ studies have utilised tin or aluminium foils (Patterson and Farley, 1998; McGee et al., 2010; Chavrit et al., 2016). The blanks measured after heating empty packets are presented in Figure 3.4. Whilst heating of silver and tantalum foils released negligible additional helium (the average laser-heated, or 'hot' silver and 'hot' tantalum blanks are within error of 'cold blanks' – the background blank levels of the preparatory line without any laser heating), the blank measured from the heating of tin foil produced comparable volumes of helium to measured samples. These high blank values measured on a tin foil may be related to its manufacturing process; though the important conclusion in the context of this study was simply that it was not an appropriate sample wrapper.

The effectiveness with which the laser coupled to the metal foil and melted the sample powders was examined visually: a packaging method was judged a success if the sample powder had melted after heating (Figure 3.5). Measurements of helium release from multiple replicates of the same (decarbonated limestone) sample were used to support the results of these visual melting tests (Figure 3.6a). Initially 'large' (~150 mg of powder) silver and tantalum-wrapped packets were tested. The laser coupled poorly to both silver and tantalum; the powder within these packets often looked unchanged after heating, and very little helium was released from heating of samples packaged in this way (see 'large silver packets' and 'large tantalum packets' in Figure 3.6a). These 'large' packets of powder also had a tendency to 'burst' whilst being heated, spraying the quartz window with a

dark residue and, sometimes, melted silver. Once the quartz window had been dirtied in this way it was very difficult to heat other samples in that sample cell.

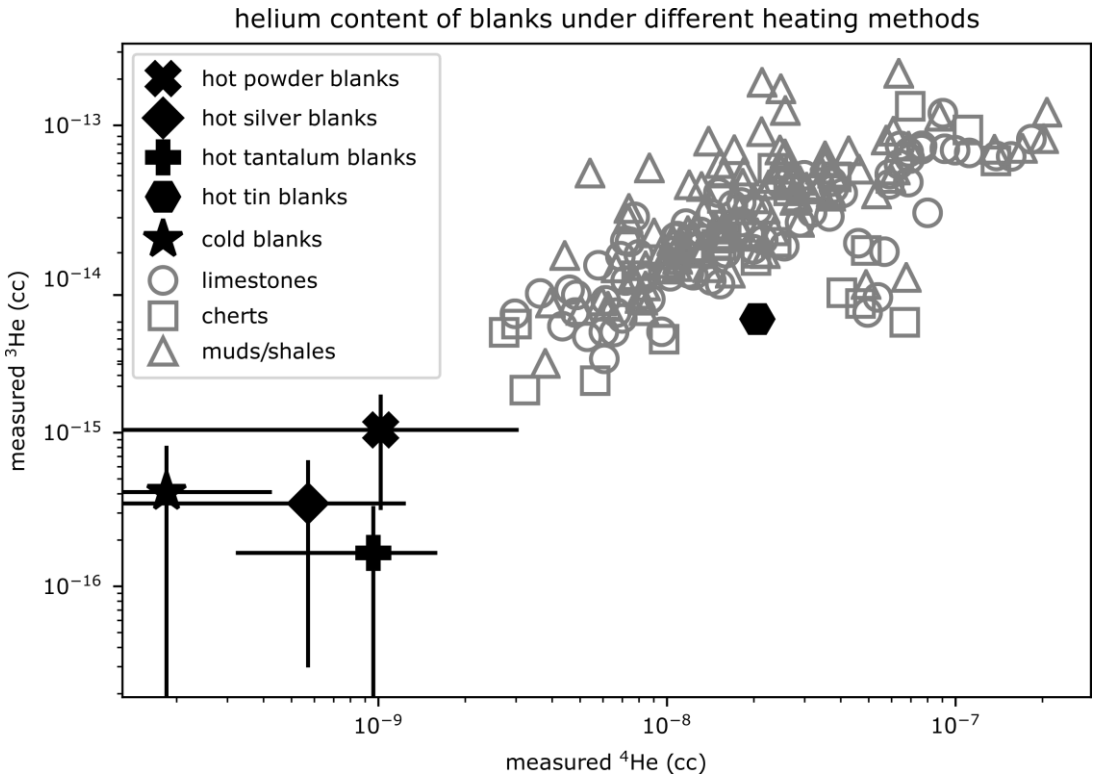

Figure 3.4: Comparison of average blank values associated with different sample packing, against a background of measured helium from samples.

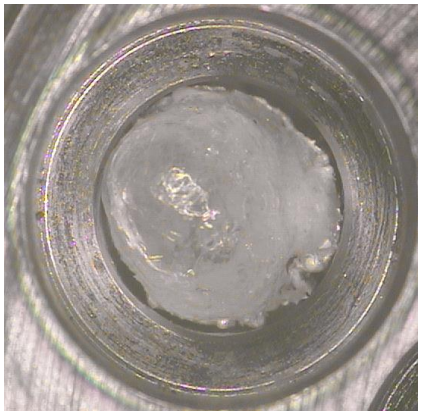

Figure 3.5: Glassy residue of melted silver foil-wrapped sample following heating.

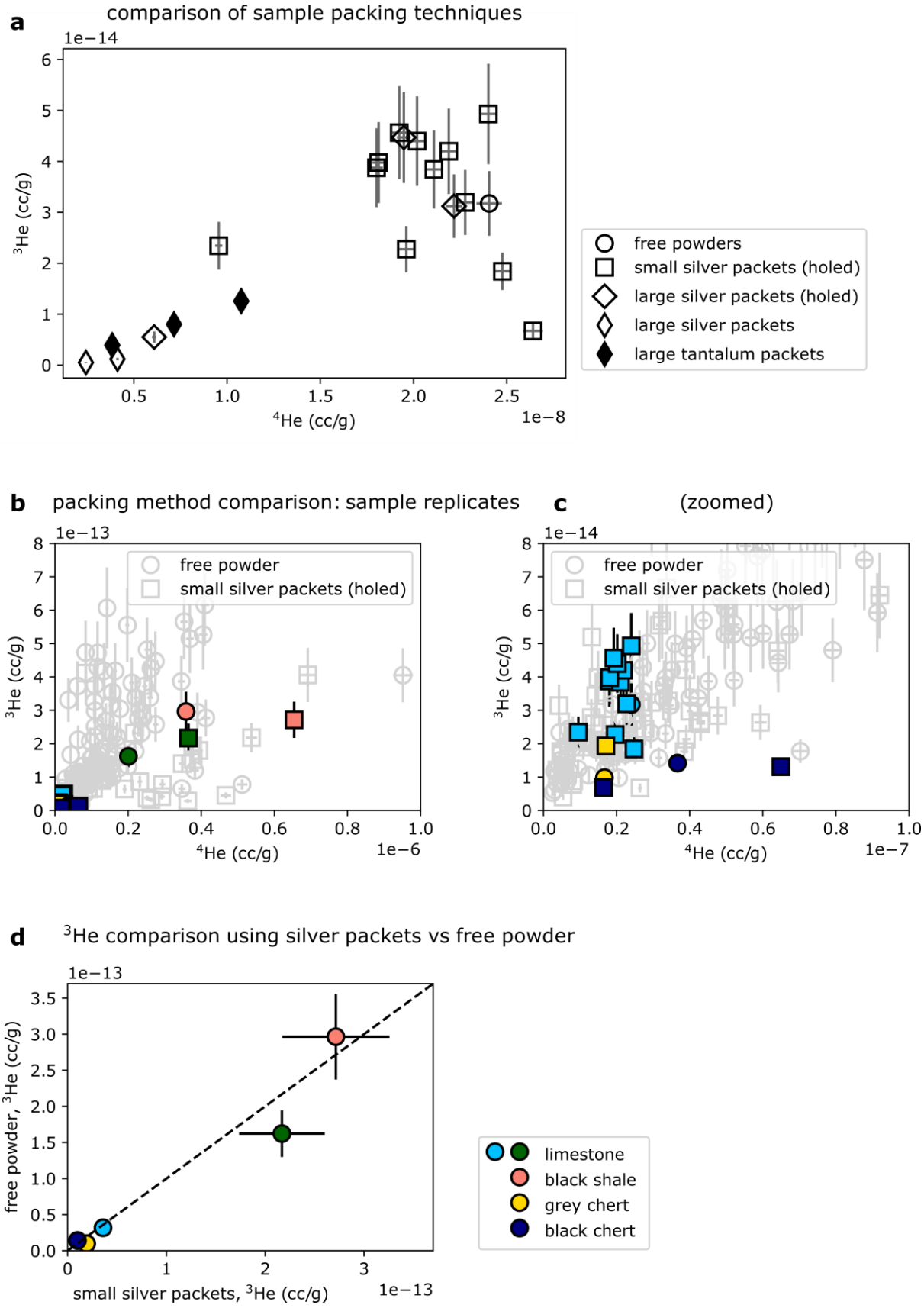

Figure 3.6: Helium measured during trials of sample packing techniques. ***(a)*** *Helium measured during trials of all sample packing techniques. All data are replicates of one (decarbonated limestone) sample. Samples prepared either as free powder or in small (holed) silver packets were judged*

visually to be the most melted after laser heating, similarly, the most consistent high helium release is obtained using these packing methods. ^{3}He concentrations between replicates of a given sample are not expected to be identical due to the 'nugget effect' (explored further in Section 3.1.5). ^{3}He (cc/g) error bars on all plots in this figure represent the expected 20% variation between replicates, whilst error bars on ^{4}He (cc/g) represent analytical error; ***(b, c)*** *comparison of helium released from sample replicates using two different sample packing techniques. Filled symbols of different colours represent different sample replicates. All measured samples are plotted as a background of grey open symbols to give an indication of the inter-sample range of measured helium concentrations. No systematic difference seems to exist between the two packing methods;* ***(d)*** *cross-plot of ^{3}He (cc/g) measured in sample replicates prepared in small (holed) silver packets against ^{3}He (cc/g) measured in replicates prepared as free powders. Average ^{3}He concentrations are plotted in cases where multiple replicates were measured using the same packaging style. The dashed line represents a 1:1 relationship between the two axes. Measured replicates fall along this line – no systematic difference is apparent between the two packing methods.*

Mixing sample powders with borax flux ($Na_2B_4O_7$) was also tested, in the hope that molten borax would act to transfer heat to the sample powders and facilitate their melting. The addition of this flux did not contribute to blank levels but melting tests of different sample powder/borax mixtures indicated that its addition did not substantially improve the melting of sample powders.

In order to overcome the effects of poor coupling between the laser and the metal packets, small holes were poked in the top sides of sample packets after they had been placed in the wells of the sample holder. (From this point onwards, silver packets were used – mostly for convenience as thinner silver foils were available.) Silver-wrapped samples were prepared as multiple 'small' packets (typically 5× ~40 mg), which were less likely to messily 'burst' than larger packets. As each well in the sample holder held only one sample packet, measurement of a single sample required the heating of multiple wells. A sample holder with 31 small wells (Figure 3.3b) was used to maximise the number of samples in each sample cell; this reduced the number of times the sample cell needed to be opened and refilled.

During heating, the laser was focussed on the sample powder visible through the hole in the wrapping packet until melting was initiated. A spot size of 3 mm was used, and the laser was typically run at ~52.5 W (~70% of its maximum power), though on occasion higher power of up to ~65 W was needed to initiate melting. Using this heating method, sample powders typically began melting in under a minute. After melting began, the centre of the laser spot was moved from focussing on the position of the sample packet hole to the centre of the well, and if the laser power had been increased to initiate melting it was at this point set back to ~52.5 W. Each well was heated for 5 minutes in total (so typically a total laser run-time of 25 minutes per sample). After heating, these small silver-wrapped samples were found to be fused into glass, and measurements of the helium released from samples packaged in this way indicated that this packing/heating method was much more effective at releasing helium (see 'small silver packets (holed)' in Figure 3.6a).

However, heating samples packed in silver foils still often resulted in the deposition of some residue on the quartz window. Given that the laser clearly coupled much better with the sample powders than the silver packets, loading of unwrapped powder into wells was trialled as an alternate sample packing method. Using a sample holder with 12 large wells (Figure 3.3c), with ~200 mg of sample in each well, ~11 samples could be measured per sample cell, almost double the number of samples prepared in small silver packets. The risk of ejecting material from sample wells was minimised by increasing laser power slowly during heating, and by placing a quartz window directly on top of the sample well. Thin channels from the edges of wells (shown on Figure 3.3c) allowed movements of gases below the window whilst preventing easy movement of solid particles (after Ray Burgess, pers. comm.).

Each well was heated for 10 minutes, the first 5 minutes spent ramping the power up slowly from 0 to ~52.5 W, the second 5 minutes spent heating at this power. A 3 mm laser spot sized was used, slightly smaller than the diameter of the well, so during heating the laser was circled around the sample to ensure that no portion was left un-heated. (When measuring helium in chert samples, where a larger sample size of ~400 mg was necessary (see Figure 3.1), the sample powder was divided between multiple wells.) Following heating, sample powders were not completely glassy: typically, the uppermost 1–2 mm was fused into a glassy crust whilst the powder below was unfused but noticeably darker in colour. Testing by Hillegonds (pers. comm.) indicates that when samples that had undergone the above heating process were heated for a second time a negligible amount of helium was re-released (though it should be noted that Hillegonds used a somewhat broader and flatter well shape). Hot blanks for this sample method were obtained by heating an empty sample well using the heating method described above; average ‘hot powder blanks’ were within error of the background blank levels of a cold preparatory line (Figure 3.4).

Heating in this manner released helium from sample powders as effectively as heating of small (holed) silver-wrapped packets (see Figures 3.6a, b, c, d). Matched-pair t-tests (using a significance

level of 10%) performed on both measured ^{3}He (cc/g) and ^{4}He (cc/g) in the replicates presented in Figures 3.6 b, c, d confirm that there is no significant difference between packaging methods. Ultimately, preparation of samples as 'free powders' was adopted as a 'best practice' sample packaging method, both because more samples could be measured per-sample cell, and because there was less chance of dirtying the quartz window during heating. All Bonarelli Level samples (examined in Chapter 5) were prepared in this way. However, as this conclusion took some time to reach, all 'precession cycle' samples (examined in Chapter 4) were prepared in small (holed) silver packets. Samples used in the determination of background flux (see Section 4.5.1) were packaged in both styles (as discussed above, this was not likely to have introduced any systematic differences).

Prior to lasering, the sample cell was pumped down to vacuum and baked with heating tape at ~80 °C for at least 24 hours to liberate gases adsorbed on its surfaces. Baking the sample cell during pumping reduced cell 'pump-down' time, increasing sample throughput. Significant helium release from pelagic sediments begins at temperatures >250 °C (Mukhopadhyay and Farley, 2006), so this process was not expected to release any of the helium contained within sediment grains, a hypothesis confirmed by comparison of baked and un-baked sample replicates (Figure 3.7).

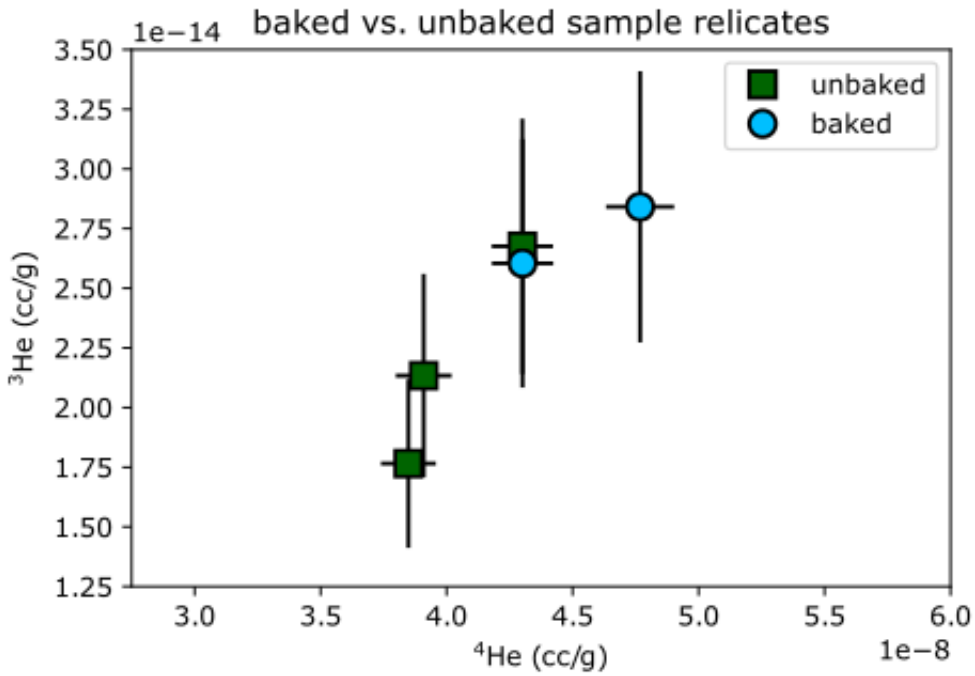

Figure 3.7: Replicates of a pelagic limestone sample measured both with and without baking of the sample cell during pumping to vacuum. Baking of the sample cell does not appear to liberate helium from samples. ^{3}He (cc/g) error bars on this figure represent the expected 20% variation between replicates (see Section 3.1.5), whilst error bars on ^{4}He (cc/g) represent analytical error.

Clean-up and gas separation

A schematic of the preparatory line is presented in Figure 3.3a. Most gases released on heating were frozen down immediately on a cold finger containing a mixture of 5 g activated charcoal and 12 g 5Å molecular sieves cooled with liquid nitrogen. This clean-up step between the laser heating system and the rest of the mass spectrometer preparatory line was introduced to limit the exposure of the preparatory line to the carbon dioxide and sulphur released from 'dirty' black shale samples. An initial clean-up step of extracted gases between the furnace and the main line was also carried out in the methodology applied by Patterson and Farley (1998) and Chavrit et al. (2016).

Gases were further purified using MP10 getters (SAES st101 alloy, as provided with the commercial noble gas prep line), and helium and neon were separated using a cryogenic trap containing

activated charcoal held between ~10-90 K (Janis Research Company, Inc.); this procedure is similar to that of Patterson and Farley (1998) and subsequent studies.

Mass spectrometer settings

Helium was measured on a HELIX SFT mass spectrometer, allowing both isotopes to be measured simultaneously, with ^{4}He on a Faraday cup and ^{3}He on a secondary electron multiplier. To maximise the sensitivity and accuracy of measurement of a small ^{3}He peak, the ion source trap current was raised to 300 µA (from 200 µA), and a long integration time (67.11 s) and mass settling time (10,000 ms) were used during measurements, with manual centring of ^{3}He and ^{4}He peaks performed every three measurements over five cycles through the run.

Neon was measured on an Argus IV multicollector mass spectrometer. ^{20}Ne and ^{22}Ne were measured on Faraday cups, with the less abundant ^{21}Ne measured on a compact discrete dynode electron multiplier. ^{40}Ar was also measured to allow correction of the ^{20}Ne+ peak for ^{40}Ar++ at m/z 20. Peaks were manually centred for all isotopes, using a mass settling time of 2000 ms and an integration time of 4.19 s.

3.1.3 Post-collection data processing

Calculating less abundant isotopes

^{3}He/^{4}He ratio was calculated for each sample by extrapolating the ^{3}He/^{4}He ratio measured in successive readings. The intensity of ^{3}He was then calculated from the intensity of the more abundant ^{4}He isotope, and the ^{3}He/^{4}He ratio. Analytical errors on ^{3}He intensity are determined from the errors on ^{3}He/^{4}He and ^{4}He. Typical analytical errors are 0.04% for ^{4}He, and 7% for the low intensity ^{3}He.

Minor isotopes of neon were calculated in a similar manner, with the intensity of ^{21}Ne and ^{22}Ne calculated from the measured intensity of the more abundant ^{20}Ne isotope and the measured

$^{20}Ne/^{22}Ne$ and $^{21}Ne/^{22}Ne$ ratios. The contribution of doubly charged ^{40}Ar to ^{20}Ne measurements was corrected for by measuring ^{40}Ar and applying the correction:

$$^{20}Ne_{(corrected)} = {}^{20}Ne_{(measured)} - (0.1255 \times {}^{40}Ar_{(measured)})$$

Equation 3.1

where the constant, 0.1255, is the ratio of $^{40}Ar^{+}/^{40}Ar$ as previously calibrated on the Oxford mass spectrometer.

Blank corrections

Measurements were blank-corrected by subtracting the average blank measured alongside each 'suite' of measurements (a full sample cell, usually ~11 samples). For samples wrapped in silver packets, 'hot blanks' were procedural blank measurements in which an empty silver packet was heated instead of a sample. In the case of unwrapped samples, the sources of He and Ne in blanks were simply gases sorbed to the inside walls of the sample cell, bellows and preparatory line; procedural blank measurements could be run without heating any sample. Blank values were typically ~4% of ^{4}He and ~5% of ^{3}He, similar to ^{3}He blanks reported elsewhere (Patterson and Farley, 1998; Mukhopadhyay et al., 2001a; McGee et al., 2010). It was hoped that the use of a laser heating system in this study to liberate noble gases would result in lower blanks; instead, the two heating methods appear comparable.

Neon blank values were very high relative to the abundance of neon in the samples, an observation that is explored further in Section 3.3. Blank values were, on average, ~20–30% of measured neon abundances (24% for ^{20}Ne, 29% for ^{22}Ne, and 21% for ^{21}Ne), though, due to the very variable volume of neon released from samples, blank contributions to samples varied from <1% to >300% in some cases.

Drift corrections

The stability of the mass spectrometer over the period of its use was estimated from the degree of variation in daily 'air standard' measurements. Typical 1σ values for ^{4}He and ^{3}He of air standards over a sampling period were ~1% and ~5% respectively. Typical 1σ values for all neon isotopes of air standards over a sampling period were ~1.5%. These automated standards, run daily on the mass spectrometer line downstream of the furnace clean-up (see above), also allowed correction of the daily samples for any drift on the machine, though typically no drift was observed over the sampling period.

Converting to volume

The volumes at standard temperature and pressure (ccSTP) of noble gas isotopes in samples were calculated by comparison to Procedural Air standards; these were air shots of a known volume analysed using the same procedure as the samples, following McGee et al. (2010). The helium content of these air shots was calculated using values from Porcelli et al. (2002) for helium concentrations in air: $[^{4}He] = 5.24\pm0.005\times 10^{-6}$ ppv, $[^{3}He] = 7.34\pm0.007 \times 10^{-12}$ ppv, $^{3}He/^{4}He = 1.393\times10^{-6}$. 1σ values over all Procedural Airs (normalised to that day's air standard) were ~7% for both ^{4}He and ^{3}He. Variability (particularly in ^{4}He) was rather higher than in 'air standard' measurements. This inconsistency may be the result of adsorption of He onto surfaces within the preparatory line: Procedural Airs (and sample runs) were exposed to a much larger surface area, including the sample cell and cold finger, than daily 'air standards'.

The neon content of these air shots was, likewise, calculated from the neon concentrations in air from Porcelli et al. (2002): $[^{20}Ne] = 1.65\pm0.004 \times 10^{-5}$ ppv, $[^{22}Ne]= 1.68\pm0.004 \times 10^{-6}$ ppv, $[^{21}Ne]= 4.87\pm0.01 \times 10^{-8}$ ppv, $^{20}Ne/^{22}Ne = 9.8$, $^{21}Ne/^{22}Ne = 0.029$. 1σ values over all Procedural Airs (normalised to that day's air standard) were ~10% for all neon isotopes, likely influenced by the same factors that caused high variability in Procedural Air helium measurements.

3.1.4 Deconvolution of sources of helium

The extraterrestrial ^{3}He component of the measured helium was calculated from the observed ^{3}He concentration ($[^{3}He_{observed}]$) and $^{4}He/^{3}He$ ratio ($^{4}He/^{3}He_{observed}$) using a two-component mixing model (Patterson and Farley, 1998).

$$[^{3}He_{ET}] = [^{3}He_{observed}] \times (^{4}He/^{3}He_{observed} - {}^{4}He/^{3}He_{terrestrial})/(^{4}He/^{3}He_{ET} - {}^{4}He/^{3}He_{terrestrial})$$

Equation 3.2

The use of this mixing model assumes that there are only two major contributors to helium in sediments: interplanetary dust particles with an extraterrestrial signature and terrestrial detrital material with a radiogenic signature. This assumption is discussed further in 'Deconvolving the extraterrestrial component of noble gases in sediments', Section 2.1.3.

The extraterrestrial endmember composition was taken from the average value of interplanetary dust particles measured in the atmosphere, $^{3}He/^{4}He_{ET} = 2.4\times10^{-4}$ (Nier and Schlutter, 1990, 1992), a value used in common with many other studies (Farley, 1995; Marcantonio et al., 1995, 2009; McGee et al., 2010; Farley et al., 2012).

A $^{3}He/^{4}He_{terr}$ ratio of 3×10^{-8} was used in this study to describe the terrestrial endmember composition (following Farley and Patterson, 1995; Patterson and Farley, 1998; Farley, 2001; Mukhopadhyay et al., 2001a, 2001b; Farley and Eltgroth, 2003; Murphy et al., 2010; Farley et al., 2012). This choice of terrestrial endmember value derives from the $^{3}He/^{4}He$ ratio of 'average terrestrial crust': $2–4\times10^{-8}$ (Farley, 2001; Farley et al., 2012). The isotopic composition of the terrigenous material delivered to different regions is known to change depending on the composition of its source (Marcantonio et al., 1998), and examinations of $^{3}He_{ET}$ in Holocene and Quaternary sediments often use site specific values for the terrestrial endmember, ranging from $1\times10^{-8} – 3\times10^{-7}$ (e.g. McGee et al., 2010; Torfstein, 2012; Chavrit et al., 2016). However, in this study, an average crustal value is used for the terrestrial endmember as the exact composition of the fine-

grained dust source to the region over the Cretaceous is not known. Furthermore, this choice of terrestrial endmember value matches that of Farley et al. (2012) in their study of the Scalia Bianca Formation. As discussed in Section 2.1.3, the estimated fraction of ^{3}He that is of extraterrestrial origin may be strongly affected by the choice of terrestrial endmember, though samples containing a low proportion of terrigenous ^{3}He are much less sensitive (see Figure 2.1, Farley, 2001). Deconvolving the components of helium in this study's samples as described above, terrigenous ^{3}He accounts for typically <5% of the total ^{3}He, meaning that the estimation of $^3He_{ET}$ concentration in these sediments is relatively insensitive to the choice of terrestrial endmember.

Two additional potential contributors to the helium content of the studied sections are considered below: spallogenic ^{3}He produced by the interaction of cosmic rays with rock exposed at the Earth's surface, and ^{3}He and ^{4}He produced after sediment deposition through radioactive decay.

Spallogenic helium produced during surface exposure

This thesis uses samples taken from exposed outcrops. Where sections have been exposed at the Earth's surface a component of ^{3}He produced by the interactions of cosmic ray particles with rock must be considered (Niedermann, 2002). Assuming no erosion, and that samples are collected from at or near the surface of the section, the concentration of cosmic ray-derived ^{3}He in a sample (C) depends on exposure time (T) and production rate (P_0) (Niedermann, 2002):

$$C(T) = TP_0 \qquad \text{Equation 3.3}$$

Samples used in this study were taken from quarries excavated in the last seventy years. Using a production rate of 115 atoms/g/yr, appropriate for mid-latitude locations (Licciardi et al., 1999), and an exposure time of 70 years, gives a concentration of around 8000 atoms/g in sampled sediments, or 3.3×10^{-20} ccSTP/g. The shielding effect of the near vertical dip of sampled sections, along with the surrounding hills, will further reduce this value (Niedermann, 2002), though in any case the predicted contribution to ^{3}He is so low comparative to the average ^{3}He measured in samples that it can be safely ignored.

Radiogenic ^{4}He and nucleogenic ^{3}He in black shales

This study expands the use of extraterrestrial ^{3}He timescales to lithologies including shales, which typically contain high concentrations of uranium and lithium compared to other sedimentary lithologies (Parker, 1967). Radiogenic ^{4}He is produced from the decay of U and Th through the following reactions: $^{238}U \rightarrow {}^{206}Pb + 8\ {}^{4}He$, $^{235}U \rightarrow {}^{207}Pb + 7\ {}^{4}He$, $^{232}Th \rightarrow {}^{208}Pb + 6\ {}^{4}He$ (Andrews, 1985). Nucleogenic ^{3}He is produced by the action of neutrons on Li: $^{6}Li(n,\alpha)^{3}H \rightarrow_{\beta\ decay} {}^{3}He$; these neutrons are typically produced as a consequence of (α,n) reactions on light nuclei with α particles from U and Th decay (Andrews, 1985). The high uranium and lithium content of shales mean that radiogenic ^{4}He and nucleogenic ^{3}He produced after deposition must be seriously considered as potential contributors to the helium content of this lithology.

Using Andrews' (1985) model of radiogenic helium production, and U and Li concentrations from the Bonarelli Level and Scaglia Bianca black shales measured by Turgeon and Brumsack (2006), a radiogenic $^{3}He/^{4}He$ production ratio of $\sim 1.5\times10^{-8}$, and a ^{4}He production rate of $\sim 2.5\times10^{7}$ atoms/g/yr were estimated for these shales. Using these values, over the ~90 Myr since the deposition of these sediments, $\sim 8\times10^{-5}$ ccSTP/g of ^{4}He and $\sim 1\times10^{-12}$ ccSTP/g of ^{3}He were produced.

The likelihood of radiogenic ^{4}He, produced as high energy alpha particles, escaping into pore spaces where it may be lost depends on the grain size of the uranium host phase, but it is likely in such fine-grained sediment that a large amount of the radiogenic ^{4}He is lost after production, because the grains are smaller than the ^{4}He recoil distance (Ballentine and Burnard, 2002). Uranium is often associated with organic matter; in sediments rich in organic carbon, organic matter is likely to be an important host phase for uranium. Though the exact nature of the uranium-organic matter interaction in organic-carbon rich sediments is still not entirely known, uranium in these contexts is often sorbed onto mineral surfaces (see review of Cumberland et al., 2016), a position facilitating the loss of radiogenic ^{4}He after production. Uranium may also be hosted in accessory minerals of terrigenous origin, such as apatite, zircon, rutile and sphene (e.g. Evans et al., 2005). Typical stopping

distances for alpha particles in these minerals are ~20 µm (Ballentine and Burnard, 2002), comparable to or rather larger than the grain size of the most significant fraction of the terrigenous component in pelagic sediments, 4–20 µm (see Torfstein, 2012). Nucleogeic ^{3}He has a similar recoil distance to radiogenic ^{4}He, ~30µm (Ballentine and Burnard, 2002; Farley et al., 2006b) so it might be expected to show a similar pattern of loss after production.

That almost none of the radiogenic ^{4}He is preserved in the rocks is evident by comparing the estimated concentration of ^{4}He produced *in situ* (8×10^{-5} ccSTP/g) with the average ^{4}He concentration of measured samples (almost 600× lower). If all nucleogenic ^{3}He concentration produced *in situ* remained in sediments, it would account for ~10% of the average ^{3}He concentration measured in shales. However, due to the similarity in stopping distances between radiogenic ^{4}He and nucleogenic ^{3}He, it is likely that almost all of the nucleogenic ^{3}He produced *in situ* is lost as well. For this reason, it is a justifiable decision to discard the contribution of radiogenic and nucleogenic He produced *in situ* and model the helium content of these rocks using a binary mixing model.

3.1.5 Sample reproducibility and sources of error

Sources of error on $^{3}He_{ET}$ concentration

Across every study of sedimentary helium, the observed sample reproducibility is much worse than the analytical precision of measurements, most likely due to the statistically small number of helium-bearing interplanetary dust particles hosted in the sediment (Patterson and Farley, 1998; Farley, 2001; further explored in 'Reproducibility', Section 2.1.3). Analytical precision is therefore often regarded as negligible as a source of error in estimates of overall $^{3}He_{ET}$ concentration (Patterson and Farley, 1998; Mukhopadhyay et al., 2001a).

Common practice is to replicate, or even triplicate measurements of all samples, in order to reduce the effect of inconsistent sampling of IDPs (Patterson and Farley, 1998; McGee et al., 2010; and

subsequent studies). The expected reproducibility of $^{3}He_{ET}$ measurements has been simulated by Farley et al. (1997), though recent work (e.g. by Torfstein, 2012) suggests that these simulations may, in fact, over-estimate the degree of this error which is instead better determined through practical study of the reproducibility of samples.

The observed reproducibility of samples in this study is presented in Figure 3.8. The observed spread of measured replicates can be approximated using a Gaussian distribution with 1σ ~20% (as in Farley, 2001). The majority of ^{3}He in these samples is of extraterrestrial origin; 20% errors may therefore be applied to measured concentrations of $^{3}He_{ET}$ in this study, reflecting the inconsistent capture of $^{3}He_{ET}$-bearing particles in sample aliquots as the dominant source of error. As can be seen in Figure 3.8, the Gaussian distribution roughly approximates the distribution of the observed data although, as observed by Farley (2001), discrepant values occur at the higher end of the distribution. Particularly poor reproducibility is thought to be due to the inclusion in some samples of rare 'helium-rich particles', which are discussed further below.

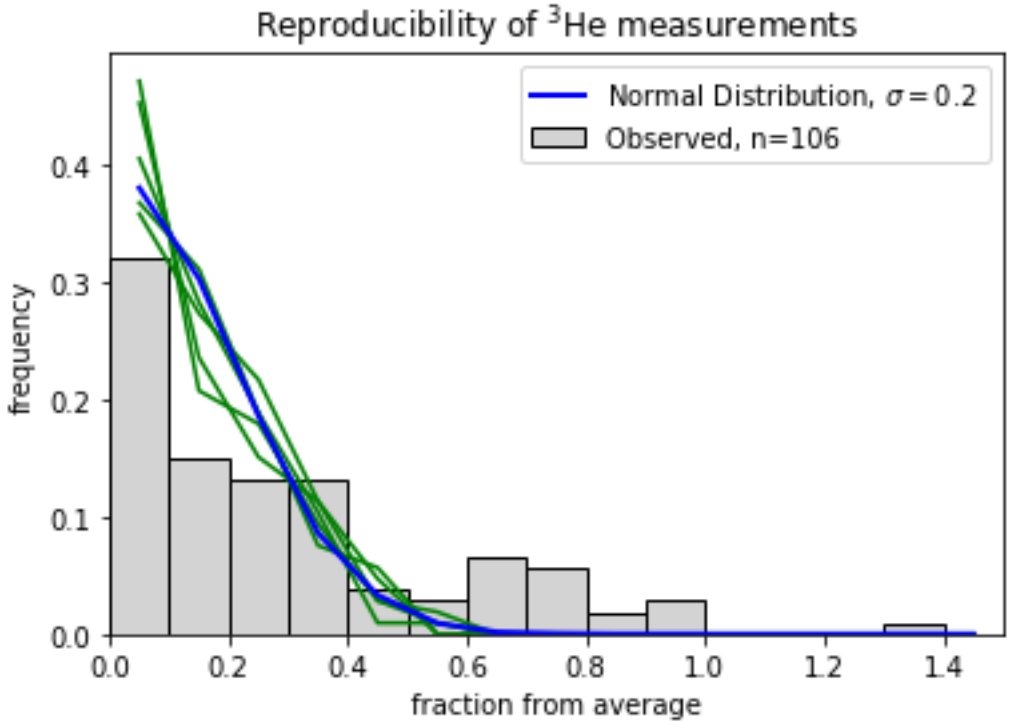

Figure 3.8: Observed reproducibility of ^{3}He concentration between all sample replicates measured in this study (from Furlo, Contessa, Bottaccione and Peacehaven), compared to that predicted using a Gaussian distribution, σ = 0.2, (blue curve). Thin green curves were plotted from limited sample sets (n = 106 to match observed data) taken randomly from a σ = 0.2 Gaussian distribution, and give a sense of the variation expected from this limited sample set.

Outliers

Some sample aliquots may contain rare 'helium-rich particles', and so display 'anomalously' high $^3He_{ET}$ concentrations and $^3He/^4He$ ratios; although not aberrant measurements, these 'outliers' are typically excluded in order to improve reproducibility of measurements (Patterson and Farley, 1998; Mukhopadhyay et al., 2001a; McGee et al., 2010; Murphy et al., 2010; Torfstein, 2012). Excluding these 'outliers' results in an underestimation of the overall $^3He_{ET}$ concentration for a given bed, as the contribution from helium-rich particles is discarded. However, the rarity of helium-rich particles means that they are already not present in most sample aliquots; as they are rarely captured, their contribution to overall $^3He_{ET}$ concentration in a given bed is effectively never included (Farley et al., 1997). Excluding sample aliquots containing helium-rich particles as 'outliers' is therefore consistent

with the sampling methodology which already effectively excludes helium-rich particles by choosing sample aliquots that are not inconveniently large (Farley et al., 1997). It is typically assumed that these systematic underestimates of $^3He_{ET}$ concentration in the section of interest and the $^3He_{ET}$ concentration used to calculate background flux cancel out in Equation 3.4. This assumption must, however, be kept in mind when drawing conclusions from results (Farley et al., 1997).

Although some studies have made use of five- or three-point running means to dampen the effect of outliers (e.g. Mukhopadhyay et al., 2001b; Murphy et al., 2010; Farley et al., 2012), this technique was not used in this study. Although running means have been used in studies that create age models (Mukhopadhyay et al., 2001b; Murphy et al., 2010), their use is perhaps most appropriate in studies interested in long term records of $^3He_{ET}$ background flux (e.g. Farley et al., 2012) and even in that context, using running means carries the risk of creating false 'trends' as large outliers skew the averages. Large outliers are, in fact, expected in studies of extraterrestrial helium in sediments as a result of 'helium-rich particles' (Patterson and Farley, 1998; Mukhopadhyay et al., 2001a; Torfstein, 2012), so in this study outliers were instead individually identified and discarded.

For the stratigraphic sections studied in this thesis that were relatively thin (<30 cm), such as those covering precession cycles, at least two measurements were made of every sample. Initially, each sample was measured twice; if ^3He concentrations measured in these duplicates were not within error of one another ($1\sigma = 20\%$ – see Section 3.1.5) a third measurement was made, and outliers identified using Chauvenet's criterion, where a replicate is discarded if the probability of obtaining the particular deviation from the mean is less than 1/(2n), 'n' being number of replicates (following Patterson and Farley, 1998; Mukhopadhyay et al., 2001a; McGee et al., 2010; Torfstein, 2012). It has been estimated that excluding 'outliers' in this way doubles reproducibility (Torfstein, 2012).

Through relatively thicker stratigraphic sections, such as the Bonarelli Level, outliers were identified following the method of Murphy et al. (2010); samples were considered 'anomalous' if their ^3He content (cc/g) differed by >2.4× from the two immediately adjacent samples. This choice of

rejection threshold was recognised as "somewhat arbitrary" by Murphy et al. (2010) and was accepted in their study as it flagged a number of outliers consistent the predictions of Farley et al. (1997)'s modelled 'helium-rich particle' distribution. A 2.4× rejection threshold was adopted as a starting point for outlier identification in this study based on Murphy et al.'s (modest) 'proof of concept'. After being identified in this way, 'anomalous' samples were investigated further before being either retained or discarded (as described below), with the final proportion of identified outliers consistent with both theoretical models and previous studies of $^{3}He_{ET}$.

That variation in measurements of over 2.4x could be a result of large and transient changes in $^{3}He_{ET}$ flux was considered unlikely by Murphy et al. (2010). In the setting of their study, these changes were also considered unlikely to have been influenced by rapid changes in sedimentation rate. However, in the context of the Bonarelli Level and its highly heterogeneous lithology, large changes in $^{3}He_{ET}$ concentration prompted by changes in sedimentation rate would not be unexpected. For this reason, once 'anomalous' samples had been identified as described above, replicates of the suspect sample were made; if the ^{3}He concentrations measured in these replicates were like those of the 'anomalous' samples they were not regarded as outliers. Using this two-stage process meant that 'anomalous' values confirmed by replicates were not discarded. (Around 33% of sample measurements initially flagged as 'anomalous' were subsequently identified as acceptable following the measurement of sample replicates, with the remaining 67% confirmed as outliers.)

Over the studied sections, both the Bonarelli Level and precession cycles, 6–13% of measurements were identified as 'outliers', consistent with both the average percentage of outliers identified in other studies (between 4–15%) and with the number of 'highfliers' expected as a result of helium-rich particles based on previous study of the size distributions of He-bearing interplanetary dust particles (Farley et al., 1997; Patterson and Farley, 1998; Mukhopadhyay et al., 2001a; Murphy et al., 2010; Torfstein, 2012).

Sources of error on $^3He_{ET}$ age-models

The choice of background flux is the largest contributor to uncertainty within $^3He_{ET}$ age-models. During the construction of an age-model, sedimentation rate is calculated from $^3He_{ET}$ concentration using the relationship of Takayanagi and Ozima (1987):

$$[^3He_{ET}] = F / \alpha \qquad \text{Equation 3.4}$$

(where $[^3He_{ET}]$ is the concentration of extraterrestrial ^3He, F is the background flux of extraterrestrial ^3He into sediments and α is the accumulation rate of sediment. One value of background flux is used in all calculations used in constructing the age-model, and is determined from a section with a known sedimentation rate that is close both spatially and temporally to the target for the age model (see Farley and Eltgroth (2003), and further discussion in Section 2.1.3). Uncertainty on this calculated background flux value is often large, in part because over timescales of ~10^5 years background flux may fluctuate essentially randomly by a factor of four or five (Farley and Patterson, 1995; Marcantonio et al., 1996; Farley et al., 2012). For this reason, uncertainty in sedimentation rates and age models is often propagated only from uncertainty in determination of background flux (Farley and Eltgroth, 2003; Murphy et al., 2010). A detailed exploration of appropriate methods for determining background flux in sections with heterogeneous lithology, along with associated errors, is presented in Chapter 4.

3.2 An exploration of Neon isotopes in Cretaceous pelagic sediments from the Scaglia Bianca

IDPs also deliver extraterrestrial neon to sediments, as thoroughly explored by Chavrit et al. (2016) in pelagic carbonates from IODP cores and the Paris Basin, ranging from 3–183 Myr in age. Though not the main focus of this study, the neon content of samples from the Scaglia Bianca and Bonarelli

Level were measured in order to investigate the contribution from different sources of neon to these sediments.

Extraterrestrial neon in sediments has been far less well-studied than extraterrestrial helium; prior to Chavrit et al. (2016) few studies had been carried out, mostly focussed on the magnetic fraction (Amari and Ozima, 1988; Nier et al., 1990; Darrah and Poreda, 2012). This dearth of study is partly because neon is difficult to measure; the typically low abundance of neon in samples can mean very high blank contributions. This issue of contribution from blanks, along with the difficulty of measuring the rare ^{21}Ne isotope, is summarised in the overview of Moreira (2013) in the context of measurements of neon in mantle samples; as the sedimentary samples analysed by Chavrit et al. (2016) contain comparably low abundances of certain neon isotopes, similar obstacles to determining isotopic ratios in sedimentary samples might be expected. Low sample/blank ratios were a major issue when measuring neon from samples in this study. ~18% of measurements in this study (34/187) were eliminated as unreliable given their high blank contributions. (Samples were eliminated if their sample/blank ratio <2.) The large errors on the isotopic ratios measured in this study mean that it is hard to draw reliable conclusions, nevertheless, the results of this study of neon are presented below for interest.

The three major components of the neon released from sedimentary samples are atmospheric, nucleogenic and extraterrestrial in origin (Chavrit et al., 2016). Each of these sources is characterised by a distinct position in ^{20}Ne/^{22}Ne and ^{21}Ne/^{22}Ne isotopic space.

The ^{20}Ne/^{22}Ne and ^{21}Ne/^{22}Ne ratios of Scaglia Bianca and Bonarelli Level samples from Furlo are plotted in Figure 3.9a (see Sections 2.2.1 and 2.2.3 for description of sampling locations and the Scaglia Bianca Formation). The isotopic ratios of all samples are similar to the characteristic value of air. A large atmospheric component of neon is present in all these samples; a similar observation has been made from other studied sediments (Chavrit et al., 2016), and a large proportion of other terrestrial samples such as basalts (see overview of Moreira, 2013). This atmospheric component has

been widely suggested to be contamination by modern air, introduced during sample handling and/or storage (Ballentine and Barfod, 2000; Moreira, 2013). In the extrusive igneous rocks in which atmospheric contamination has been best studied, the degree of contamination has been related to a sample's vesicularity; it has been suggested that air-contaminated vesicles linked to the surface by narrow channels are not fully emptied by the process of pre-measurement heating and pumping (described in Section 3.1.2) used to remove adsorbed gasses from sample surfaces (Ballentine and Barfod, 2000; Trieloff et al., 2003; Raquin et al., 2008; Moreira, 2013). Although the atmospheric contamination observed in the powdered sedimentary samples of this study, and that of Chavrit et al. (2016), cannot, of course, be explained by air held in vesicles, it may be the case that the standard heating and pumping regime is not sufficient to remove all gas adsorbed to the very large surface area provided by powdered samples – also of concern may be the sorption of air-saturated water vapour to hydrophilic clay minerals (e.g. Essington, 2015), or the diffusion of noble gases into microfractures. A correlation between high degrees of atmospheric contamination and high blank values was described by Moreira (2013), explained as atmospheric gas 'leaking' from the samples; congruous with this observation, Furlo samples both contain both a high contribution of atmospheric neon and display high neon blank values.

Despite this dominant contribution from an atmospheric component, other contributions to the neon measured in Furlo samples may be observed. Elevated $^{21}Ne/^{22}Ne$ ratios (above atmospheric values) are likely to demonstrate neon contribution from a nucleogenic source (Chavrit et al., 2016); the red arrow on Figure 3.9a indicates the trend towards nucleogenic values following the nucleogenic production calculations of Leya and Wieler (1999). In the context of the Furlo samples this nucleogenic component is likely to be delivered by 'continental' terrigenous material, perhaps dust: the same material which delivers 'terrestrial' radiogenic He as described in Section 3.1.4. The most 'nucleogenic' $^{21}Ne/^{22}Ne$ ratio measured in these samples was 0.0308±0.0019; this is rather less elevated than the most 'nucleogenic' $^{21}Ne/^{22}Ne$ ratio of Chavrit et al. (2016), 0.0344±0.0003,

measured in Toarcian-age carbonates from the Paris Basin, perhaps reflecting differences in input of terrigenous material between the source regions to these two sections.

Many samples measured in this study have higher $^{20}Ne/^{22}Ne$ ratios than the characteristic atmospheric ratio, indicating a significant contribution of an extraterrestrial component of neon, delivered to sediments, like extraterrestrial helium, via interplanetary dust particles (Chavrit et al., 2016). The highest $^{20}Ne/^{22}Ne$ ratio measured in these samples was 12.2±0.1. Samples containing more extraterrestrial neon would also be expected to contain a higher proportion of extraterrestrial helium; $^{20}Ne/^{22}Ne$ ratios are plotted against $^{3}He/^{4}He$ ratios in Figure 3.9b alongside a mixing line between a proposed extraterrestrial and terrigenous endmember, though the flat shape of the portion of the mixing curve the measured samples fall on makes this plot rather ambiguous. Chavrit et al. (2016) proposed that the extraterrestrial endmember has the composition of implanted solar wind (Eberhardt et al., 1970, 1972); this endmember composition reflects the fact that the IDPs which host extraterrestrial gases in sediments are thought to be small enough to not have been appreciably heated during atmospheric entry, and hence retain high $^{3}He/^{22}Ne$ ratios as helium has not been preferentially lost. $^{3}He/^{22}Ne$ ratios measured in the samples of this study are, however, very low (<0.0001), much lower than those measured in other studies of extraterrestrial helium and neon in sediments (~0.03–0.2, Darrah and Poreda, 2012; ~0.003–0.5, Chavrit et al., 2016); this difference arises from significantly higher neon concentrations measured in this study, perhaps due to a greater degree of atmospheric contamination.

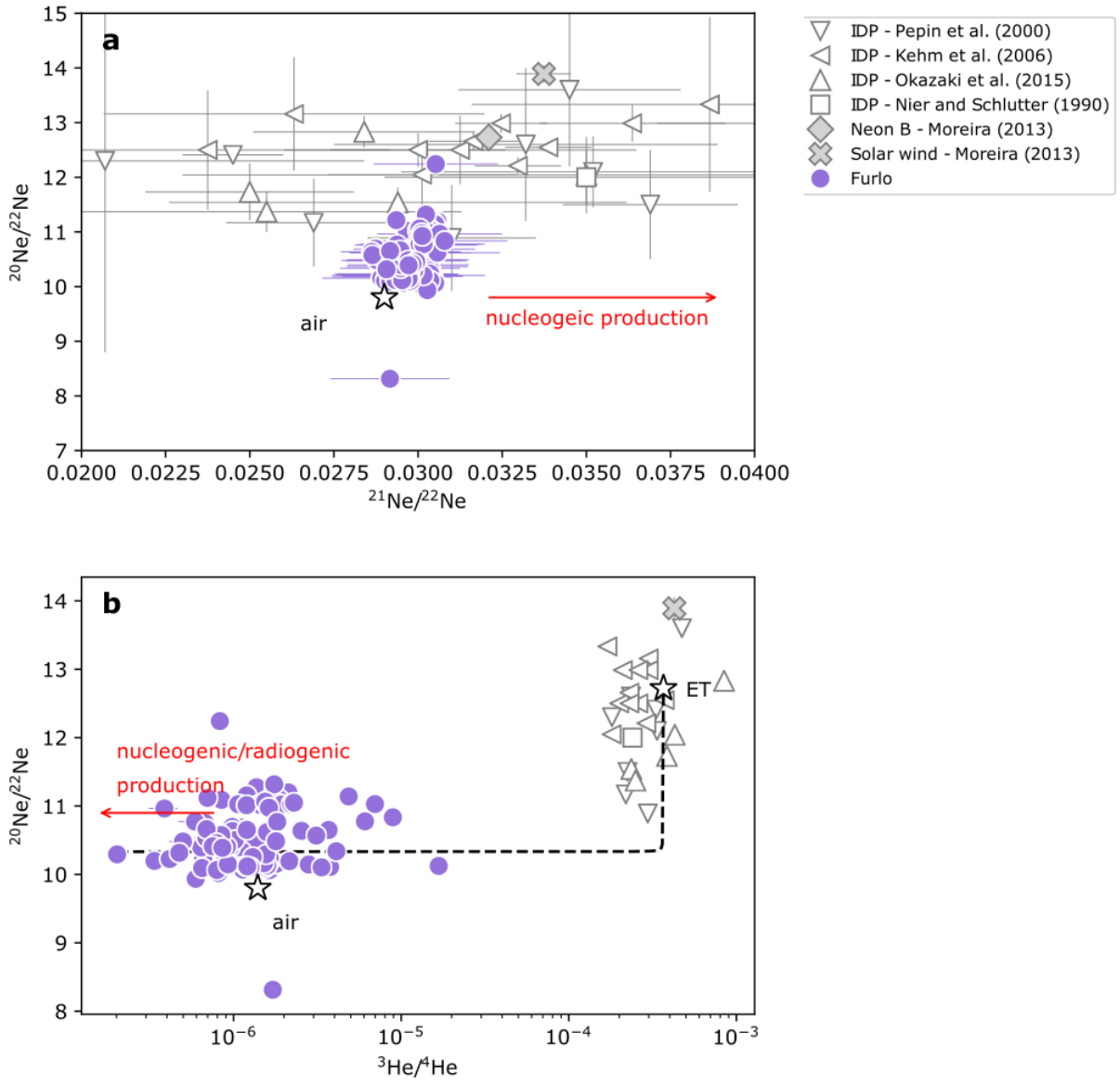

Figure 3.9: $^{20}Ne/^{22}Ne$ ratios versus $^{21}Ne/^{22}Ne$ ratios, and $^{20}Ne/^{22}Ne$ ratios versus $^{3}He/^{4}He$ ratios of Furlo samples. ***(a)*** *$^{20}Ne/^{22}Ne$ ratios versus $^{21}Ne/^{22}Ne$ ratios of Furlo samples. Atmospheric neon ratios ($^{20}Ne/^{22}Ne$ = 9.80, $^{21}Ne/^{22}Ne$ = 0.029) are from Porcelli et al. (2002). The slope of the nucleogenic production line (red arrow) is derived from the nucleogenic production calculations of Leya and Wieler (1999). The wide range of neon ratios measured in IDPs by Nier and Schlutter (1990), Pepin et al. (2000), Kehm et al. (2006) and Okazaki et al. (2015), particularly $^{21}Ne/^{22}Ne$, demonstrates the potential variation in the isotopic composition of the extraterrestrial component of these samples. Chavrit et al. (2016) suggest that the extraterrestrial component of sedimentary samples has an isotopic composition similar to solar wind, or to the Neon B component, plotted as filled grey symbols. One sample with an unexplainably low $^{20}Ne/^{22}Ne$ ratio (8.31±0.07, lower than air) may be an aberrant measurement.*

(b) *$^{20}Ne/^{22}Ne$ ratios versus $^{3}He/^{4}He$ ratios. Samples are expected to fall on a binary mixing line between extraterrestrial and terrestrial (radiogenic/nucleogenic) endmembers in this isotopic space, as the $^{20}Ne/^{22}Ne$ ratio of air is very similar to that of the terrestrial component (Chavrit et al., 2016). The mixing line was plotted using the binary mixing equation (Vollmer, 1976; Langmuir et al., 1978)*

between the most radiogenic sample of this study ($^{3}He/^{4}He = 2.02\times10^{-7}$, $[^{4}He] = 6.50\times10^{-8}$ cc/g, $^{20}Ne/^{22}Ne = 10.29$, $[^{22}Ne] = 2.94\times10^{-8}$ cc/g) and a predicted extraterrestrial endmember with an implanted solar wind composition, $^{3}He/^{4}He = 3.67\times10^{-4}$, $[^{4}He] = 2.43\times10^{-1}$ cc/g, $^{20}Ne/^{22}Ne = 12.72$, $[^{22}Ne] = 7.85\times10^{-5}$ cc/g (Eberhardt et al., 1970, 1972). The steepness of the hyperbolic curve is governed by the concentrations of ^{4}He and ^{22}Ne in the chosen endmembers; the steepness of the curve in this study (compared to that of Chavrit et al., 2016) is likely due to the relatively high concentration of ^{22}Ne in the radiogenic endmember (the most radiogenic sample in this study).

If the isotopic composition of the three proposed endmembers is known, the proportion of each isotope of neon can be estimated using a ternary mixing model (following Chavrit et al., 2016). A potential mixing triangle is presented in Figure 3.10. The isotopic composition of air is well established ($^{20}Ne/^{22}Ne$ = 9.80, $^{21}Ne/^{22}Ne$ = 0.029; Porcelli et al., 2002), and these ratios are used to describe the atmospheric component. The nucleogenic Ne production ratios of Leya and Wieler (1999), $^{20}Ne/^{22}Ne$ = 0.285, $^{21}Ne/^{22}Ne$ = 2.98, are used to describe the nucleogenic endmember. Selecting an extraterrestrial endmember is more difficult. Chavrit et al. (2016) used the Neon-B component (represented as a grey diamond on Figure 3.10) as their extraterrestrial endmember. However, many samples in this study with elevated $^{20}Ne/^{22}Ne$ ratios have $^{21}Ne/^{22}Ne$ ratios similar to or even lower than air, suggesting that an extraterrestrial endmember with a lower $^{21}Ne/^{22}Ne$ ratio than the Neon-B component may be more appropriate. With that in mind, an extraterrestrial endmember was chosen with the same $^{20}Ne/^{22}Ne$ ratio as Neon-B, $^{20}Ne/^{22}Ne$ = 12.7, (Moreira, 2013; Chavrit et al., 2016) and the highest possible $^{21}Ne/^{22}Ne$ ratio that included all samples within the mixing space, $^{21}Ne/^{22}Ne$ = 0.0275. The composition of this extraterrestrial endmember was, therefore, arbitrarily selected, though these isotopic ratios fall within the range of measured IDPs (see Figure 3.10). From this mixing model the relative contribution of different sources of neon to the sediments can be estimated. In the majority of samples most ^{22}Ne is of atmospheric origin, with the remaining ^{22}Ne derived from an extraterrestrial source; in all samples nucleogenic neon accounted for <1% of ^{22}Ne (see bar charts of Figure 3.10). One sample (a black shale, $^{20}Ne/^{22}Ne$ = 12.2, $^{21}Ne/^{22}Ne$ = 0.0305) contains a very high fraction of extraterrestrial neon, with ~85% of ^{22}Ne of extraterrestrial origin; with the exception of this sample, extraterrestrial neon accounts for 5–55% of ^{22}Ne in samples, with atmospheric ^{22}Ne accounting for 45–95% (Figure 3.10).

Atmospheric contamination appears to have had a strong influence on the neon content of these samples, but the contribution this process makes to measured helium is less clear. Using an atmospheric $^{4}He/^{20}Ne$ ratio of 0.318 (Porcelli et al., 2002) it is possible to calculate how much atmospheric ^{4}He would be expected in these samples if the degree of atmospheric contamination

were the same for both elements. However, the predicted atmospheric ^{4}He concentration is in most cases greater than the measured ^{4}He, for some samples over 10× greater, indicating that the processes involved in the atmospheric contamination of samples must affect the two elements differently. It seems likely that, if atmospheric contamination occurs by adsorption of air-saturated water vapour onto the large surface area of powdered samples during preparation in the lab, the overnight heating and pumping protocol may be able to effectively liberate atmospheric helium without being able to totally purge the heavier neon, which is more soluble in water (Ballentine et al., 2002). Although an evacuation time of ~12/24 hours, as used in this study, is commonly used when measuring extraterrestrial helium in sediments (e.g. Patterson and Farley, 1998), a longer duration may be necessary when measuring neon isotopes to prevent the domination of the atmospheric component of neon.

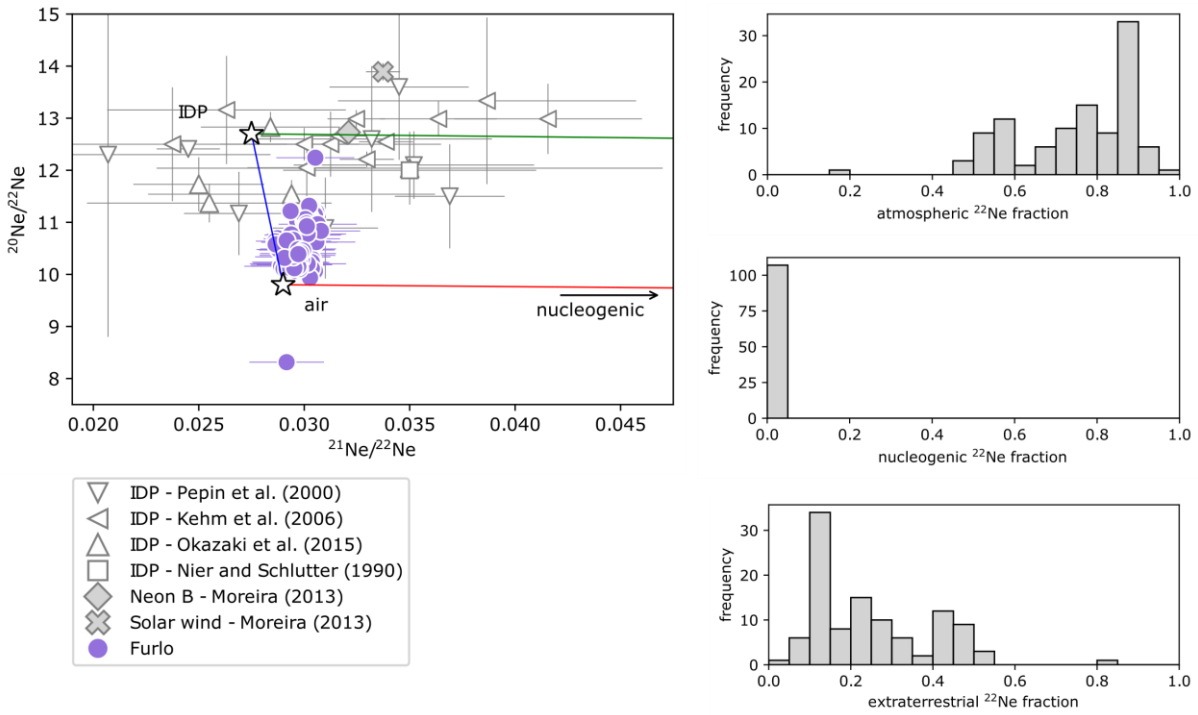

Figure 3.10: Estimated proportions of ^{22}Ne from atmospheric, extraterrestrial and nucleogenic endmembers. The choice of these endmembers is expanded on in the text. Proportions were calculated using a ternary mixing model (following Chavrit et al., 2016); the sample with ^{20}Ne/^{22}Ne lower than air was excluded from this analysis.

3.3 Application of the analytical approach to diverse pelagic lithologies

3.3.1 He-isotopes in pelagic carbonates and black shales

In order to compare measurements of extraterrestrial ^{3}He and terrestrial ^{4}He made on the Oxford system with those of other established labs, a comparison was made between helium concentrations of Bottaccione Gorge samples used in method development measured on the Oxford system, and concentrations measured in samples from the same stratigraphic section by Farley et al. (2012). This comparison is presented in Figure 3.11. Results from the Oxford set-up closely overlap those of Farley et al.; it was judged that that the Oxford system was successfully able to replicate their results, and that liberating helium from samples using laser heating is a valid alternative to heating in a vacuum furnace.

The apparent skew visible in Figure 3.11b towards comparatively low $^{3}He/^{4}He$ ratios in the Oxford dataset arises from the inclusion of multiple replicate measurements of a single horizon containing a high concentration of terrigenous ^{4}He (just below the Bonarelli Level in Figures 3.11c, d). This much-replicated sample was used in trials of sample packing techniques so is over-represented in the Oxford dataset.

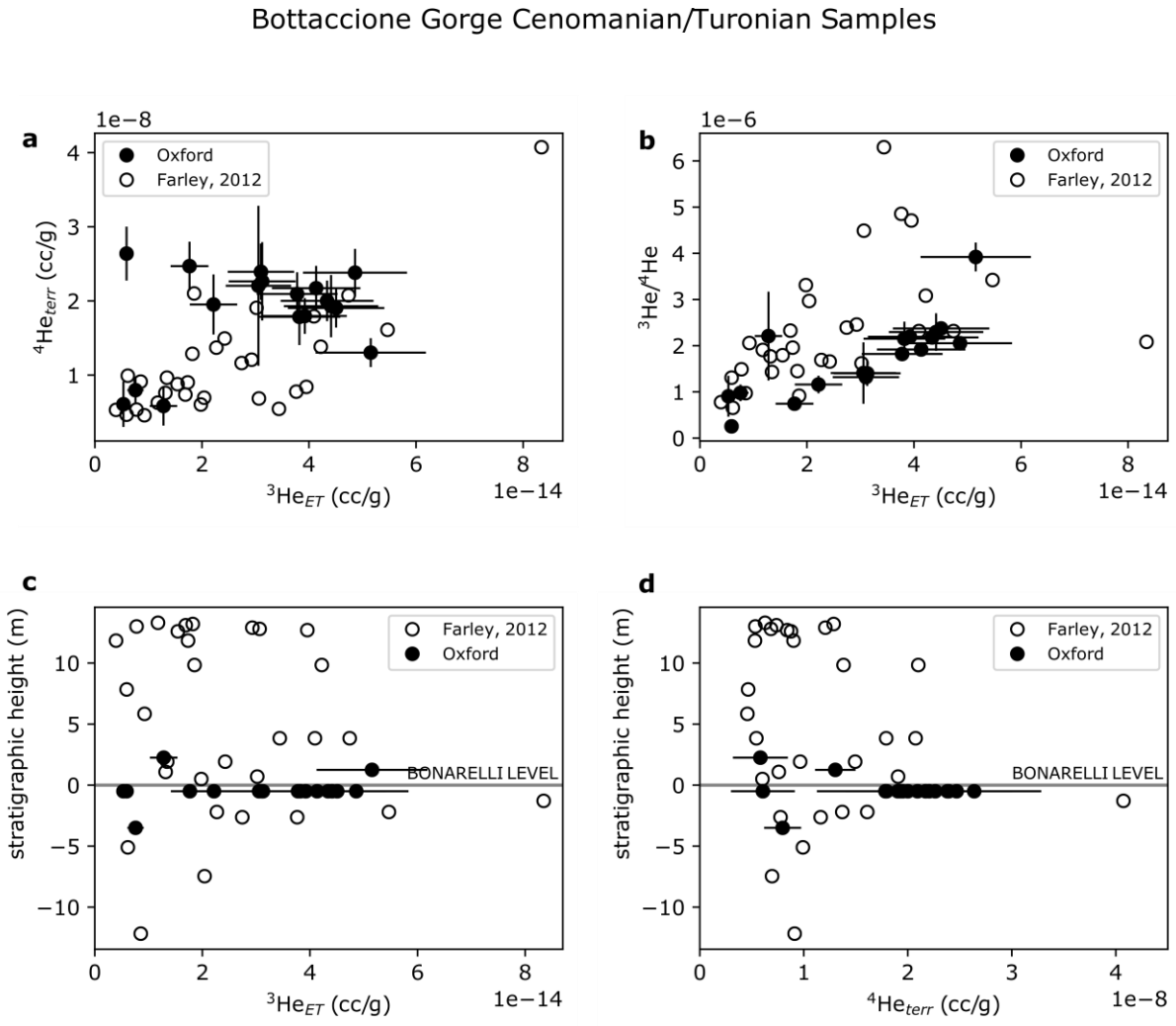

Figure 3.11: Comparison of helium measurements made on the Oxford system, and by Farley et al. (2012), on samples from the Cenomanian Scaglia Bianca Formation in the Bottaccione Gorge, Italy. Samples are taken from the same section, though remeasurement of the exact samples used by Farley et al. was not possible. In all plots, error bars on $^3He_{ET}$ (cc/g) measurements made in this study represent the expected 20% reproducibility error, whilst analytical errors are presented for $^4He_{terr}$ (cc/g) measurements. ***(a)*** *extraterrestrial ^{3}He and terrestrial ^{4}He measured in this study and in Farley et al. (2012) are presented as overlapping clouds;* ***(b)*** *comparison of $^3He_{ET}$ (cc/g) and $^3He/^4He$ measurements from this study and from Farley et al. (2012);* ***(c)*** *$^3He_{ET}$ (cc/g) from the two studies plotted against stratigraphic height (relative to the Bonarelli Level);* ***(d)*** *$^4He_{terr}$ (cc/g) from the two studies plotted against stratigraphic height.*

3.3.2 He-isotopes in pelagic cherts within pelagic carbonate sequences

It has been well documented that the process of heating and burial associated with diagenesis can lead to the diffusive loss of helium from IDPs (Mukhopadhyay et al., 2001a; Mukhopadhyay and Farley, 2006). In the burial diagenesis of carbonates or shales this should not, however, lead to differences in the relative abundance of preserved IDPs. By contrast, chert formation involves the secondary precipitation of a new mineral phase that may be hypothesised to alter the relative distribution of IDPs within adjacent beds. Though prior to this study the effect of the formation of chert from biogenic opal on extraterrestrial helium preservation was unknown, informally it was anticipated that this process might lead to helium loss. Chert is a prominent lithology in the Scaglia Bianca Formation (the subject of this thesis); more generally, pelagic records (which are generally well-suited for the construction of $^{3}He_{ET}$ timescales, see Section 2.1.2) often contain bedded or nodular cherts (see, for example, Deep Sea Drilling Project records of Calvert (1971) and subsequent work). Therefore, in order to expand the use of extraterrestrial ^{3}He timescales into the large number of sections where chert is a significant lithology, it is important to address whether the diagenetic processes involved in the formation of chert beds could promote the loss of extraterrestrial helium lodged in IDPs and artificially lower the $^{3}He_{ET}$ concentration measured in cherts compared to other lithologies.

Theories of chert formation

The dominantly accepted theory of chert formation in deep-sea settings is that biogenic silica (opal-a, likely sourced in the Late Cretaceous from radiolaria, sponge spicules or perhaps diatoms) is dissolved and recrystalised as opal-CT (in the form of micrometre-scale bladed spherulites known as lepispheres), which, as the sediment is buried and the temperature increases, is converted to microcrystalline quartz primarily through solid-state inversion (Heath and Moberly, 1971; Wise and Weaver, 1974; Knauth, 1994). Bedded cherts are thought to form following the deposition of siliceous oozes (Knauth, 1994); in some instances (particularly those in which the primary lithology has a relatively high clay:silica ratio), migration of dissolved silica to particular horizons may result in

a rock record of chert-shale couplets formed from what was once a single original lithology (Murray et al., 1992; Abrajevitch, 2020).

Where chert is found as beds and nodules within pelagic carbonate deposits, silica is thought to directly replace carbonate during the reprecipitation of opal C-T, either through 'force of crystallisation' as carbonate solubility is enhanced due to the pressure exerted by growing quartz crystals, or as a result of changing pore water chemistry: a drop in the pH of pore waters promotes carbonate dissolution, which may be replaced by silica if the pore fluids are also rich in dissolved biogenic opal-A (Knauth, 1994). The process of chert formation may, in fact, itself promote a drop in pH: it has been suggested that chert formation in carbonate sediments involves the formation of nuclei containing $Mg(OH)_2$ and subsequently opal-CT lepispheres (Kastner et al., 1977). This process would decrease local alkalinity and perhaps decrease pH during chert formation by effectively adding hydrogen ions to interstitial waters.

If chert formation proceeds in this manner, the main concern for measured $^3He_{ET}$ concentrations is whether extraterrestrial helium is housed in phases that would be dissolved and recrystallised during this process. There are several candidates for the host phase (or phases) of helium in IDPs, including magnetite and Fe-Ni sulphides (Mukhopadhyay and Farley, 2006). If extraterrestrial helium is housed in Fe-Ni sulphides its retention would likely be sensitive to the pH changes during chert diagenesis described above. However, the strongest candidate for the host phase of extraterrestrial helium is extraterrestrial silicates (Mukhopadhyay and Farley, 2006). The hypothesis explored here is that extraterrestrial silicates will not habitually be recrystalised, being fundamentally different in structure and less easily dissolvable than biogenic opal. Dissolution experiments have demonstrated that amorphous biotic silica is much more readily dissolved than silica in clays (Eggimann et al., 1980), and lithogenic silica of terrestrial origin has been long established as less soluble than biogenic silica when considering sources of dissolved silica to the oceans (Tréguer and De La Rocha,

2013). The stability of aluminosilicates during chert formation is already an assumption made when considering chemical fractionation in chert formation (e.g. Murray et al., 1992).

An alternate model of chert formation was proposed by Lancelot (1974), in which chert nodules develop outwards by accretion, excluding clay minerals and dissolved cations that cannot be accommodated along a "quartzification front". If chert develops by this model, we might expect extraterrestrial helium bearing IDPs to be excluded also. (It is also worth noting that when proposing this model, Lancelot (1974) specifically notes that amorphous silica is selectively dissolved over silica in its crystalline forms, as interstitial waters are typically undersaturated with respect to amorphous silica and supersaturated with respect to its crystalline forms.)

Experimental results

In order to test whether there is $^{3}He_{ET}$ loss between chert nodules and the surrounding sediment, two bedding-parallel transects were collected through chert nodules into laterally-equivalent, but non-chert-bearing, carbonates. The first transect is from the Cenomanian Scaglia Bianca Formation (collected from Furlo, Central Italy), the second from the Lower Campanian Newhaven Chalk (collected from Peacehaven, Sussex, UK). These transects allowed investigation of the change in concentration of helium over both a gradual carbonate content change (from 50–70% over 4 cm) in the Scaglia Bianca sample and a sharper, more dramatic carbonate content change (from 1–100% across a nodule boundary) in the Newhaven Chalk. Chert nodules of contrasting nature (with respect to the sharpness of silicification front) and from different stratigraphic stages were chosen in order to broaden the scope of this preliminary investigation: this sample selection allowed conclusions to be drawn about the behaviour of extraterrestrial helium during diagenesis of at least two differing 'styles' of chert and therefore, tentatively, about behaviour during chert diagenesis more generally.

Figure 3.12 presents ^{3}He and ^{4}He concentration across these bedding-parallel transects. If diagenesis of chert liberates extraterrestrial helium, an inverse relationship between measured helium concentration and 'degree of chertification' would be expected (in carbonate-hosted cherts, 'degree

of chertification' is likely best represented by decrease in carbonate content, though measured helium concentration is also plotted against distance from the centre of the chert nodule for interest).

For each isotope in each transect, the sample Pearson correlation coefficient (r_s) was calculated. The probability (p) that the degree of observed correlation might occur by chance in a population with no systematic relationship between helium concentration and carbonate content/distance from the centre of the chert nodule was calculated using a two-tailed Student's t-test (Figure 3.12). The two-tailed Student's t-test was used in order to allow investigation of both the hypothesised inverse relationship between helium concentration and 'degree of chertification' and the potential opposite scenario, in which helium concentrations might be higher in chert samples.

In fact, the most significant correlation observed is an apparent positive correlation between ^{3}He concentration and 'degree of chertification' across the Furlo transect (Figure 3.12). This positive correlation is counter to previous expectations of the effects of chert diagenesis on $^3He_{ET}$ concentrations (see above), but, if a consistent observation, might still hamper the use of $^3He_{ET}$ timescales through sections containing chert. However, though the observed correlation between ^{3}He concentration and carbonate content/distance from the centre of the chert nodule across the Furlo transect is judged significant when a 5% threshold value of p is adopted, it would be rejected under a more stringent 1% threshold value. It is therefore worth comparing the ^{3}He concentration pattern across the Furlo transect with that across the second transect from Peacehaven.

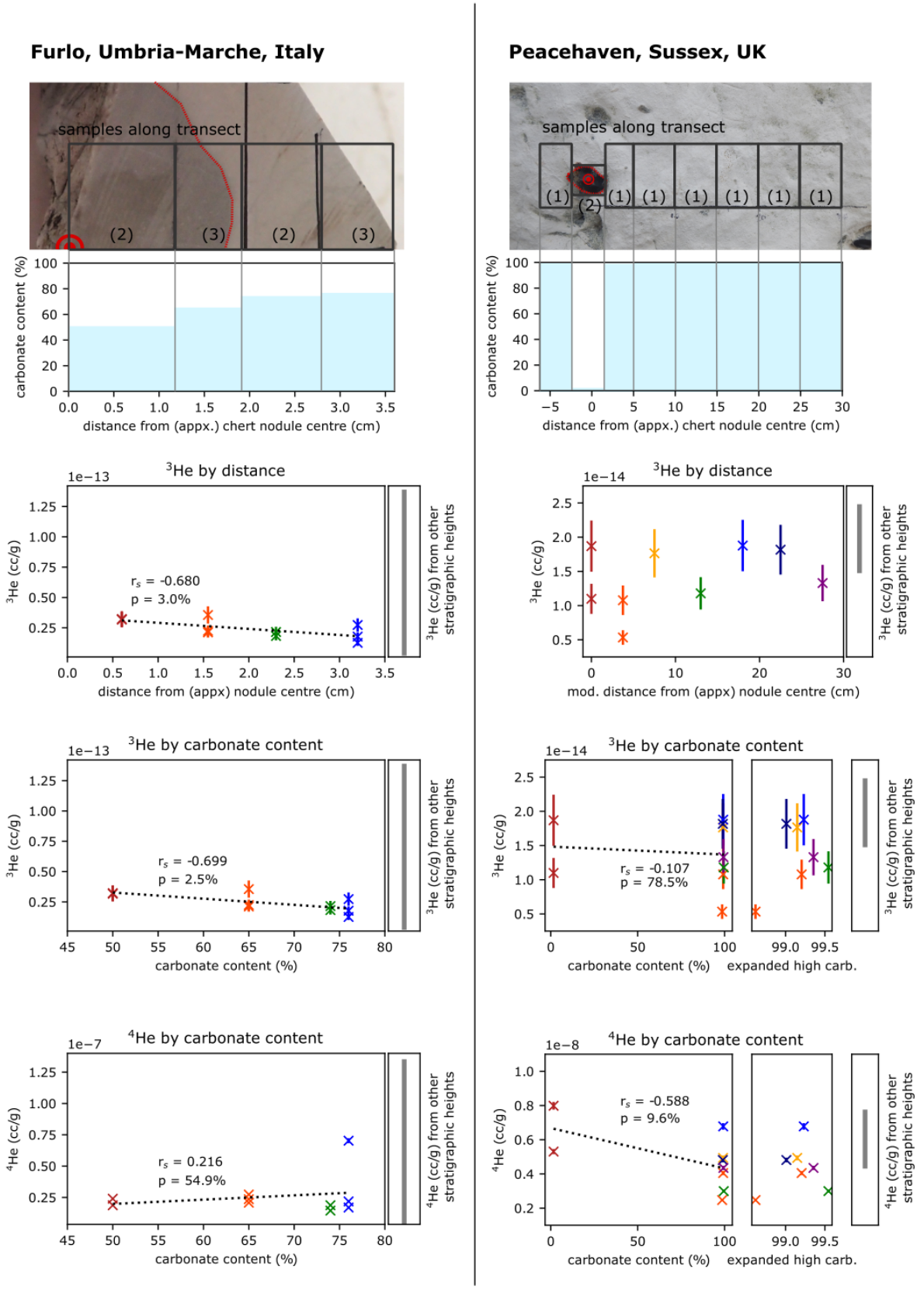

Figure 3.12: Helium content across two chert nodules (outlined in red) from the Cenomanian Scaglia Bianca, Furlo, and Campanian Newhaven Chalk Formation, Peacehaven. The number of replicates of each sample are given in brackets on the photographs of each transect. ^{3}He concentration is plotted

against distance from the centre of the chert nodule (red bullseye). ^{4}He (the most abundant isotope) and ^{3}He (the isotope most useful in calculating sedimentation rate) are plotted against carbonate content, a proxy for degree of chertification. As the overwhelming majority of ^{3}He is of extraterrestrial origin in these settings (~97% at Furlo, ~99% at Peacehaven), plots for ^{3}He and $^{3}He_{ET}$ are virtually identical. ^{3}He (cc/g) error bars represent the expected 20% variation between replicates, whilst error bars on ^{4}He (cc/g) represent analytical error.

An indication of the degree and nature of the correlation between the concentration of helium isotopes and distance/carbonate content is given by the sample Pearson correlation coefficient (r_s). Also presented is the probability (p) that the degree of observed correlation might occur by chance in a sample taken from a population in which there is no systematic relationship between variables, as calculated using a two-tailed Student's t-test.

The grey bar on the right-hand side of plots displays the range of helium concentrations measured at other stratigraphic heights (within ~2 m of the transect measured), to give context to the scale of variability across the transects.

The lower ^{3}He (and, by extension $^{3}He_{ET}$) concentrations measured at Peacehaven relative to Furlo may indicate slower sedimentation rates at this latter locality. A lower background flux of $^{3}He_{ET}$ at Peacehaven would also result in lower measured [^{3}He]; though the information collected for this chert transect is not sufficient to determine the background flux at Peacehaven, a long-term study of Late Cretaceous background flux through Tethyan sediments in Italy suggests that the average background flux of $^{3}He_{ET}$ did not appreciably change between the Cenomanian and Campanian (Farley et al., 2012).

Across the Peacehaven transect no significant correlation between ^{3}He and carbonate content is observed: the probability of obtaining the degree of correlation observed in the measured samples by chance is very high. (Calculation of correlation between ^{3}He and distance from the centre of the chert nodule is not meaningful across the Peacehaven transect due to the sharp silicification front, though a plot of ^{3}He against distance is presented in Figure 3.12 for the sake of comparison.) The lack of any replication of the ^{3}He concentration patten observed at Furlo across this second transect suggests that the observed correlation is not, in fact, significant. Across both transects concentration of ^{4}He displays no significant correlation with 'degree of chertification'.

In order to contextualise the scale of variation observed along a transect, samples of the carbonate lithology were collected from a few metres under- and overlying the beds in which the transects were carried out. Variation in ^{3}He concentration (which is dominated by the extraterrestrial ^{3}He component) measured in these samples from different stratigraphic heights may arise partially from differing accumulation rates between beds, or differences in the background flux of $^{3}He_{ET}$ during the beds' deposition, but within a single lithology and over a metre scale stratigraphic interval these effects are expected to be minimal. Instead, variation in ^{3}He concentration is likely due to the effect of the small number of He-bearing IDPs in each sample aliquot (see Sections 2.1.3 and 3.1.5 for previous discussion of this effect). Variation in helium concentrations across the bedding-parallel transects is generally at or below the scale of variation between samples taken at different stratigraphic heights, as would be expected if chert formation had no effect on the concentration of helium within samples.

Based on these results, it appears that chertification does not lead to the loss of extraterrestrial helium, meaning that measured helium concentrations from cherts can be used to determine sedimentation rates and build age models, alongside limestones, marls and black shales.

3.4 Conclusion

The key innovation in the methodology of this study is the use of a laser heating system to liberate helium from powdered sedimentary samples and a gas clean-up protocol prior to mass spectrometry. Analysis of the reproducibility of ^{3}He measurements made on this system reveal that the observed spread of measured replicates can be approximated using a Gaussian distribution with 1σ ~20%. This reflects the predicted degree of variability in ^{3}He concentration due to the 'nugget effect'; by far the largest contributor to ^{3}He in sediments is extraterrestrial ^{3}He hosted in discrete and relatively rare interplanetary dust particles (see Farley, 2001). Methods for identifying outliers flagged 6–13% of measurements across the different sections studied, consistent with both the theoretical number of 'highfliers' expected as a result of helium-rich particles and with the average percentage of outliers identified in comparable studies (Farley et al., 1997; Patterson and Farley, 1998; Mukhopadhyay et al., 2001a; Murphy et al., 2010; Torfstein, 2012).

Neon measurements made on this system, though demonstrating the expected three-component mixing between an atmospheric component, a radiogenic component and an extraterrestrial component in samples (see Chavrit et al., 2016), were judged too overwhelmingly dominated by an atmospheric signal to be useful in this study. This atmospheric signal appears to be present only in neon and not helium, perhaps because the ~24 hour heating/evacuation of the powdered samples prior to measurement was insufficient to liberate atmospheric neon hosted in air-saturated water vapour sorbed to the surfaces of clay minerals, whilst any (less soluble) helium of atmospheric origin was removed. For effective future study of sediment-hosted neon, longer heating/evacuation times are likely to be necessary; in addition, much larger samples sizes would be required to overcome the issue of low sample/blank ratios. However, issues with both sample throughput and complete gas release are likely to arise when heating samples of a significantly larger size than those used in this

study: the laser heating system is not, therefore, thought to be a particularly well-suited heating method for use in studies of sediment-hosted neon.

Following the development of a successful protocol to measure helium isotopes, comparison of $^{3}He_{ET}$ and $^{4}He_{terr}$ measurements on a suite of pelagic carbonates made in Oxford with those made by another lab (Farley et al., 2012) were used to confirm that the Oxford system could be used to successfully replicate such measurements made in other places.

A key goal of this thesis was, however, to expand the use of extraterrestrial helium timescales beyond pelagic carbonates and into sections with highly heterogeneous lithologies, necessitating an investigation into the possible effects of chert diagenesis on helium preservation. Examination of measured helium concentrations across two bedding-parallel 'chert nodule to host carbonate' transects did not indicate significant correlation between the concentration of helium and the 'degree of chertification'; chert diagenesis is therefore concluded to not have an effect on the concentration of helium hosted in sediments, allowing extraterrestrial helium timescales to be calculated through sections containing this lithology.

4. High-resolution timescales through precession cycles

Abstract

High-resolution $^{3}He_{ET}$ timescales were produced for four precession cycles from the rhythmically bedded Scaglia Bianca Formation, a sequence of Upper Cretaceous (Cenomanian) deep-marine pelagic limestones from central Italy that are well characterised by cyclostratigraphy. Using $^{3}He_{ET}$ concentrations as a proxy for sedimentation rate allows instantaneous sedimentation rates and organic-carbon mass accumulation rates to be calculated for each bed within a precession cycle. Eccentricity is known to modulate the amplitude of precession forcing, and precession cycles deposited under eccentricity maxima and minima were selected for comparison. Lithological changes through these chert-limestone cycles are explained using the concept of 'palaeoenvironmental thresholds'; calculation of the proportion of time per cycle represented by siliceous- and organic-rich facies indicates that when the amplitude of precessional insolation forcing was greatest (at eccentricity maxima) the palaeoenvironmental system spent longer in the more nutrient-rich environment under which these types of sediment were deposited, reflecting increased time spent above a 'threshold' insolation level. An increase in the flux of terrestrial helium during the deposition of cherts may be coincident with an increase in terrestrially derived nutrients. Estimates of primary productivity are relatively elevated for organic-rich beds. Various methods of calculating $^{3}He_{ET}$ background flux in sections with heterogeneous lithology are evaluated, and a best-practice method proposed.

4.1 Introduction

Orbitally forced, cyclic changes in lithology and geochemistry have been identified in sediments from the Palaeozoic to the Quaternary (e.g. Hinnov, 2013). Although cyclostratigraphy offers considerable insight into the overall duration and bundling of these cycles, the smallest 'increment' of time that can be explored using cyclostratigraphy is the period of the shortest cycle: the short precession cycle, ~19 kyr in modern sediments (Hinnov, 2013). For precession cycles themselves to be identifiable some distinct change in either lithology or geochemistry must occur within them, but so far the tools to quantify in geologically old sediments how fast these changes occur, or how long they last, have been lacking.

Of particular interest to this study is how forcing functions of different amplitudes (i.e. precession cycles at different points within a modulating short eccentricity cycle) affect how "strongly" the environment responds: does the lithology change more dramatically, and does the division of time represented by different lithologies change? To address these questions, records of the same cycle in different parts of a basin are examined to investigate how the same forcing mechanisms affect sections deposited under slightly different environmental regimes. Deciphering the division of time within a precession cycle will also help understand how the, essentially, sinusoidal-shaped insolation curve may be represented in the sedimentary record.

Using extraterrestrial ^{3}He ($^{3}He_{ET}$) concentrations allows the calculation of an instantaneous sedimentation rate on a bed-by-bed basis (see Section 2.1.3) and, consequently, the production of high-resolution timescales within precession cycles. Four precession cycles are examined within the Cenomanian (Upper Cretaceous) deep-marine pelagic Scaglia Bianca Formation of Marche-Umbria, Italy, identified using the cyclostratigraphic analysis of Batenburg et al. (2016). The light-coloured Scaglia Bianca sediments primarily comprise planktonic foraminifera set in a matrix of solution-welded nannofossils and carbonate-replaced radiolaria, interbedded with darker cherts in which

siliceous microfossils are better preserved (Cresta et al., 1989). Dramatic lithological shifts from limestone to chert to (in some cycles) black shale are seen within each precession cycle, and the modulating effect of short eccentricity on precession is clearly visible in the patterns of lithological change (Batenburg et al., 2016).

The concentrations of $^{3}He_{ET}$ from measured precession cycles (chosen over a span of a few hundred kyr) are also used to investigate changes in the background flux of extraterrestrial ^{3}He over time. The largest source of error when calculating absolute durations on a $^{3}He_{ET}$ timescale arises in the determination of the $^{3}He_{ET}$ background flux (Farley and Eltgroth, 2003, further discussed in Section 2.1.3). For the use of $^{3}He_{ET}$ timescales to be expanded into a wider range of depositional settings and lithologies, it is important to refine how the $^{3}He_{ET}$ background flux is calculated in sections with varying lithology.

4.2 Geological Setting

Two locations from the Umbria-Marche region of central Italy are used in this study (Figure 2.2). Both Furlo (GPS co-ordinates: 43°38'42"N; 12°42'40"E) and Contessa (GPS co-ordinates: 43°22'32"N; 12°33'389"E) are quarried sections that have been extensively studied both lithologically and geochemically (eg. Cresta et al., 1989; Coccioni and Galeotti, 2003; Tsikos et al., 2004; Turgeon and Brumsack, 2006; Mort et al., 2007; Turgeon and Creaser, 2008; Gambacorta et al., 2014, 2015, 2016; Batenburg et al., 2016).

Precession cycles discussed in Sections 4.4, 4.5.2 and 4.5.3 of this chapter were sampled from the upper part of the Upper Cretaceous Scaglia Bianca Formation. The Scaglia Bianca has been subdivided by some workers into four members (Coccioni and Galeotti, 2003), of which the topmost unit, the 'Greyish Member', is the prime focus in this chapter. The Greyish Member begins after the

mid-Cenomanian positive $\delta^{13}C$ excursion (MCE = mid-Cenomanian Event) and, in Furlo, contains black shale layers interpreted as reflecting the enhanced sensitivity of the sedimentary regime at this time to changes in the hydrological cycle under warmer conditions (Coccioni and Galeotti, 2003; Turgeon and Brumsack, 2006; Gambacorta et al., 2019). That these black shale layers do not appear in Contessa indicates a subtle difference in the environmental regimes under which the two otherwise very similar sections were deposited.

The rhythmical bedding of the Scaglia Bianca has been long recognised, with many studies linking the alternations of limestone and black chert to Milankovitch cycles, specifically linking the ~20 cm alternations of limestone and chert to ~21 kyr precession cycles (Arthur and Premoli Silva, 1982; de Boer, 1982; Schwarzacher, 1994; Beaudoin et al., 1996; Mitchell et al., 2008; Lanci et al., 2010; Sprovieri et al., 2013; Batenburg et al., 2016; Laurin et al., 2016; Gambacorta et al., 2019). Both short and long eccentricity modulate the amplitude of these precession cycles; although cycles containing black cherts (and in places black shales) have been suggested to correspond to eccentricity minima by Lanci et al. (2010), these cycles are more generally thought to occur during eccentricity maxima (Mitchell et al., 2008; Batenburg et al., 2016; Laurin et al., 2016).

4.3 Methodology

Four Scaglia Bianca precession cycles were studied in detail: three cycles from Furlo (Figure 4.1) and one cycle from Contessa (co-incident with Furlo Cycle B). Detailed sedimentary logs were created for each precession cycle and continuous samples were collected through them. For marls, shales and cherts occurring in thin ~1 cm beds this meant sampling the entirety of each bed. Thick limestone beds were sampled as blocks, and usually homogenised in 5 cm sections. Sampling at a higher resolution than this through the limestone was thought to be unnecessary, as the limestones are well bioturbated and therefore already likely to be homogenous on this scale (Coccioni and Galeotti,

2003; Gambacorta et al., 2014). An additional cycle from the Scaglia Bianca above the Bonarelli Level at Furlo was sampled in the same manner, solely for use in the calculation of background flux (Section 4.5.1).

A Rock-Eval 6 was used to determine Total Organic Carbon (TOC) content, carbonate content, and Hydrogen Index of samples (see Behar et al., 2001). An internal standard, SAB 134 (Blue Lias Fm, St Audrie's Bay, Somerset), previously calibrated to international standards, was used to check long-term reproducibility; ±1σ errors on Rock-Eval measurements (as calculated from 38 analyses of the internal standard) are ±0.04% for TOC (%), ±0.09% for mineral carbon (%) – so ±0.76 for carbonate content (%) – and ±14 for Hydrogen Index (mg HC/g TOC).

Helium concentration was measured on a HELIX SFT mass spectrometer (Section 3.1.2) and the extraterrestrial ^{3}He component deconvolved using a two-component mixing model (Patterson and Farley, 1998 – described further in Section 3.1.4). The He content of each sample was measured twice, with additional measurements made if duplicates were not within error of one another (the largest contributor to these measurements' error was error in the measured $^{3}He/^{4}He$ ratio). Outliers were then identified using Chauvenet's criterion (see Section 3.1.5). ~13% of all measurements were identified as outliers in this manner.

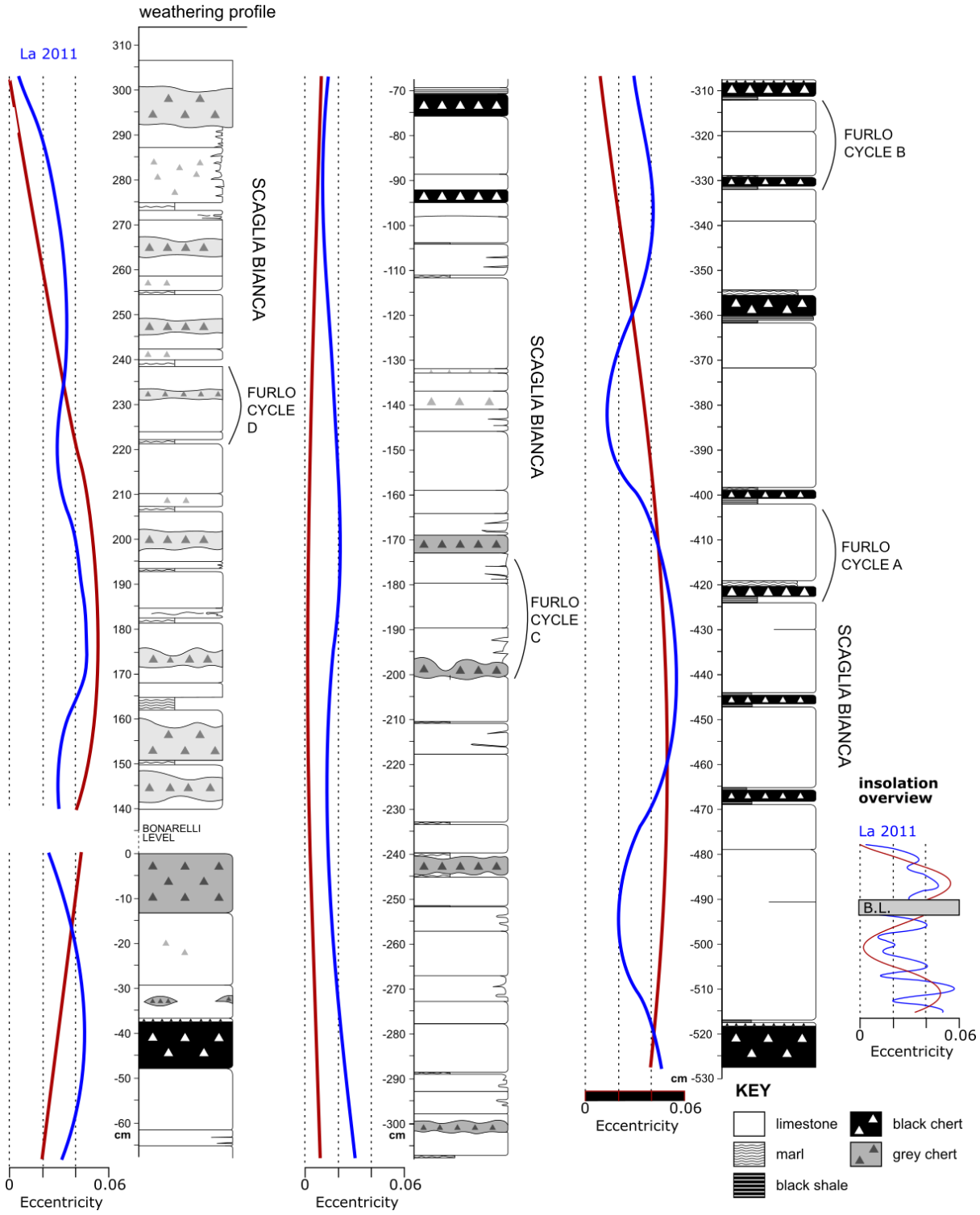

Figure 4.1: Position of studied cycles within overall Furlo section. Cycles were chosen from different points in the 405 kyr eccentricity cycle. Cyclostratigraphic interpretations are from Batenburg et al., (2016); the blue curve represents their tuning of La2011 eccentricity (Laskar et al., 2011a, 2011b) to the Umbria-Marche succession, the red curve just 405 kyr eccentricity.

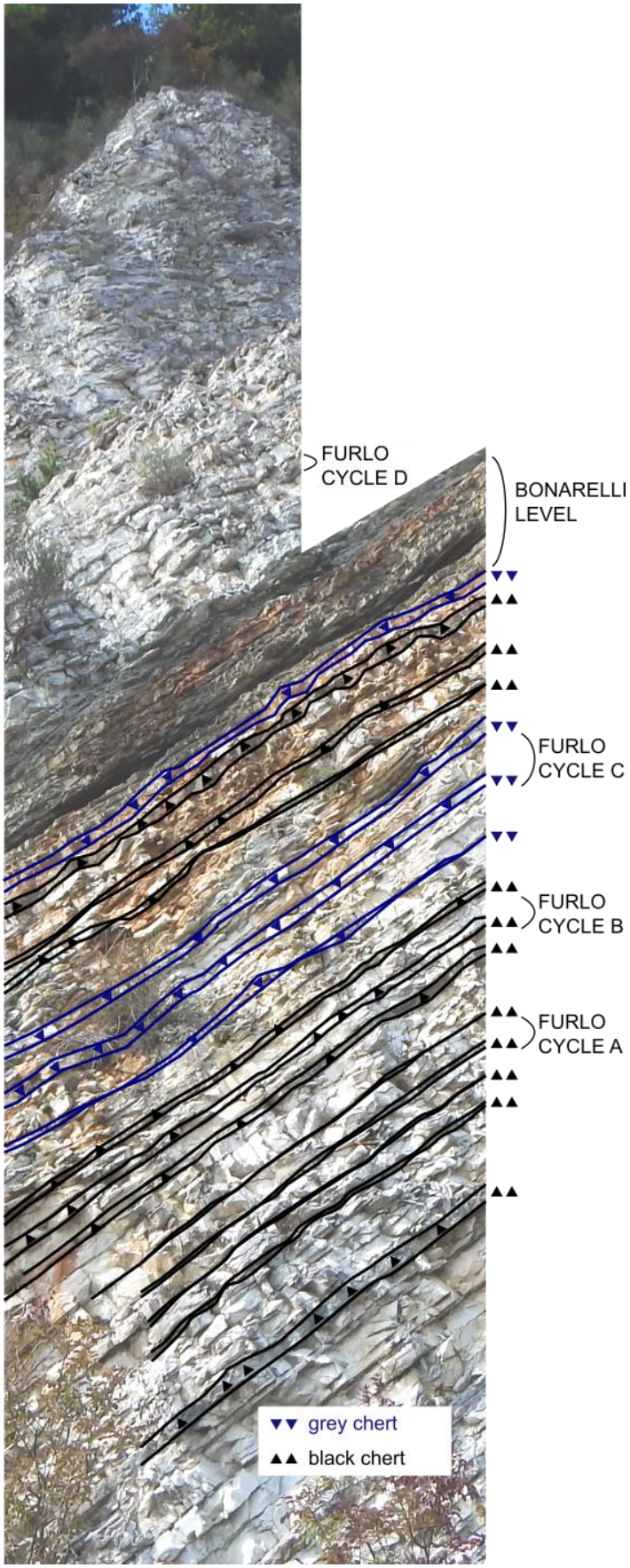

Figure 4.2: Annotated outcrop photograph of Furlo section, showing position of studied precession cycles.

Sedimentation rate is calculated using the following relationship, reflecting the dilution of extraterrestrial-helium-bearing IDPs by other sedimentation (Takayanagi and Ozima, 1987):

$$\alpha = F / [^3He_{ET}]$$

Equation 4.1

Where α is the accumulation rate of sediment (g/cm^2/yr), F is the background flux of extraterrestrial ^{3}He into sediments (cc/cm^2/yr) and [$^3He_{ET}$] is the concentration of extraterrestrial ^{3}He (cc/g).

Background flux can be calculated from Equation 4.1 over intervals where sedimentation rate (α) can be calculated by independent means. In this case study of the Scaglia Bianca Formation, a sedimentation rate of 1.1 cm/kyr is used, taken from the cyclostratigraphic analysis of Batenburg et al. (2016).

As part of this study, three sampling methods for the determination of background flux were evaluated (Figure 4.3). In brief, background flux calculated from spot samples (following Mukhopadhyay et al., 2001a; Farley and Eltgroth, 2003; Murphy et al., 2010) was compared to two calculations that utilised continuous sampling through an entire precession cycle (the 'homogenised cycle' and 'by-bed' methods). The first of these techniques calculated background flux over a precession cycle using the homogenised cycle's average $^3He_{ET}$ concentration. This estimate was contrasted with 'by-bed' cycle averages calculated from the $^3He_{ET}$ concentrations of each bed within a cycle.

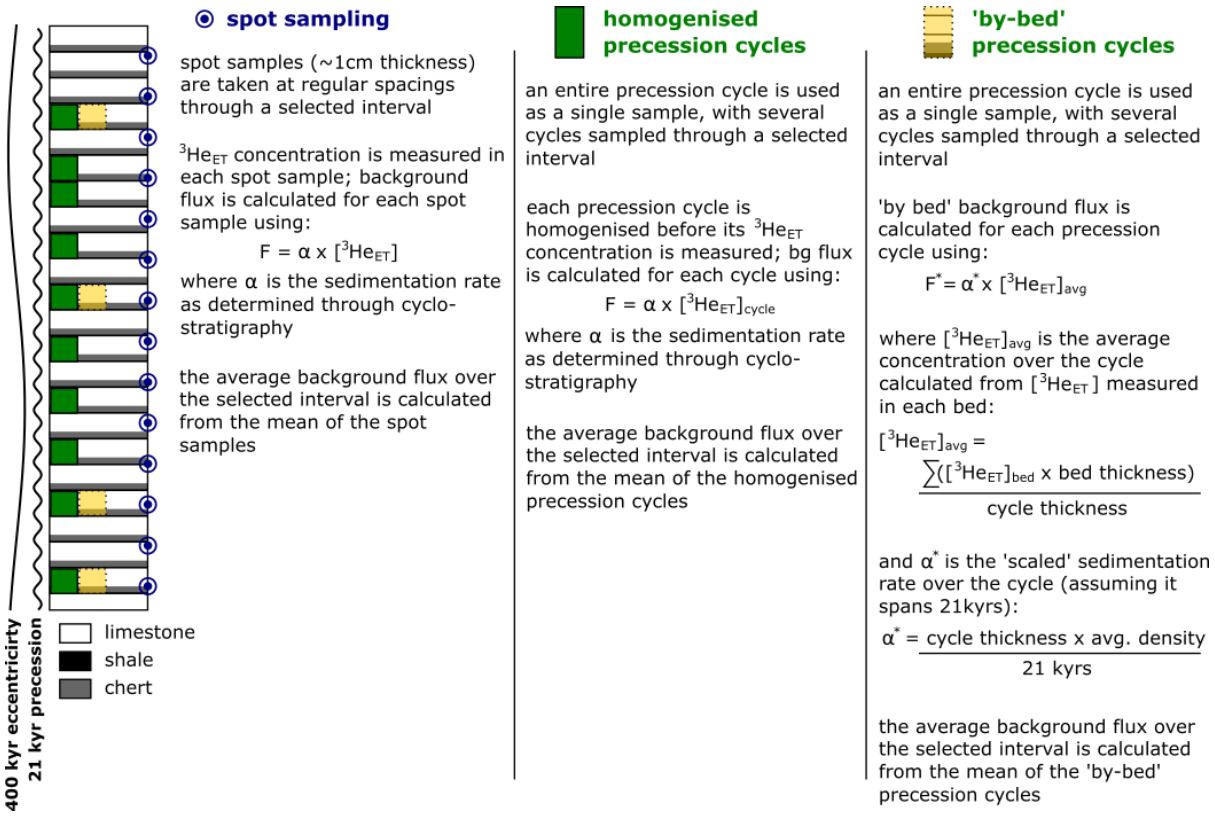

Figure 4.3: Summary of the three trialled methods for determining background flux through intervals with heterogenous lithology: spot sampling, homogenised precession cycles and 'by-bed' precession cycles.

These methods are detailed further in Section 4.5.1. For the calculations of sedimentation rates and durations presented in the discussion (including organic-carbon mass-accumulation rate) background flux values specific to each cycle were used in Equation 4.1, calculated using the 'by-bed' precession cycle method. All methods make use of the assumption that each precession cycle spans ~21 kyr, though this is in fact an average of the four precession cycle periods in the Cenomanian (23.03±0.37 kyr, 21.79±0.34 kyr, 18.53±0.29 kyr and 18.68±0.30 kyr), which cannot be distinguished in the Scaglia Bianca (Waltham, 2015; Batenburg et al., 2016).

4.4 Results

4.4.1 Sedimentology of Scaglia Bianca precession cycles

Many cycles of the Scaglia Bianca are easily picked out by eye as alternations of black chert and limestone. In Furlo, these ~3cm-thick black chert beds are typically underlain by a ~0.5cm layer of black shale; Furlo Cycles 'A' and 'B' are cycles containing black shale (Figures 4.1, 4.2). Cycles at Contessa do not contain black shales, although the black chert of Contessa Cycle 'B' is underlain by a marl distinctly elevated in TOC content from the underlying limestone. In other Scaglia Bianca cycles, cherts are grey and less organic-rich; in Furlo these grey chert beds are not underlain by black shale, though in Furlo Cycle 'C' the uppermost limestone bed does display a slightly elevated TOC content: 0.12% compared to the underlying 0.07% (Figure 4.4). Contacts between lithologies within these cycles are sharp (see Figures 4.5a, b, c, d), suggesting that bioturbation, though prevalent within limestone beds, has not significantly mixed the different lithologies.

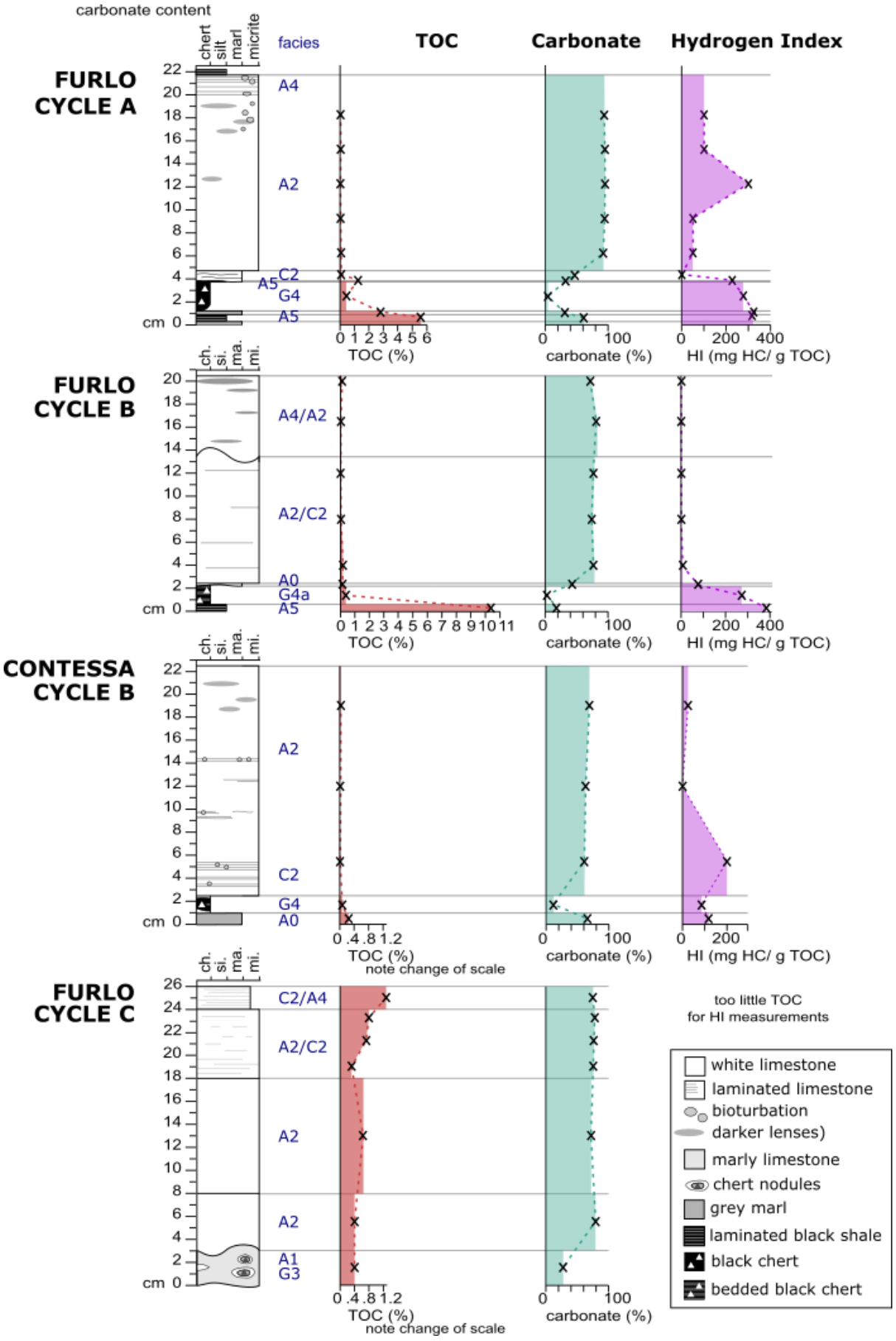
carbonate content
chert
silt
marl
micrite
facies
TOC
Carbonate
Hydrogen Index
FURLO CYCLE A
A4
A2
C2
A5
G4
A5
cm
TOC (%)
carbonate (%)
HI (mg HC/ g TOC)
FURLO CYCLE B
A4/A2
A2/C2
A0
G4a
A5
CONTESSA CYCLE B
A2
C2
G4
A0
note change of scale
FURLO CYCLE C
C2/A4
A2/C2
A2
A2
A1
G3
too little TOC for HI measurements
white limestone
laminated limestone
bioturbation
darker lenses)
marly limestone
chert nodules
grey marl
laminated black shale
black chert
bedded black chert

Figure 4.4: Lithology, total organic carbon content, carbonate content and Hydrogen Index values for the four studied cycles. Number codes for facies are from Gambacorta et al. (2014); A0=marl, A1=homogenous marly limestone, A2=homogenous limestone, A4=alternating micritic and organic rich lamina-sets, A5=black shale, C2=limestone with plane-parallel laminations, G3=grey chert, G4(a)=(bedded) black chert.

A facies numbering scheme was developed in the Scaglia Bianca by Gambacorta et al. (2014), adopted in Figure 4.4. 'A1' and 'A2', 'homogenous marly limestone' and 'homogenous limestone' are composed of planktonic foraminifera (with rare benthic foraminifera) in a micritic matrix made up of solution-welded coccoliths with varying amounts of clay. In a typical thin section of a limestone bed, examined using a petrographic microscope (Figure 4.6a), planktonic foraminifera comprised about 15% of the sediment, the rest being micritic matrix. The foraminifera examined were judged to be weakly oriented parallel to bedding, though Gambacorta et al., (2014) found that in general there is no orientation of foraminifera in homogenous limestone. Both A1 and A2 are thought to be formed by planktonic settling, with the transition from A2 to A1 reflecting varying degrees of dilution (Gambacorta et al., 2014). Both facies often contain diffuse mottling, interpreted as homogenisation by bioturbation (Gambacorta et al., 2014); this mottling was observed over much of the homogenous limestone logged in these studies. Marls, 'A0', contain an even higher clay content. 'Limestones with plane-parallel lamination' ('C2') were interpreted by Gambacorta et al., (2014) as the result of discrete winnowing events by strengthened bottom currents.

Limestones below the black shales commonly contain organic-rich laminae; this facies was labelled 'A4', 'alternating and organic-rich laminasets', by Gambacorta et al., (2014) and is thought to record the onset of anoxic/dysoxic conditions. These laminae are obvious in hand specimen due to their colour contrast, in thin-section they appear as a concentration of flakes of organic matter (Figure 4.6b).

Black shales ('A5') have fine papery lamination and are very dark in colour, interpreted as having been deposited under anoxic conditions. Detailed analysis by Gambacorta et al. (2014) revealed highly variable TOC and carbonate content from lamina to lamina, indicating that oceanographic controls on deposition vary over the sub-precessional duration of black shale deposition. In thin section, long stringers of organic matter form a pervasive fabric parallel to the bedding plane (Figure 4.6c, d). Microfossils (including coiled planktonic forams and more indistinct circular shapes that may

be the remains of radiolarian tests) appear to make up ~45% of one sectioned black shale bed (Figure 4.6d). Both silica and carbonate cements are observed infilling microfossils in thin section, as in Figure 4.6c; although most microfossils appear to have (recrystalised) microspar rims, silica infill is more common than calcite – this silica infill may be associated with the diagenesis of the overlying chert bed. The matrix hosting these organic-matter stringers and microfossils appears sparry (Figure 4.6d): unlike the black shales of the Bonarelli Level, which are devoid of carbonate, the Cenomanian black shales associated with precession cycles (termed here "sub-Bonarelli black shales") still have moderately high carbonate contents, from 20% to 60%. Also hosted in the groundmass are additional flecks of organic matter and opaque, euhedral minerals, probably pyrite.

Cherts vary in colour through the Scaglia Bianca: they can be black ('G4'), grey ('G3') or even pink; this is interpreted as reflecting the oxidation state at the time of their deposition (Gambacorta et al., 2014). Contacts between chert and neighbouring lithologies are abrupt and may be plane parallel or undulose. In some cherts, milimetre scale bedding is clearly visible in hand specimen (Figure 4.5e). Grey and black bedding is formed by alternating layers of silt to sand-sized radiolaria and finer beds containing more clay and organic matter (Gambacorta et al., 2014). The granular texture that cherts display in hand specimen is created by 'ghost' radiolarians, which sit in a matrix of microquartz (Figure 4.6e, f).

In contrast to the sub-Bonarelli black shales, cherts have almost no carbonate content; this is as expected, since silica replaces carbonate during chert formation (Heath and Moberly, 1971; Wise and Weaver, 1974; Knauth, 1994). A thin section across the boundary between a black shale and overlying black chert indicates that between these two lithologies is ~0.5mm of matrix devoid of the abundant microfossils characteristic of both black shale and black chert and, largely, of organic matter – though still containing pyrite (Figure 4.7a, b). Within this matrix, microcrystalline calcite (immediately above the black shale) and microcrystalline silica (immediately below the black chert) interfinger.

Examination of a limestone bed immediately above a chert revealed replacement of both calcitic and siliceous microfossils by chalcedonic quartz (Figure 4.7d, e, f), as well as what may be a centimetre-scale chert nodule (Figure 4.7c). More radiolarians were present in this bed than in the 'homogenous limestone' above, perhaps due to better preservation. Both chert nodule and silicified microfossils are rimmed by microspar within the otherwise micritic matrix; the origin of this rim may be the original calcite which was replaced by silica during chertification.

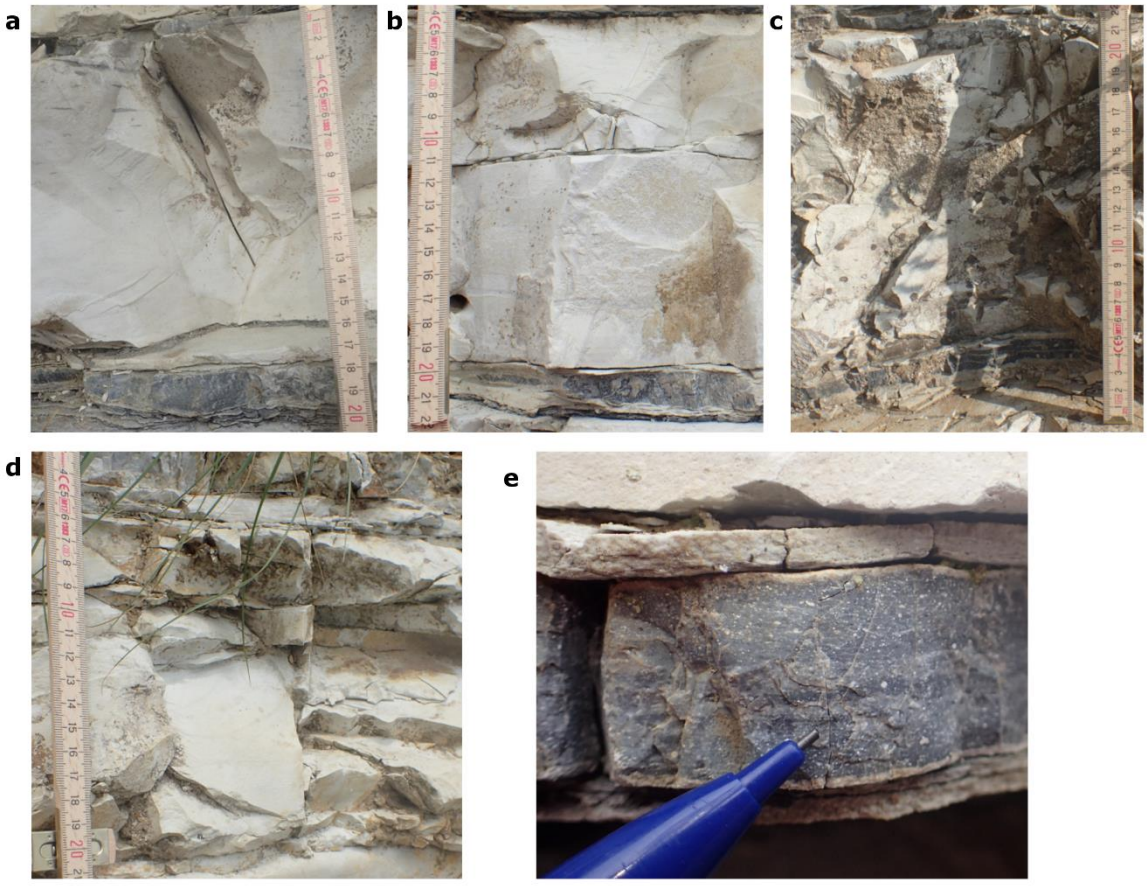

Figure 4.5: Precession cycle outcrop photographs. ***(a)*** *Furlo Cycle A;* ***(b)*** *Furlo Cycle B;* ***(c)*** *Contessa Cycle B;* ***(d)*** *Furlo Cycle C;* ***(e)*** *Bedded black chert. (Position: 0.6–2.1 cm in Furlo Cycle B).*

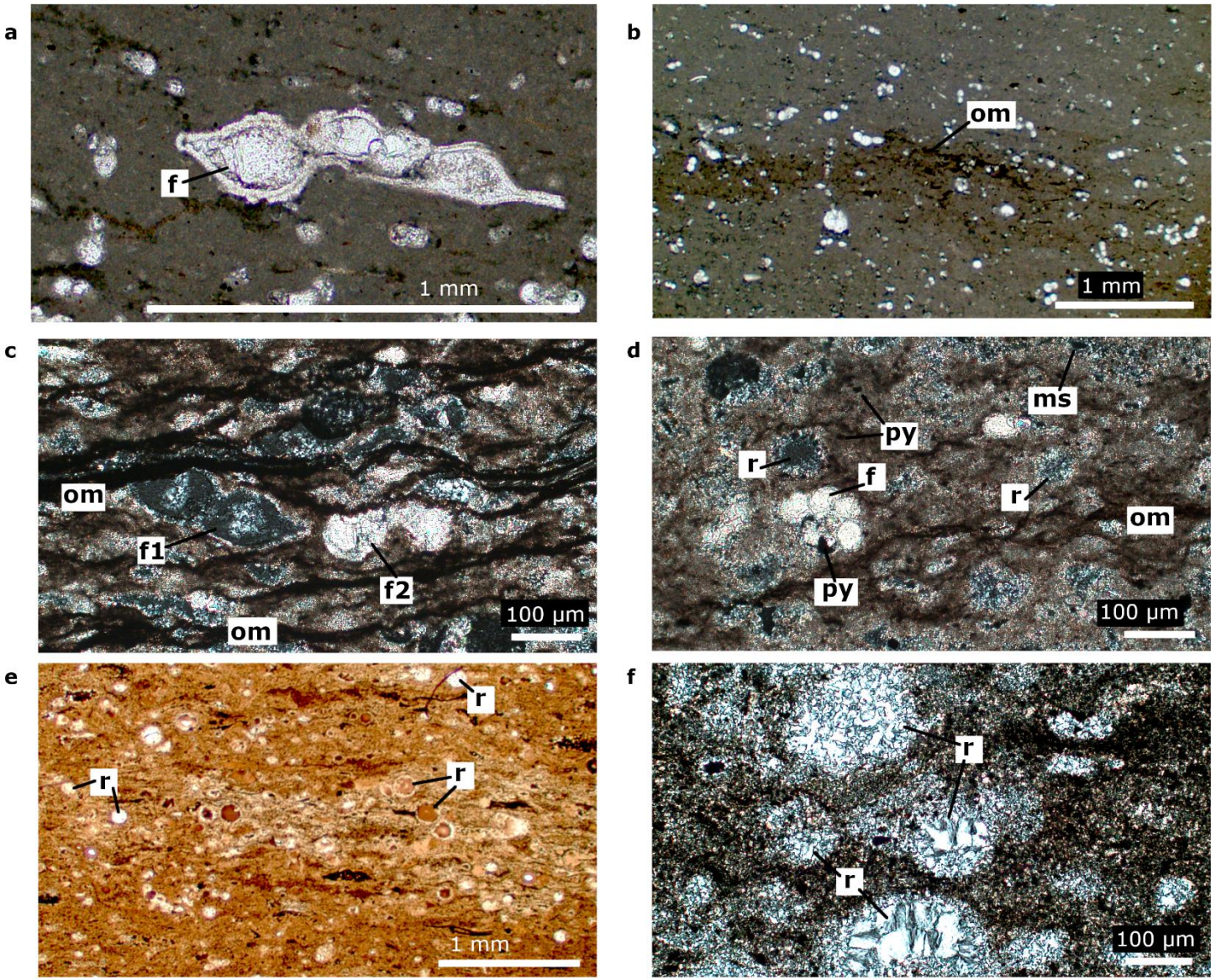
a
f
1 mm
b
om
1 mm
c
om
f1
f2
om
100 µm
d
ms
py
r
f
r
om
py
100 µm
e
r
r
r
1 mm
f
r
r
100 µm

Figure 4.6: Thin section images of precession cycle lithologies. ***(a)*** *Large keeled foraminifera (f) within a limestone bed. (Position: 21 cm in Furlo Cycle A, under plane polarised light (PPL), younging direction upward);* ***(b)*** *Organic-rich lamina (om) in a limestone bed. (Position: 21 cm in Furlo Cycle A, PPL, younging direction upward);* ***(c)*** *Equatorial view through two coiled planktonic forams in a black shale bed. Both forams have walls of microcrystalline calcite, though one is infilled with silica (f1), whilst the other is infilled in large crystals of spar (f2). Stringers of organic matter (om) form a pervasive fabric parallel to bedding. (Position: 0.5 cm in Furlo Cycle B, under crossed polars (XPL), younging direction upward);* ***(d)*** *Abundant microfossils in a black shale bed. Clearly visible is a spar-filled coiled foram (f), the opaque mineral in the inner chamber (py) is likely pyrite associated with organic matter. Some of the circle-like microfossils infilled with silica may be radiolarians (r). The matrix is composed largely of microspar, with some irregular patches of microcrystalline silica (ms). Note the euhedral shape of pyrite in the groundmass (py), and the stringers of organic matter (om). (Position: 0.5 cm in Furlo Cycle B, XPL, younging direction upward);* ***(e)*** *'Ghost' radiolarians (r) in a black chert bed. A patchy variation in the darkness of the groundmass is evident. (Position: 1.5–4 cm in Furlo Cycle A, PPL, younging direction upward);* ***(f)*** *Radiolarians (r) in the lower part of a black shale bed. Test walls have been replaced by finer-grained silica than the interior fill. (Position: 1 cm in Furlo Cycle B, under crossed polars (XPL), younging direction upward).*

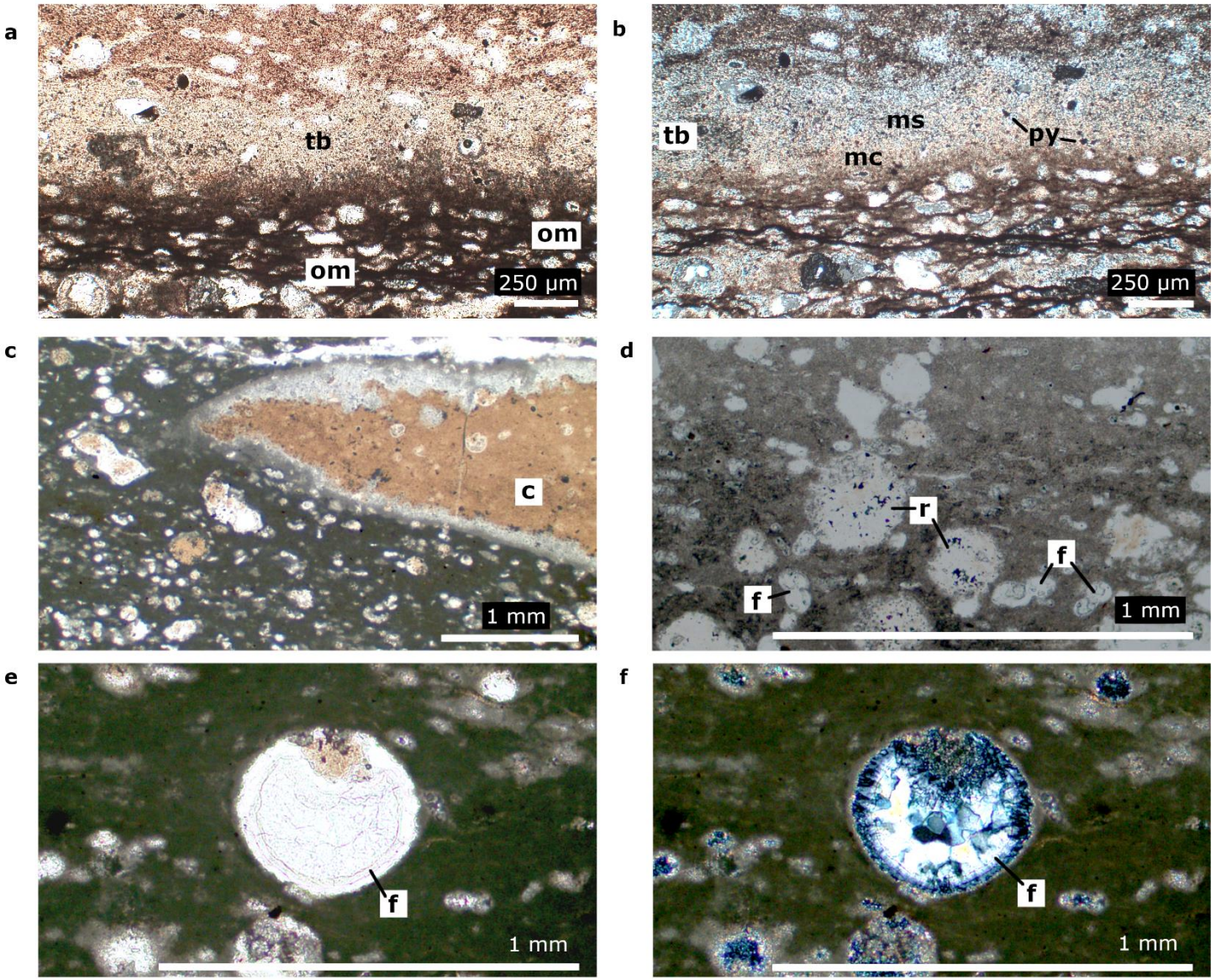
a
tb
om
om
250 µm
b
tb
ms
mc
py
250 µm
c
c
1 mm
d
r
f
f
1 mm
e
f
1 mm
f
f
1 mm

Figure 4.7: Thin section images of precession cycle lithologies. ***(a)*** *Section across the boundary between black shale (base) and black chert (top). Abundant organic matter (om) can be seen in the black shale, with rather less in the black chert, and very little in the ~500 µm transitional band (tb) between them. This band is also largely devoid of microfossils. (Position: 0.6 cm in Furlo Cycle B, under plane polarised light (PPL), younging direction upward);* ***(b)*** *Same image as previous under crossed polars (XPL). It can be seen that the transitional band is made up of interfingering microcrystalline calcite (mc) and microcrystalline silica (ms). It also contains relatively large euhedral opaque crystals which may be iron oxides or pyrite (py) – possibly the former after the latter following weathering at outcrop. (Position: 0.6 cm in Furlo Cycle B, XPL, younging direction upward);* ***(c)*** *Chert nodule (c) rimmed by calcite in a laminated limestone bed. This nodule contains the same microfossils as the surrounding limestone but has a silicic matrix. An alternate interpretation of this feature, given its angularity, might be a chert intraclast, indicating erosion between the chert and overlying limestone in this cycle (Position: 4–5 cm in Furlo Cycle A, PPL);* ***(d)*** *Silicified radiolarians (r) and foraminifera (f) in a micrite matrix made up of solution-welded nannofossils. (Position: 4–5 cm in Furlo Cycle A, PPL);* ***(e)*** *Silicified foraminifer test (f). (Position: 4–5 cm in Furlo Cycle A, PPL);* ***(f)*** *Silicified foraminifer test (f) under crossed polars. The test wall has been replaced by fibrous silica, with a chalcedonic quartz infill. Triple point junctions in the chalcedony indicate these rocks have experienced some deformation for these minerals to reach this equilibrium texture. The test is surrounded by a thin microspar cement and sits in a micritic matrix. (Position: 4–5 cm in Furlo Cycle A, XPL).*

Sub-Bonarelli black shales show enrichments in TOC of up to 10%. Interestingly, associated black cherts have much lower TOC contents (<1%), despite their colour. Other measurements of TOC content in sub-Bonarelli black shales at Furlo indicate that values are very variable, even between different samples of the same bed: over the same stratigraphy as measured in this study, TOC values of up to 20% in sub-Bonarelli black shales were recorded by Jenkyns et al. (2007), whereas Owens et al. (2016) did not record values higher than 5%.

The predominance of organic matter with Type II Hydrogen Index (HI) values (Figure 4.8) suggests a marine source for the majority of the organic carbon in the Furlo precession cycles. Black shales, black cherts and marls typically have higher Hydrogen Indices than limestones, perhaps indicating either a greater contribution from Type I organic matter, or enhanced organic matter preservation under low-oxygen conditions. Hydrogen Index values from Contessa samples are uniformly lower than at Furlo, which may suggest a slightly different balance of sources of organic matter in this region or alternatively, along with the overall lower organic-carbon content in this section, that Contessa samples are more oxidised, weathered, and/or thermally matured. Study of vitrinite reflectance across sediments in another part of the Apennine fold-and-thrust belt indicates that large changes in thermal history are possible between relatively nearby sites in this setting (Caricchi et al., 2015); Furlo and Contessa are ~40 km apart, although T_{max} values measured in this study did not appear particularly different between the two sites (T_{max} = 327–451°C at Furlo, and 300–442°C at Contessa). Less favourable conditions for organic matter preservation at Contessa could also have occurred because conditions in the water column during deposition, or in the sediments during early diagenesis, were more oxidising, or because modern surface weathering is deeper and more pervasive at Contessa, or because of different burial histories of the two locations.

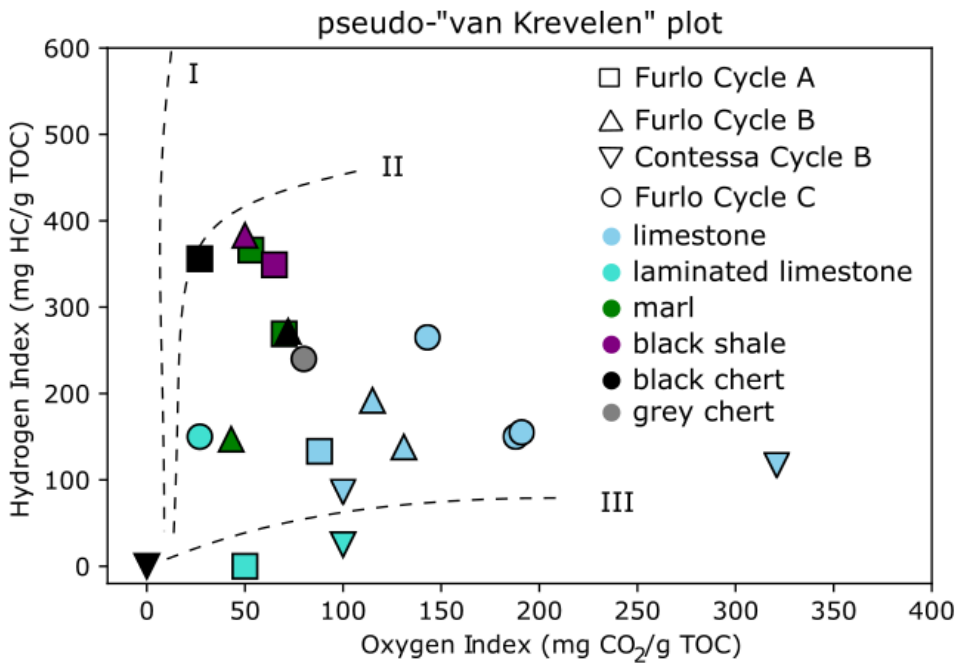

Figure 4.8: Van Krevelen-type plot showing the variation of organic matter types with lithology in the studied Scaglia Bianca precession cycles.

4.4.2 Helium concentration

The measured concentrations of extraterrestrial ^{3}He and terrestrial ^{4}He are presented in Figure 4.9.

The average concentration of $^{3}He_{ET}$ in limestones is similar across all Furlo cycles: ~2×10^{-14} cc/g, with a somewhat lower concentration (~1.1×10^{-14} cc/g) measured in the limestone of the Contessa cycle. Lithologies with greater clay content such as shales and, to a lesser extent, marls typically have the highest concentrations of $^{3}He_{ET}$. This enrichment is most pronounced in the black shales of Furlo Cycles A and B, which contain average concentrations of $^{3}He_{ET}$ of 1.92±0.27 $\times10^{-13}$ cc/g and 2.69±0.38 $\times10^{-13}$ cc/g respectively, whilst the marl of Contessa Cycle be has a more modestly elevated $^{3}He_{ET}$ concentration of 4.65±0.66 $\times10^{-14}$ cc/g. The black chert beds in these cycles do not display this $^{3}He_{ET}$ enrichment; average $^{3}He_{ET}$ concentration in these black cherts ranges from ~1.0±0.1–2.6±0.3 $\times10^{-14}$ cc/g, comparable to concentrations measured in the limestones. In contrast to the other studied cycles, $^{3}He_{ET}$ concentration does not vary significantly through Furlo Cycle C.

The background flux of $^{3}He_{ET}$ would be expected to remain constant over the interval of a precession cycle, so within these cycles $^{3}He_{ET}$ concentration is likely inversely proportional to sedimentation rate (a relationship expressed in Equation 4.1). However, the calculation of numerical values for sedimentation rates is dependent on the chosen value of background flux; sedimentation rates are, therefore, discussed in a separate section below.

The concentration of terrestrial ^{4}He also varies across precession cycles. Typically, the lowest average concentrations of $^{4}He_{terr}$ occurs in limestones, though the actual values vary from cycle to cycle (between ~0.6–2.5×10^{-8} cc/g). Over Furlo Cycle C, however, there appears to be no significant variation in $^{4}He_{terr}$ concentration. By contrast, spikes in the concentration of $^{4}He_{terr}$ are observed in the black chert and marl beds of Furlo Cycles A and B and Contessa Cycle B. Extremely high concentrations are measured in the black shales of Furlo Cycles A and B (average $^{4}He_{terr}$ concentrations of 4.6×10^{-7} cc/g and 5.1×10^{-7} cc/g, respectively). The black cherts in Furlo Cycles A and, to a lesser degree, B also contain a noticeably elevated concentration of $^{4}He_{terr}$ relative to the limestones (average concentrations from chert beds are 3.1×10^{-7} cc/g and 3.9×10^{-8} cc/g, respectively).

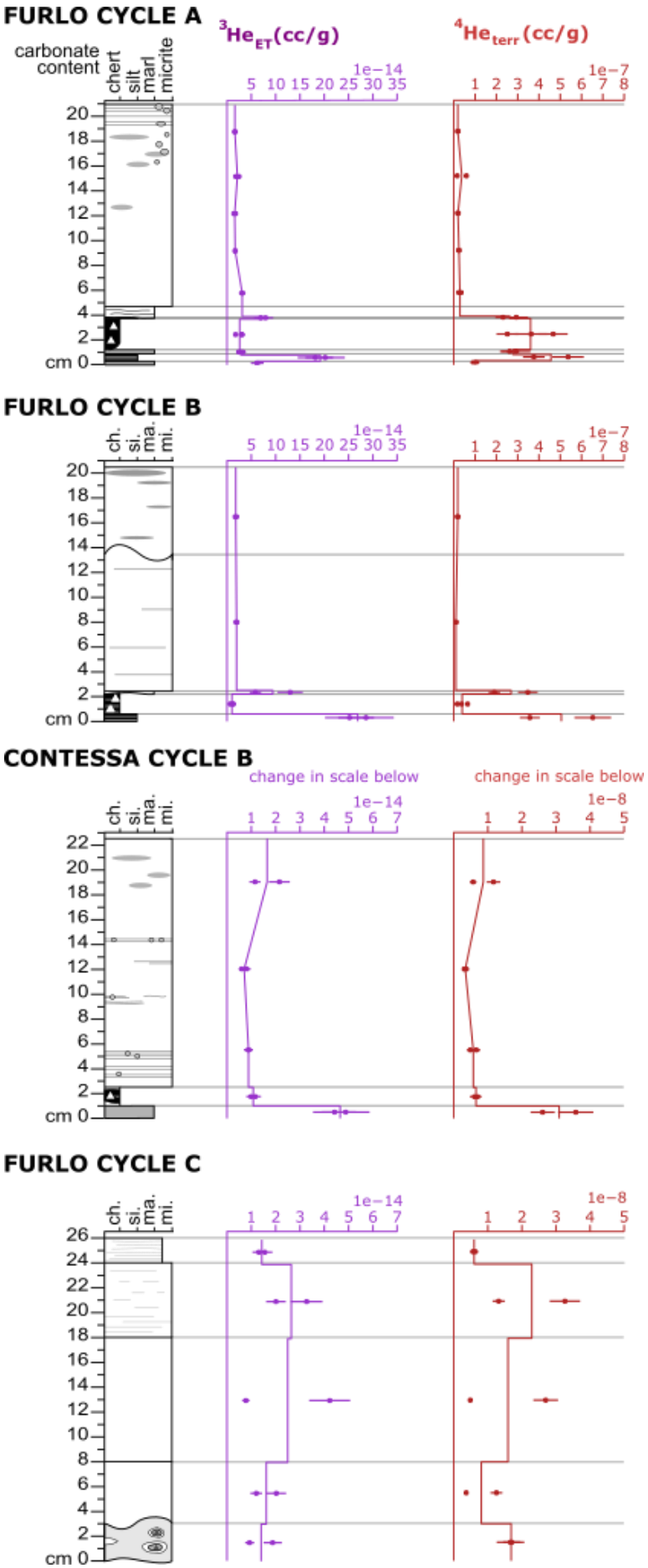
FURLO CYCLE A
carbonate content
chert
silt
marl
micrite
$^3He_{ET}$(cc/g)
$^4He_{terr}$(cc/g)
1e−14
1e−7
cm
FURLO CYCLE B
ch.
si.
ma.
mi.
CONTESSA CYCLE B
change in scale below
1e−8
FURLO CYCLE C

Figure 4.9: Extraterrestrial ^{3}He and terrestrial ^{4}He concentration through the studied precession cycles. Data points represent individual measurements, solid lines average values. Error bars on $^{3}He_{ET}$ (cc/g) represent 20% reproducibility error due to the nugget effect (see Section 3.1.5), error bars on $^{4}He_{terr}$ derive from analytical error.

4.5 Discussion

4.5.1 Background Flux

Before timescales can be constructed from $^{3}He_{ET}$ concentration measurements, the background flux of extraterrestrial ^{3}He must be determined ('F' in Equation 4.1). Developing an effective technique for measuring background flux in sections with heterogeneous lithology is key not only for interpreting the $^{3}He_{ET}$ data in this study, but for expanding the use of $^{3}He_{ET}$ timescales; previous studies have largely been carried out in sections where background flux can be calculated from sediments of a constant lithology, typically limestone, chalk, or carbonate ooze (Mukhopadhyay et al., 2001a; Farley and Eltgroth, 2003; Murphy et al., 2010). The highly heterogeneous nature of the Scaglia Bianca provides a useful testing ground to evaluate different methods for calculating background flux. Three such methods are outlined below: calculation from spot samples, from homogenised whole precession cycles and from measurements of each bed within a precession cycle (methods summarised in Figure 4.3, results summarised in Figure 4.10).

Spot sampling

Spot sampling is the method most commonly used to estimate background flux in homogeneous lithologies (Mukhopadhyay et al., 2001a; Farley and Eltgroth, 2003; Murphy et al., 2010). Background flux is calculated for a series of spaced spot samples from their measured $^{3}He_{ET}$ concentrations using Equation 4.1 ($\alpha = F / [^{3}He_{ET}]$) and an independently determined value for sedimentation rate (α), usually from cyclostratigraphy. In this study a value of 1.1 cm/kyr was used, taken from Batenburg et al. (2016). Using this method, a final value for background flux is taken from the average of the spot samples.

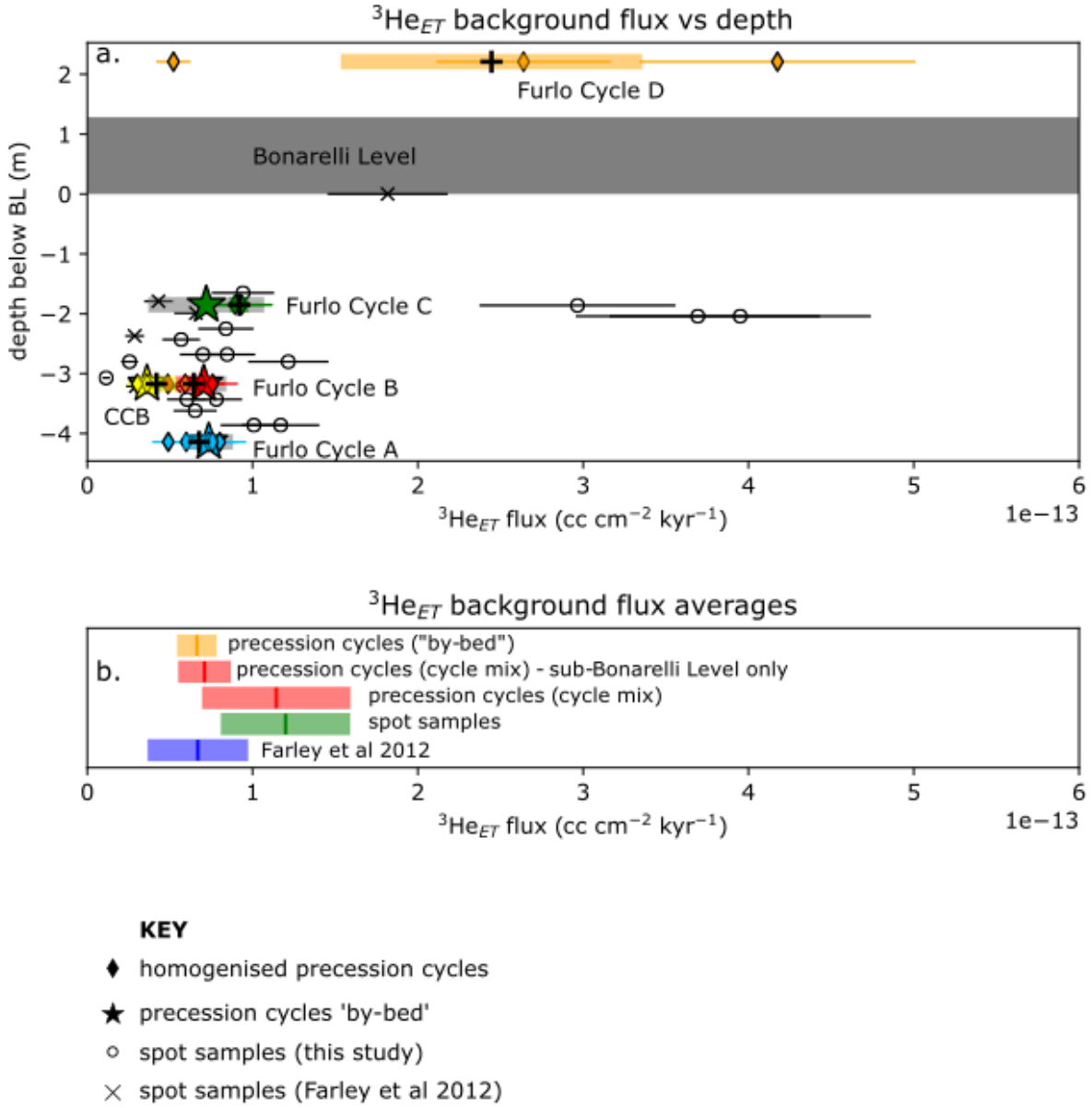

Figure 4.10: Comparison of background flux determined through different means.

***(a)** Calculated background flux through the Scaglia Bianca. Blue-filled symbols correspond to Furlo Cycle A, red to Furlo Cycle B, yellow to Contessa Cycle B (CCB), green to Furlo Cycle C and orange to a precession cycle above the Bonarelli Level. All samples from this study are from Furlo; data from Farley et al. 2012 are from Contessa.*

Averages of homogenised precession-cycle replicates are presented as a black plus sign, within broad coloured error bars spanning the standard error on the average. Broad grey error bars on precession cycle 'by-bed' values (filled stars) are a result of error propagation from the measurements that went into their calculation. All other error bars on individual measurements arise from the expected reproducibility of individual measurements.

***(b)** Comparison of average background flux values determined through different means; error bars presented are $1\sigma_x$ (standard error).*

Background flux calculated from spot samples through the Scaglia Bianca are presented in Figure 4.10a, along with background flux spot samples from Farley et al. (2012). The value of calculated background flux can be seen to vary widely from spot to spot, with a standard deviation about the average of ~27%. It seems likely, however, that the variation seen in spot samples is greater than the actual variation in background flux over time, as samples are taken from different lithologies with different sedimentation rates, even though an average sedimentation rate is used for all calculations. If, for example, a particular lithology has a higher sedimentation rate than the average used, background flux will be underestimated for that particular spot sample, and *vice versa*.

Most concerningly, spot sampling through heterogeneous lithologies also carries the risk of oversampling a particular lithology, because varying sedimentation rates mean that the proportion of any given lithology in depth isn't necessarily representative of its proportion in time. This complication could then skew the calculated average background flux. Because of this heightened potential for systematic error in mean calculation through spot sampling in heterogeneous lithologies, it was thought prudent to investigate other methods of sample collection for background flux calculations.

Homogenised precession cycles

The second method used to calculate background flux, namely calculation from whole homogenised precession cycles, attempted to mitigate the effect of sedimentation rate variation with lithology by a different choice of sampling unit. Although the sedimentation rate through the Scaglia Bianca at Furlo is presented as 1.1 cm/kyr (Batenburg et al., 2016), the smallest increment of time that can be distinguished through cyclostratigraphy in this sequence is the ~21 kyr precession cycle, so the sedimentation rate should perhaps be instead thought of as 23.1 cm (thickness of a single precession cycle)/21 kyr (the implications of using this average value of unresolved precession cycles with periods 18–23 kyr are explored later in this section). Background flux was therefore calculated from homogenised mixtures of whole precession cycles as follows:

$$F^* = [^3He^{ET}]_{cycle} \times \alpha$$

Equation 4.2

where $[^3He_{ET}]_{cycle}$ is the $^3He_{ET}$ concentration measured in the homogenised precession cycle and α is the sedimentation rate as determined through cyclostratigraphy. In order to create these homogenised mixtures, each bed within a precession cycle was powdered separately; these were then combined into mixtures containing proportional volumes of sediment from each bed (the mass of powder needed was calculated from the thickness of the source bed and the density of the original lithology).

The average background flux calculated from replicates of homogenised precession cycles is presented in Figure 4.10a. Variation between replicates is not unexpected, due to the 'nugget effect' (expanded on in Sections 2.1.3 and 3.1.5). Although homogenised precession cycles from the Scaglia Bianca both stratigraphically below and above the Bonarelli Level were measured, the other evaluated methods for determining background flux use only samples from the sub-Bonarelli Level Scaglia Bianca. Therefore, in order to compare like with like, background flux determined using only sub-Bonarelli Level precession cycles (presented in red and labelled as 'precession cycles (cycle mix) – sub-Bonarelli Level only' in Figure 4.10b) is used for comparison with background flux determined through other methods. The overall value for 'sub-Bonarelli Level Scaglia Bianca' background flux determined using this method is not dissimilar to that of the spot samples of Farley et al. (2012). It is somewhat lower than the background flux determined using the spot samples measured in this study, though still within the span of error, which may reflect the potential for a skewed average 'spot sample' flux in heterogeneous lithology, as discussed above. The standard deviation of the 'sub-Bonarelli Level Scaglia Bianca' background flux calculated using this method is ~13%.

It must be borne in mind, however, that improved methodology can only reduce the scatter of apparent background flux values measured to some minimum that reflects the actual variation in incoming $^3He_{ET}$ over the time interval. The average background flux measured over the precession

cycle above the Bonarelli Level (displayed as an orange bar in Figure 4.10a) is distinctly higher than the background flux measured lower in the section, which could reflect such a variation in incoming $^{3}He_{ET}$.

The choice of precession cycles as a sampling unit is not without caveats. For a start, precession cycles must be identified in outcrop to ensure that an entire cycle is sampled. In the Scaglia Bianca, a large body of evidence links the chert-limestone cycles to precession (Arthur and Premoli Silva, 1982; de Boer, 1982; Mitchell et al., 2008; Lanci et al., 2010; Batenburg et al., 2016; Gambacorta et al., 2019), so by sampling from chert bed to chert bed one can be reasonably confident that an entire precession cycle has been sampled.

Secondly, using the sedimentation rate of 1.1 cm/kyr in these calculations effectively assumes that, as stated above, the precession cycles are 23.1 cm thick and span 21 kyr. However, overall cycle thickness varies between different precession cycles within the stratigraphy (see Figures 4.1, 4.23), the thinnest being Furlo Cycle D at ~18 cm and the thickest Furlo Cycle C at 26 cm. In addition, the 21 kyr precession cycle is itself an average of the four precession cycle periods that occurred through the Cenomanian (23.03±0.37 kyr, 21.79±0.34 kyr, 18.53±0.29 kyr and 18.68±0.30 kyr), and different precessional periods may have dominated at different points of the long eccentricity cycle (Berger et al., 1992; Berger and Loutre, 1994; Laskar et al., 2011a, 2004; Waltham, 2015; Zeeden et al., 2015).

If thicker/thinner cycles represented proportionally longer/shorter intervals, the 1.1 cm/kyr sedimentation rate would still hold, but there is no reason to believe that this is necessarily the case; for instance, Furlo Cycle C contains much more limestone, a lithology known to accumulate relatively fast in comparison to the marly lithologies present in Cycles A and B, and so may well be thicker without being temporally longer. In a “worst case” scenario of the thinnest cycle (Furlo Cycle A, 21 cm) corresponding to the longest period of precession at this time (23.03 kyr, from Waltham, 2015), or the thickest (Furlo Cycle C, 26 cm) to the shortest (18.53 kyr), the “appropriate” sedimentation rate to use may vary by up to 30%. This 30% variation in ‘potential sedimentation rate’ between

different homogenised cycles is, however, orders-of-magnitude lower than the differences in $^{3}He_{ET}$ concentration (the other variable governing calculated sedimentation rate) across the target sections for this study's $^{3}He_{ET}$ age models (see comparison of $^{3}He_{ET}$ concentrations measured in cherts and limestones, and sub-Bonarelli black shales in Section 4.4.2). In the absence of any way to tell exactly which period of precession cycle each homogenised cycle represents, Batenburg's (2016) sedimentation rate of 1.1 cm/kyr is used for all.

This uncertainty in sedimentation rate deriving from varying lengths of precession cycle might be eliminated by choosing an alternative sampling period. Obliquity, for instance, has a single period, but although obliquity cycles have been identified in stable carbon and oxygen isotope records through the Scaglia Bianca there is not an obvious lithological expression of this cycle, as there so clearly is for precession (Batenburg et al., 2016). Creating homogenised mixes over longer intervals, say that of 405 kyr eccentricity, was considered prohibitively difficult at these outcrop localities as a homogenised mixture would have had to be created from around 100 individual beds. This task would be easier in sections that could be sampled with a U sampling tool (as in less lithified lithologies, such as ooze or chalk), though this is seldom possible for older Mesozoic sections and therefore a less useful tactic when expanding the use of helium timescales back in geological time. In addition, homogenising over 400 kyr would mean losing any sense of the potential variability of background flux on a sub-400 kyr timescale.

Finally, there is a risk that variability in background flux between samples could be due to variable levels of erosion between different cycles. Although the deep pelagic palaeoenvironmental setting of the chosen sections were selected specifically to avoid erosion, evidence of bottom currents has been recorded in the Scaglia Bianca (Gambacorta et al., 2014). Although no sedimentary features indicative of erosion were seen in selected precession cycles, it is very possible that the dramatic shifts in lithology may have resulted in some missing recorded time and therefore an underestimate of the background flux. If the variation in calculated background flux is due to erosion, these large

errors may be a constant in sections with varying lithology, a consideration that could drive the choice of sections using this technique in the future.

Some insights into the potential effects of erosion may be gained by comparing Furlo Cycle B and Contessa Cycle B. The background flux values as measured at these two localities are within error of one another; an expected result as they both represent the same interval of time. The Furlo and Contessa deposits were laid down in different locations under slightly different palaeoceanographic conditions (Gambacorta et al., 2016), but substantially different levels of erosion do not appear to have impacted calculated background flux at the two sites.

'By-bed' precession cycles

The creation of high-resolution timescales through the sub-Bonarelli Level Scaglia Bianca precession cycles provided a third method of determining background flux. Although using the background flux calculated from each homogenised precession cycle in Equation 4.2 (which itself was predicated on the assumption that cycles were 21 kyr long) should have guaranteed that the sum of the durations of all beds was 21 kyr, this was not always the result obtained. Using the error on the value of background flux determined in these initial calculations as the largest contributor to overall error, the sum of the duration of all beds in Furlo Cycles A and B were 22.5±1.7 kyr and 22.6±2.3 kyr respectively, an expected result. By contrast, the sum of the duration of all beds in Contessa Cycle B was 17.3±3.0 yr, and in Furlo Cycle C was 12.4±0.1 kyr, both outside of error of the expected 21 kyr duration (albeit, in the case of Contessa Cycle B, only just). It is worth stressing again here that, although the value of 21 kyr is simply an average of precession cycles of varying lengths through the Cenomanian, this figure was used as the time spanned by each precession cycle in the determination of background flux, so in order to "close the circle" should have necessarily been the duration measured for each cycle.

This difference between the calculated sum of bed durations and the expected 21 kyr sum could have arisen through error in the creation of the homogenised precession cycles, for example, if the

wrong proportions of different lithologies were used, though substantial care was taken during preparation to avoid exactly this circumstance. It is harder to see where substantial error could have arisen in these bed-by-bed measurement of cycles; beds were sampled continuously, and each one was measured multiple times for its helium content in order to create a timescale.

A 'by-bed' background flux (F*) was back-calculated from each of these measured cycles:

$$F^* = [^3He^{ET}]_{avg} \times \alpha^*$$

Equation 4.3

where $[^3He^{ET}]_{avg}$ (cc/g) is the average $^3He_{ET}$ concentration over the cycle:

$$[^3He^{ET}]_{avg} = \Sigma([^3He_{ET}]_{per\ bed} \times \text{bed thickness}) / \text{cycle thickness}$$

Equation 4.3

and α^* (g/cm^2/kyr) is the 'scaled' sedimentation rate over the cycle (assuming it spans 21 kyr):

$$\alpha^* = \text{cycle thickness} \times \text{average cycle density} / 21\ \text{kyr}$$

Equation 4.5

The results of back-calculating background flux based on precession cycle timescales as scaled to 21 kyr are presented as filled stars in Figure 4.10a.

Producing replicates of these back-calculated background flux values would involve measuring the entire cycle again; however, the flux values calculated from Cycle B at both Furlo and Contessa can be compared (red and yellow stars in Figure 4.10a), and are seen to be similar.

A significant downside to the 'by-bed' background flux process is its unwieldiness, requiring the measurement of at least 10 samples to produce a flux value for just one cycle. This drawback may make this technique too effort-intensive to be truly useful, with effort more usefully expended in determining background flux values from a larger number of cycles.

Method evaluation

The background flux values as calculated from the three different methods detailed above, with associated standard error, are displayed in Figure 4.10b and summarised in Table 4.1. The standard errors on the mean background flux over the sub-Bonarelli Level Scaglia Bianca range between 8 and 27% using the three methods. The most appropriate procedure for determining background flux in sections with heterogeneous lithology must balance ease of sampling/analysis with reduction of error.

In conclusion, the most appropriate method for calculating background flux in heterogeneous sections is using homogenised cycles, ideally by analysis of at least 10 cycles. Despite similar standard errors between the methods in this study, the risk of introducing systematic error through spot sampling is considered significant. It is also likely that the standard error of the homogenised cycle method is likely to decrease if more cycles are used. Whilst sample collection and preparation for the homogenised cycle method is marginally more laborious, it requires the same amount of ^{3}He measurements to be run 'per data point' as spot sampling (far fewer than calculating background flux 'by bed').

	spot samples (this study)	spot samples (from Farley et al., 2012)	**homogenised precession cycles**	'by bed' precession cycles
average bg flux and standard error	11.99±3.24 x 10^{-14} (ccSTP/cm^2/kyr)	6.69±2.37 x 10^{-14} (ccSTP/cm^2/kyr)	7.09±0.92 x 10^{-14} (ccSTP/cm^2/kyr)	6.63±0.53 x 10^{-14} (ccSTP/cm^2/kyr)
% error	27%	35%	13%	8%
n	16	6	3	3

Table 4.1: Background flux values through the sub-Bonarelli Level Scaglia Bianca and associated standard error, as calculated using three different methods using data from this study and Farley et al. (2012). The preferred method for calculating background flux in lithologically heterogeneous sections is using homogenised precession cycles (in bold).

Overall background flux over the Cenomanian-Turonian interval in these localities (required in order to create a $^{3}He_{ET}$ timescale over the Bonarelli Level in Chapter 5) is therefore calculated using homogenised cycles. All homogenised precession cycles were included in this calculation (the 'sub-Bonarelli Level only' background flux described above was used only for the purposes of comparing background flux calculation methods). Using precession cycles both above and below the interval of interest (in this case the Bonarelli Level) is more likely to capture the true variability in in the flux of incoming $^{3}He_{ET}$ over time. Using this method a background flux value of $1.14\pm0.38 \times 10^{-13}$ ccSTP/cm^2/kyr was calculated. It should be noted that the error on this background flux estimate ($1\sigma_x$) is ~33%, much higher than the ~8% errors from studies where background flux was determined from a largely homogeneous lithology (Farley and Eltgroth, 2003; Murphy et al., 2010). The large error on background flux will propagate through to sedimentation rate, making errors on background flux a significant consideration when choosing an appropriate section to apply $^{3}He_{ET}$ timescales. Although addressing questions of relative duration (e.g. the proportion of time taken within a precession cycle) will not be affected, questions of absolute duration can only be answered if an uncertainty of ~33% is acceptable.

Throughout the above discussion, suggestions have been made as to how the variation seen in measurements of background flux through the section might have been artificially increased, but it is possible that the fluctuations observed in background flux through time reflect a primary signal. As detailed in Section 2.1.3, Farley et al. (2012) carried out a study of the background flux through the Cretaceous, recording several 'spikes' where background $^{3}He_{ET}$ flux increases by close to an order of magnitude, interpreted as being time intervals associated with comet showers or asteroid collisions. None of these spikes occur during the time interval covered by this study but, even outside of intervals containing these 'spikes', fluctuation of background flux values on the order of ~30–70% (1σ) is a common feature of $^{3}He_{ET}$ records (Mukhopadhyay et al., 2001a, 2001b; Farley and Eltgroth, 2003; Murphy et al., 2010; Farley et al., 2012). Where three-point moving averages of flux values are used, the scatter on background flux values is smaller, but still significant at ~20–50%

(Mukhopadhyay et al., 2001a; Farley et al., 2012). If $^{3}He_{ET}$ background flux through the Cenomanian/Turonian varied on the scale recorded in this study and did so essentially randomly, these random fluctuations simply need to be accounted for in the size of the error. Stability of background flux over the interval of interest is something future studies must take into account when assessing the potential usefulness of $^{3}He_{ET}$ timescales to a particular problem. A large error due to background flux variation may simply be the 'cost of doing business' in the Cenomanian.

Precession cycle $^{3}He_{ET}$ timescales

Best-practice methods for calculating background flux used to construct $^{3}He_{ET}$ timescales on the order of ~100–1000 kyr are not necessarily the same as those needed to determine background flux when constructing $^{3}He_{ET}$ timescales over individual precession cycles. The methods of background flux determination described above deal with the calculation of an overall average background flux value encompassing the time spanned by the upper part of the sub-Bonarelli Level Scaglia Bianca, the Bonarelli Level, and the overlying uppermost Scaglia Bianca from an average of measurements taken at different depths (see Figures 4.3, 4.10). Over this period, background flux is expected to have fluctuated to some degree, as discussed above. Because precession cycles represent extremely short snapshots of time within this interval, an overall average value of background flux may not well represent the actual flux during a given snapshot. In this study, for example, the overall average background flux appropriate for study of the Bonarelli Level is rather higher than the background flux estimated in individual sub-Bonarelli Level precession cycles (Figure 4.10). With this in mind, when constructing $^{3}He_{ET}$ timescales over precession cycles in this study, a background flux value unique to each cycle is used, determined through the 'by bed' method (the background flux value used for each cycle corresponds to the appropriately coloured star in Figure 4.10a).

The 'by bed' calculation of background flux within each precession cycle was selected over calculation from a homogenised cycle as it is thought to be a slightly superior method (calculated background flux values from the same cycle at different localities are more similar when the 'by bed'

method is used than when calculated from homogenised precession cycles). Although calculating background flux 'by bed' was judged as prohibitively intensive to be recommended as a best practice method for future studies, in this case the required measurements had already been made.

It is worth reiterating that using this method to calculate background flux implicitly assumes that each precession cycle spans ~21 kyr, an assumption that impacts calculated sedimentation rates and durations within the constructed $^{3}He_{ET}$ timescales (with a knock-on effect on calculated organic-carbon mass accumulation rates and fluxes of terrestrial ^{4}He). If, for any reason, this estimate of the overall timespan of each cycle were to be inaccurate, the relative sedimentation rates within cycles would still stand, though the exact numbers would be incorrect.

4.5.2 $^{3}He_{ET}$ age models

Instantaneous sedimentation rates were calculated using Equation 4.1 for each bed within the studied precession cycles. Background flux values specific to each cycle were calculated using the 'by-bed' approach, as discussed above. Calculated linear sedimentation rate, organic-carbon mass-accumulation rate and terrestrial ^{4}He flux through the precession cycles are presented in Figure 4.11. $^{3}He_{ET}$ timescales were created over each precession cycle using these calculated sedimentation rates: time-scaled logs of the precession cycles are presented in Figure 4.12.

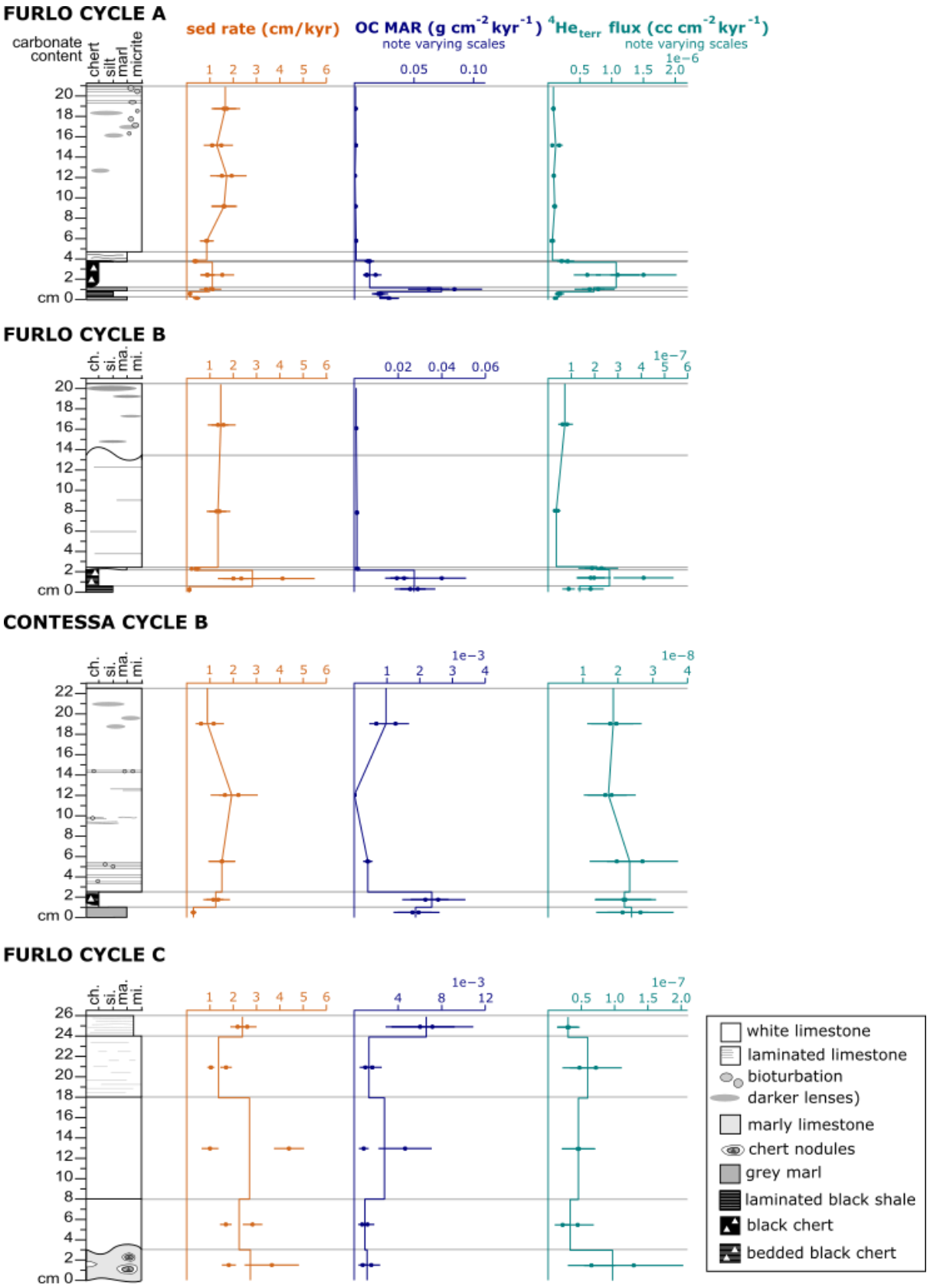

Figure 4.11: Linear sedimentation rate, organic-carbon mass-accumulation rate and flux of terrestrial ^{4}He through the studied precession cycles. Data points represent individual measurements, solid lines average values.

Sedimentation rates

Before any discussion of 'sedimentation rates' begins, it is worth making explicit that the linear sedimentation rates presented below relate to the rock in outcrop. 'Sedimentation rate' as discussed below is, therefore, a result not only of the rate of accumulation of sedimentary components in the Cenomanian Tethys, but also post-depositional compaction, along with any diagenetic effects, such as pressure solution, that act to increase or decrease the thickness of a bed. The diagenetic effects that may impact the interpretation of sedimentation rates derived from cherts (a diagenetic lithology in which these considerations are, perhaps, particularly important) are expanded on in Section 4.5.3 of the discussion. Despite this complexity, sedimentation rates remain a useful tool: particularly meaningful when comparing two beds of the same lithology which might be assumed to have similar diagenetic histories, but also allowing different lithologies to be contrasted.

Sub-Bonarelli black shales represent the periods of slowest deposition within the precession cycles, with sedimentation rates of 0.14±0.02 cm/kyr in Furlo Cycle A and 0.10±0.02 cm/kyr in Furlo Cycle B. Though there is no appreciable difference in the TOC content between the marl beneath the black chert of Contessa Cycle B and the limestones that underlie it, the sedimentation rate in the marl bed is considerably lower than the typical value of homogenous limestone (0.29±0.07 cm/kyr compared to 1.45±0.23 cm/kyr), confirming a pattern in Cycle B at both localities of a slower depositing bed (of black shale at Furlo and marl at Contessa) beneath the chert layers. Sedimentation rates in the black cherts of these cycles, 1.10±0.23 cm/kyr in Furlo Cycle A, 2.81±0.53 cm/kyr in Furlo Cycle B, and 1.25±0.32 cm/kyr in Contessa Cycle B, are notably faster than those in the underlying black shales or marl (the other 'black bed' lithologies). Significant differences in sedimentation rate are, by contrast, not observed across the laminated limestone (1.87±0.92 cm/kyr), homogenous limestone (1.15±0.21 cm/kyr) and grey chert (2.14±1.05 cm/kyr) of Furlo Cycle C.

Sedimentation rates do not appear to vary much through the homogenous limestone beds. This similarity may be because these beds were all deposited at a uniform rate. However, the effects of

bioturbation have almost certainly (re)homogenised this signal such that it is impossible to tell anything about inter-bed variability. Instead, the average sedimentation rate across the homogenous limestone beds is considered.

The average sedimentation rates of the limestones are very similar across the three cycles at both localities (1.33±0.19 cm/kyr, Furlo Cycle A; 1.27±0.27 cm/kyr, Furlo Cycle B; 1.23±0.24 cm/kyr Contessa Cycle B; 1.15±0.21 cm/kyr, Furlo Cycle C) and also rather similar to the average sedimentation rate for the whole cycle: 1.1 cm/kyr (from Batenburg et al., 2016). The similarity between sedimentation rates in limestones and overall sedimentation rates of cycles probably arises in part because limestones make up the bulk of the cycle by time.

Organic-carbon mass-accumulation rates

$^{3}He_{ET}$ helium timescales allow the calculation of organic-carbon mass-accumulation rates (OC MARs) for each lithology, presented in Figure 4.12. OC MARs in the limestones are similar across all four cycles, 0.0005–0.0016 g/cm^2/kyr, reflecting similar sedimentation rates and consistently low TOC. Peak organic-carbon mass-accumulation rates are, as expected, higher in cycles that contain more TOC-rich lithologies (Furlo Cycles A and B, see Figure 4.4).

Unsurprisingly, organic-carbon mass-accumulation rates peaked during the deposition of black cherts and shales; in the black cherts of Furlo Cycles A and B organic carbon accumulated at a rate of 0.013–0.027 g/cm^2/kyr, and in the black shales at a rate of 0.021–0.027 g/cm^2/kyr. OC MARs are lower in the black chert of Contessa Cycle B (~0.0024 g/cm^2/kyr), and its underlying marl (~0.0019 g/cm^2/kyr) than in the corresponding Furlo Cycle, reflecting the fact that overall organic-carbon content is lower at Contessa. Though black shales, where present, have a much high TOC% than the black cherts (Figure 4.4), their much slower sedimentation rate means that overall OC MARs are similar between the two lithologies.

Grey cherts do not appear to display such elevated OC MARs: the OC MAR measured in the grey chert of Furlo Cycle C (~0.0012 g/cm^2/kyr) is very similar to that measured in the limestones of this

cycle. The highest OC MAR recorded in these precession cycles (0.073±0.014 g/cm^2/kyr) is actually seen in a marl bed in Furlo Cycle A, which has both relatively high TOC% and a faster sedimentation rate than the underlying black shale.

Terrestrial ^{4}He flux

Evident in both Furlo Cycles A and B is a spike in the flux of terrestrially derived ^{4}He co-incident with chert occurrences(see Figure 4.11), with $^4He_{terr}$ flux reaching values of 1.07±0.22 ×10^{-6} cc/cm^2/kyr, and 2.63±0.53 ×10^{-7} cc/cm^2/kyr respectively. There was, however, no significant (i.e. outside of error) increase in $^4He_{terr}$ flux during the deposition of black shales. Although terrigenous material (i.e. clays) may be concentrated in black shale beds due to the absence of other (biogenic) sedimentary components, there is no evidence of a higher flux of terrestrially derived clay at this time. No particular spike in terrestrial ^{4}He flux is observed in Contessa Cycle B, which also saw a lower overall $^4He_{terr}$ flux.

Timings within precession cycles

Precession cycle logs plotted against time are presented in Figure 4.12. It is worth noting here that the calculation of time spanned by a bed is unaffected by differential compaction or diagenetic effects, allowing many of the complexities involved in the interpretation of 'sedimentation rate' (and its relationship to the contemporary 'at the sea floor' accumulation rate of sedimentary components) to be set aside. By time, 61–87% of these precession cycles are made up of homogenous limestone (Table 4.2), with an additional ~5% of Furlo Cycle C made up of 'laminated limestone'. Limestone was deposited over a notably smaller proportion of Furlo Cycles A and B than Furlo Cycle C, whilst the proportion of limestone by time in Contessa Cycle B falls between these two extremes.

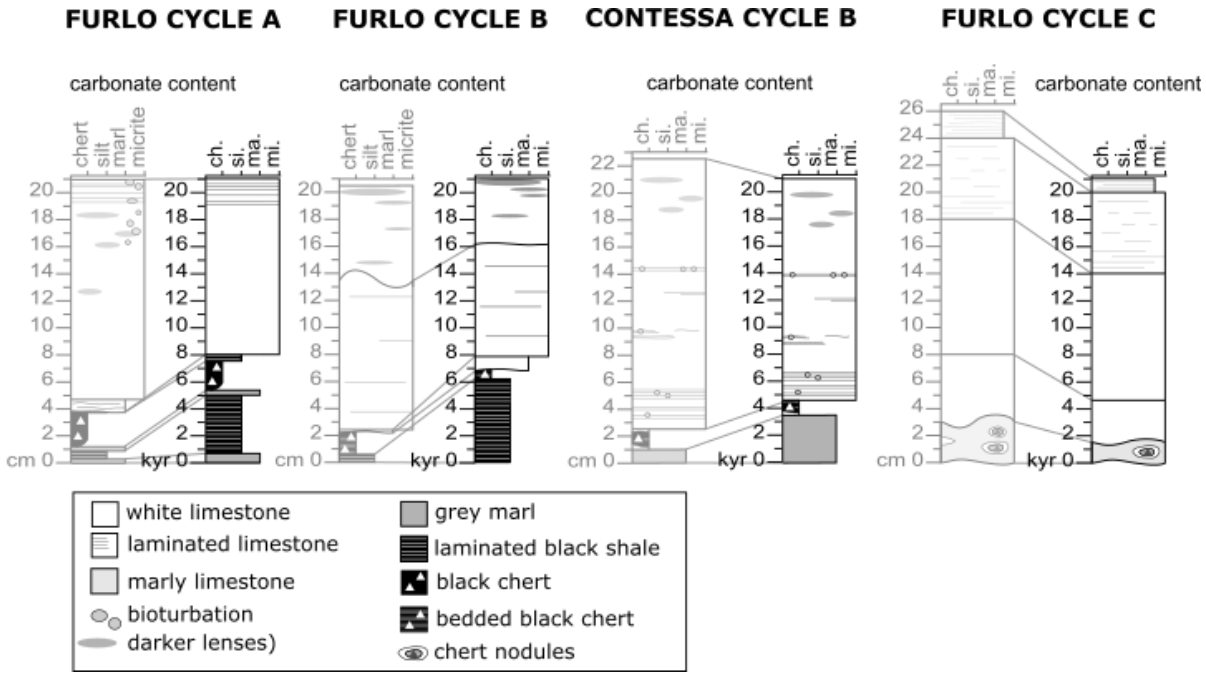

Figure 4.12: Precession cycle logs against time.

In cycles containing black shales, this lithology comprises ~25–29% of the precession cycle by time (Table 4.2). The slower depositing marl beneath the black chert in Contessa Cycle B comprises ~18% of the cycle by time, comparable to that accounted for by the black shales. Chert beds occupy between ~3–11% of the precession cycles by time (Table 4.2).

As Furlo and Contessa Cycles B were deposited at the same time, the proportion of time spanned by each lithology might be expected to be the same between cycles. As seen in Table 4.2, the time spanned by "homogenous" limestone is indeed within error between the two cycles, as is the time spanned by black shale (in Furlo) and marl (in Contessa). The time spanned by the black chert beds of the two cycles is, however, just outside error, with the black chert bed in Furlo apparently deposited over less time than the chert bed in Contessa.

	Furlo Cycle A	Furlo Cycle B	Contessa Cycle B	Furlo Cycle C
"homogenous" limestone	12.83±1.86 kyr	14.19±2.98 kyr	16.31±3.13 kyr	18.34±3.54 kyr
'laminated limestone'				1.08±0.33 kyr
marl below chert			3.84±1.08 kyr	
black shale below chert	5.22±1.35 kyr	6.18±1.98 kyr		
black shale above chert (Furlo Cycle A only)	0.55±0.22 kyr			
chert	2.40±0.73 kyr	0.63±0.19 kyr	1.21±0.37 kyr	1.58±0.49 kyr

Table 4.2: Proportion of time occupied by each lithology within the studied precession cycles, presented as time occupied within a 21 kyr precession cycle.

4.5.3 Orbitally forced changes in climate

Mechanisms of chert formation and their effects on a $^{3}He_{ET}$ timescale

In order to interpret $^{3}He_{ET}$ timescales through the precession cycles studied here it is first important to understand their potential limitations and ambiguities. This is particularly relevant when dealing with heterogeneous lithologies through a cycle, most especially when one of these is chert.

When considering 'sedimentation rates' and 'depositional durations' of chert beds in these cycles it is important to remember that chert is a diagenetic rather than primary sedimentary lithology. Figure 4.13 presents various mechanisms under which the interplay between diagenesis and changes in primary sedimentation could result in the stratigraphy observed in the Scaglia Bianca. These are discussed in more detail below.

It is possible for dissolved silica to move metres through host sediments to concentrate in cherts; nodular cherts in various pelagic settings are suggested to have formed from the nucleation of silica (at locations controlled by textural or redox changes) from siliceous fluids derived from a largely homogenous primary lithology of carbonate containing significant amount of siliceous material (radiolarians in this case), a scenario corresponding to Figure 4.13 A (Knauth, 1979; Bromley and Ekdale, 1986; Clayton, 1986; Hesse, 1989). The fact that Scaglia Bianca cherts occur cyclically means that there must be some regular and reoccurring (likely orbitally forced) process causing cherts to

form where they do. This process might be some textural aspect of the host sediment that promotes the nucleation of silica, the regular development of a stationary redox boundary, or a different primary lithology containing a higher concentration of biogenic silica.

That siliceous fluids have moved at least some distance through carbonate ooze in the Scaglia Bianca is evident from the cementation histories of the limestones immediately above cherts, which contain microfossils (both foraminifera and radiolarians) infilled with silica (Figure 4.7d). A higher proportion of radiolaria are observed in the limestones immediately above chert layers than in the limestone higher in the cycle, though it may be fair to assume that some deposition of radiolarians and other siliceous material occurred throughout the cycle, with siliceous tests simply not preserved in most limestone beds. However, it is most likely that the position of chert beds reflects a change in primary lithology, a conclusion reached by many as the chert beds are tabular and laterally continuous, and silicified foraminifera within the cherts indicate that they do not simply represent times of increased carbonate dissolution (Arthur and Premoli Silva, 1982; Mitchell et al., 2008; Batenburg et al., 2016; Gambacorta et al., 2016).

Abundant preserved 'ghost' radiolarians (see Figure 4.6e, f) suggest that if the chert and shale beds represent different primary lithologies; as illustrated in Figure 4.13 B, the proto-chert may have been a radiolarian sand. (Although Abrajevitch (2020) proposes a radically different depositional model, in which proto-chert beds were originally more Si-poor than proto-shales, most studies which consider chert beds to have formed from a distinct primary lithology follow Hesse (1988) in considering the proto-chert lithology to have been Si-rich (e.g. Hori et al., 1993).) The mechanism for the deposition of the putative radiolarian sands that preceded the formation of chert is still debated, and the sedimentation rates and duration of deposition of the chert beds may provide insight into whether these deposits were laid down under conditions of high *in-situ* biosiliceous productivity or through wash-in events of radiolaria from elsewhere (Gambacorta et al., 2014, 2016).

Even if chert beds are thought to represent a distinct primary lithology, it is necessary to keep the effects of diagenesis in mind when interpreting their $^{3}He_{ET}$ data. For example, early lithification of cherts could reduce compaction and so elevate linear sedimentation rate (cm/kyr) – the diagenesis of Scaglia Bianca cherts is thought to have occurred at an early stage of sedimentary compaction (Salmon et al., 2003). Whilst this may prevent the consideration of changes in the linear sedimentation rate of cherts as straightforwardly correlating with changes in flux of siliceous material to the sea floor, diagenesis should not, however, have had an effect on the overall amount of time spanned by chert beds, as chertification does not liberate extraterrestrial ^{3}He (see Section 3.3).

The time spanned by chert beds may provide insight into the nature of their deposition. Assuming that the limits of the chert beds roughly correspond to the limits of the 'original' radiolarian sands (scenario B in Figure 4.13), deposition of these beds took place over a period of between ~600–2400 years. Though geologically quite rapid, this span of time would seem to preclude the wash-in of a thick radiolarian sand in a single event, which would appear geologically instantaneous.

It does not, however, preclude the deposition of radiolarian sands through a series of wash-in events over a span of hundreds to thousands of years, perhaps overlying a slow background deposition of black shale. This interpretation is put forward by Gambacorta et al. (2014, 2016) for the 'bedded black cherts' commonly seen in the Umbria-Marche basin. Bedding in these cherts is visible by eye as an alternation of dark and light layers; under the microscope darker layers are revealed to be fine-grained interbeds of organic matter-rich and radiolarian-rich shale, interrupted by paler silt- to sand-sized radiolarian beds with sharp tops and erosional bases which are thought to be winnowed/redeposited (Gambacorta et al., 2014).

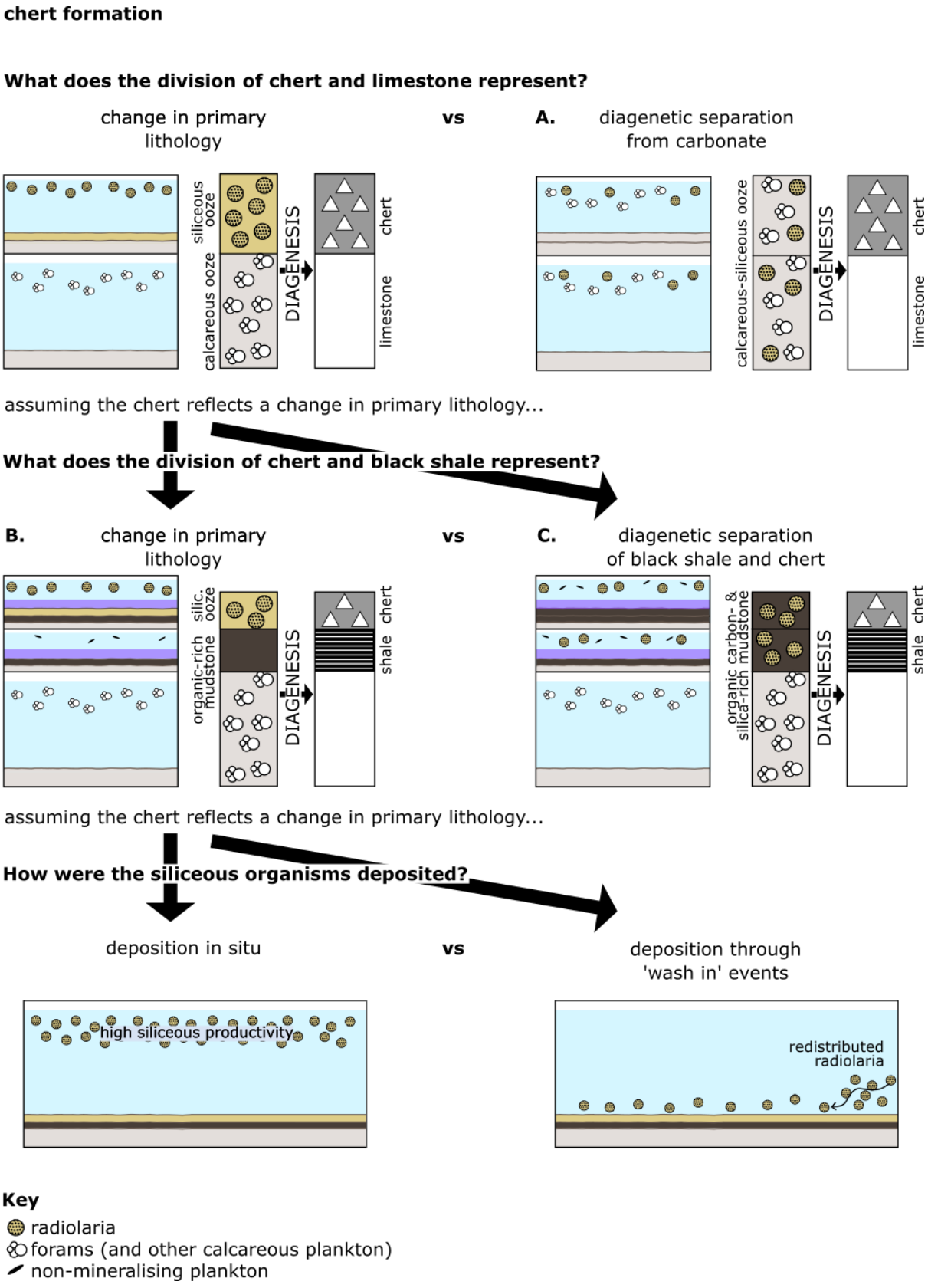

Figure 4.13: Summary of postulated methods of chert formation in the Scaglia Bianca.

A key question, therefore, is whether redistribution of radiolaria was accompanied by redistribution of $^{3}He_{ET}$-bearing particles. If $^{3}He_{ET}$-bearing particles are redistributed, then measured $^{3}He_{ET}$ concentration in these redistributed beds would no longer correlate with the duration of their deposition. The different times spanned by chert beds from the same cycle in Furlo and Contessa (Cycle B: 0.63±0.19 kyr and 1.21±0.37 kyr at Furlo and Contessa, respectively) may indicate that some redeposition of He_{ET}-bearing material did occur, even if this redeposition was minor on the scale of the whole precession cycles. If radiolaria and the He_{ET}-bearing particles were remobilised and redeposited together, the addition of this material to a site would effectively have increased the apparent time spanned by a chert bed. This would not necessarily have been consistent from cycle to cycle, or from site to site depending on the local oceanographic conditions at the time. Mobilisation and removal of He_{ET}-bearing material from a site would correspondingly have resulted in a decrease in the apparent 'time taken'. This means that the apparent time spanned by chert beds should be treated with some caution; time could potentially have been 'imported' from somewhere else or 'exported' away.

If, on the other hand, radiolaria were redistributed within the basin without significant redistribution of He_{ET} bearing particles, a 'wash in' or accumulation in one place might inflate the apparent sedimentation rate, but $^{3}He_{ET}$ timescales would still be useful in interpreting climatic conditions at the time. One would, for instance be able to say that, over the time interval spanned by the chert, 'blooms' of radiolaria occurred somewhere in the basin, even if their skeletal remains were subsequently redeposited.

The hydrographic properties of radiolaria make them more likely to be redistributed than He_{ET}-bearing particles. Redistribution of radiolaria is suggested to occur both during their production in the surface water and post-depositionally, their transport made easier by their relatively low-density, high-surface area structure (Gambacorta et al., 2014). By contrast, as most $^{3}He_{ET}$-bearing particles are in the 1–10 μm size fraction (Brook et al., 2009; McGee et al., 2010; Torfstein, 2012),

thanks to the process of flocculation they are likely to be both deposited as larger aggregates and be more difficult to remobilise once deposited, making them less prone to redistribution (Curran et al., 2004; McCave and Hall, 2006). Extraterrestrial ^{3}He is also suspected to be hosted in magnetite, or an associated phase, so $^{3}He_{ET}$-bearing particles are also likely to have a relatively high density compared to radiolaria (Mukhopadhyay and Farley, 2006). In a study of Quaternary sediments in the North Atlantic McGee et al. (2010) found that even in settings with extreme sediment redistribution, $^{3}He_{ET}$-based sedimentation rates were minimally affected, which they ascribed to the cohesive behaviour of the fine He_{ET}-bearing particles. The idea that redistribution of radiolaria as suggested by Gambacorta et al. (2014, 2016) can co-exist with an undisturbed $^{3}He_{ET}$ timescale through chert beds is therefore not unreasonable.

In fact, when the Furlo and Contessa sections are compared over the span of a precession cycle (as opposed to comparison of just one chert bed), no significant redistribution of He_{ET}-bearing particles across the basin is observed. The background flux values determined from precession cycles 'by-bed' (summarised in Figure 4.3) of Cycle B at Furlo and Contessa are very similar (see Figure 4.10). If there were significant redistribution of He_{ET}-bearing particles across the basin these values would be expected to be different, as import of $^{3}He_{ET}$-bearing material would effectively increase the apparent background flux, and *vice versa*.

Differences in observed chert bed durations between different sites might have arisen without redistribution of $^{3}He_{ET}$-bearing particles if the chert-shale distinction within carbonate-poor beds were a result of diagenetic separation (see Figure 4.13 C). This process has been suggested to result in chert/shale or chert/marl 'couplets' in various sequences globally, including the Scaglia Bianca and Scaglia Rossa (Murray et al., 1992; Salmon et al., 2003; Trabucho-Alexandre et al., 2011; Abrajevitch, 2020), and has been suggested as an explanation for the varied TOC content measured in black shales of the same stratigraphic level (see Jenkyns et al., 2007; Owens et al., 2016; this study). As a general rule, black chert beds in the upper part of the Scaglia Bianca in both Furlo and Contessa are

preceded by ~1cm of a slowly deposited lithology, a black shale or a marl, respectively (Figure 4.4), but some cycles deviate slightly from this pattern: Furlo Cycle A, for example, contains a thin black shale layer above the bed of black chert, whilst other Furlo precession cycles contain thicker black chert beds but no associated black shales (see Scaglia Bianca log, Figure 4.1). These 'unusual' cycles may reflect an overprint of varying degrees of diagenetic separation affecting the patterns of lithology.

The discussion above regarding differing time intervals spanned by cherts hinges on the assumption that the limits of the chert beds roughly correspond to the limits of the original radiolarian sands. Diagenetic re-organisation of silica within 'black beds' would make this assumption invalid, thus making it impossible to distinguish between the two proposed methods by which high volumes of siliceous organisms were deposited using $^{3}He_{ET}$ timescales. It is worth noting at this point that the differing sedimentation rates measured in cherts and black shales are not necessarily incompatible with the process of diagenetic separation from the same original primary lithology with a relatively constant accumulation rate. Though no extraterrestrial helium is liberated during chert formation, early diagenesis and hence reduced compaction of cherts could inflate the measured sedimentation rate, even if calculations of duration are unaffected by the process.

Distinguishing between primary lithological change and diagenetic unmixing as the mechanisms for the formation of Scaglia Bianca black cherts and black shales (B and C on Figure 4.13) is very difficult with the existing data. Black shales underlying black cherts are, like the cherts themselves, radiolarian-rich (see Figures 4.6d, 4.7a, b). Other compositional differences between black shales and black cherts might reflect primary lithological change, but could also be explained by the effects of diagenesis. For instance, although black cherts contain markedly less organic matter than the underlying black shales this may be due to oxidative destruction during diagenesis (Salmon et al., 2003). Additionally, the lack of foram microfossils in chert beds (see Figure 4.7a, b) might be explained by replacement of carbonate during chertification (Knauth, 1994), though the 'ghosts' of

forams have frequently been recorded alongside those of radiolaria in cherts from other formations (e.g. Heath and Moberly, 1971; von der Borch et al., 1971), perhaps lending significance to their absence in the Scaglia Bianca cherts.

However, the ~0.5 mm 'transitional band' observed between the black shale and black chert (Figure 4.7a, b), does not appear to be a compositional intermediary between the over- and underlying lithologies. It contains markedly less organic matter than the underlying black shale and, crucially, than the overlying black chert. The 'transitional band' also contains a lower concentration of microfossils than both over- and underlying lithologies (though does contain some radiolarians). These observations, especially the lower concentration of organic matter in the 'transitional band' compared to the black chert, suggest that this layer reflects a change in primary lithology; the primary lithology of the 'transitional band' is likely to have been primarily fine-grained carbonate, which was partially replaced by silica. A layer with compositionally distinct primary lithology between black shale and black chert beds implies that the difference between the shale and chert beds themselves reflects a primary lithological change.

In conclusion, neither primary lithological change nor diagenetic unmixing can be entirely ruled out to explain the position of the chert layers which may, indeed, be partly a result of both. In the further discussion below, the evidence from this study is considered with regard to both possible scenarios. The change in lithology within a cycle from limestone to chert likely reflects a change in oceanographic conditions at the time to those favouring siliceous production and preservation; the effect of diagenetic unmixing may or may not be significant in the distinction between black chert and black shale beds. The complex interplay of deposition, redistribution and diagenesis within these beds hampers the straightforward interpretation of $^{3}He_{ET}$-derived sedimentation rates and timescales. Redistribution of $^{3}He_{ET}$-bearing material during radiolaria 'wash-in' events can increase or decrease the apparent time represented by chert beds, whilst early diagenesis and reduced compaction of cherts (compared to, for example, increased compaction of mudrocks) is likely to

increase apparent linear sedimentation rates, and silicification may extend beyond the bounds of the radiolarian-rich 'proto-lithology' to encompass the surrounding shales. The extent to which any of these processes may be acting within an individual chert bed cannot be quantified exactly.

Despite these limitations, caveated conclusions can be reached. The interval of elevated silica deposition was short: if the limits of chert beds correspond to the limits of an original proto-lithology (Figure 4.13 B) deposition typically lasted only a few kyr, and enough siliceous material was deposited to significantly increase the sedimentation rate compared to underlying black shales or marls. If diagenetic separation alone controlled the distinction between cherts and shales, 'black beds' must be considered as a whole unit. In Furlo Cycle A these 'black beds' were deposited over 8.03±1.54 kyr, with an average sedimentation rate of 0.49±0.09 cm/kyr. In Furlo Cycle B these values are 6.81±1.89 kyr and 0.37±0.11 cm/kyr, whilst, if the grey marl that underlies the black chert of Contessa Cycle B is included as a 'black bed', in Contessa Cycle B 'black beds' span 4.69±1.14 kyr with an average sedimentation rate of 0.53±0.13 cm/kyr. Taken as a whole, 'black beds' accumulated more slowly than limestones (which have an average accumulation rate of ~1.2 cm/kyr).

Organic-carbon accumulation and primary productivity

Accompanying the enhanced silica deposition during formation of the sub-Bonarelli black beds was an increase in organic-carbon mass-accumulation rate, which spikes in the black shales and cherts. This elevated accumulation rate indicates that the TOC enrichment of these beds was controlled by factors other than organic-matter dilution by carbonate. Enhanced preservation under dysoxic conditions was likely to have played a role, as also was an increase in primary productivity.

The degree of productivity in the Cretaceous oceans during the deposition of black shales has been debated (see Section 2.3.1). Broadly speaking, opinion is divided as to whether the organic-carbon enrichment represents only enhanced preservation, or whether primary productivity was also higher, with differing climate mechanisms therefore suggested as driving the change between

carbonate and black shale and cherts (de Boer, 1982, 1991; Herbert and Fischer, 1986; Premoli Silva et al., 1989; Mitchell et al., 2008; Batenburg et al., 2016; Gambacorta et al., 2016).

Estimates of primary productivity through the precession cycles studied here would help shed light on this debate. Organic-carbon mass-accumulation rates calculated in the black shales of Furlo Cycles A and B are high, ~0.025 g/cm^2/kyr, at the very upper limit of the OC MARs estimated in the TOC-rich shales of the underlying Marne al Fucoidi (0.0055 – 0.022 g/cm^2/kyr; Herbert et al., 1986; Pratt and King, 1986). (These higher values may be largely due to differences in calculated sedimentation rate: Al_2O_3 concentration is used as a proxy for sedimentation rate in the Marne al Fucoidi (Herbert et al., 1986; Pratt and King, 1986), assuming that clay input is constant throughout; given that deposition of black shales may be coincident with times of increased input of terrigenous material (see following section) this may not be a reasonable assumption.) However, estimating primary productivity from calculated OC mass-accumulation rates is difficult as the degree of organic-carbon preservation is unknown and is sensitive to multiple factors including changes in redox conditions, type of organic matter deposited and background sedimentation rate (Canfield, 1994).

Previous estimates of primary productivity associated with Cretaceous black shales, including in the Umbria–Marche Basin, have used organic-carbon preservation factors of ~2% of gross primary production (Bralower and Thierstein, 1984; Pratt and King, 1986). This value was derived from the organic-carbon preservation factors from Holocene sediments in the Black Sea, used as an analogue for Cretaceous black shales, in which the burial of ~3% of the organic carbon from primary production has been calculated – a further 20–30% of the preserved organic carbon is then assumed to be lost during diagenesis in the anoxic sediment column below the uppermost transitional layer (Berner, 1982; Bralower and Thierstein, 1984). In the context of the Scaglia Bianca, organic-carbon preservation factors are expected to differ across the varying lithologies as they would have been controlled by both bulk accumulation rate and bottom-water redox conditions (Müller and Suess,

1979; Bralower and Thierstein, 1987; Canfield, 1994; Aller, 2014). Consequently, the use of the Black Sea analogue for all lithologies may be too simplistic and a more refined approach, considering a range of analogues, might be more appropriate.

Various studies have collated modern measurements of primary productivity, sedimentation rate and C_{org} preservation factor across different marine settings, providing a range of analogues for use in estimating palaeo-productivity from measured OC MARs. However, differing estimates of C_{org} preservation derived from different modern datasets may impact the rates of productivity calculated and thus the interpretations drawn. Organic-carbon productivity estimates derived from two such datasets (collected in Bralower and Thierstein (1984, 1987) and Aller (2014)) are presented in Table 4.3.

The first set of organic-carbon productivity estimates, 'Bralower and Thierstein, 1984; 1987' in Table 4.3, uses the same source collection of C_{org} preservation factors across various marine sedimentary settings as previous work on Umbria–Marche black shales (Pratt and King, 1986). As mentioned above, Pratt and King (1986) use a 2% preservational factor for Umbria–Marche black shales, derived from measurements of C_{org} preservation factor in Holocene sediments in the Black Sea by Bralower and Thierstein (1984, 1987). Therefore, in order to estimate organic-carbon preservation factors for other Scaglia Bianca lithologies (limestones and cherts) consistent with this value, conditions under which these lithologies were deposited were considered analogous to Holocene settings investigated by Bralower and Thierstein (1984, 1987) with similar bulk sediment accumulation rates. On the basis of comparable bulk accumulation rates, the Canary Basin is used as an analogue from this Holocene dataset for Scaglia Bianca limestones and grey cherts, whilst preservation of organic carbon in TOC-rich black cherts may be more analogous to that in Black Sea (Bralower and Thierstein, 1984, 1987). The organic-carbon preservation factors measured in these settings were then reduced by 30% to account for diagenetic organic-carbon loss, and estimates of primary productivity were calculated for different lithologies. By the choice of Holocene analogues with oxic and anoxic sediments

respectively, the estimated organic carbon preservation factors for limestone and grey chert assume deposition under oxic conditions, whilst the OC preservation factor for black chert assumes deposition under dysoxic conditions. The estimates of palaeo-productivity derived in this way imply slightly higher palaeo-productivity in black shales, 12±2 $gC/m^2/yr$, than in limestones, 6±1 $gC/m^2/yr$, where errors derive from errors in calculated OC MAR (much larger, but unquantifiable, errors are expected to originate from the estimate of organic carbon preservation factor).

The second set of organic-carbon productivity estimates, 'Blair and Aller, 2012; Aller, 2014' in Table 4.3, was calculated using a more recent dataset for the relationship between accumulation rate and the percentage of export organic carbon preserved under oxic and dysoxic conditions (Blair and Aller, 2012; Aller, 2014) and indicates a somewhat larger difference in productivity between black shales and limestones in the Scaglia Bianca. Using average bulk mass-accumulation rates, appropriate organic-carbon preservation factors were determined for various lithologies in Furlo Scaglia Bianca precession cycles, assuming that the bioturbated limestones were deposited under normal marine conditions and largely unbioturbated black shales and black cherts under O_2-depleted conditions (see Figure 4.14), with a further 30% reduction applied to account for later diagenetic organic-carbon loss (following Berner, 1982; Bralower and Thierstein, 1984; Pratt and King, 1986). This methodology allows the estimation of export carbon for each lithology, which was converted into primary productivity using the relationship of Eppley and Peterson (1979) expressed in Equation 4.6 – where total primary productivity <200 $gC/m^2/yr$:

$$\text{primary productivity} = (\text{export productivity}/0.0025)^{0.5}$$

Equation 4.6

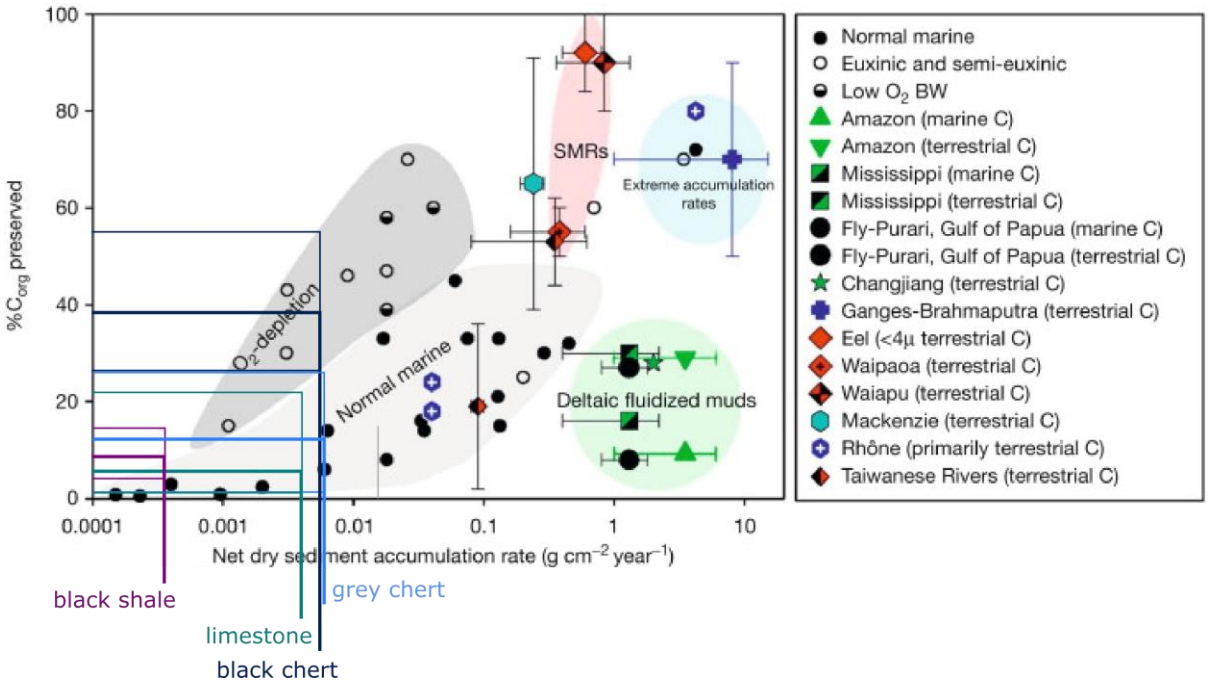

Figure 4.14: The percentage of C_{org} deposited on the seafloor that is then preserved varies with the bulk mass accumulation rate of the sediment depending on the environment of deposition (figure taken from Aller (2014), data from Henrichs and Reeburgh, 1987; Canfield, 1994; Aller, 1998; Blair et al., 2003, 2010; Goñi et al., 2005; Kao et al., 2006; Galy et al., 2007; Aller et al., 2008; Huh et al., 2009; Thompson, 2009; Pastor et al., 2011a, 2011b). C_{org} preservation factors for lithologies from Furlo Scaglia Bianca precession cycles are estimated (thick coloured bars), along with estimates of upper and lower bounds (thin coloured bars).

Even accounting for the spread of organic-carbon preservation factors associated with a given bulk MAR, there is a clear difference in primary productivity between limestones and grey cherts (6–26 $gC/m^2/yr$, and 5–26 $gC/m^2/yr$ respectively), black shales (30–59 $gC/m^2/yr$), and, to a lesser extent, black cherts (15–27 $gC/m^2/yr$), as presented in Table 4.3. There is, therefore, clear evidence of a change in primary productivity between lithologies. However, since all these productivity estimates fall within the range of expected values for 'low productivity regions' in modern oceans (Eppley and Peterson, 1979; Demaison and Moore, 1980; Falkowski et al., 1998), it is more appropriate to describe the primary productivity during black shale deposition as 'higher' rather than 'high'.

Accompanying the shift in primary productivity recorded in black shale beds is a change in the characteristics of the preserved organic matter (as seen in changes in measured Hydrogen and Oxygen Indices). High Hydrogen Index (HI) values are observed in the black shales (and one black chert), whilst limestones typically have low HI and high Oxygen Index (OI) values (Figure 4.8). This trend is, however, likely to be entirely preservational: better preservation of high-HI organic matter is typically correlated with the total organic-carbon content of sediments (Hartman-Stroup, 1987; Bouloubassi et al., 1999), and it is in the high-TOC black shales that high HI values are observed. Lower HI values in black cherts relative to black shales are thought to reflect oxidative destruction of amorphous kerogen during chert diagenesis (Salmon et al., 2003). The uniformly lower HI values observed in Contessa Cycle B are interpreted as evidence that organic matter is more degraded in this section.

			Bralower and Thierstein, 1984; 1987				
Lithology	Avg. OC MAR ($gC/cm^2/kyr$)		Preserved OC/ primary productivity %	after 30% diagenetic loss		Avg. primary productivity estimate ($gC/m^2/yr$)	
black shale	0.0242		-	2%		12	
black chert	0.0201		5%	3.5%		6	
limestone	0.0012		0.3%	0.2%		6	
grey chert	0.0012		0.3%	0.2%		6	
			Blair and Aller, 2012; Aller, 2014				
			Preserved OC/ export OC %	after 30% diagenetic loss	Export OC ($gC/m^2/yr$)	Avg. primary productivity estimate ($gC/m^2/yr$)	Primary productivity range ($gC/m^2/yr$)
black shale			9%	6%	3.84	39	30–59
black chert			39%	27%	0.76	17	15–27
limestone			6%	4%	0.28	10	6–26
grey chert			12%	8%	0.14	7	5–26

Table 4.3: Estimated primary productivity from Furlo precession cycles calculated using two different collations of modern measurements of primary productivity, sedimentation rate and C_{org} preservation factor across different marine settings (Bralower and Thierstein, 1984, 1987 and Blair and Aller, 2012; Aller, 2014). Primary productivity is calculated from export carbon using the relationship of Eppley and Peterson (1979). The primary productivity range is derived from the range in possible C_{org} preservation factor from the broad fields of Aller (2014).

There is a slim possibility that the high HI values observed in black shales and cherts reflect some variation in the source of organic matter during the deposition of these beds. An elevated input of marine organic matter associated with brief periods of stimulated productivity was proposed in certain black shales from the Marne al Fucoidi (a rhythmically bedded limestone and organic-rich shale unit of Aptian-Albian age, lower in the stratigraphy of the Umbria–Marche Basin); Marne al Fuciodi shales had similar HI and OI values to shales of the Scaglia Bianca, and also contained a greater proportion of marine biomarkers than the surrounding limestone. Palynological evidence of freshwater algae has also been found in some organic carbon-rich Marne al Fucoidi shales (Fiet, 1998), though the Scaglia Bianca is both a deeper water and more distal unit, so transport of freshwater algae is perhaps more unlikely to this setting. The organic matter in Scaglia Bianca black shales and cherts is dominated by 'amorphous particles' formed by the condensation of more labile organic compounds of marine origin, with a contribution from woody debris and pollen and spore microfossils (Salmon et al., 2000; 2003). However, without information on the biomarker or palynological records of Scaglia Bianca limestones, the HI/OI values of the Scaglia Bianca black shales alone are not sufficient evidence to confirm a change in the type of organic matter through precession cycles.

In conclusion, estimated primary productivity suggests that, within precession cycles, black shales and cherts were deposited under conditions of enhanced organic-carbon productivity. Such conditions likely contributed, along with dysoxic seafloor conditions, to the relatively higher organic-carbon mass-accumulation rates recorded in these lithologies. The question of whether this increased productivity was accompanied by a shift in the type of organic matter being deposited cannot be answered with the data from this study: the differences in HI and OI values between lithologies is likely a preservational trend. Low estimated primary productivity in grey cherts suggests that, in precession cycles containing grey rather than black cherts (interpreted as occurring at eccentricity minima), conditions conducive to higher productivity did not develop.

Terrestrial input – variations in the flux of terrestrial ^4He

The variation in terrestrial helium flux through precession cycles provides further evidence of changing palaeoenvironmental conditions. In Furlo Cycles A and B the flux of $^4He_{terr}$ (the terrestrial ^4He fraction) increases by around an order of magnitude over the period of chert deposition (Figure 4.9), apparent evidence of a transient increase in terrestrial input during the deposition of cherts. At the very least this observation indicates a change in patterns of terrestrial weathering, as it is possible that some of the observed increase in $^4He_{terr}$ flux may be due to a change in the source region of terrigenous material rather than the overall terrigenous input flux: weathering of different source rocks containing higher concentrations of ^4He would appear similar to an increase in flux of terrigenous material in a $^4He_{terr}$ flux record. A change in the provenance of clay minerals between limestones and cherts has, for instance, been observed in the Scaglia Rossa (which stratigraphically overlies the Scaglia Bianca but is lithologically similar), interpreted as a result of orbitally forced changes in climate and terrestrial weathering (Trabucho-Alexandre et al., 2011).

Under the 'monsoonal' model, cherts are thought to have been deposited at times of increased fertility corresponding to a strong monsoon (Mitchell et al., 2008; Batenburg et al., 2016; Gambacorta et al., 2016; Gambacorta et al., 2019). Evidence of elevated $^4He_{terr}$ in black chert beds suggests that an increase in nutrients (which acted to drive increased silica productivity) coincided with an increase in the flux of $^4He_{terr}$. This co-incidence may be suggestive of a terrestrial source for nutrients at this time, as well as suggesting that the increase in $^4He_{terr}$ flux is, at least in part, due to an increase in terrigenous input. ($^4He_{terr}$ flux is, however, far from a 'smoking gun' proxy for terrigenous input, let alone input of terrestrially-sourced nutrients; even if nutrients were terrestrially sourced, the delivery mechanism of nutrients and $^4He_{terr}$ to the oceans may have been quite different, as discussed below.)

In contrast to the Furlo cycles, no increase in $^4He_{terr}$ flux during black chert deposition is seen in Contessa Cycle B. Although the lower sedimentation rate of the Contessa B chert may have

influenced this low flux value, as $^4He_{terr}$ flux is calculated by multiplying $^4He_{terr}$ concentration and sedimentation rate, the $^4He_{terr}$ concentration in the Contessa B chert is also notably lower than in the chert of Furlo Cycle B.

$^4He_{terr}$ flux measured in limestones is fairly consistent across all three Furlo cycles (~5–9×10^{-8} cc/cm^2/kyr), with slightly lower values measured in Contessa limestones (~2×10^{-8} cc/cm^2/kyr). The fact that a 'spike' in $^4He_{terr}$ flux during black chert deposition (up to 3–11×10^{-7} cc/cm^2/kyr) is seen only in Furlo may indicate that there is some palaeogeographic control on this terrestrial input signal (a difference in the palaeogeography of the two sites has, for example, been invoked by Gambacorta et al. (2016) to explain the presence of black shales at Furlo but not Contessa) although Furlo and Contessa are separated today by only ~40 km, a small distance over which to expect significant palaeogeographic change within the Umbria–Marche Basin. (Although it is, of course, likely that the two sites were further apart prior to Apennine folding.)

One potential delivery mechanism for terrigenous ^{4}He-bearing material is aeolian transport. Aeolian transport of terrigenous material has, in fact, been suggested as the mechanism for nutrient delivery to the oceans during the deposition of proto-black cherts in the Scaglia Bianca (Gambacorta et al., 2019), and strengthened winds have been interpreted during intervals of black shale deposition in the Marne al Fucoidi (stratigraphically below the Scaglia Bianca), in which aeolian deposition of terrestrial organic matter is thought to have been important (Pratt and King, 1986; Tiraboschi et al., 2009).

Alternatively, the main control on the delivery of ^{4}He-bearing material may be fluvial input, perhaps as a result of increased terrestrial run-off accompanying an intensification of the hydrological cycle. Overall, limited contribution of fluvial input to the Umbria-Marche during the Cenomanian time has been suggested, with only a few or ephemeral rivers on the Tethyan margin and the shielding of the deeper basin by carbonate platforms (Bernoulli and Jenkyns, 1974). It has been suggested by Gambacorta et al. (2016) that the Furlo site may have been more proximal than other sites in the

Umbria–Marche Basin to a sediment plume emanating from a 'deltaic system'; however, the Cenomanian palaeogeography is not known in nearly enough detail to assess this conjecture. For more terrigenous clastic material with a terrestrial ^{4}He signature to have reached Furlo in times of an intensified hydrological cycle, whilst not reaching Contessa, would require a peculiar quirk of geography – if not a 'deltaic system' *per se*, perhaps association with the distal extent of a sediment plume emanating from a point of fluvial input. When considering the relationship between $^{4}He_{terr}$ flux records and fluvial processes of terrestrially-sourced nutrient delivery it should also be noted that, whilst $^{4}He_{terr}$ is hosted in sediment (Takayanagi and Ozima, 1987; Farley, 2001; Torfstein, 2012), nutrients which control ocean fertility, such as silica and phosphorus, are likely to be dissolved when delivered fluvially (Delaney, 1998; Tyrrell, 1999; Tréguer and De La Rocha, 2013).

Given the palaeogeographic context, the marked difference in the magnitude of $^{4}He_{terr}$ flux spikes in black cherts between Contessa and Furlo is surprising. This degree of heterogeneity in two neighbouring sites would not be expected in a signal governed by aeolian transport, but, equally, strong fluvial influence in the dominantly pelagic setting of the Scaglia Bianca is thought to be unlikely. The differing $^{4}He_{terr}$ flux records, and presence/absence of black shales between Furlo and Contessa suggests, at the very least, that the two sections derive from different sub-basins, with water masses that were not exactly the same over the Scaglia Bianca's deposition.

Palaeoenvironmental thresholds – a model for understanding the observed sedimentary changes

The palaeoenvironmental conclusions discussed above, when integrated with the high-resolution $^{3}He_{ET}$ timescale, provide insight into the nature of the drivers of these precession cycles. Of particular interest is how the time encoded in each facies changed with the 'strength' of orbital forcing.

One framework put forward to explain the pattern of chert and limestone deposition through the Scaglia Bianca utilises the concept of palaeoenvironmental 'thresholds' (Batenburg et al., 2016). Under this model (summarised in Figure 4.15), black shales and cherts developed during extremes of

the precession cycle, at times where the local palaeoceanographic system has passed some kind of threshold into a different depositional regime. This 'threshold' may have been an increase in nutrient availability, under which conditions the largely k-strategist calcareous plankton that dominated the 'limestone world' were overwhelmed and replaced by r-strategist non-mineralising phytoplankton which dominated under mesotrophic to eutrophic conditions (Margalef, 1978; Premoli Silva et al., 1999; Leckie et al., 2002; Erba, 2004; Erba and Tremolada, 2004). An increase in primary productivity associated with this change would likely have resulted in an increase in zootrophic radiolaria (as proposed by e.g. Gebhardt et al., 2010). Although results from this study indicate a clear increase in the estimated primary productivity in sub-Bonarelli black shales compared to limestones (whether or not a modest increase in the primary productivity of black cherts compared to limestones is seen depends on the method used to calculate said productivity), in absolute terms primary productivity appears to have remained relatively low throughout (see above). Conditions above the proposed palaeoenvironmental threshold have been described as 'eutrophic' (Mitchell et al., 2008), though in light of the moderate primary productivity estimates it may be more appropriate to describe the trophic level and primary productivity above the threshold as 'higher' rather than 'high'; above the threshold the system is described simply as 'nutrient world'.

A summary of suggested processes that drove the local palaeoenvironment over this threshold, and their proposed relationship to insolation forcing, are presented in Figure 4.15. In brief, the trigger condition for 'nutrient world' is thought to be intensification of the hydrological cycle, leading to increased influx of nutrients to the oceans. During 'black cycles', deposited at eccentricity maxima, 'monsoonal conditions' are suggested to have developed, where an intensified hydrological cycle and increased run-off led to freshwater stratification and the development of anoxic conditions (Fiet, 1998; Mitchell et al., 2008; Tiraboschi et al., 2009; Batenburg et al., 2016). In addition, 'black cycles' display the development of greater organic-carbon productivity. Evidence for this proposed intensification of the hydrological cycle, increased influx of nutrients, and increase in primary productivity are discussed more fully in the sections above.

$^{3}He_{ET}$ timescales allow aspects of this threshold model to be tested as the time spent in the development of each facies within a precession cycle can be calculated. Under the threshold model, the palaeoceanographic system would be expected to stay in 'nutrient world' for longer during eccentricity maxima (i.e. Cycles A and B), as the intensity of precession forcing would be above the proposed 'threshold' for a longer period of time. Conversely, at times of eccentricity minima (i.e. Cycle C), the system might be expected to spend longer under a regime promoting limestone deposition.

First, the pattern of limestone deposition is examined with respect to the proposed 'threshold model'. In agreement with this 'threshold' framework, limestone was indeed deposited over a noticeably longer period in Cycle C: ~19 kyr, than in Cycles A and B: 13–14 kyr (Table 4.2). This finding does depend in part, however, on how the laminated limestone lithology that precedes the chert in Furlo Cycle C is interpreted. Under the threshold model, this Furlo Cycle C laminated limestone was presumably deposited just below or at the threshold prior to the entrance into 'nutrient world', so it might also be expected to have formed prior to (i.e. stratigraphically below) the black shales (or equivalent) in Cycles A and B. Though present as a distinct bed in Furlo Cycle C, a laminated limestone facies is not as obviously separable in Furlo Cycles A and B (Figure 4.4); however, it is highly plausible that the lack of a distinct bed boundary is a result of the 'smearing' and homogenising effect of bioturbation. Visually, the limestone below the black shale beds in Furlo Cycles A and B does tend to be more mottled and contain more micritic laminae, although TOC does not increase to the values observed in Cycle C's laminated limestone (Figure 4.4). Given the clear homogenising effect that bioturbation has had throughout the formation of the Scaglia Bianca limestones, it seems reasonable to assume that the 'laminated limestone' facies identified in Cycle C was also present in Furlo Cycles A and B at the top of what is now identified as 'homogenous limestone'; for this reason the sum of the duration of 'laminated' and 'homogenous' limestones in Cycle C was taken as the value of total limestone duration.

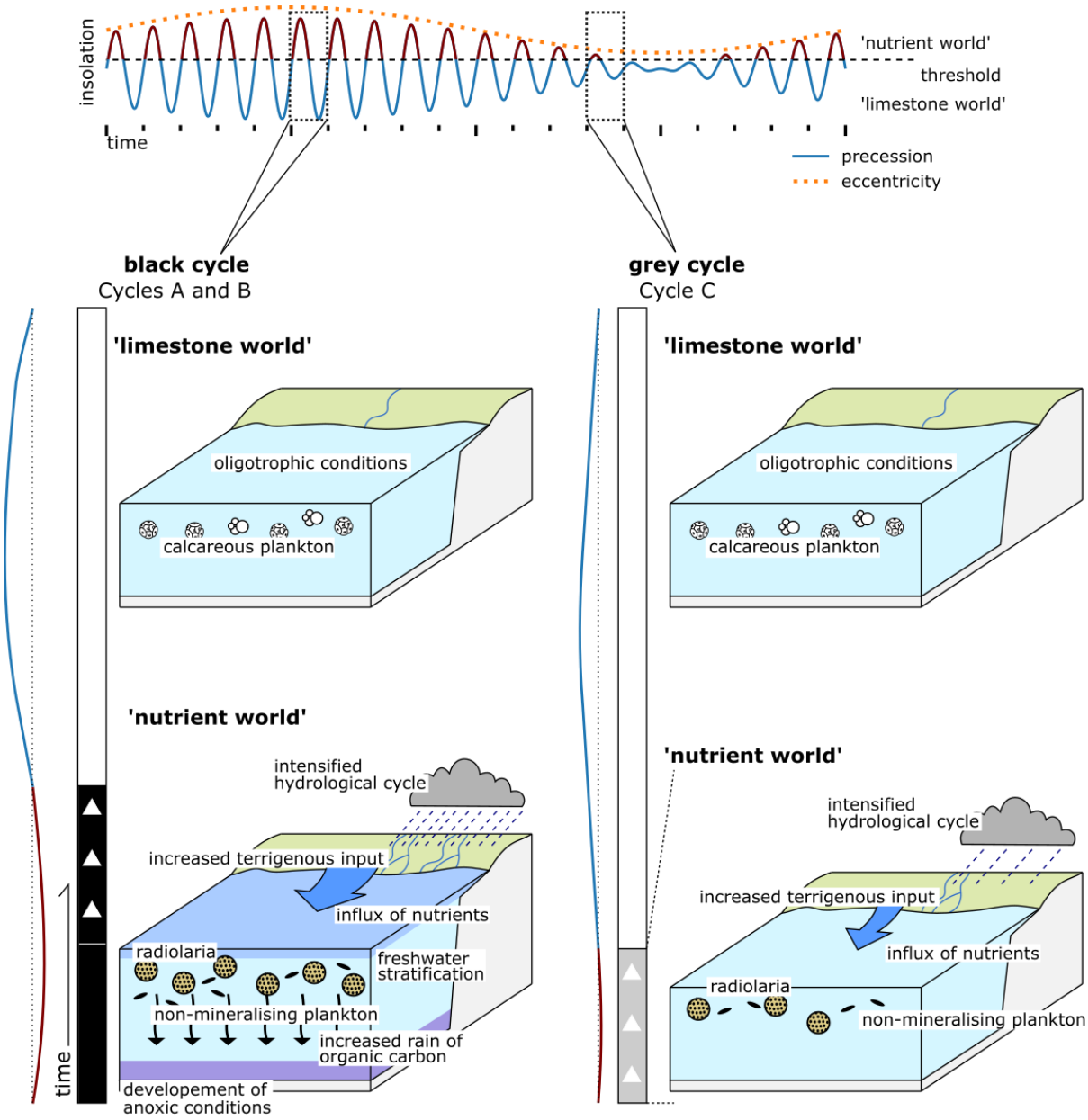

Figure 4.15: Summary of 'threshold model' linking insolation forcing and the drivers of palaeoceanographic change.

Next, the deposition of sub-Bonarelli TOC-rich chert and shale are examined with respect to the 'threshold model'. As discussed above, it is possible that the apparent division of black chert and black shale into distinct lithologies may simply be an artefact of diagenetic segregation, rather than reflecting a change in primary lithology (see Figure 4.13). In previous conceptions of 'thresholds'

relevant to the formation of the Scaglia Bianca, sub-Bonarelli TOC-rich chert and shale beds are typically considered together as 'black beds' (Mitchell et al., 2008; Batenburg et al., 2016). Precession cycle-driven environmental change, and particularly the 'threshold' model, was evaluated both considering the separation of black shales and cherts as purely diagenetic, and considering this distinction as representing different primary lithologies.

When considering the division of shales and cherts as due only to diagenetic segregation (Figure 4.13 C), the interpretation of 'threshold crossing' is straightforward. In Furlo Cycles A and B ~7–8 kyr (the total time spanned by 'black beds') was spent in conditions favourable to siliceous deposition and organic-matter preservation (with ~5 kyr spent under these conditions in Contessa Cycle B if the slowly-depositing marl is considered as analogous to the black shales expressed in Furlo), whilst in Furlo Cycle C only ~1.6 kyr (the time spanned by the chert) was spent depositing sediment under these conditions. This diagenetic separation model affects the interpretation of changing sedimentation rates and terrestrial ^{4}He flux through the cycles: both black shales and black cherts must be considered as a single 'black bed' unit. Working in this framework black beds do still, on balance, deposit more slowly than limestones (with sedimentation rates in the 'black beds' 0.49±0.09 cm/kyr, 0.37±0.11 cm/kyr and 0.53±0.13 cm/kyr in Furlo Cycles A, B and Contessa Cycle B, respectively). At Furlo, where $^{4}He_{terr}$ flux is elevated in the black cherts of Furlo Cycles A and B (Figure 4.9), $^{4}He_{terr}$ flux over the 'black beds' (~1.8–4.1×10^{-7} cc/cm^{2}/kyr) remains elevated relative to the cycles' limestones.

If, on the other hand, the two 'black bed' lithologies are considered separately, with black shale and black chert representing two different primary lithologies (Figure 4.13 B), the relationship between lithological change and 'threshold crossing' is rather more complex. It appears that in cycles coincident with eccentricity maxima (A and B) ~4–6 kyr was spent in a slowly depositing lithology (black shale in Furlo or marl in Contessa) prior to ~0.5–2 kyr of a more siliceous lithology that would develop into a chert (Figure 4.12, Table 4.2). This siliceous-rich primary lithology is thought to have

been interbedded radiolarian-rich black shales and layers of sand-sized radiolaria (Gambacorta et al., 2014). In Furlo, where cycles contain black shales, organic-carbon mass-accumulation rates suggest that organic-carbon productivity remained comparatively elevated throughout this interval. This interpretation would indicate that, once the threshold into 'nutrient world' had been crossed, these locations experienced ~5–6 kyr of anoxic conditions and increased organic-carbon productivity before the deposition of an even more silica-rich lithology that would later develop into a chert.

In cycles deposited during eccentricity minima, however, the Earth System response to 'threshold crossing' (as interpreted from the sedimentary record) appears to be rather different. Chert beds directly overlie limestone in cycles deposited during eccentricity minima: there are, for example, no thin grey shales accompanying the grey chert of Furlo Cycle C. It seems, perhaps, unusual that a brief foray over the threshold into 'nutrient world' at Furlo would have resulted in a period of siliceous deposition (e.g. ~1.6 kyr of grey chert in Cycle C), but a longer sojourn (e.g. Furlo Cycles A and B) resulted first in ~5–6 kyr of shale deposition before the elevated siliceous productivity became significant (~0.6–2.2 kyr of black chert).

One of many speculative explanations for these differences in sedimentation pattern in cycles deposited during eccentricity minima *vs.* maxima might be related to water temperature change. Gambacorta et al. (2016) suggested that black shales may have been deposited during the shift from oligotrophic to eutrophic conditions, during an interval when carbonate producers had decreased but increased siliceous production was not yet at a sufficient level to overcome dissolution in the water column or on the sea floor and be preserved within the sediment. Although the abundant radiolarians seen in sub-Bonarelli black shales (Figures 4.6d, 4.7a, b) indicate that many silica producers were, in fact, preserved in black shales, it may be the case that black chert beds represent primary lithologies that contained a much greater volume of siliceous fossils than the underlying beds, prompting their development into black cherts. As the solubility of biogenic silica is, in part, dependent on sea surface temperature (see review of Ragueneau et al., 2000), slightly warmer

waters in ‘nutrient world’ during eccentricity maxima than during eccentricity minima (Batenburg et al., 2016) might have resulted in a situation where a greater degree of silica productivity was needed to overcome dissolution in the water column/on the sea floor during eccentricity maxima than minima. This might contribute somewhat to the apparent lag in the deposition of the proto-chert lithology between ‘black’ and ‘grey’ cycles, though the magnitude of the observed response compared to the change in forcing would require a rather delicately poised system. Although the difference in sea surface temperature between eccentricity maxima and minima is unlikely to be more than one or two degrees (e.g. end-Cenomanian sea surface temperature records of Jarvis et al., 2011), the sensitivity of biogenic silica dissolution kinetics to surface water temperature (Ragueneau et al., 2000) means that these small temperature differences between eccentricity maxima and minima may still have had some impact on the observed change in sedimentation patterns between cycles.

Another observation to be tallied with the ‘threshold model’ is the apparent difference in the degree of anoxia that developed in cycles deposited at eccentricity maxima vs minima. Although an independent geochemical proxy for anoxic conditions (separate from productivity) was not measured in this study, the absence of bioturbation has been used as a ‘rough and ready’ indicator of dysoxic conditions in comparable Umbria–Marche successions and in global studies of organic-carbon-rich laminated sediments (e.g. Demaison and Moore, 1980; Pratt and King, 1986). Well-developed laminated sediments, both black shale and bedded black chert (Figure 4.5e), are evident in ‘black’ cycles (Cycles A and B). By contrast, no sedimentary structures are as obvious in the grey chert of ‘grey’ cycles (Cycle C). The lack of observable sedimentary structures in the grey cherts may be indicative of bioturbation, as may their somewhat mottled internal texture, but total erasure of pre-existing texture and structures during chert diagenesis should not be ruled out, making it difficult to state definitively whether the pre-chert lithology was bioturbated or not. On balance, however, some degree of bioturbation within the grey cherts seems likely, implying that anoxic conditions were not as well developed during the deposition of ‘grey’ cycles. A major contributor to

the development of anoxic conditions in these precession cycles is thought to be stratification of the water column, either by an influx of a freshwater under monsoonal conditions or by variations in surface-water temperature (Mitchell et al., 2008; Tiraboschi et al., 2009; Batenburg et al., 2016; Gambacorta et al., 2016). Increased primary productivity and export of organic carbon to the seafloor may also have contributed to dysoxic conditions at the seabed.

The development of anoxic conditions might be expected to vary under different 'strengths' of precessional forcing either due to the intensity of the forcing, or to the time over which that forcing was applied. Considering the contribution of freshwater stratification, for example: this may have developed through a more intense hydrological cycle at a higher forcing 'peak', or through the cumulative effect of an intensified hydrological cycle over a longer period of time. The data collected in this study are not sufficient to differentiate between these two mechanisms; however, if the development of anoxic conditions were related to time spent above the threshold in 'nutrient world' the $^{3}He_{ET}$ timescale would allow limits on the time needed to reach these conditions to be estimated. The timescales of Cycles A and B would indicate a maximum time of ~6.8 kyr needed to reach these anoxic conditions, with a lower limit of ~1.6 kyr from Cycle C.

Effects of varying sedimentation rates on cyclostratigraphic analysis

Finally, it is worth noting that this study confirms that large differences in the relationship between 'depth' and 'time' may occur through the different lithologies of a precession cycle in the Scaglia Bianca (and, perhaps, in similar lithologically heterogeneous cycles) due to varying sedimentation rates (a term encompassing the result of both contemporary rate of sediment accumulation and subsequent differential compaction). This complicating factor means that, were geochemical data to be plotted against depth as a proxy for time for cyclostratigraphic analysis, the expected orbitally forced sinusoidal signal would be stretched/shrunk with the passage through different lithologies.

4.6 Conclusion

The geological record contains multiple examples of small changes in insolation forcing during orbital cycles that ultimately provoked dramatic lithological and geochemical shifts. By providing constraints on the rates and timescale of sedimentological changes, $^{3}He_{ET}$ timescales allow the relationship between orbital forcing and environmental change to be better understood.

The lithological changes in the Upper Cretaceous Scaglia Bianca of Marche–Umbria, Italy, can be explained using the concept of 'palaeoenvironmental thresholds' (summarised in Figure 4.15). Cherts and TOC-rich beds, facies interpreted as representing more productive conditions, comprise a larger temporal proportion of cycles deposited at times of eccentricity maxima: an observation consistent with the idea that, as the amplitude of these precession cycles became greater, insolation values stayed above a certain 'threshold' for longer during their deposition.

The palaeoenvironmental context of this 'threshold' and crossover into 'nutrient world' is a change from dominantly calcareous to siliceous or non-mineralising planktonic communities prompted by an increase in nutrient availability. An observed spike in the terrestrial ^{4}He flux in the black cherts at Furlo may indicate increased terrestrial run-off at this time, suggestive of the provision of nutrients through intensification of the hydrological cycle. Increased productivity in 'nutrient world' is indicated by the high organic-carbon mass-accumulation rates measured in black shales and black cherts within the Scaglia Bianca, along with higher estimated primary productivity values.

The question of what environmental conditions led to the deposition of black shales in cycles at eccentricity maxima cannot be definitively answered; there is a distinct possibility that the distinction between black shale and black chert is due either in part or entirely to diagenetic segregation. In the absence of a clear means of determining whether the differentiation between black shales and black cherts reflects such an unmixing process or a change in primary lithology conclusions are presented for both possibilities: deposition under 'nutrient world' conditions during

eccentricity maxima took place either over an extended period (between ~20–40% of the duration of measured cycles) where conditions were favourable both to siliceous deposition and organic-matter preservation, or this time may have been divided into a long period where conditions favoured organic-matter preservation followed by a much shorter interval that saw more rapid deposition of siliceous material.

The suggested primary lithology that produced these chert beds (assuming that they did not form entirely through diagenetic separation) was a radiolarian sand. The time spanned by the chert beds indicates that the original siliceous skeletal were not washed in as a single unit but represents either deposition largely in place or as multiple wash-in events extending over ~600–2400 yr. The interplay of deposition, redistribution and diagenesis within these chert beds is both very complex and very hard to quantify, a fact that must be borne in mind when interpreting $^{3}He_{ET}$ timescales through this lithology. Transport of He_{ET}-bearing material would affect the apparent 'time taken' through cherts; in addition, early diagenesis of cherts prior to compaction of the surrounding sediments has the potential to inflate calculated linear sedimentation rates.

Differences in the degree of anoxia between cycles deposited at eccentricity maxima *vs* minima may have been due either to the intensity of the insolation forcing or to the time spent above a certain threshold. For example, a greater degree of insolation forcing may have driven a more intense hydrological cycle contributing to freshwater stratification, or freshwater stratification may have developed through the cumulative effect of an intensified hydrological cycle over a longer period of time. Although the data collected in this study provide no insight into the 'intensification' hypothesis, temporal limits on the 'anoxia over time' hypothesis can be calculated: this process would have taken longer than ~1.5 kyr but less than around 7 kyr.

Using $^{3}He_{ET}$ concentration to calculate sedimentation rates within a precession cycle also highlights the fact that, in a cycle comprised of heterogeneous lithologies, the relationship between 'depth'

and ‘time’ changes from bed to bed, an observation relevant to cyclostratigraphic studies as it may distort the expected shape of signals.

Finally, this study establishes a best practice methodology for calculating $^{3}He_{ET}$ background flux through sections with heterogeneous lithology. Where possible, if the sedimentation rate used in calculation of background flux originates from cyclostratigraphy, background flux in heterogeneous sections should be calculated from the average values of homogenised orbital cycles (precession cycles are used in the Scaglia Bianca). Calculating background flux in this way reduces the risk of introducing systematic error by spot-sampling through lithologies deposited under varying sedimentation rates.

5. A high-resolution timescale through the Bonarelli Level

Abstract

A high-resolution $^{3}He_{ET}$ timescale was constructed over the Bonarelli Level, a ~1m thick interval of black shales and radiolarian sands which is the expression of Oceanic Anoxic Event 2 in the Umbria–Marche Basin, central Italy. An overall duration of the Bonarelli Level, 478±160 kyr, was determined. $^{3}He_{ET}$ concentrations allow the calculation of an instantaneous sedimentation rate for each measured bed, allowing changing sedimentation and organic-carbon mass-accumulation rates (OC MAR) through the interval to be examined in detail, along with the relationship between OC MAR and bulk accumulation rates in different lithologies. Though the accumulation rates of OC through the Bonarelli Level were highly heterogeneous, peak OC MAR values of ~0.22 g/cm^2/kyr were reached in black mudstone/shale beds; primary productivity in beds with high OC MARs was estimated at 60–110 gC/m^2/yr. Condensed horizons/intervals were recognised in the section as 'spikes' in $^{3}He_{ET}$ concentration. A condensed interval was identified within the Bonarelli Level, ~40 cm above its base, within which 5 cm of black shale and radiolarian sand are thought to have been deposited over a span of ~50 kyr. Reductions in sedimentation rate are also seen coincident with the dramatic lithological changes at the top and base of the Bonarelli Level. Above the Bonarelli Level, a transient increase in the accumulation rates of carbonate sediments is thought to reflect enhanced carbonate accumulation due to build-up of excess alkalinity over OAE 2 caused by low carbonate productivity through this interval, similar to carbonate overshoots observed following other major periods of environmental perturbation such as the Paleocene–Eocene Thermal Maximum.

5.1 Introduction

Oceanic Anoxic Event 2 (OAE 2, also known as the Cenomanian-Turonian Oceanic Anoxic Event), a globally recognised carbon-cycle perturbation ~94 Ma, was a period of climate change during which rapid warming was accompanied by an accelerated hydrological cycle, enhanced continental weathering, increased nutrient input to the oceans, intensified upwelling, increased organic productivity and expansion of marine anoxia/euxinia (summarised more extensively in Chapter 2.3.2). As a result of this environmental perturbation many sedimentary records of OAE 2 are composed of variable lithologies. Over these lithologically complicated sections the use of extraterrestrial ^{3}He concentration as a proxy for sedimentation rate allows the construction of high-resolution timescales: an instantaneous sedimentation rate is determined for each sample measured, allowing sedimentological changes to be examined in detail and meaning that the resolution of such a timescale is theoretically limited only by sampling density (and the mixing effects of any bioturbation).

The extraterrestrial ^{3}He technique is used to construct a high-resolution timescale for the Bonarelli Level, a ~1-metre-thick interval of black shales and radiolarian sands which is the local expression of the Cenomanian-Turonian OAE in central Italy, and a historically important and well-studied section (Arthur and Premoli Silva, 1982). A new duration estimate for the Bonarelli Level is determined from the $^{3}He_{ET}$ timescale. In addition, the variations in sedimentation rates and mass-accumulation rate of organic carbon over the event are examined in detail, allowing identification of a condensed horizon within the Bonarelli Level. Elevated accumulation rates in carbonates after the Bonarelli Level echo those observed after the Paleocene-Eocene Thermal Maximum (Farley and Eltgroth, 2003; Murphy et al., 2010); the implications of these elevated accumulation rates are discussed with regards to the local oceanographic conditions during the recovery from OAE 2.

5.2 Methodology

Samples were collected continuously through the Bonarelli Level at Furlo (see Section 2.2.1), accompanied by a detailed sedimentary log beginning ~10 cm below the base and ending ~20 cm above what was judged to be the top of the unit (Figure 5.1). Within the Bonarelli Level, millimeter-scale beds could be collected individually, whereas the thick limestone beds stratigraphically above and below this unit were divided into 1 cm chunks for sampling.

A Rock-Eval 6 instrument at Oxford University was used to determine Total Organic Carbon (TOC) content, carbonate content, and Hydrogen Index of samples as described in Chapter 4.3. Organic carbon isotope ($\delta^{13}C_{TOC}$) measurements were carried out by Simona Nicoara of the Open University on powdered samples using a MAT253 mass spectrometer and calibrated with a three-point calibration using IAEA-CH-6 sucrose, NIST 8573 L-glutamic acid and IR-R041 L-alanine. Standard deviation (±1σ) of repeat measurements of standards was less than 0.15‰.

Helium concentration was measured on a HELIX SFT mass spectrometer (see Section 3.1.2 for details), and the extraterrestrial ^{3}He component deconvolved from a two-component mixing model (see Section 3.1.4). Samples with unusually high ^{3}He concentration may contain exceedingly ^{3}He-rich particles that are rare enough not to appear in every sample aliquot; these were rejected from further analysis as 'outliers'. ~6% of all measured samples were identified as outliers following the procedure of Murphy et al. (2010), with measurements considered 'anomalous' if their ^{3}He content (cc/g) differed by >2.4× from measurements of the two immediately adjacent samples. Duplicates were made of these 'anomalous' samples, if the resulting data were within error of the 'anomalous' measurement it was retained, and, if not, it was discarded. A fuller description of this outlier identification method is given in Section 3.1.5.

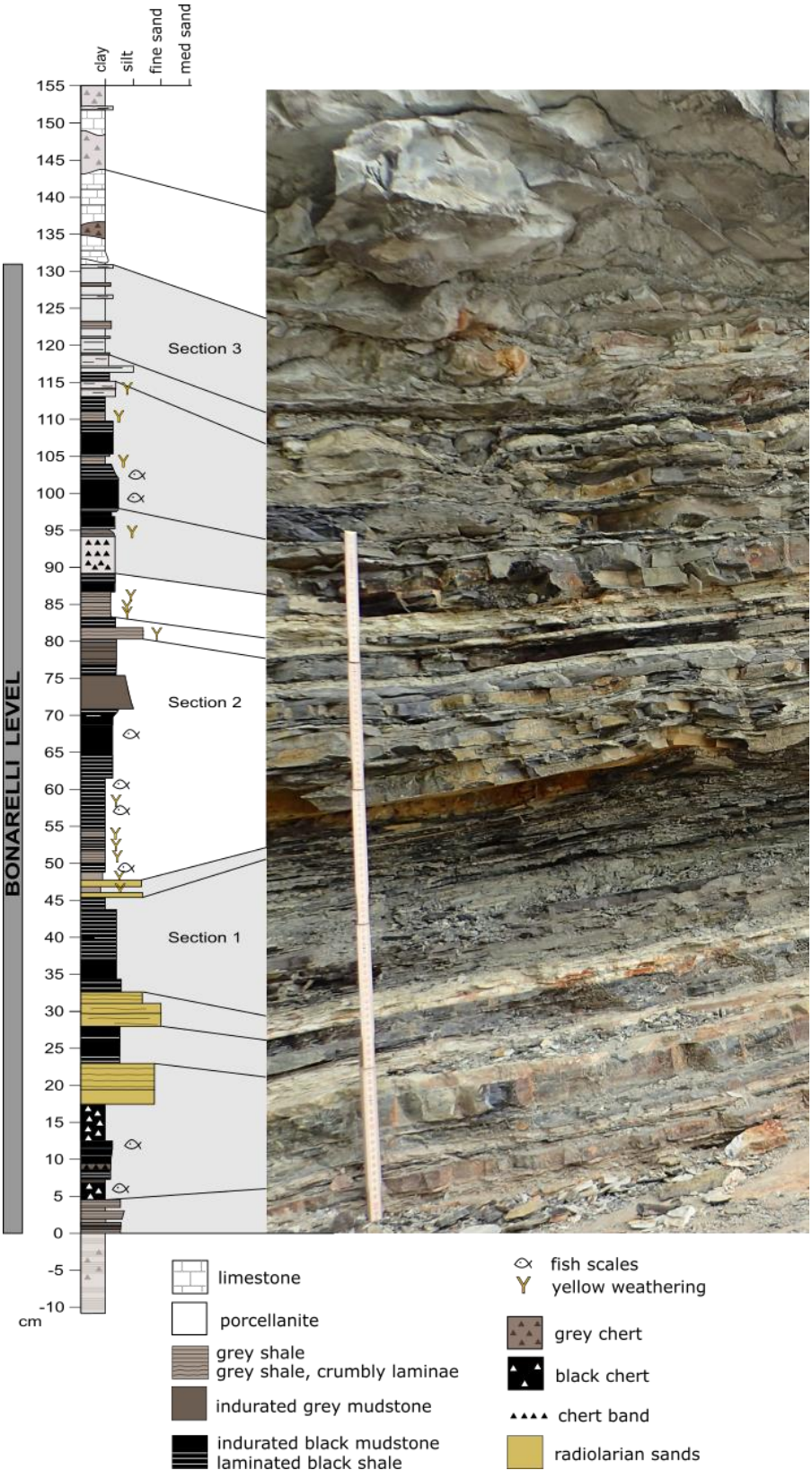

Figure 5.1: High-resolution sedimentary log of the Bonarelli Level with outcrop photograph.

Sedimentation rate was calculated from extraterrestrial ^{3}He concentration using the following relationship, reflecting the dilution of helium-bearing interplanetary dust particles (IDPs) by other sediment (Takayanagi and Ozima, 1987):

$$\alpha = F / [^{3}He_{ET}]$$

Equation 5.1

Where α is the accumulation rate of sediment (g/cm^2/kyr), F is the background flux of extraterrestrial ^{3}He into sediments (ccSTP/cm^2/kyr) and $[^{3}He_{ET}]$ is the concentration of extraterrestrial ^{3}He (ccSTP/g). A background flux value of 1.14±0.38 x 10^{-13} ccSTP/cm^2/kyr was used for the interval spanning the Bonarelli Level. Full details of this background flux calculation are given in Section 4.5.1 but, in brief, the background flux was calculated using the average $^{3}He_{ET}$ concentration from samples composed of the homogenised records of precession cycles (lithologically expressed as pelagic limestones, cherts and, where present, black shales) spanning the interval ~400 kyr before and ~100 kyr after the Bonarelli Level, with an average sedimentation rate of 1.1 cm/kyr from the cyclostratigraphic analysis of Batenburg et al. (2016).

5.3 Results

Stable carbon isotopes, total organic carbon content, carbonate content, Hydrogen Index, extraterrestrial ^{3}He and terrestrial ^{4}He concentration measured through the Bonarelli Level are plotted in Figure 5.2, alongside linear sedimentation rate (calculated using Equation 5.1) and organic-carbon mass-accumulation rate.

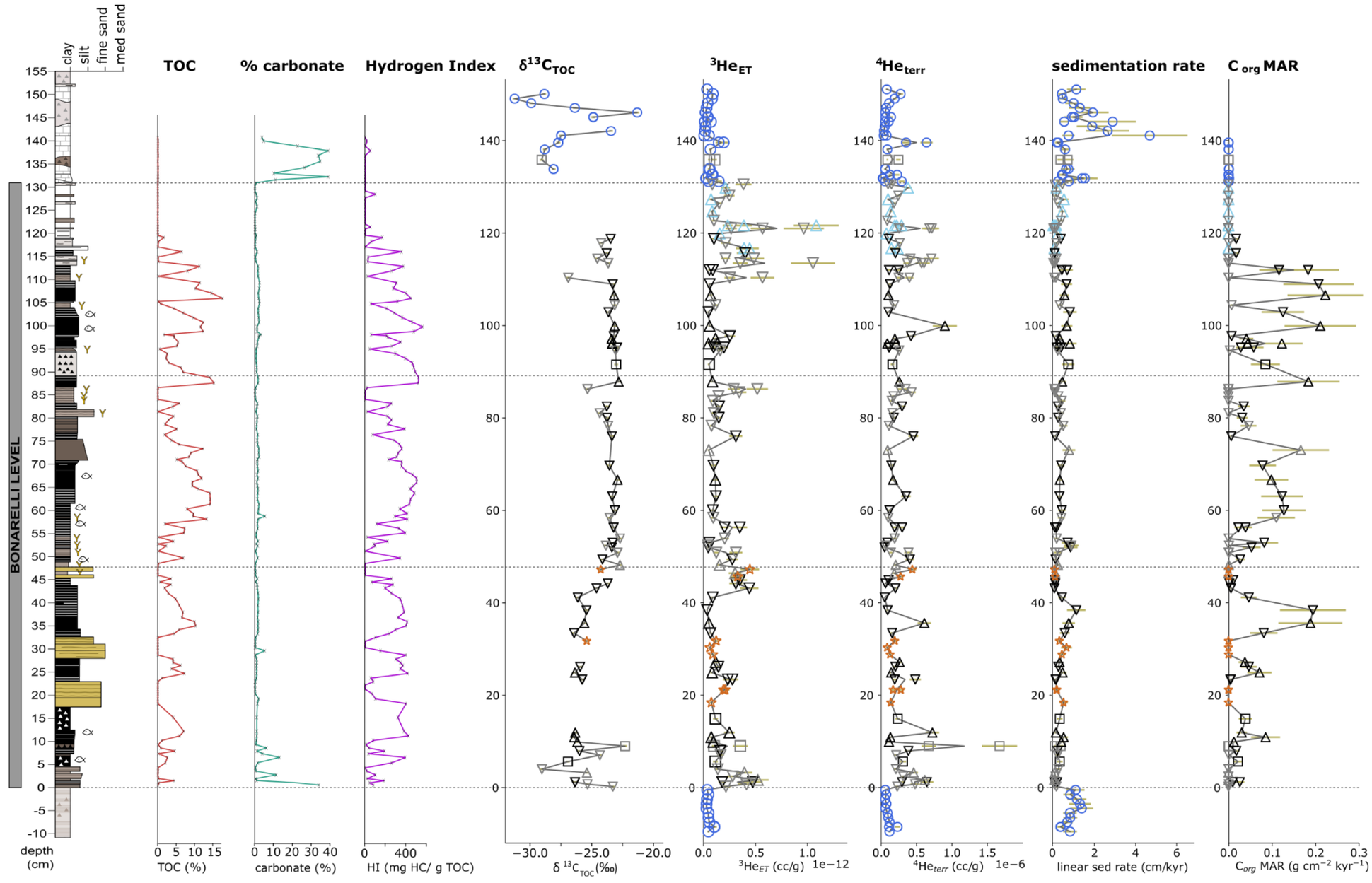
clay
silt
fine sand
med sand
BONARELLI LEVEL
depth (cm)
TOC
TOC (%)
% carbonate
carbonate (%)
Hydrogen Index
HI (mg HC/ g TOC)
δ13CTOC
δ 13CTOC(‰)
3HeET
3HeET (cc/g) 1e−12
4Heterr
4Heterr (cc/g) 1e−6
sedimentation rate
linear sed rate (cm/kyr)
C org MAR
Corg MAR (g cm−2 kyr−1)
Log
limestone
porcellanite
grey shale
grey shale, crumbly laminae
indurated grey mudstone
indurated black mudstone
laminated black shale
radiolarian sands
fish scales
yellow weathering
grey chert
black chert
chert band
Graphs
limestone
porcellanite
grey chert
black chert
black mudstone
black shale
grey mudstone
grey shale
radiolarian sands

Figure 5.2: High-resolution log of the Bonarelli Level presented alongside total organic carbon content, carbonate content, Hydrogen Index of organic matter (HI), $\delta^{13}C_{TOC}$, extraterrestrial ^{3}He and terrestrial ^{4}He concentration, linear sedimentation rate and organic-carbon mass-accumulation rate measured in each bed. Error bars on $^{3}He_{ET}$ (cc/g) represent 20% reproducibility error due to the nugget effect (see Section 3.1.5), error bars on $^{4}He_{terr}$ derive from analytical error. Errors on sedimentation rate and OC MAR are dominated by the error on the background $^{3}He_{ET}$ flux.

5.3.1 Total Organic Carbon content, carbonate content and Hydrogen Index

The Bonarelli Level owes its distinctive appearance to its organic-carbon-rich black beds, but the TOC content within the level is, in fact, highly heterogeneous (see Figure 5.2). Black shales and mudstones measured in this study contained up to 15% organic carbon, but certain beds (notably those identified as radiolarian sands) did not contain enough organic carbon for detection. As might be expected, black shales and mudstones contain the highest percentage of TOC; the organic matter in these lithologies typically exhibits high Hydrogen Index (HI) and low Oxygen Index (OI) values (Figure 5.3a).

Carbonate content through the Bonarelli Level is very low (though not totally non-existent – a small number of beds do contain up to 5% carbonate). A decrease from ~40% carbonate just below the Bonarelli Level to the 'typical' near-0% values occurs over the basal ~10 cm of the Bonarelli Level, with a dramatic rise in carbonate content from near-0% to ~40% immediately above its stratigraphically highest bed.

A few centimetres of white porcellanite occur between the last bed with significant TOC (~119 cm) and the first bed containing significant carbonate (~132 cm). In outcrop these beds are indistinguishable from the overlying limestone, they are not vitreous and do not fracture conchoidally, but under thin section they are composed primarily of microcrystalline quartz (Figure 5.4). (The term 'porcellanite' is used in this study as a descriptive term for non-vitreous cherts, without the specific connotation of opal-CT mineralogy.)

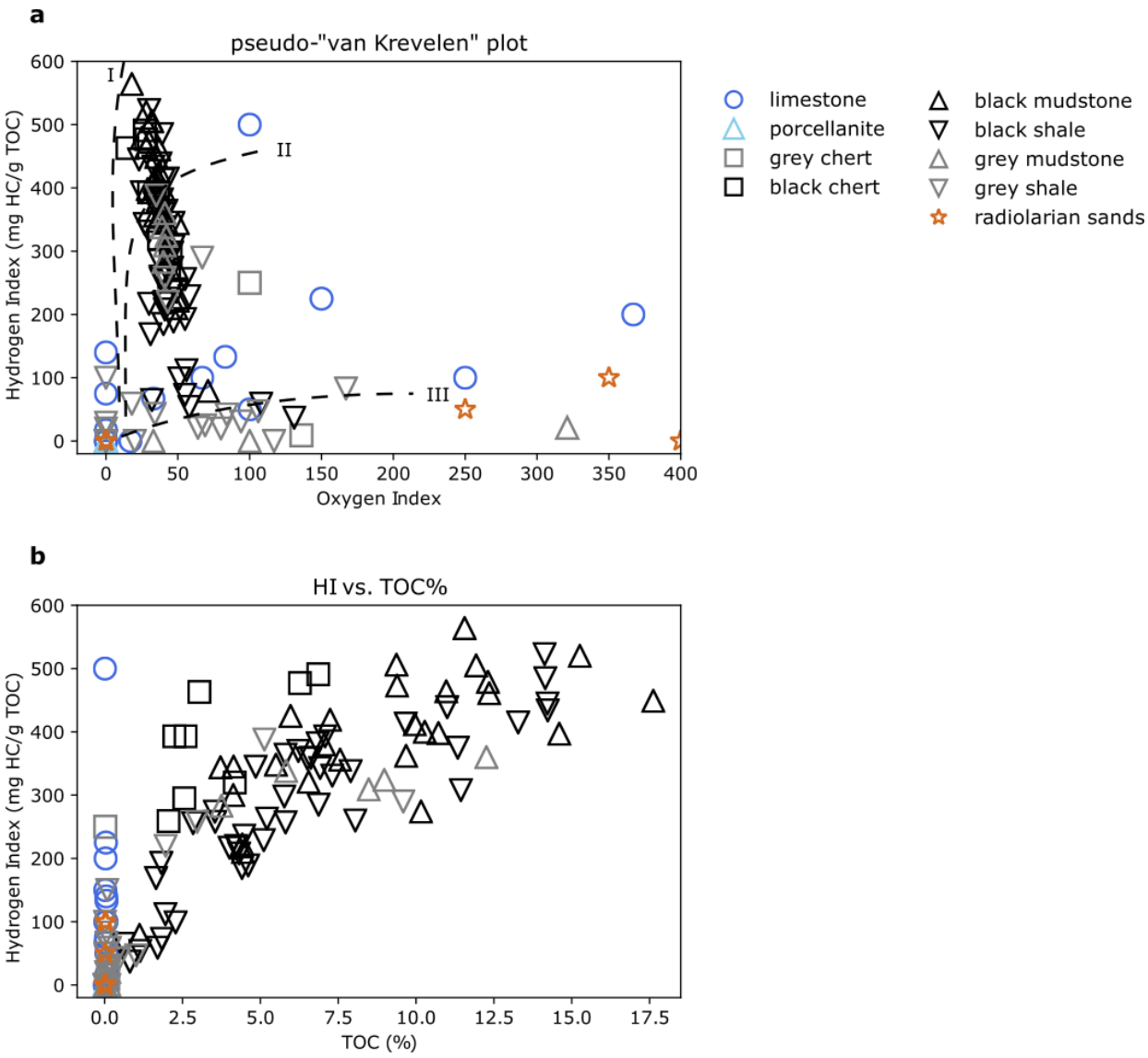

Figure 5.3: Rock Eval results for the Bonarelli Level succession; ***(a)*** *Van Krevelen-type plot showing the variation of organic-matter types with lithology in Bonarelli Level sediments and the overlying limestones;* ***(b)*** *Hydrogen Index values plotted against total organic-carbon content.*

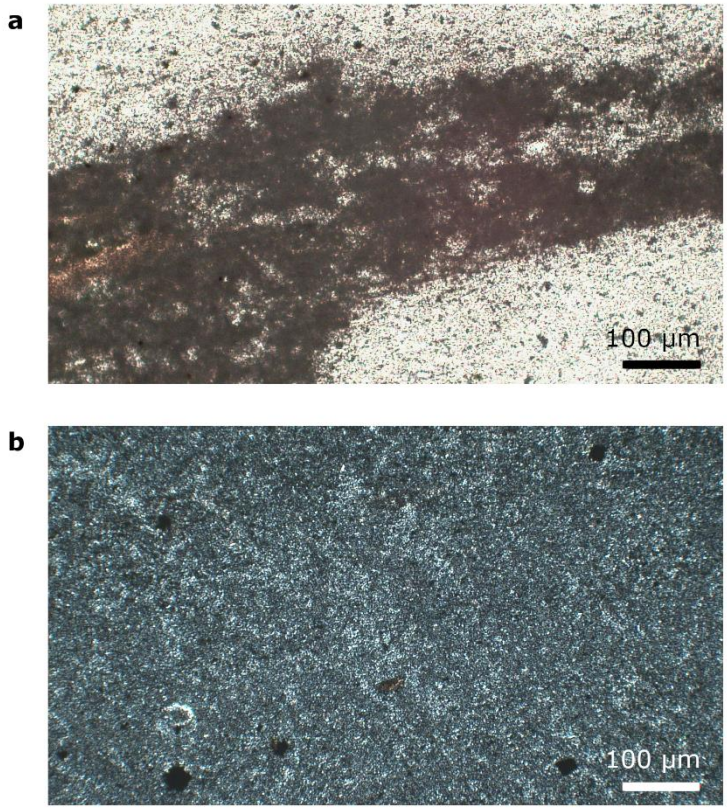

Figure 5.4: Porcellanite bed from the top of the Bonarelli Level; ***(a)*** *Crook-shaped clast within a porcellanite bed from the top of the Bonarelli Level. The matrix is composed primarily of microcrystalline quartz, with some opaque, euhedral grains which may be iron oxides or iron sulphides. In hand specimen, this clast appears white within the cream porcellanite bed; in thin-section it appears to be composed of organic- matter residue, the original lithology having been replaced by microcrystalline quartz. (Position: 130 cm in Bonarelli Level, under plane-polarized light, scale bar = 100 µm, bedding parallel to long edge of image);* ***(b)*** *More typical image of this porcellanite bed; the bulk of this rock is composed of microcrystalline quartz, with some iron oxides/sulphides. (Position: 130 cm in Bonarelli Level, under crossed-polars, scale bar = 100 µm, bedding parallel to long edge of image).*

5.3.2 Helium concentration

$^{3}He_{ET}$ concentrations are, in general, elevated within the Bonarelli Level. Since $^{3}He_{ET}$ is inversely proportional to sedimentation rate (as described in Equation 5.1), these elevated concentrations are likely to reflect an overall slower sedimentation rate through this interval. 'Spikes' in $^{3}He_{ET}$ concentration may indicate condensed horizons or hiatal surfaces: in intervals where oceanographic conditions caused pelagic sedimentation to cease there may have been no reason for extraterrestrial sedimentation to have halted, and a high concentration of helium-bearing interplanetary dust particles may have built up on a particular level. $^{3}He_{ET}$ 'spikes' were identified near the top of the Bonarelli Level and at its base, along with a 'spike' in the middle of the Level (~45 cm). These potential condensed horizons are discussed further in Section 5.4.4.

Terrestrial ^{4}He concentrations do not appear to systematically vary through the Bonarelli Level but are, in general, a little higher within it than outside it. This elevated concentration could be due to an increased input of terrigenous material carrying $^{4}He_{terr}$, but the co-incidence of an increase in both $^{4}He_{terr}$ and $^{3}He_{ET}$ concentrations suggests that both may be due to the same process: a slowing of sedimentation rate.

5.3.3 Sedimentation rates

Calculated linear sedimentation rates of the various lithologies within the Bonarelli Level are presented in Figure 5.5a. Sedimentation rates appear to be broadly similar across all lithologies within the Bonarelli Level (see Table 5.1), ranging between 0.04–1.13 cm/kyr. Sedimentation rates calculated in cherts and radiolarian sands are similar to those in mudstones and shales. The overall average sedimentation rate across the Bonarelli Level is 0.272±0.091 cm/kyr.

A distinct elevation is noted in the sedimentation rate of the limestone beds above the Bonarelli Level (above ~140 cm, Figure 5.2), with peak sedimentation rates of ~2.7 cm/kyr, over twice as high as the average sedimentation rate of limestones directly below the Bonarelli Level (~1.03 cm/kyr) and in precession cycles from earlier in the Cenomanian (~1.25 cm/kyr). From the peak in sedimentation rates at ~141 cm, rates gradually decrease up section towards 'pre-OAE average' values. These post-Bonarelli Level observations are discussed further in Section 5.4.5.

5.3.4 Organic-carbon mass-accumulation rates

The average organic-carbon mass-accumulation rate (OC MAR) over the Bonarelli Level is 0.044±0.011 g/cm^2/kyr, though OC MAR varies by lithology, ranging from below the detection limit of organic carbon in some grey shales and porcellanites to a maximum value of 0.222±0.086 g/cm^2/kyr in a black mudstone (see Figure 5.5b). Ranges and averages for each lithology are presented in Table 5.2 (this contains data from all measured samples, including the limestones below and above the Bonarelli Level). Spikes in OC MAR are typically co-incident with high TOC beds (see Figure 5.2).

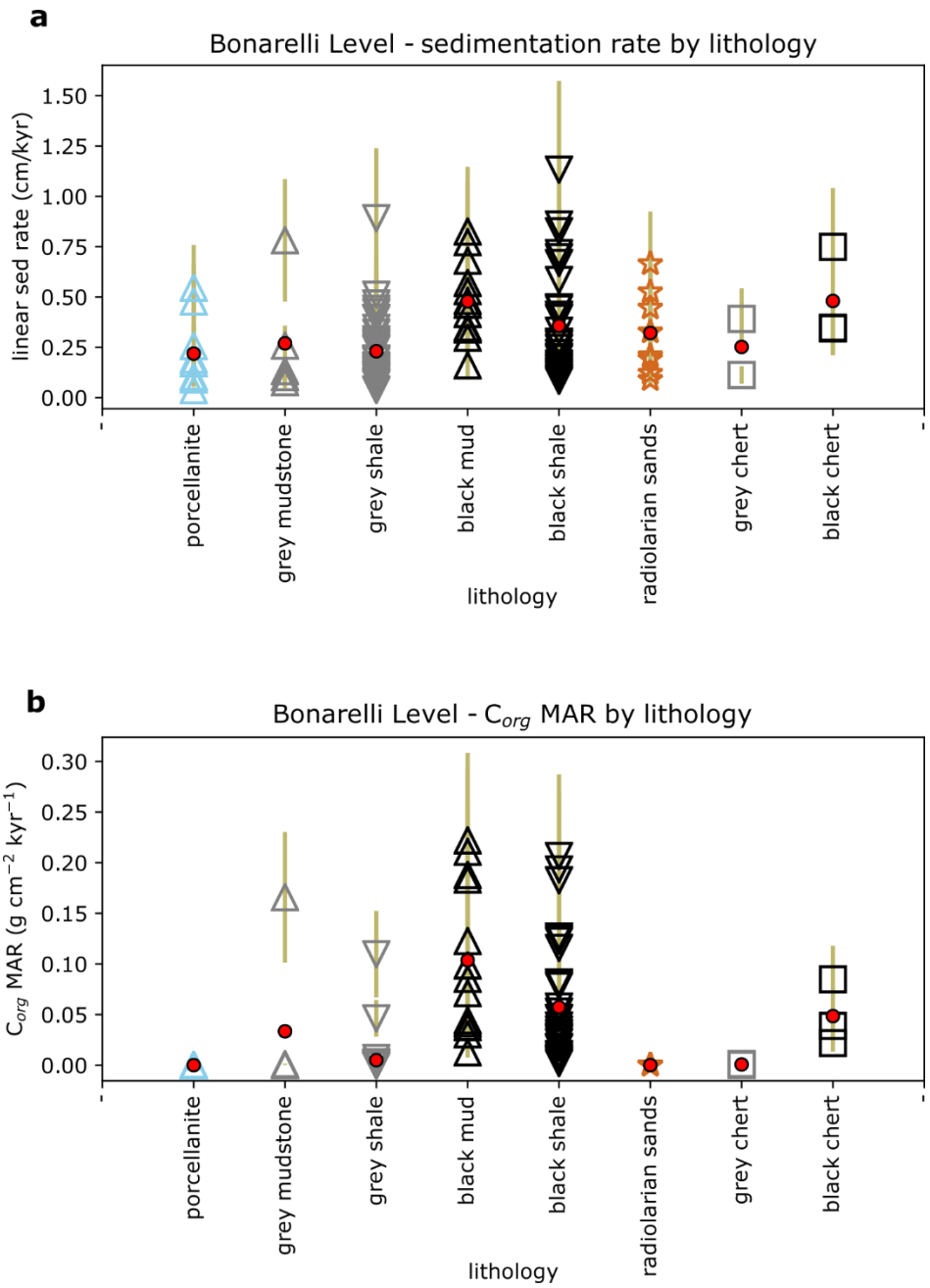

Figure 5.5: ***(a)*** *Sedimentation rates within the Bonarelli Level, plotted by lithology;* ***(b)*** *organic-carbon mass-accumulation rates of lithologies within the Bonarelli Level. Red circles indicate average values.*

Linear sedimentation rate (cm/kyr)	porcellanite	grey mudstone	grey shale
range	0.04–0.55	0.07–0.78	0.04–0.89
average	0.22	0.27	0.23

Linear sedimentation rate (cm/kyr)	black mudstone	black shale	radiolarian sands	grey chert	black chert
range	0.16–0.82	0.08–1.13	0.09–0.67	0.11–0.39	0.34–0.75
average	0.48	0.36	0.32	0.25	0.48

Table 5.1: Linear sedimentation rate ranges and averages in different lithologies from the Bonarelli Level.

C_{org} mass-accumulation rate ($g/cm^2/kyr$)	limestone	porcellanite	grey mudstone	grey shale
range	2.92×10^{-4} – 0.00167	0.0 – 2.95×10^{-4}	7.10×10^{-5} – 0.166	0.0 – 0.110
average	8.42×10^{-4}	8.69×10^{-5}	0.0335	0.00507

C_{org} mass-accumulation rate ($g/cm^2/kyr$)	black mudstone	black shale	radiolarian sands	grey chert	black chert
range	0.0126 – 0.222	0.00215 – 0.207	4.82×10^{-5} – 1.74×10^{-4}	3.34×10^{-4} – 0.00116	0.0218 – 0.0848
average	0.104	0.0573	1.14×10^{-4}	7.15×10^{-4}	0.0485

Table 5.2: Organic-carbon mass-accumulation rate ranges and averages in different lithologies from the Bonarelli Level and enclosing sediments.

5.4 Discussion

5.4.1 Duration of the Bonarelli Level

A $^{3}He_{ET}$ timescale was constructed over the Bonarelli Level. The duration spanned by each bed was calculated from its thickness and the instantaneous sedimentation rate as derived from $^{3}He_{ET}$ concentration. This methodology allows the lithological change through the Bonarelli Level to be plotted against time, as presented in Figure 5.6. The overall duration of deposition of the Bonarelli Level is estimated to be 478±160 kyr.

The estimated duration of the Bonarelli Level lies within the 320–800 kyr range of durations posited by other studies (Ohkouchi et al., 1999; Scopelliti et al., 2006; Turgeon and Brumsack, 2006; Trabucho-Alexandre et al., 2011; Batenburg et al., 2016): confirmation of these duration estimates is therefore provided using the novel $^{3}He_{ET}$ technique. Although the errors on this duration estimate (which derive from the uncertainty in the background flux over this interval) mean that conclusions drawn must be somewhat conservative, results of the $^{3}He_{ET}$ timescale suggest that the duration of the Bonarelli Level is likely to be at the shorter end of the above range, in keeping with estimates from cyclostratigraphic analysis, which range from 320–540 kyr (Scopelliti et al., 2006; Trabucho-Alexandre et al., 2011; Batenburg et al., 2016). It must be noted when considering the variation among duration estimates that virtually all studies mentioned use different outcrops across the Umbria-Marche Basin; local palaeogeographic controls on potential hiatuses at the top and base of the Bonarelli Level may mean that the shale interval actually does represent a slightly different span of time in different places. A duration estimate from cyclostratigraphic analysis at Furlo (allowing direct comparison to the $^{3}He_{ET}$ timescale in this thesis) of 413 kyr was determined by Batenburg et al. (2016).

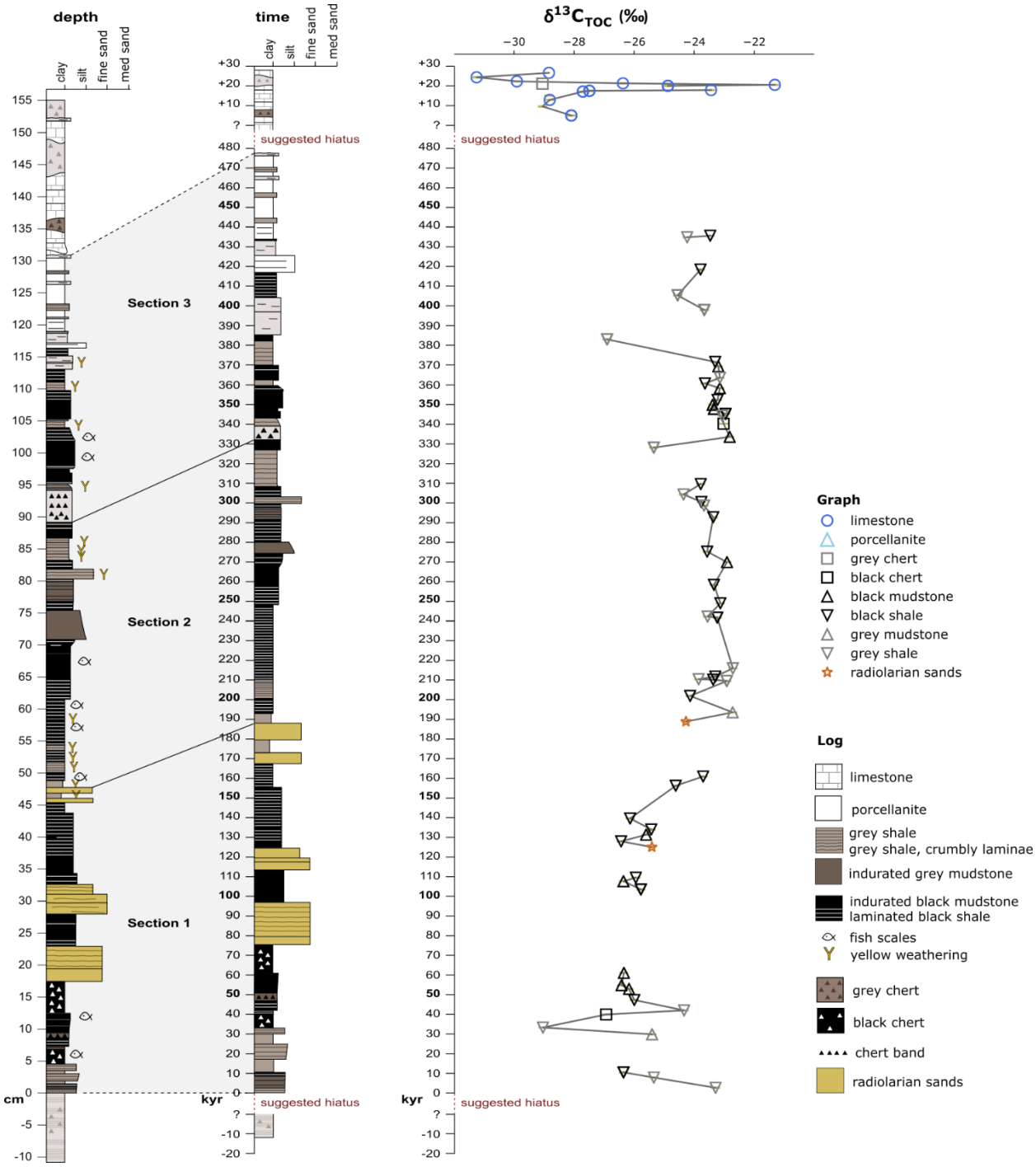

Figure 5.6: Log of the Bonarelli Level plotted against depth and time (bed durations from $^{3}He_{ET}$ timescale).

Previous studies linking the expression of the Bonarelli Level to orbital forcing assume that the interval of black-shale deposition lasted ~490 kyr, very similar to the timespan calculated using the $^{3}He_{ET}$ method (Mitchell et al., 2008; Lanci et al., 2010; Batenburg et al., 2016). Though different phases of the orbital forcing that drove OAE 2 are proposed in these different studies, all note that the abnormal conditions under which the Bonarelli Level was deposited must have been sustained over at least one long eccentricity cycle (i.e., longer than 400 kyr), an observation confirmed by the results of this study.

The Bonarelli Level duration calculated in this study is expected to be less than the total duration of OAE 2, though estimates of how much less vary depending on the interpretation of the stable carbon-isotope record of the Bonarelli Level and its correlation to more continuous stratigraphic records elsewhere. One interpretation of the stable carbon-isotope record is that the OAE 2 excursion plateau of high $\delta^{13}C_{carb}$ and $\delta^{13}C_{TOC}$ values extends for around a metre above the Bonarelli Level (Tsikos et al., 2004; Batenburg et al., 2016). In this case the duration of deposition of the Bonarelli Level would be expected to be less than the total duration of the OAE 2 carbon isotopic excursion (CIE) as the end of the excursion plateau is interpreted as some distance stratigraphically above the top of the Bonarelli Level.

This interpretation was contested, however, by Voigt et al. (2007) and Gambacorta et al. (2015), who proposed that the high $\delta^{13}C$ values measured in limestones above the Bonarelli Level instead reflect the later Turonian age of these beds, with the middle to upper part of the OAE 2 carbon-isotope excursion and the C–T boundary interval thought to be missing. Gambacorta et al. (2015) estimated a hiatus of ~320–470 kyr at Furlo by correlating $\delta^{13}C_{TOC}$ curves from Furlo and Wunstorf, Germany, and using the cyclostratigraphic timescale of Voigt et al. (2008); this interpretation, with correlation to the $\delta^{13}C_{TOC}$ curve of this study, is shown in Figure 5.7. In this case the duration of deposition of the Bonarelli Level would also be expected to be less than the total duration of the OAE 2 CIE, as the latter part of the excursion plateau is interpreted as being missing in this section.

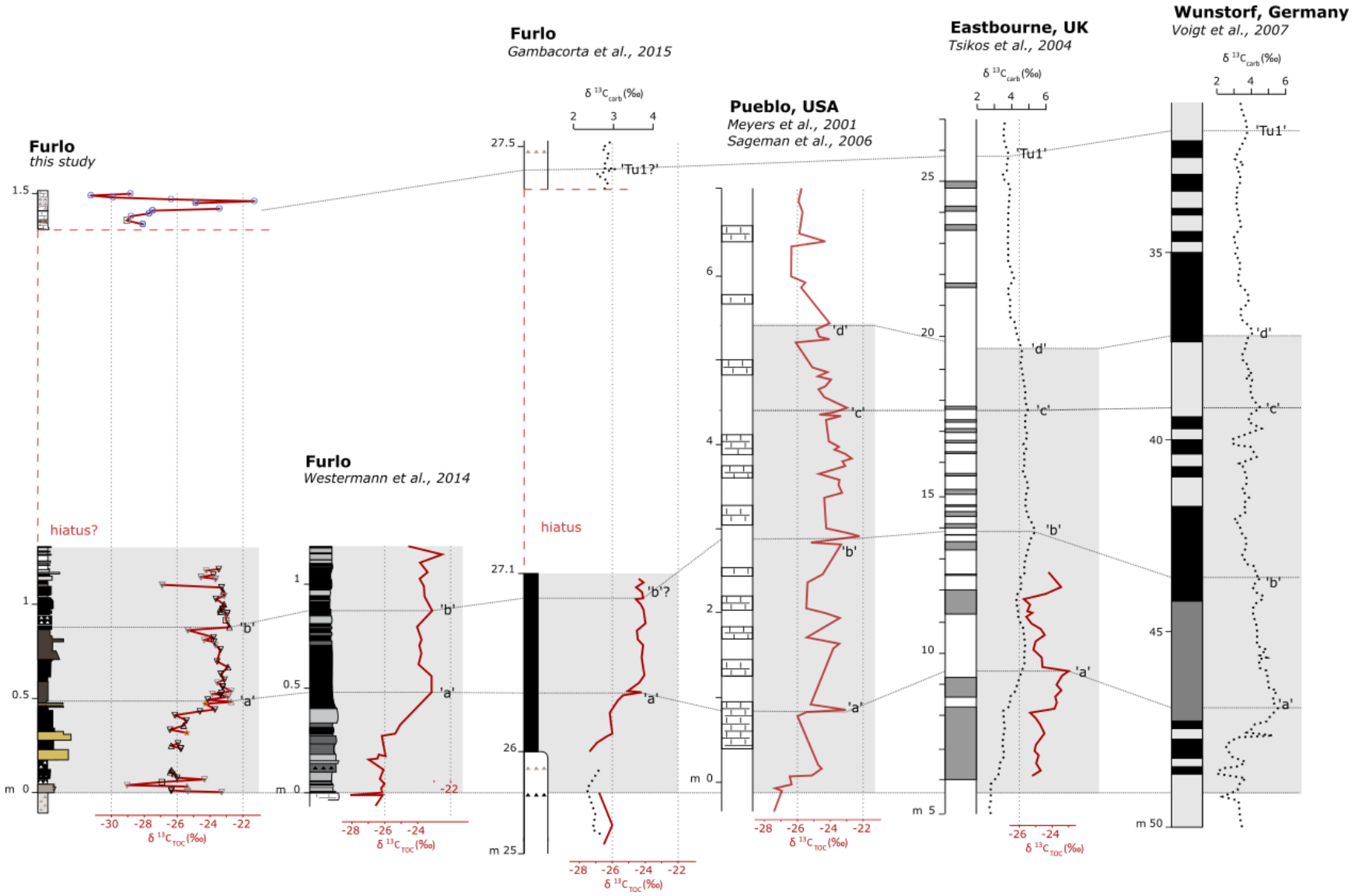
Furlo
this study
Furlo
Gambacorta et al., 2015
Furlo
Westermann et al., 2014
Pueblo, USA
Meyers et al., 2001
Sageman et al., 2006
Eastbourne, UK
Tsikos et al., 2004
Wunstorf, Germany
Voigt et al., 2007
hiatus?
hiatus
'Tu1?'
'Tu1'
'a'
'b'
'b'?
'c'
'd'
δ 13Ccarb (‰)
δ 13CTOC (‰)
m

Figure 5.7: Comparison of $\delta^{13}C_{TOC}$ (red) and $\delta^{13}C_{carb}$ (black dashed) profiles through global sections spanning OAE 2 (after Gambacorta et al., 2015). The shaded area on each log indicates the span of the OAE 2 CIE following Jarvis et al. (2006, 2011) and labelling of peaks follows Voigt et al. (2007). A hiatus of disputed length (see body text) overlies the Bonarelli Level at Furlo; the $\delta^{13}C_{TOC}$ record of this study is presented following the interpretation of Voigt et al. (2007) and Gambacorta et al. (2015): that the upper part of OAE 2 and the Cenomanian–Turonian boundary are missing at Furlo.

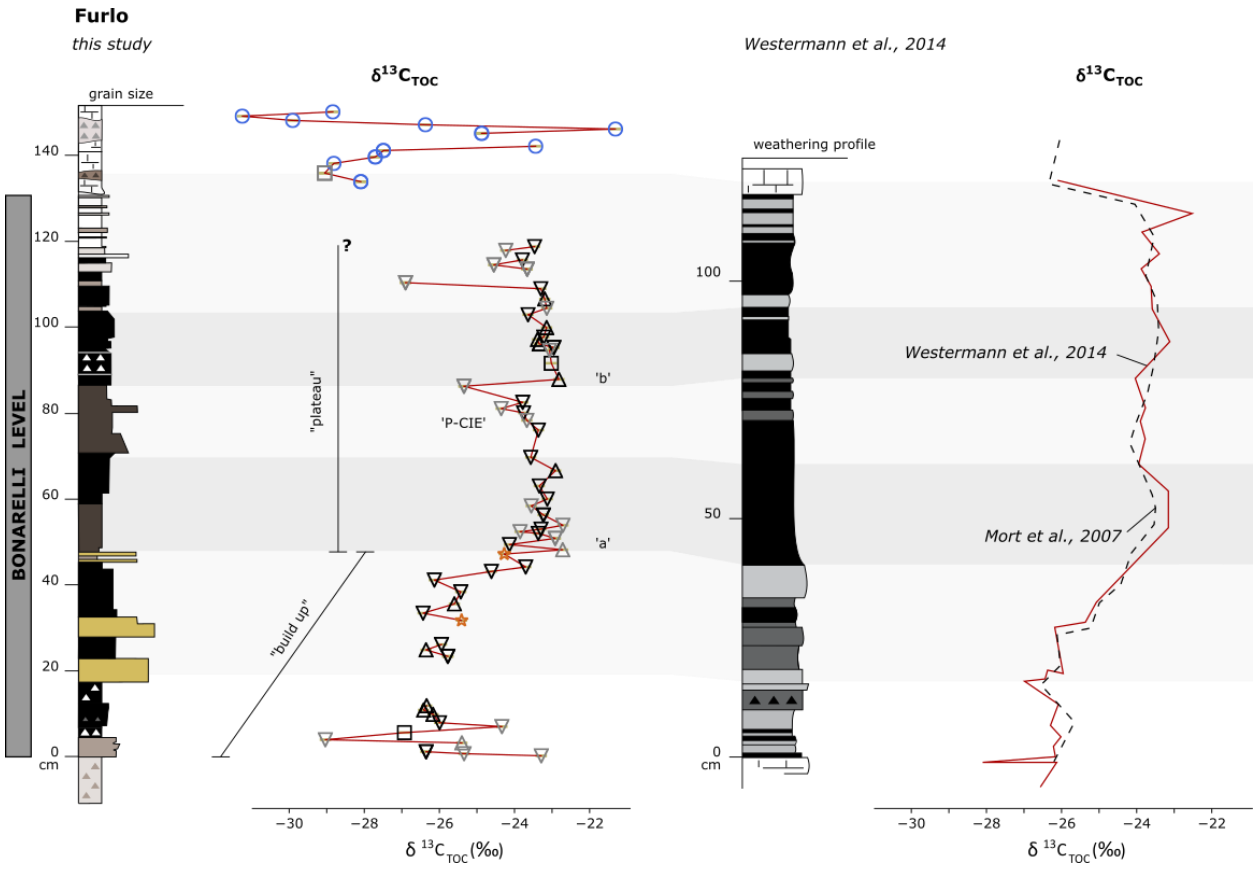

Figure 5.8: $\delta^{13}C_{TOC}$ curve through the Bonarelli Level at Furlo measured in this study, correlated to the carbon isotope curves of Mort et al. (2007) and Westermann et al. (2014) as presented in Westermann et al. (2014). Plenus carbon isotopic excursion is labelled 'P-CIE'. Carbon isotope peaks 'a' and 'b' are identified following Tsikos et al. (2004). Whilst the move to more positive carbon isotope values ("build up") is clearly visible in the isotopic record, the full extent of the high $\delta^{13}C_{TOC}$ "plateau" characteristic of OAE 2 is not recorded. Low TOC content in the upper Bonarelli Level prevented the measurement of $\delta^{13}C_{TOC}$ in those beds; in addition, the uppermost part of the OAE 2 plateau is suspected to be missing in the Furlo section due to a hiatus (Voigt et al., 2007; Gambacorta et al., 2015).

The total duration of the OAE 2 CIE has been calculated using cyclostratigraphy in sections judged to be more complete than those of the Umbria–Marche Basin. Although the cyclostratigraphic timescale of Voigt et al. (2008) in Wunstorf, Germany, estimates the duration of the OAE 2 CIE from its onset to the end of the "plateau" phase as only 430–445 kyr (shorter than this study's Bonarelli Level duration), longer estimates of CIE duration are typical from other global sections (e.g. 563–601 kyr, Sageman et al., 2006, Portland, USA; ~650 kyr, Li et al., 2017, Gongzha, Tibet). Using these latter estimates of OAE 2 CIE duration, and the duration of the Bonarelli Level determined in this study, it may be estimated that strata representing the final ~85–172 kyr of the CIE plateau are missing at Furlo.

$\delta^{13}C_{TOC}$ over the Bonarelli Level, as measured in this study, is correlated to the carbon isotope curve of Westermann et al. (2014) in Figure 5.8 and to global carbon isotope curves in Figure 5.7. The initial rise in $\delta^{13}C$ values is captured in the isotopic record (Figure 5.8); using the $^{3}He_{ET}$ timescale, this "build up" spans 174±58 kyr. The $^{3}He_{ET}$ timescale allows the refinement of the previous broad estimate of 130–310 kyr, calculated in an Umbria–Marche Basin section at Gorgo Cerbara by assuming a constant average sedimentation rate over the Bonarelli Level (Kuroda et al., 2007). The duration calculated in this study is similar to that estimated using a cyclostratigraphic timescale for the "build up" phase of the $\delta^{13}C$ record in the Western Interior Seaway, 149–178 kyr, by Ma et al. (2014), and to the older estimate of Sageman et al. (2006), ~240 kyr, in the same section, though is a little shorter than the 280±25 kyr duration estimated from a cyclostratigraphic timescale through an expanded Tibetan record by Li et al. (2017). The Carbon Isotopic Excursion, identified, following O'Connor et al. (2020), as the trough in $\delta^{13}C_{TOC}$ values between peaks 'a' and 'b' at a stratigraphic height of ~69–87 cm (see Figure 5.8) spans 58±21 kyr, comparable to the duration of ~65 kyr estimated by O'Connor et al. (2020) based on the age model of Kuhnt et al. (2017).

The Bonarelli Level has been divided into three sections on the basis of lithology (following Arthur and Premoli Silva, 1982; Cresta et al., 1989; Kuroda et al., 2005). Section 1 comprises ~48 cm of interbedded

organic-rich shales/mudstones and radiolarian sands and was deposited over 188±63 kyr (Figure 5.6). Overlying it, Section 2, ~42 cm of uninterrupted organic-rich shales and mudstones, was deposited over 144±48 kyr. Section 3, ~41 cm of organic-rich shales/mudstones interbedded with cherts and, increasingly, marls was deposited over 145±49 kyr. The average linear sedimentation rates over all three sections were similar: 0.253–0.288 cm/kyr. It is worth noting that *c.* 20 kyr couplets of 'radiolarian-rich' and 'organic-carbon-rich' lithologies (a suggested subdivision of the Bonarelli Level by Arthur and Premoli Silva, 1982; de Boer, 1982; Kuroda et al., 2005; Scopelliti et al., 2006; Trabucho-Alexandre et al., 2011) are not apparent from this time-scaled log.

5.4.2 Sedimentation rates through the Bonarelli Level

Overall average sedimentation rate through the Bonarelli Level (0.27±0.09 cm/kyr), as calculated using $^{3}He_{ET}$ concentration, is on the higher end of the range suggested by previous studies: ~0.13–0.26 cm/kyr (Arthur and Premoli Silva, 1982; Ohkouchi et al., 1999; Kuroda et al., 2005; Scopelliti et al., 2006; Mort et al., 2007), reflecting the short estimated duration. This study is unique in also providing a break down for sedimentation rate on a bed-by-bed level.

A wide range of sedimentation rates (0.04–1.13 cm/kyr) were determined for the mudstones and shales of the Bonarelli Level. This variation in sedimentation rate is not thought to be linked to changes in terrigenous input as there is no significant correlation between sedimentation rates in the Bonarelli Level and the flux of terrestrial ^{4}He (Figure 5.9a). It should be noted that, as $^{4}He_{terr}$ flux is influenced by both the flux of terrigenous material and the ^{4}He concentration of the terrigenous source rock, it is theoretically possible that times of increased terrigenous input may not be visible in the $^{4}He_{terr}$ flux record (if, for example, change in terrigenous input was accompanied by changes in provenance such that reduced ^{4}He concentrations in the source rocks exactly balanced out the volumetric increase in

terrigenous material). It is, however, judged to be more likely that the lack of correlation between sedimentation rates in the Bonarelli Level and the flux of terrestrial ^{4}He does indeed reflect a lack of varying terrigenous input. Instead, variations in accumulation rates of mudstones and shales are thought to be largely governed by variations in biosiliceous productivity, as explained below.

The accumulation rate of all sedimentary matter that is not organic carbon is calculated to give the 'non-OC' mass-accumulation rate. The carbonate content of Bonarelli Level sediments is negligible, so 'non-OC' mass-accumulation rate is dominated by the accumulation rates of biotic silica and abiotic clays (with some minor contribution from the accumulation of iron minerals such as pyrite, which may be sourced from an euxinic water column or from porewaters). Although the calculated 'non-OC' mass-accumulation rate encompasses abiotic material (the majority of which is ultimately of terrigenous origin) along with biotic silica, changes in this term are ascribed to changes in biotic silica as no correlation is observed between non-OC MAR and the flux of terrestrial ^{4}He (a proxy for terrigenous input, see Figure 5.9a). Nor is any correlation observed or between intervals of elevated non-OC MAR and intervals with high Al_2O_3 concentration (from Batenburg et al. (2016), see Figure 5.9c). Evidence supporting the proposed responsibility of changes in the accumulation rate of biotic silica for changes in 'non-OC' mass-accumulation rate might be provided if times of elevated 'non-OC' mass-accumulation rate corresponded to an elevated Si/Al ratio. Although time and equipment constraints prevented measurements of Si/Al from being carried out on the samples collected in this study, comparison of 'non-OC' MAR and Si/Al ratios measured by Batenburg et al. (2016) through the Bonarelli Level at Furlo does appear to show a co-incidence of intervals with both high OC and non-OC MARs (highlighted in green), and intervals with elevated Si/Al ratios (Figure 5.9c).

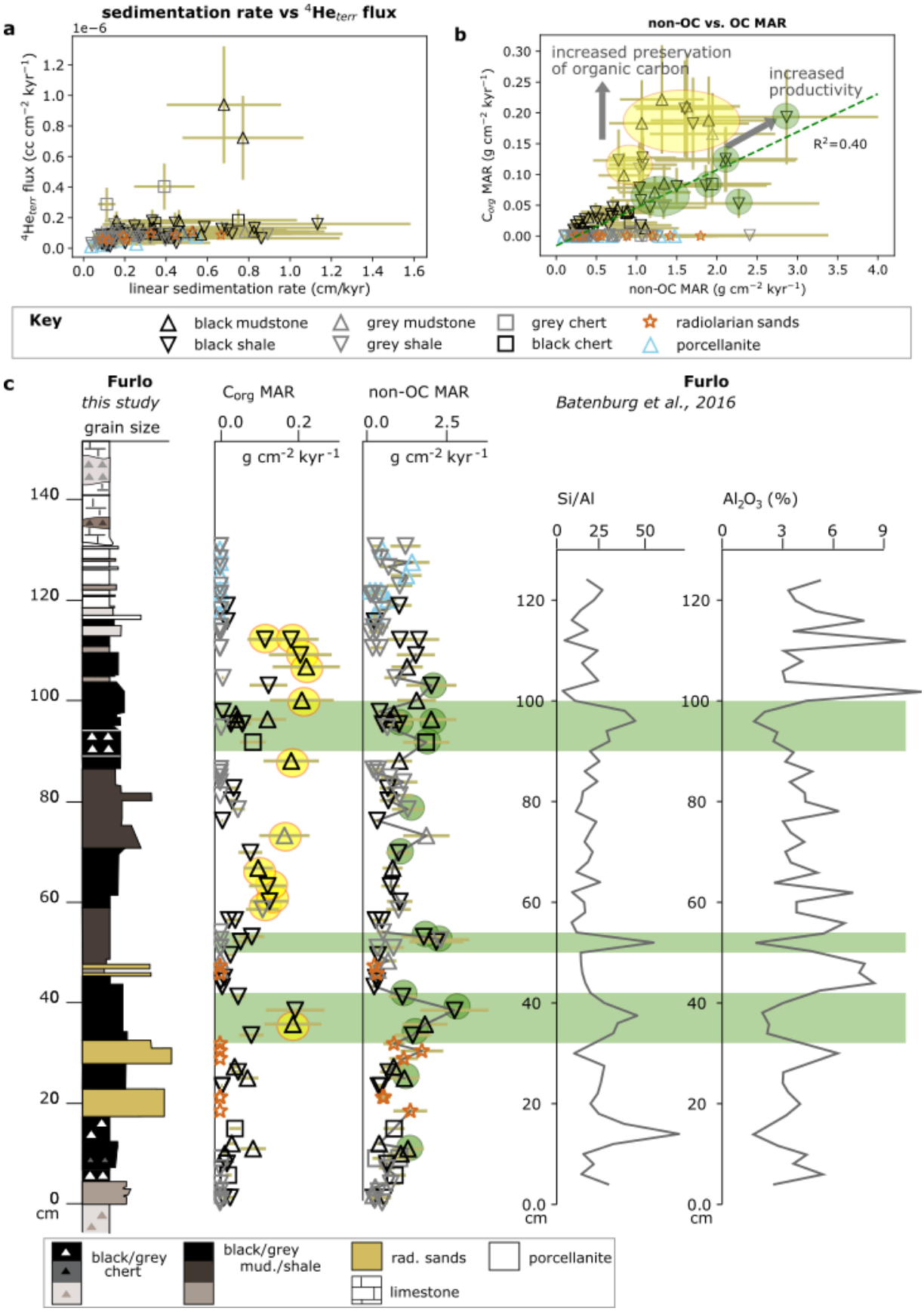
a
sedimentation rate vs $^4He_{terr}$ flux
1e−6
$^4He_{terr}$ flux (cc cm^{-2} kyr^{-1})
linear sedimentation rate (cm/kyr)
b
non-OC vs. OC MAR
increased preservation of organic carbon
increased productivity
R^2=0.40
C_{org} MAR (g cm^{-2} kyr^{-1})
non-OC MAR (g cm^{-2} kyr^{-1})
Key
black mudstone
black shale
grey mudstone
grey shale
grey chert
black chert
radiolarian sands
porcellanite
c
Furlo
this study
grain size
C_{org} MAR
non-OC MAR
g cm^{-2} kyr^{-1}
Furlo
Batenburg et al., 2016
Si/Al
Al_2O_3 (%)
cm
black/grey chert
black/grey mud./shale
rad. sands
limestone
porcellanite

Figure 5.9: Productivity-associated OC MAR elevation. ***(a)*** *Flux of terrestrial ^{4}He plotted against linear sedimentation rate. No significant correlation is observed;* ***(b)*** *organic-carbon mass-accumulation rate plotted against mass-accumulation rate of 'non-OC' material. As the proportion of carbonate material in Bonarelli Level sediments is negligible, 'non-OC' accumulation rate (the accumulation rate of all sedimentary components with organic carbon removed) is dominated by the accumulation of siliceous material, with some contribution from authigenic minerals such as pyrite. Increasing productivity results in a proportional increase in both organic-carbon and siliceous accumulation rates. 'High-productivity' samples are highlighted in green. A cluster of shales and mudstones, highlighted in yellow, lie off this productivity track and were likely deposited under more anoxic seafloor conditions that promoted organic-carbon preservation;* ***(c)*** *both OC and 'non-OC' mass-accumulation rates through the Bonarelli Level at Furlo are plotted against Si/Al ratios and Al_2O_3 concentration through a Bonarelli Level section sampled at the same outcrop by Batenburg et al. (2016). Suspected 'high preservation' samples are highlighted in yellow on the plot of OC MAR, with suspected 'high productivity' samples highlighted in green on the plot of 'non-OC' MAR. The co-incidence of intervals with both high OC and non-OC MARs (highlighted in green), and intervals with elevated Si/Al ratios (shaded in green), gives credence to the suggestion that these intervals represent times of increased productivity.*

If preservational conditions in the sediment remained the same, an increase in productivity would be expected to have increased the accumulation rates of both biogenic silica and organic carbon. Correlation between 'non-OC' and OC MARs is observed in the mudstones and shales of the Bonarelli (Figure 5.9b); following the line of reasoning above, this may indicate a coincident increase in deposition of biotic silica and organic carbon. It is worth noting that the increase in biotic silica MAR may not be a direct result of primary productivity: biotic silica in Cretaceous Tethyan Sediments is thought to be primarily supplied by radiolaria (Coccioni et al., 1992; Erbacher et al., 1996; Premoli Silva et al., 1999; Leckie et al., 2002; Erba, 2004; Erba and Tremolada, 2004), which are zooplankton rather than primary producers. However, an increase in primary productivity is likely to have the knock-on effect of increasing the number of radiolaria by increasing their food supply; in the modern oceans radiolaria are typically found in high-productivity upwelling zones (see reviews of Racki and Cordey, 2000; Lazarus, 2005).

A cluster of samples (highlighted in yellow on Figure 5.9b and Figure 5.10) lie above the proposed productivity track: this deviation may be a result of changing seafloor conditions, as intervals of euxinia promote the greater preservation of organic carbon. Some of these samples do indeed correspond to times when increased abundance of framboidal pyrite or enrichment in redox-sensitive trace metals suggests euxinic conditions (Kuroda et al., 2005; Westermann et al., 2014).

Four 'high OC MAR' intervals may be highlighted within the Bonarelli Level; stratigraphically these intervals span 33–42 cm, 54–75 cm, 87–94 cm and 98–113 cm (Figures 5.1, 5.10), and all correspond to samples above the proposed productivity track. The durations of these 'high OC MAR' intervals are 14 kyr, 65 kyr, 12 kyr and 34 kyr respectively; from this it may be concluded that more dysoxic/euxinic conditions were transiently established for 10s kyr within the Bonarelli Level. The stratigraphically highest 'high OC MAR' interval is, in fact, divided into three shorter intervals of 'high OC MAR' black shales and mudstones separated by two grey shale beds (see Figure 5.11). If these grey shales, which

contain negligible organic carbon, were deposited under conditions with poor OC preservation potential (i.e. more oxygenated conditions), the sub-10 kyr switching between black and grey beds is a testament to the rapidity with which different bottom water conditions were established then replaced during the deposition of the Bonarelli Level.

Unlike the noticeable difference between sedimentation rates measured in the cherts and black shales of the Scaglia Bianca precession cycles below the Bonarelli Level (see Chapter 4), sedimentation rates measured in Bonarelli Level cherts lie within the range of those measured in shales and mudstones. Linear sedimentation rates measured in Scaglia Bianca precession cycle cherts range from 1.2–2.8 cm/kyr, much higher than those measured in the Bonarelli Level: 0.11–0.75 cm/kyr. Interpretations of sedimentation rates measured in chert (a diagenetic lithology) are explored in more detail in Section 4.5.3 but the differences in sedimentation rates between the two chert groups may either be due to different diagenetic histories, or a difference in the primary (pre-chert) lithology. In the Bonarelli Level, black cherts containing up to 4% TOC follow similar patterns of 'non-OC' and organic-carbon accumulation to black shales and mudstones (Figure 5.9b), perhaps an indication that the primary lithology for these black cherts was something quite similar to black shales, and that, rather surprisingly, only relatively minor transfer of silica and differential compaction occurred between the different proto-lithologies. The positions of chert beds within the Bonarelli Level may reflect strata at which the formation of chert was promoted, perhaps due to the position of a stationary redox boundary (Williams and Crerar, 1985; Hesse, 1989), or slight differences in primary lithology (cherts may form at horizons containing a slightly elevated proportion of biogenic silica, with organic-matter-rich or clay-rich lithologies typically held to impede chert formation (see Hesse, 1988), though Abrajevitch (2020) suggests, conversely, that in bedded chert sequences chert horizons form at what were original clay-rich beds).

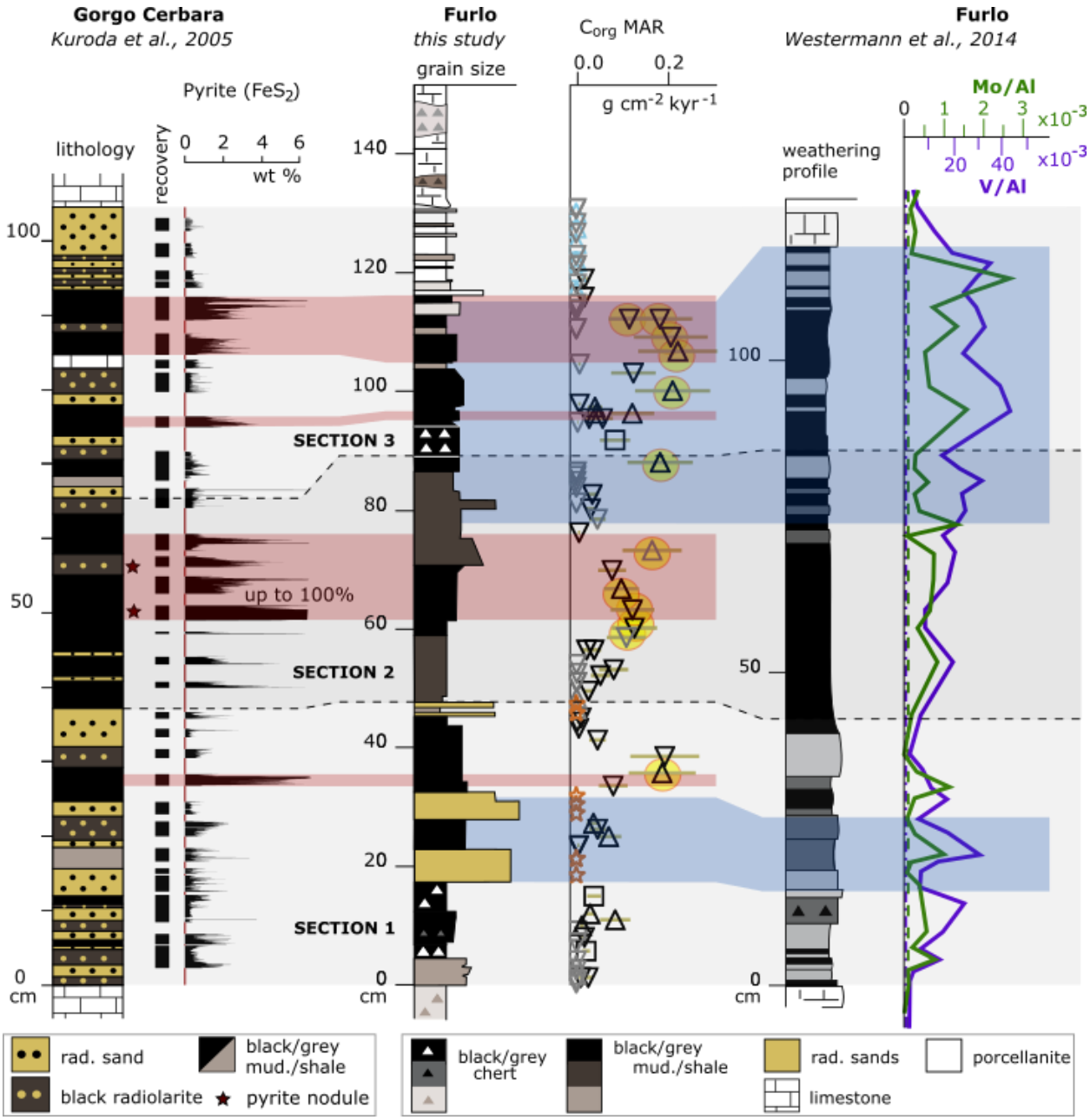

Figure 5.10: Samples in which OC MARs are thought to be elevated by enhanced preservation (highlighted in yellow circles) are compared to records of pyrite abundance (found as framboidal pyrite) from Kuroda et al. (2005) and redox-sensitive trace element (RSTE) enrichment from Westermann et al. (2014). Some yellow-highlighted samples can be correlated to more anoxic/euxinic intervals identified in these two records (highlighted in red and blue bars) – though not all RSTE-rich intervals can be correlated in this way. Note the incomplete sample recovery in the pyrite record of Kuroda et al. (2005): recovered samples are indicated as black bars. On the plot of Westermann et al. (2014), dashed lines represent the 'Post-Archean Average Shale' values from Taylor and McLennan (1985).

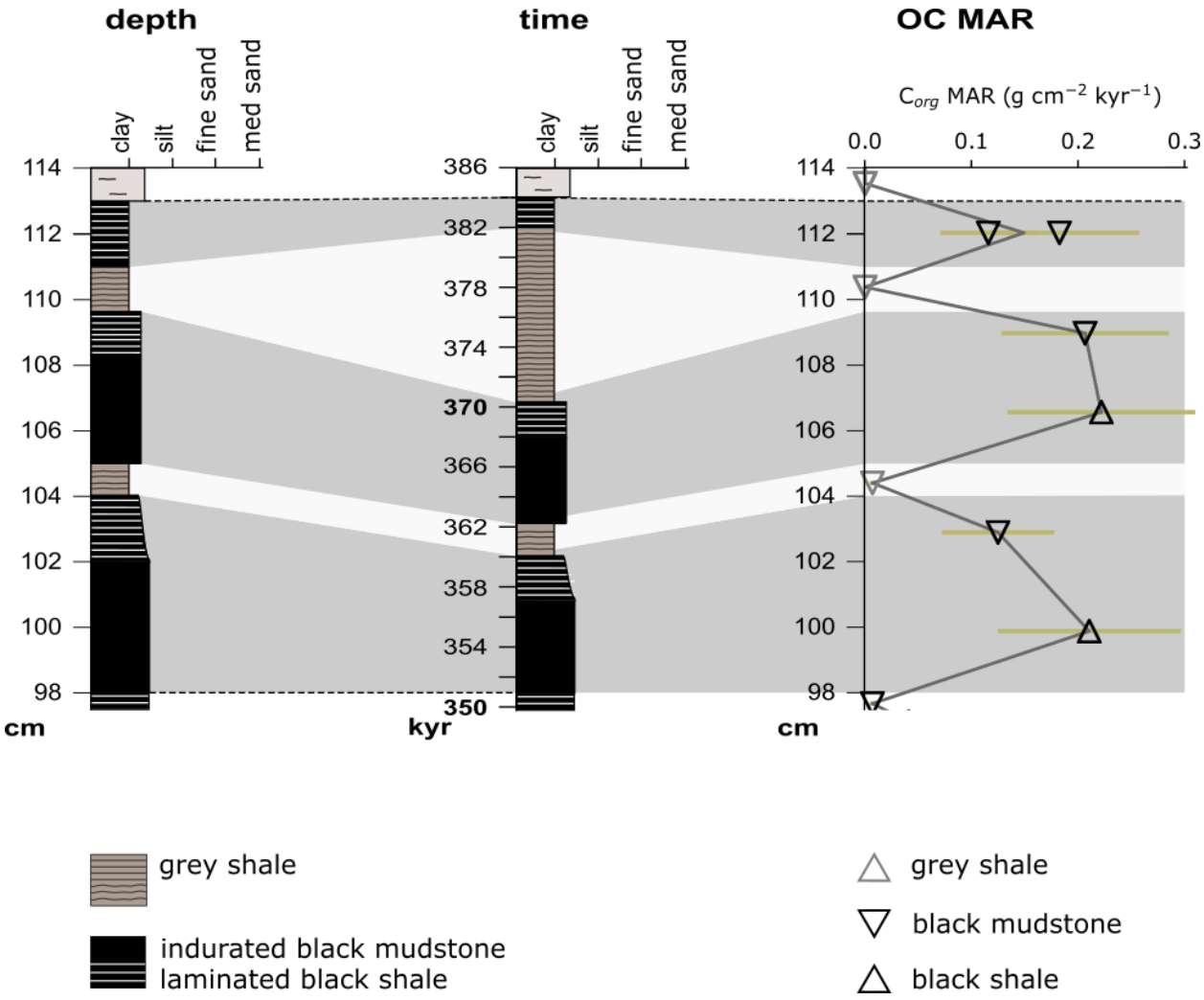

Figure 5.11: Detail of a 'high OC MAR' interval, presented against a scaled-time log.

The relationship between OC and 'non-OC' MARs in radiolarian sands appears to be different to that in the Bonarelli Level cherts described above; radiolarian sands contain virtually no organic carbon and across the lithology 'non-OC' MAR varies whilst organic-carbon MAR remains at a low constant value (Figure 5.9b). This finding would appear to cast doubt on the proposed correlation between primary productivity and radiolarian occurrence proposed above, though the relationship between 'non-OC' and organic-carbon MARs within radiolarian sands could be explained if the radiolaria in these beds have

been transported laterally. The hydrographic properties of radiolaria (low density, high surface area) make them easily redistributed: concentration of radiolaria in radiolarian sand beds by this mechanism would elevate 'non-OC' MAR with no significant change to OC MAR as radiolaria contain proportionally little organic carbon. (Additionally, radiolarian transport may have been from areas of more oxic bottom-waters.) The low linear sedimentation rates measured in radiolarian sands (0.09–0.67 cm/kyr), and the calculated bed durations of 1.8–17.5 kyr indicate that, if radiolaria were redistributed, each bed is likely to represent a collection of wash-in events (each of which would appear geologically instantaneous) over a longer background interval. If this is the case, however, it implies the existence of a high-productivity, radiolaria-rich zone elsewhere in the basin at this time from which the radiolaria were redistributed. Such a situation might indicate that productivity was elevated in different places across the basin at different times during the deposition of the Bonarelli Level. However, evidence of grading within the Bonarelli Level radiolarian sand beds, which might be expected if they were deposited following transport, is not found in any Umbria–Marche localities (Arthur and Premoli Silva, 1982).

Alternately, the low TOC content in these radiolarian sand beds may be due to poor preservation of organic matter (perhaps under brief windows of more oxygenated conditions), which could also cause a decoupling between measured organic-carbon and 'non-OC' MARs. In a similar vein, the low OC MARs observed in the porcellanite beds at the top of the Bonarelli Level (Figure 5.9b) seem particularly likely to be due to a return to better oxygenated conditions at the end of the period of black shale deposition. These porcellanite beds were deposited after the last grey shale bed containing a significant TOC (%), but before the return to limestone deposition (Figure 5.2).

5.4.3 Carbon cycle through the Bonarelli Level

$\delta^{13}C$ record

A brief negative excursion of ~4‰ close to the base of the Bonarelli Level over a ~3 cm interval between 3.5–6.8 cm can be identified in the $\delta^{13}C_{TOC}$ record (Figure 5.8). The duration of this excursion was calculated, using the $^{3}He_{ET}$ timescale, as 10.1±7.3 kyr. This negative excursion has been previously recognised in Umbria-Marche sections by Kuroda et al. (2007), and was hypothesised to be due either to local upwelling of water containing isotopically light dissolved inorganic carbon or, if correlatable to other negative $\delta^{13}C_{TOC}$ excursions observed at a similar stratigraphic height across the globe (e.g. in the North Atlantic; Erbacher et al., 2005), to be a result of the input of isotopically light carbon into the atmosphere through volcanic activity.

Organic-carbon mass-accumulation rates and productivity estimates

The distribution of OC MAR values calculated in this study (0.0–0.22 g/cm^2/kyr) is very similar to previous estimates from the Bonarelli Level (0.0–0.35 g/cm^2/kyr, Mort et al., 2007). The most rapid OC MARs of ~0.2 g/cm^2/kyr measured in black shale and mudstone beds (the highest measured OC MAR was 0.22±0.09 g/cm^2/kyr in a black mudstone bed close to the top of the Bonarelli Level) are comparable to rates of organic-carbon accumulation measured in the Selli Level, the Italian expression of the Early Aptian OAE1a (Hochuli et al., 1999). OC MARs measured in the Bonarelli Level are much lower than OC MARs measured across OAE 2 in the rapidly accumulating sediments of the Northwest African Shelf (average OC MAR ~0.7 g/cm^2/kyr, maximum ~2.8 g/cm^2/kyr, Kolonic et al., 2005), which might be expected given the deeper water setting of the Umbria–Marche sediments.

It is worth noting that although calculated organic-carbon mass-accumulation rates are very high in certain beds, the overall OC MAR over the whole Bonarelli Level is much lower: 0.044±0.011 g/cm^2/kyr.

This smaller figure is largely a reflection of the fact that, despite the Bonarelli Level being an interval typified by its high organic-carbon content, not every bed is actually TOC-rich (see Figure 5.2). To drive this lithological variation considerable palaeoenvironmental changes are inferred to have occurred over the deposition of the Bonarelli Level. The 'overall Boneralli Level OC MAR' calculated in this study may be compared to the compilation of OC MARs over OAE 2 in the review of Owens et al. (2018), which range globally between 0.0–2.15 g/cm^2/kyr. As summarised by Owens et al. (2018), similar 'overall OC MARs' to that calculated in this study have been measured in marginal sediments from central Italy and Sicily, southern Spain, Turkey, the Western Interior Seaway and the northern margin of Africa (0.03–0.05 g/cm^2/kyr), with an average (area weighted) OC MAR across all ocean margins included in the review of 0.11 g/cm^2/kyr.

Covariation of overall mass-accumulation rate and OC MAR is discussed in detail above; in summary, both productivity and preservation are thought to govern organic-carbon mass-accumulation rate through the Bonarelli Level (see Figures 5.9, 5.10), an observation in tune with the growing understanding that both these processes are important in controlling organic-carbon accumulation over OAE 2 (Demaison and Moore, 1980; Pedersen and Calvert, 1990; Jenkyns, 2010).

The high Hydrogen Index (HI) and low Oxygen Index (OI) values measured in Bonarelli Level black shales and mudstones (Figure 5.3a) are consistent with a marine source for the organic carbon in these TOC-rich beds (Mort et al., 2007, following Espitalié et al., 1985). High HI values measured in these sediments are likely to reflect the fact that they have not been subject to (much) oxidation, which acts to lower the overall HI measured in sediments (Bouloubassi et al., 1999). There is a strong relationship in the Bonarelli Level samples between HI and TOC content (Figure 5.3b), and high TOC content is known to result in better preservation of high-HI organic matter in sediments (Hartman-Stroup, 1987; Bouloubassi et al., 1999).

Estimating productivity from organic-carbon mass-accumulation rates is complicated by the effects of sedimentation rates and redox conditions on the preservation of organic carbon (see Canfield, 1994). Organic-carbon productivity rates estimated for high OC MAR sediments are presented in Table 5.3 using two different preservation factors (preserved OC/gross primary production) for organic carbon in anoxic black shales. The first of these preservation factors (2%) is derived from a comparison to the Holocene Black Sea, and has been used previously by Bralower and Thierstein (1984) and Pratt and King (1986) to estimate primary productivity in Cretaceous black shales. The second of these preservation factors is calculated using the relationship between bulk sediment MAR and preserved OC/export OC from Aller (2014), allowing the determination of a preservation factor specific to a sample's bulk mass-accumulation rate, a factor known to strongly impact OC preservation potential (Müller and Suess, 1979; Canfield, 1994; Aller, 2014). Preservation factors of exported organic carbon were estimated for each black-shale bed in Table 5.3 by comparison with the preservation factors measured in modern O_2-depleted settings collected in Aller (2014) (see Figure 4.14). A further 30% reduction in preservation factor was applied to account for later diagenetic organic-carbon loss (following Berner, 1982; Bralower and Thierstein, 1984; Pratt and King, 1986), and export OC estimates were converted into primary productivity using the relationship of Eppley and Peterson (1979) – where total primary productivity <200 $gC/m^2/yr$:

$$\text{primary productivity} = (\text{export productivity}/0.0025)^{0.5}$$

Equation 5.2

It should be noted that, although the second method of estimating preservation factors in black shales detailed above is tailored to account for variations in bulk mass-accumulation rate, the effects of changing redox conditions are impossible to quantify. For example, a sub-set of high-OC MAR beds are thought to have been deposited in conditions more favourable to organic-carbon preservation (see

Figure 5.10), so it may not be appropriate to use the same relationship between bulk MAR and preservation factor for these two groups of samples. These two groups are differentiated in Table 5.3; it is possible that preservation factors in 'productivity-dominated' samples may be relative overestimates (and productivity rates therefore relative underestimates).

Using a 2% preservation factor, black shales and mudstones with the highest OC MARs of 0.17–0.22 gC/cm^2/kyr may have been associated with productivity rates of ~80–110 gC/m^2/yr, comparable to rates estimated in OAE 2 sediments on the Northwest African shelf (~40–100 gC/m^2/yr, Kolonic et al., 2005), and elevated compared to modern open-ocean productivity rates of ~30 gC/m^2/yr (Demaison and Moore, 1980; Falkowski et al., 1998). Using preservation factors dependent on bulk MAR, following Aller (2014), productivity rates are estimated at a more modest ~60–75 gC/m^2/yr, although these are still elevated compared to modern open-ocean values. Both estimates of primary productivity are significantly lower than modern productivity rates in 'high productivity' upwelling settings such as the west coasts of Africa and South America, which reach at least ~300–400 gC/m^2/yr (Falkowski et al., 1998; Behrenfeld et al., 2005). In light of the discussion above on the multitude of hard-to-quantify factors that impact the preservation of organic carbon, all numerical estimates of productivity rates should, however, be treated with extreme caution.

sample height (cm)	bulk MAR ($g/cm^2/kyr$)	OC MAR ($gC/cm^2/kyr$)	preservation factor	primary productivity ($gC/m^2/yr$)
106.55	1.54	0.222	2% 3%	111 74
99.90	1.84	0.211	2% 3%	105 69
108.95	1.81	0.207	2% 3%	103 69
38.40	3.06	0.193	2% 3%	97 61
35.60	2.08	0.188	2% 3%	94 66
87.85	1.25	0.183	2% 3%	92 71
112.00	1.88	0.183	2% 3%	91 65
73.05	2.11	0.166	2% 3%	83 62

Table 5.3: Primary productivity values estimated for all samples with organic-carbon mass-accumulation rates higher than 0.15 $gC/cm^2/kyr$. Two different estimates of primary productivity are provided using two different organic-carbon preservation factors (organic carbon preserved in sediment/primary productivity). The first listed preservation factors of 2% follow values commonly used in Cretaceous shales (Bralower and Thierstein, 1984; Pratt and King, 1986). The second listed preservation factors are calculated based on measured bulk mass-accumulation rate (following Aller (2014), full description in text). Samples highlighted in grey are thought to have been deposited under conditions of enhanced preservation, as determined in Figures 5.9b and 5.10.

5.4.4 Condensed horizons

The $^{3}He_{ET}$ timescale provides some evidence for slowdowns in sedimentation rate at the top and base of the Bonarelli Level. 'Spikes' in $^{3}He_{ET}$ concentration may indicate condensed horizons or hiatal surfaces: in intervals where oceanographic conditions caused pelagic sedimentation to cease without halting the accumulation of interplanetary dust particles, a high concentration of helium-bearing IDPs may build up on a particular horizon. Examination of condensed horizons and slowdown intervals using this study's high-resolution $^{3}He_{ET}$ timescale, in which instantaneous sedimentation rate is calculated for each bed, allows links to be made between accumulation rate, lithological change and prospective palaeoceanographic drivers.

Suspected 'spikes' in $^{3}He_{ET}$ concentration are highlighted in Figure 5.12. Using this method, slowly-accumulating intervals are identified at stratigraphic locations roughly consistent with the suggested hiatuses at the top and base of the Bonarelli level (Tsikos et al., 2004; Jenkyns et al., 2007; Voigt et al., 2007; Trabucho-Alexandre et al., 2011; Gambacorta et al., 2015). A potential condensed horizon close to the middle of the Bonarelli Level has also been identified.

Base of the Bonarelli Level

The interval of slow sedimentation at the base of the Bonarelli Level spans multiple beds, so does not seem to represent a hiatal 'surface' *sensu stricto*. Instead, what might more accurately be described as a 'slowdown' spans ~3.5 cm of shales and mudstones deposited coincident with the dramatic drop in carbonate content at the base of the Bonarelli Level, and immediately below the sharp negative $\delta^{13}C_{TOC}$ excursion (see Figure 5.12). These beds were deposited at an average rate of 0.12±0.04 cm/kyr, spanning 30±10 kyr. A hiatus at the base of the Bonarelli Level has previously been suggested on the basis of the abrupt jump in a number of isotopic records ($\delta^{13}C_{TOC}$, $\delta^{15}N$, $\delta^{57}Fe$) at this horizon (Jenkyns, 2010).

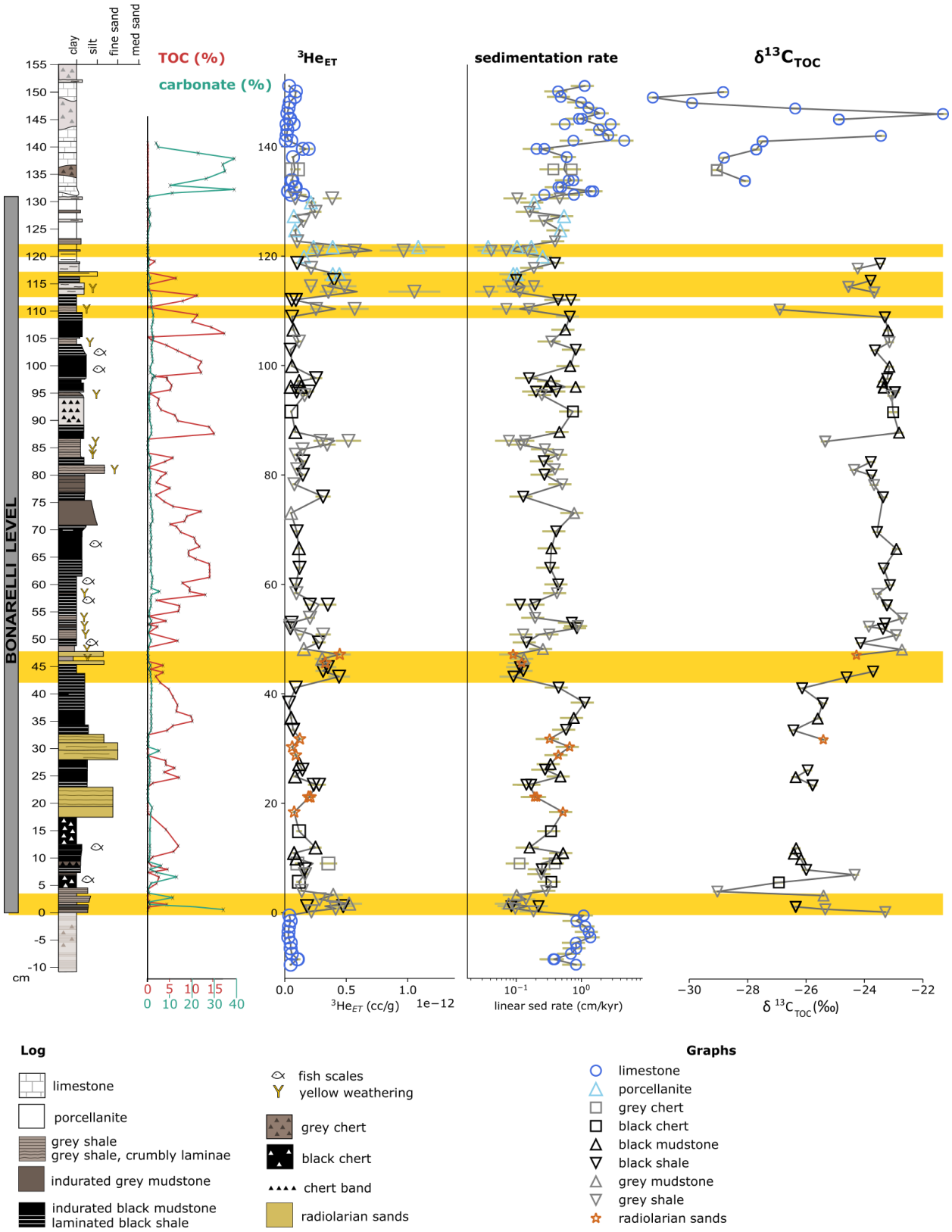

Figure 5.12: Lithological change over suspected condensed intervals. Periods of low sedimentation rate appear as spikes in the $^3He_{ET}$ record and are highlighted in yellow.

The sharp lithological shift at the base of the Bonarelli Level from a dominantly carbonate succession to black shales reflects a significant change in palaeoceanographic conditions. The lack of carbonate in the Bonarelli Level is a result of decreased carbonate accumulation due to either reduced preservation in an acidified ocean, and/or the out-competition of carbonate-producing plankton under changing nutrient conditions (Erba, 2004; Tiraboschi et al., 2009; Jenkyns, 2010; Du Vivier et al., 2015). This shut-off in the supply of carbonate material is likely to be a contributing factor in the decrease of the overall average sedimentation rate across the Bonarelli Level (0.27±0.09 cm/kyr) from that in the underlying Scaglia Bianca (1.1 cm/kyr, Batenburg et al., 2016). The simultaneous drop in both accumulation rate and carbonate content at the base of the Bonarelli Level is, therefore, not surprising; however, accumulation rates in the basal 'slowdown' interval are significantly lower than most of the rest of the Bonarelli Level (Figure 5.12), despite no change in the carbonate content, indicating that the accumulation of some other sedimentary component(s) must also have been important in controlling sedimentation rate over the basal 'slowdown'.

Identifying sedimentological differences between the shales and mudstones that make up the 'slowdown' interval and the overlying shales and mudstones is difficult: lithologically they appear very similar. It might be hypothesised that the 'slowdown' at the base of the Bonarelli Level represents an interval of reduced accumulation between the effective cessation of carbonate accumulation and the development of appropriate oceanographic conditions (i.e. anoxia) to preserve organic matter; however, the first bed containing significant TOC content lies within the 'slowdown' interval, and there is no obvious increase in organic-carbon mass-accumulation rate at the interval's end: both observations that are inconsistent with this hypothesis.

Another sedimentary component that might have influenced overall accumulation rate is terrigenous material; however, a significant change in terrigenous input over the basal 'slowdown' interval seems unlikely, as no significant change in terrestrial ^{4}He content is observed over this span.

The fourth and final significant sedimentary component in this succession is biogenic silica. The accumulation rate of biogenic silica was not directly estimated in this study, however, by a process of elimination it seems likely that rates of accumulation of siliceous skeletons were lower in the basal 'slowdown' interval than in the overlying Bonarelli Level. A change in nutrient regime over OAE 2 is thought to have led to an increase in siliceous plankton and hence an increase in the accumulation rate of skeletal silica (Gebhardt et al., 2010): the observed basal 'slowdown', therefore, is suggested to span the time between an effective cessation of carbonate accumulation and a ramp-up in biogenic silica accumulation.

Top of the Bonarelli Level

The presence or absence of a hiatus at the top of the Bonarelli Level has been debated. A proposed hiatus at the top of the Bonarelli Level, spanning ~320–470 kyr at Furlo, has been identified from $\delta^{13}C_{TOC}$ and $\delta^{13}C_{carb}$ records (Voigt et al., 2007; Gambacorta et al., 2015), though Batenburg et al. (2016) have questioned the presence of such an extensive hiatus on the basis of sedimentological and biostratigraphic evidence, as well as their own timescale through the event. No record of a hiatus of the magnitude suggested by Voigt et al. (2007) and Gambacorta et al. (2015) is present in this study, though due to the nature of the $^{3}He_{ET}$ record this does not constitute proof of its absence. Although spikes in $^{3}He_{ET}$ concentration may be used to identify condensed horizons, they will not be present if, during a hiatus, sediment has been entirely removed. Erosive surfaces have been identified at the top of the Bonarelli Level (Trabucho-Alexandre et al., 2011; Gambacorta et al., 2015), so it is eminently possible that a hiatus may exist unrecorded.

The $^{3}He_{ET}$ record does, however, provide evidence of a gradual slowdown in sedimentation rate towards the top of the Bonarelli Level (~20 cm below its uppermost bed or ~100 kyr before its end, from ~110–

122 cm on Figure 5.2). This putative slowdown took place through ~12 cm of grey shales and porcellanites, alongside the final decline in TOC content, spanning ~85 kyr overall with an average sedimentation rate of 0.15±0.05 cm/kyr. This extensive interval may, however, be made up of at least three slowly accumulating intervals, as highlighted in Figure 5.12.

The lowermost of these slowly accumulating intervals, a single ~1 cm-thick grey shale bed (at ~110 cm on Figures 5.1, 5.12), is thought to have been deposited at a rate of 0.11±0.04 cm/kyr, spanning ~11 kyr. Above this, ~4 cm of grey and black shale capped by the lowest porcellanite of the section (~113–117 cm on Figures 5.1, 5.12), were deposited at an average rate of 0.10±0.03 cm/kyr, spanning ~40 kyr. The uppermost slow interval is made up of a grey shale and porcellanite (~1 cm total, ~121–122 cm on Figures 5.1, 5.12) and was deposited at an average rate of 0.10±0.03 cm/kyr, spanning ~12 kyr. It should be noted when considering these intervals that $^{3}He_{ET}$ enrichment in beds may have occurred either through the slow accumulation of the beds themselves, or by discrete $^{3}He_{ET}$-rich condensation surfaces at the tops or bases of measured beds contributing to their apparent $^{3}He_{ET}$ content. Erosion associated with gaps in sedimentation at these horizons may mean that their calculated duration is an underestimate.

It has been suggested that a hiatus at the top of the Bonarelli Level may have occurred due to a combination of erosion and reduction in sedimentation rates associated with the changeover from biogenic silica and organic matter deposition to carbonate deposition (Gambacorta et al., 2014, 2015). Though the effect of erosion cannot be determined from $^{3}He_{ET}$ measurements, the ~85 kyr slowdown in accumulation rate referenced above coincides with a shift in lithology from grey and black shales containing significant TOC to porcellanites (Figure 5.4a). These observations suggest that the interval of low to non-accumulation at the top of the Bonarelli Level occurred coincident with a change to less favourable conditions for organic-matter preservation (i.e. increased oxygenation and/or decreased primary production).

The first bed with significant carbonate content (at ~131 cm on Figures 5.1, 5.12) sits around 15 cm above the uppermost black shale bed (at ~116 cm), a 'lag time' of ~60 kyr, with porcellanite being the dominant lithology in this transitional interval. The total diagenetic replacement of the original lithology of these porcellanite beds by microcrystalline quartz (Figure 5.4) makes it complicated to interpret this lithology in the context of environmental shifts. It is possible that the microcrystalline quartz matrix of the porcellanites is a replacement of an original micritic matrix (a common mechanism for porcellanite formation, e.g. Madsen and Stemmerik, 2010); no trace of this potential 'original' carbonate mineralogy remains in thin section, however. Alternatively, as is proposed for the black cherts lower in the Bonarelli Level, the 'original' lithology of these porcellanite beds may have been carbonate-free and composed primarily of clays and the tests of siliceous organisms. Although no conclusive evidence exists for either of these processes, it seems likely that even if the 'original' lithology of what are now porcellanites contained some carbonate it was also significantly more silica-rich than the overlying limestone beds. This lithological pattern would indicate that the ~60 kyr interval of porcellanites represents the time between the return of more oxygenated conditions (which prevented the preservation of organic carbon) and the completion of the biotic turnover which restored carbonate deposition. The stratigraphically lowest few centimeters of these porcellanite beds form the upper part of the slowly accumulating interval described above (see Figure 5.12), suggesting this biotic turnover was associated with a decrease in accumulation rate.

The low organic-carbon content of the uppermost part of the Bonarelli Level meant that it was not possible to produce a $\delta^{13}C_{TOC}$ record through the upper slowdown interval, leaving the relationship of this slowdown to the chemostratigraphic record somewhat ambiguous. Carbon isotope curves spanning the Bonarelli Level produced by other studies suggest that this upper slowdown interval lies at the stratigraphic height of the 'plateau' phase of the carbon isotope excursion (e.g. Westermann et al., 2014, see Figure 5.8, also Tsikos et al., 2004; Gambacorta et al., 2015).

Other condensed horizons

Another pronounced spike in $^{3}He_{ET}$ occurs in the middle of the Bonarelli Level (~43 cm above its base, see Figure 5.12), representing ~5 cm of slowly accumulating beds (average linear sedimentation rate: 0.11±0.03 cm/kyr) spanning ~50 kyr. This condensed interval is lithologically nondescript, encompassing the uppermost 3 cm of a ~8 cm thick black shale, and two overlying radiolarian sand beds. Sedimentation rates in the Bonarelli Level black shales and mudstones are thought to have been largely controlled by productivity (see discussion above); this slowdown may therefore reflect a period of low productivity spanning ~50 kyr. The Plenus Cold Event, identified, following O'Connor et al. (2020), using the trough in $\delta^{13}C_{TOC}$ values between peaks 'a' and 'b' (see Figure 5.8), does not appear to be associated with a significant change in sedimentation rate.

5.4.5 Above the Bonarelli Level

Sedimentation rates are notably elevated in the limestones overlying the Bonarelli Level (see Figure 5.2). Peak sedimentation rates of ~2.7 cm/kyr were determined, with sedimentation rates most elevated through ~4 cm of limestone spanning ~3.5 kyr. The average linear sedimentation rate over this interval was 2.14±0.72 cm/kyr, notably higher than the average sedimentation rate measured in the limestones of Scaglia Bianca cycles at Furlo ~1.24±0.13 cm/kyr (though it should be noted that the large error bars on the elevated sedimentation rate estimate mean that, at their lowest and highest extent respectively, the ranges of sedimentation rates above the Bonarelli Level and average sedimentation rate in Scaglia Bianca limestones almost overlap).

This brief but distinct elevation in the sedimentation rate of the limestone beds above the Bonarelli Level may be compared to a similar feature observed following the Palaeocene–Eocene Thermal Maximum (PETM), another hyperthermal. Studies employing $^{3}He_{ET}$ timescales over this interval observe increases in the sedimentation rates of post-event carbonates to 2–4× the rate of 'background' carbonate sedimentation (Farley and Eltgroth, 2003; Murphy et al., 2010), comparable to the up to ~2× increase observed in the limestone sedimentation rates in this study.

After the PETM, rapid carbonate deposition has been linked to an 'overshoot' of the lysocline to below pre-PETM depths due to enhanced carbonate preservation under an oversaturated water column. The excess alkalinity that leads to the creation of these conditions may be contributed to by both "weathering-enhanced chemical compensation", the subsequent addition of HCO^{-}_{3} ions from silicate weathering after the acidity from invasion of atmospheric CO_2 has been neutralised by dissolution of carbonate during the PETM (Kelly et al., 2005; Zachos et al., 2005; Zeebe and Zachos, 2013; Penman et al., 2016), an interpretation favoured by Murphy et al., (2010), and/or through "biological compensation", the build-up of alkalinity over the PETM caused by the reduction of carbonate productivity during this interval (Luo et al., 2016; Boudreau et al., 2018; Frieling et al., 2018).

Similar conditions may be influencing the rapid limestone deposition seen above the Bonarelli Level. It seems likely that the lack of carbonate in Bonarelli Level sediments (Figure 5.2) is due to a decrease in the abundance of calcifying plankton during its deposition: a decrease in the rain rate of carbonate both decreases the amount of bulk carbonate material being delivered to sediments and results in a shallowing of the carbonate compensation depth (CCD) and the snowline, decreasing carbonate preservation (e.g. Boudreau et al., 2010). Unlike over the PETM, where dissolution of carbonate in deep-sea sites has been fairly universally attributed to deep-ocean acidification (see reviews of McInerney and Wing, 2011; Hönisch et al., 2012), proponents of ocean acidification over OAE 2 such as Du Vivier et al. (2015) have suggested that it occurred over only a relatively brief period in the early part of the OAE.

Hence, a decrease in carbonate supply due to a decrease in carbonate productivity is the most compelling explanation for the lack of carbonate in the Bonarelli Level. Erba (2004) suggested that the observed decrease in abundance, diversity and productivity of carbonate nannofossils over OAE 2 in Italy may have been due to a combination of out-competition by siliceous plankton under more nutrient-rich conditions, as well as the deleterious effects of toxic metals released by hydrothermal plumes and (possibly) higher water temperatures. Under these conditions of low carbonate productivity excess alkalinity could build up, leading to a deepening of the CCD across the basin and enhanced carbonate accumulation post-event (as described in the context of the PETM by Luo et al., 2016 and more generally by Boudreau et al., 2018).

Provision of HCO^{-}_{3} ions from intensified silicate weathering is also very likely to have occurred over OAE 2 (Frijia and Parente, 2008; Blättler et al., 2011; Pogge von Strandmann et al., 2013). Evidence suggests that the 'peak' of silicate weathering occurred towards the start of the OAE, in the first ~200 kyr, though a slow return to conditions similar to the 'pre-event' weathering regime (as characterised by $\delta^{7}Li$ isotopes) was not completed until after the termination of OAE 2 in some Italian sections (Pogge von Strandmann et al., 2013). Even if the peak of silicate weathering intensity actually occurred earlier than the deposition of the rapidly accumulating limestones above the Bonarelli Level, the HCO^{-}_{3} ions provided would have been able to linger in the ocean thanks to the predicted decline in calcifying plankton over OAE 2 (described above) and so partially contribute to the excess alkalinity driving rapid carbonate accumulation after the event.

Peak carbonate sedimentation rates were not reached until ~20 kyr after the end of deposition of the Bonarelli Level (defined by the transition to carbonate dominated sediments), though a slight increase in sedimentation rate does seem to be associated with the lithological change at this boundary. The duration of the time-interval between the deposition of the last Bonarelli Level bed and the peak carbonate sedimentation rates may be even longer if there is significant 'missing time' at the top of the

Bonarelli Level (Voigt et al., 2007; Gambacorta et al., 2015; c.f. Batenburg et al., 2016). This 'ramp-up' interval may reflect the time taken for the full re-establishment of a planktonic ecosystem dominated by carbonate-producers in this region. After the PETM, peak carbonate sedimentation rates were also reached ~10–40 kyr after the lithological return to carbonate sediments (Farley and Eltgroth, 2003; Murphy et al., 2010); the timing of the observed post-PETM 'overshoot' is proposed to have been controlled by the timing of the CO_2-dependant silicate weathering feedback (ultimately controlled by the timing of carbon release) and/or the timing of carbonate productivity recovery (Luo et al., 2016; Penman et al., 2016).

Observed differences in the scale and timing of post-event increased carbonate accumulation following OAE 2 and the PETM are likely to derive from differences in the causes and extent of excess alkalinity. Prior to discussion of these differences it should be noted that as changes in water column carbonate saturation during extreme climatic perturbations such as the PETM are known to be of different magnitudes in different ocean basins (Zeebe and Zachos, 2007), and the high-resolution post-event sedimentation rate records compared in this discussion are drawn from only a handful of sites, comparisons made are truly only between the post-OAE 2 Neotethys margin (this study) and the post-PETM South Atlantic and Southern Ocean (Farley and Eltgroth, 2003; Murphy et al., 2010). More OAE 2 sites in particular would need to be examined before broad statements about carbonate saturation over the ocean system as a whole during these events could be made. In making a comparison it is also important to point out that palaeoenvironmental interpretations of both the record of OAE 2 examined in this study and the records of the PETM mentioned above place these sections at similar relative paleodepths at the time of their deposition, somewhat above the CDD (Furlo: Arthur and Premoli Silva, 1982; Kuhnt, 1990; Bernoulli and Jenkyns, 2009, ODP Site 690: Thomas, 1990; Farley and Eltgroth, 2003, IODP Site 1266: Zachos et al., 2005; Murphy et al., 2010).

The relative magnitude of post-event 'peak' sedimentation rates (compared to background sedimentation rates) are rather lower in the post-Bonarelli Level limestones of Furlo (~2× background) than in measured post-PETM limestones (2–4× background: Farley and Eltgroth, 2003; Murphy et al., 2010), and the duration over which accumulation rates were elevated was also much shorter post-Bonarelli Level. Whilst it is possible that the section sampled in this study does not fully capture the 'tail end' of rapid accumulation, the distinctive 'spike' in sedimentation rates lasted ten times longer post-PETM than post-Bonarelli Level in the settings where this has been quantified; elevated sedimentation rates persisted over ~30–50 kyr post-PETM in the South Atlantic and Southern Ocean (Farley and Eltgroth, 2003; Murphy et al., 2010) and ~3 kyr post- Bonarelli Level. The rather lower and shorter sedimentation rate peak observed following the deposition of the Bonarelli Level in Furlo could reflect a less dramatic shift in the CCD at the time. This difference may partially be due to differences in palaeogeographic setting; as mentioned above, sections used for comparison of post-event carbonate accumulation between the PETM and OAE 2 are drawn from only a handful of sites. The post-PETM overshoot is, for example, known to be more minor in the Pacific Ocean than in the Atlantic (Leon-Rodriguez and Dickens, 2010; Luo et al., 2016), though the lack of a high-resolution timescale across a Pacific PETM record prevents comparison with the OAE 2 record of this thesis. Differences in the magnitude and duration of the post-event carbonate accumulation rate peak may also reflect a less extreme decrease in the productivity of calcifying organisms during OAE 2, or lower post-event alkalinity input from weathering compared to the PETM, though these factors are difficult to unpick from the effects of palaeogeographic setting with existing evidence.

5.5 Conclusion

In conclusion, this study presents a new estimate of the duration of deposition of the Bonarelli Level at Furlo of 478±160 kyr using the novel $^{3}He_{ET}$ sedimentation-rate proxy to construct a high-resolution timescale. This estimate of duration is at the shorter end of those proposed by previous Bonarelli Level studies: 320–800 kyr (Ohkouchi et al., 1999; Scopelliti et al., 2006; Turgeon and Brumsack, 2006; Trabucho-Alexandre et al., 2011; Batenburg et al., 2016), but is very similar to recent duration estimates derived using cyclostratigraphy: ~490 kyr (Mitchell et al., 2008; Lanci et al., 2010; Batenburg et al., 2016), confirming that the conditions under which the Bonarelli Level was deposited were sustained over at least one long eccentricity cycle. The initial rise in $\delta^{13}C_{TOC}$ spans 174±58 kyr, comparable to the duration estimated for this "build up" using cyclostratigraphy in the Western Interior Seaway (149–178 kyr, Ma et al., 2014) and slightly shorter than the duration determined cyclostratigraphically in the Tibetan record (280±25 kyr, Li et al., 2017). The Plenus Carbon Isotopic Excursion (as defined by O'Connor et al., 2020) spans 58±21 kyr, comparable to the previous (cyclostratigraphic) duration estimate of ~65 kyr (O'Connor et al., 2020). The large error bars on $^{3}He_{ET}$-derived duration estimates are due to uncertainties in the chosen background flux (see further discussion in Section 4.5.1). Nevertheless, $^{3}He_{ET}$ timescales remain an immensely powerful tool for investigating high-resolution changes.

Within the Bonarelli Level itself, rapid changes in lithology are reflected in varying sedimentation rates and, particularly, large differences in organic-carbon mass-accumulation rate. Although, for example, the average OC MAR over the Bonarelli Level is 'only' 0.044±0.011 g/cm^2/kyr, peak OC MAR values of up to 0.222±0.088 g/cm^2/kyr are measured in some beds. These rapidly shifting lithologies reflect short-term changes in local palaeoenvironmental conditions. For example, where increases in 'non OC' accumulation rate and OC MAR covary in organic-rich shales and mudstones, the driver for changes in

accumulation rate was likely to have been changes in biological productivity. Estimates of primary productivity in beds with high OC MARs range between 60–110 gC/m^2/yr, a figure that is elevated above modern open ocean values, if lower than those from modern upwelling zones (Demaison and Moore, 1980; Falkowski et al., 1998; Behrenfeld et al., 2005) . Other sedimentary changes were likely driven by changes in redox conditions, with beds within the Bonarelli Level largely devoid of organic carbon – typically radiolarian sands and some organic-poor mudstones – deposited under more oxygenated conditions less favourable to the preservation of organic matter. At the other end of the scale, some black shale and mudstone beds appear to show enhanced organic-carbon accumulation related to deposition under more anoxic or even euxinic conditions; these beds correspond stratigraphically to intervals found by other studies to be enriched in framboidal pyrite or redox-sensitive trace elements (Kuroda et al., 2007; Westermann et al., 2014).

The most dramatic fluctuation in sedimentation rate within the Bonarelli Level is the condensed interval identified ~40 cm above its base: a ~5cm interval composed of black shale and radiolarian sand that was deposited over ~50 kyr at a sedimentation rate of 0.11±0.03 cm/kyr (much lower than the overall average sedimentation rate over the Bonarelli Level of 0.27±0.09 cm/kyr), which may represent a prolonged interval of low primary productivity and biotic silica production. Combined, the above observations demonstrate that the Bonarelli Level was deposited under conditions of rapid palaeoenvironmental change within an overall highly productive, siliceous-dominated regime with variably dysoxic to euxinic bottom waters.

The lithological shift from the rhythmically bedded limestones and cherts of the Scaglia Bianca to the black shale-dominated Bonarelli Level reflects a biotic turnover from an ecosystem dominated by calcifying plankton to one dominated by non-mineralising and siliceous plankton, and *vice versa* for the shift back to a limestone-dominated succession stratigraphically above the Bonarelli Level (Cresta et al., 1989; Premoli Silva et al., 1999; Coccioni and Luciani, 2005; Musavu-Moussavou et al., 2007).

Slowdowns in accumulation rates identified at the top and base of the Bonarelli Level are suggested to be associated with this turnover period.

In a similar vein, the transient increase in carbonate accumulation rate to ~2× typical pre- and post-event values following the re-establishment of limestone deposition post-the Bonarelli Level (similar to that observed after other climatic perturbations such as the PETM (Farley and Eltgroth, 2003; Murphy et al., 2010)) is suggested to reflect enhanced carbonate deposition under conditions of excess alkalinity built up over OAE 2 due to the paucity of planktonic calcifiers over this interval.

6. Conclusions and Future Work

6.1 Conclusions

A condensed summary of the conclusions drawn from this study's work on the expansion of the use of $^{3}He_{ET}$ timescales into lithologically heterogeneous sections follows:

- The standard methodology developed for liberating helium from powdered sediments using a Fusions Diode .970 Laser Stepped Heating System in the Oxford Noble Gas Laboratory was able to successfully replicate measurements on a suite of pelagic carbonates made in other laboratories. The observed spread of measured replicates could be approximated using a Gaussian distribution with 1σ ~20%.

- Neon gas released from samples was overwhelmingly dominated by neon with an atmospheric isotopic signature, though contribution from radiogenic and extraterrestrial components were detected. No comparable contribution from an atmospheric source was observed in the helium released from samples, likely because the atmospheric component of noble gases in these samples was hosted in air-saturated water vapour sorbed to clays and the less soluble helium was easier to liberate during heating and evacuation.

- Chert diagenesis was confirmed not to liberate extraterrestrial helium, with no significant correlation across transects through chert nodules between the concentration of helium and the 'degree of chertification'.

- A 'best practice' method for determining background flux through lithologically heterogeneous sections was developed, with the homogenised mixture of the expression of a complete orbital cycle (in this study, a precession cycle) used as a base sampling 'unit' when measuring background flux. Multiple 'homogenised cycle' samples, measured at varying stratigraphic heights both before and after the interval of interest, provided an estimate of the variability in in the flux of incoming $^{3}He_{ET}$ over time.

The above methodological developments allowed $^{3}He_{ET}$ timescales to be constructed through selected limestone-(black shale)-chert cycles in the Scaglia Bianca Formation, Umbria–Marche, Italy. These cycles represent the sedimentary expressions of precession cycles, with cycles containing black cherts (and in some localities black shales) commonly believed to have been deposited during eccentricity maxima, and cycles containing grey chert during eccentricity minima (see de Boer, 1982, 1991; Beaudoin et al., 1996; Mitchell et al., 2008; Lanci et al., 2010; Batenburg et al., 2016; Gambacorta et al., 2019). Key insights from these $^{3}He_{ET}$ timescales were:

- Inter-cycle sedimentation rates varied by an order of magnitude in cycles containing black shale, with typical sedimentation rates measured in black shales ~0.1 cm/kyr, and sedimentation rates in cherts and limestones >1 cm/kyr. Slowly deposited marl was observed at the same stratigraphic height as black shale layers in outcrops where black shales were not present.

- No significant intra-cycle variation in the sedimentation rate of limestone beds was observed, implying that the environmental conditions impacting carbonate production and preservation during periods of limestone deposition did not change significantly between cycles.

- The marked increase in organic-carbon mass-accumulation rate (OC MAR) measured in black shales (up to ~0.025 g/cm^2/kyr) was a result of both enhanced preservation of organic carbon and an increase in primary productivity. Estimated primary productivity during deposition of black shales (30–59 gC/m^2/yr) was almost double that during limestone deposition (15–27 gC/m^2/yr), though all these productivity estimates fall within the range of expected values for 'low productivity regions' in modern oceans (Eppley and Peterson, 1979; Demaison and Moore, 1980; Falkowski et al., 1998).

- The length of time spanned by chert beds (0.6–2.4 kyrs) proves that the deposition of their primary lithology, believed to be radiolarian sand, did not occur in a single wash-in event, though it is impossible to distinguish between deposition of radiolarians through gradual rain from overlying waters over time, and multiple wash-in events of radiolaria over a protracted interval (as proposed by Gambacorta et al., 2014, 2016). Extraterrestrial ^{3}He-bearing particles were likely not redistributed during this process: average $^3He_{ET}$ concentrations over individual precession cycles do not vary between geographically separated outcrops across the Umbria–Marche basin. This result might be expected given the cohesive properties of $^3He_{ET}$-bearing particles and the much lower effective density (and hence easier remobilisation) of radiolarian tests. The identification in thin-section of a sub-millimetre thickness of 'transitional' lithology between black chert and black shale suggests that these two rock-types represent distinct primary lithologies, though it is still not entirely possible to rule out the distinction between black shale and black chert being entirely a result of diagenetic separation, as suggested by Salmon et al. (2003).

- Black chert beds at Furlo display an order of magnitude increase in the flux of terrestrial ^{4}He, likely indicating an increased flux of terrigenous material to the site at that time. The lack of any change in $^4He_{terr}$ flux across cycles in the Contessa section, separated from Furlo by only

~40 km today, implies highly local palaeogeographic control on the deposition of ^{4}He-bearing terrigenous material; the two sections likely derive from different sub-basins.

- The relationship between orbital forcing and lithological change over the sedimentary expression of these precession cycles is best explained using the concept of palaeoenvironmental 'thresholds', with black shales and cherts deposited when extremes of precessional forcing nudge the local palaeoceanographic system past some environmental threshold into a different depositional regime (following Batenburg et al., 2016). More time was spent below this threshold at eccentricity minima, when the amplitude of precessional forcing was low; cycles containing grey chert are composed of a higher proportion of limestone 'by time' (~90%) than cycles containing black chert, deposited under eccentricity maxima, where limestone only accounts for ~65% of the cycle 'by time'.
    - In palaeoenvironmental terms, this 'threshold' is proposed to reflect an increase in nutrients to a level at which an ecological change was initiated; under more eutrophic conditions, k-strategist calcareous plankton were replaced by r-strategist non-mineralising phytoplankton, with an associated increase in zootrophic radiolaria (a nutrient-driven ecological shift of this type has been described by Margalef, 1978; Premoli Silva et al., 1999; Leckie et al., 2002; Erba, 2004; Erba and Tremolada, 2004; Gebhardt et al., 2010). The increased $^{4}He_{terr}$ flux measured in black chert beds at Furlo indicates that these nutrients were terrestrially sourced, further evidence for the operation of 'monsoonal conditions' during black chert deposition (as proposed by Mitchell et al., 2008; Batenburg et al., 2016).

    - Deposition of a slowly accumulating lithology between limestone and black chert only occurred in cycles deposited under eccentricity maxima. At Furlo, black shales (representing ~28% of the cycle 'by time') underlie black chert beds (~7% of the

cycle 'by time'). This observation may reflect that, after the crossing of the proposed nutrient 'threshold' during high-amplitude precession cycles, environmental conditions promoting organic carbon production/preservation were established for some time before the development of conditions that were also favourable to deposition of pre-chert siliceous sediments. This pattern of environmental change is not observed in cycles deposited under eccentricity minima, where grey chert immediately overlies limestone. Although this thesis does not contain any independent evidence for the mechanism behind this difference, it is theorised that at high-amplitude (in comparison to low-amplitude) precession cycle maxima a greater degree of siliceous productivity may have been needed to overcome dissolution in the water column before biogenic silica could reach the sediment, with black shales deposited in the interval between the initial decrease in carbonate productivity and the establishment of sufficient siliceous productivity to overcome dissolution and be preserved in the sediment.

Following the exploration of cyclical palaeoenvironmental change over what might be termed the standard 'background' conditions of the Scaglia Bianca, the rates and durations of environmental changes over a major climatic perturbation (OAE 2, expressed as the Bonarelli Level in these sections) were investigated. The following conclusions were drawn from the high-resolution $^{3}He_{ET}$ timescale constructed over the Bonarelli Level at Furlo:

- The duration of deposition of the Bonarelli Level at Furlo was 478±160 kyr, very similar to recent cyclostratigraphic duration estimates of ~490 kyr (Mitchell et al., 2008; Lanci et al., 2010; Batenburg et al., 2016).

- This study's $\delta^{13}C_{TOC}$ record is correlated to the global carbon-isotope chemostratigraphy. The initial rise in $\delta^{13}C$ values (sometimes called the "build up" phase of OAE 2) spans 174±58 kyr, similar to the duration estimated using cyclostratigraphic timescales for this section of the carbon-isotope curve in the Western Interior Seaway ~149–240 (Sageman et al., 2006; Ma et al., 2014). The Plenus Carbon Isotopic Excursion, identified as the trough in $\delta^{13}C_{TOC}$ values between peaks 'a' and 'b', spans 58±21 kyr, comparable to the duration of ~65 kyr estimated using cyclostratigraphic timescales in Tarfaya, Morocco (O'Connor et al., 2020).

- No long interval of non-deposition stratigraphically above the Bonarelli Level was observed in the $^{3}He_{ET}$ record. This is inconclusive evidence for either the presence or absence of the debated ~400 kyr hiatus between the Bonarelli Level and the overlying limestones (cf. Voigt et al., 2007; Gambacorta et al., 2015; Batenburg et al., 2016), as erosion may have removed $^{3}He_{ET}$-bearing particles from the putative hiatal surface.

- Slowdowns in sedimentation rate were observed at the base and top of the Bonarelli Level; these intervals of low accumulation were likely associated with biotic turnover.
    - At the base of the Bonarelli Level a ~30 kyr slowdown, spanning ~3.5 cm of shales and mudstones, was coincident with a dramatic drop in carbonate content. This may represent the interval between an effective cessation of carbonate accumulation and a ramp-up in biogenic silica during the biotic turnover in which carbonate-producing plankton were out-competed under higher-nutrient conditions (an ecological change discussed by Erba, 2004). The basal slowdown in the stratigraphically lowest few centimetres of the Bonarelli Level may have been caused by the same environmental process governing the deposition of black shales below black cherts in Scaglia Bianca precession cycles (as described above), namely,

the ‘lag’ between carbonate and siliceous productivity, although the duration of the basal Bonarelli Level slowdown is ~5–6× that of the black shale layers.

- At the top of the Bonarelli Level, a ~85 kyr interval of slowly accumulating sediment was observed at the same height as the final decline in total organic carbon content. Porcellanite (non-vitreous chert) is the dominant lithology over this interval, which may represent the time between the re-establishment of oxygenated marine conditions (preventing TOC preservation) and the completion of the biotic turnover that restored carbonate deposition.

- Sedimentation rate within the Bonarelli Level was far from constant, reflecting rapid palaeoenvironmental change (and hence change in depositional conditions) within OAE 2.
  - Sedimentation rates of shales and mudstones within the Bonarelli Level varied by close to two orders of magnitude, between 0.04–1.13 cm/kyr. Sedimentation rates measured in pre-Bonarelli black shale beds (~0.1 cm/kyr) fall within this range.

  - The lithology that would later develop into black chert within the Bonarelli Level appears to have been deposited at a similar rate to shales and mudstones (with measured sedimentation rates in Bonarelli Level black cherts of 0.11–0.75 cm/kyr). This pre-chert lithology is suggested to have been similar to black shales. Sedimentation rates measured in Bonarelli Level black cherts were much lower than those of pre-Bonarelli cherts (1.2–2.8 cm/kyr).

  - Radiolarian sand beds within the Bonarelli Level were also rather slowly accumulating, with sedimentation rates of 0.09–0.67 cm/kyr. The low organic-

matter content in these beds may reflect poor preservation of organic carbon under brief windows of more oxygenated conditions.

- The average organic-carbon mass-accumulation rate over the Bonarelli Level as a whole was 0.044±0.011 g/cm^2/kyr, but peak OC MAR values reached 0.22±0.09 g/cm^2/kyr. Organic-carbon primary productivity during deposition of beds with high OC MARs reached 60–110 gC/m^2/yr.

- Four 'high OC MAR' intervals within the Bonarelli Level, with durations ranging between 12–64 kyr, were linked to the transient establishment of more dysoxic/euxinic conditions. Sub-10 kyr alternation of OC-rich and OC-poor beds indicates that over the deposition of the Bonarelli Level different bottom-water conditions (with differing organic-carbon preservation potential) were rapidly established and replaced.

- A condensed interval spanning ~50 kyr was identified ~40 cm above the base of the Bonarelli Level. This interval may represent a prolonged interval of low primary productivity and low biotic silica production.

- Around ~20 kyr after the deposition of the stratigraphically lowest bed containing significant carbonate content above the Bonarelli Level, carbonate accumulation rates rose to ~2× typical pre- and post-event values. This transient period of enhanced carbonate deposition, spanning ~3.5 kyr, was likely a response to excess alkalinity built up due to the paucity of planktonic calcifiers over OAE 2. The 'lag' between the first carbonate-rich bed and the rapidly accumulating carbonate interval may reflect the time taken for the full re-establishment of a calcifier-dominated planktonic ecosystem, although it should be noted that the timespan between the uppermost Bonarelli Level bed and the overlying rapidly

accumulating carbonate beds might have been much longer than ~20 kyr if there were a significant hiatus above the Bonarelli Level (Voigt et al., 2007; Gambacorta et al., 2015; cf. Batenburg et al., 2016).

Timing of the onset of OAE 2 has been suggested to be partially influenced by the phase of the eccentricity cycle, coinciding with a maximum in 405 kyr eccentricity (Laurin et al., 2016; Batenburg et al., 2016). Comparison between changes in palaeoenvironmental conditions, as recorded in the sedimentary record, in the Umbria–Marche Basin over the depositional interval of the Bonarelli Level and over the more transient periods of proto-black chert/shale deposition in the Scaglia Bianca precession cycles (also deposited at eccentricity maxima) highlights the similarities and differences in palaeoenvironmental response to 'background' orbital forcing and to more extreme perturbation.

- $^{3}He_{ET}$ timescales reveal similarities in the timing of the processes governing the switch from limestone to black shale/chert lithology at both the base of the Bonarelli Level and in precession cycles that contain 'black beds': in both these cases a slowdown in accumulation rate is associated with the turnover from calcareous-dominated to non-mineralising and siliceous-dominated planktonic communities (see above).

- Palaeoenvironmental changes through the orbitally forced Scaglia Bianca precession cycles are understood using the framework established in this thesis of 'thresholds'. As the base of the Bonarelli Level coincides with the same orbital configuration as the Scaglia Bianca 'black cycles' (eccentricity maximum, Laurin et al., 2016; Batenburg et al., 2016), the initiation of Bonarelli Level deposition may also have been triggered by the passing of a threshold into what, in this thesis, is termed 'nutrient world'. The same processes may have driven the observed changes in the type of sediment deposited in both cases, although the Bonarelli Level obviously differs significantly from black beds in precession cycles (having a duration

~100x longer than black beds in precession cycles and containing records of higher organic-carbon accumulation rates and primary productivity). The more 'intense' expression of 'black beds' in the Bonarelli Level would be expected, even if similar processes as those acting on precession cycle 'black beds' are influencing its sedimentation, as the Bonarelli Level spans a major climatic perturbation during which the Earth System was impacted not only by cyclical changes in insolation but also by the independent effect of massive volcanism (e.g. Sinton and Duncan, 1997; Batenburg et al., 2016). Through the 400 kyr time-span of the Bonarelli Level, linking the sedimentary record to a $^{3}He_{ET}$ timescale reveals rapid and not apparently cyclical changes in TOC (and possibly bottom-water redox conditions); whilst cyclical forcing clearly dominated the rest of the Scaglia Bianca sedimentary record, during OAE 2 non-cyclical processes appear to also have left a significant imprint, perhaps driven by non-cyclical environmental changes such as changing volcanic emissions or the availability of easily weatherable rocks (e.g. Percival et al., 2020).

6.2 Future Work

6.2.1 Redistribution of IDPs

There is scope for further development of the $^{3}He_{ET}$ sedimentation rate proxy itself, particularly the relationship between sediments' measured $^{3}He_{ET}$ concentration and their contemporary "actual" mass accumulation rate. For instance, $^{3}He_{ET}$ timescales are typically constructed from deep-marine pelagic sections in order to minimise the likelihood that erosion and redistribution of ^{3}He-bearing interplanetary dust particles (IDPs) has impacted this relationship (Farley, 2001), but sediment redistribution is known to take place even in pelagic environments (e.g. Mitchell and Lyle, 2005; Gambacorta et al., 2014). This thesis speculates about the theoretical redistributive potential of IDPs, particularly in comparison to biogenic sedimentary components such as radiolarian and

foraminiferal tests (Section 4.5.3), but future work testing IDP behaviour under erosional flow stress would be necessary to advance the conclusions drawn in this thesis beyond theoretical speculation.

Observation of the behaviour of IDPs and radiolarian and/or foraminiferal tests in a flume tank would be a useful avenue of exploration: unconsolidated pelagic sediments (particularly carbonate and siliceous oozes) from core-tops or sediment traps could be subjected to various flow regimes, and the redistribution of both IDPs and other sedimentary components quantified. It may be noted that, as individual IDPs in pelagic sediments are rare (Farley, 2001, review) and difficult to separate (see the efforts of Schmitz et al., 2017), the redistribution of IDPs might be best quantified by the comparison of the $^{3}He_{ET}$ concentration of the original bulk sediment with $^{3}He_{ET}$ concentrations measured across upstream and downstream sediments after flow-tank runs. In order for the redistribution of IDPs to be quantified in this way, it would be necessary to source sediments for study from regions in which sedimentation rates are low enough to concentrate IDPs, and hence $^{3}He_{ET}$, (e.g. pelagic sediments, see Section 2.1.2).

Alternately, the relative hydrodynamics of IDPs *versus* other sedimentary components might be explored under more controlled conditions using 'artificial IDPs': artificial grains with sizes and densities typical of $^{3}He_{ET}$-bearing IDPs. (A discussion of the size distribution of $^{3}He_{ET}$-bearing IDPs in sediment is provided in Section 2.1.2 and a discussion of IDP composition, and hence density, is provided in Section 2.1.1; it is noted that IDPs may have a variety of mineralogical compositions.) Separate flume tank experiments might be used to explore the comparative redistribution of sediments composed of solely 'artificial IDPs', carbonate ooze, siliceous ooze and clays under a range of flow regimes, as well as the redistribution of controlled mixtures of these various sedimentary components. In order to quantify the redistribution of 'artificial IDPs' as part of a sediment mixture, these grains could perhaps be colour coded such that their concentration might be measured using colour reflectance.

6.2.2 Timings within orbital cycles

It is increasingly being recognised that the distortion of cyclostratigraphic signals through rhythmically bedded sections (either through variation in sedimentation rate, diagenetically-influenced differential compaction, or through mobilisation and reprecipitation of sedimentary minerals – a particular issue in carbonate-dominated successions) may cause peaks in the insolation spectra used to identify cycles to be amplified, displaced, or supressed, and may cause the emergence of new peaks (Herbert, 1994; Westphal et al., 2004; Hinnov, 2013). The application of $^{3}He_{ET}$ timescales to cyclostratigraphic records identified as 'problematic' in this way would allow the distorting effects of varying sedimentation rate, compaction, etc. to be unpicked from the 'primary' cyclostratigraphic signal.

In addition, construction of sub-precessional $^{3}He_{ET}$ timescales through records displaying strong orbital cyclicity may promote the understanding of how astronomical forcing propagates through the climate system to affect the stratigraphic record by providing duration estimates of sedimentological and/or geochemical changes through cycles (as in the Scaglia Bianca precession cycles explored as part of this thesis). A suggested starting point for further exploration might be a Tethys-wide study testing whether the 'threshold model' proposed to explain the pattern of sedimentation through the Scaglia Bianca is applicable to other Cenomanian Tethyan sections. Eccentricity-modulated precession cycles (typically limestone-marl couplets) have been identified across the Cenomanian Tethys, for example, in the Vocontian Basin, France (Gale, 1995; Takashima et al., 2009), making such a section an obvious first target in the study proposed above, along with perhaps Wunstorf, Germany, in the Boreal Sea (Voigt et al., 2008). Comparison of the time spent in relatively organic-carbon-rich facies between these different localities might give a sense of the range of sensitivities to orbital forcing across the Tethys at this time (as controlled, perhaps, by local palaeogeographic effects).

An investigation of the timings within eccentricity-modulated precession cycles in the Cenomanian across a broader geographic range could be carried out by the inclusion of, for example, precession cycles (expressed as limestone-marl couplets) from the Western Interior Seaway (Eicher and Diner, 1991; Meyers et al., 2012) and from the Atlantic margin at Tarfaya, where they are expressed as alternations of limestones and black shales (Kuhnt et al., 2005). As an alternate approach, expansion of this study's work on the precession cycles of the Scaglia Bianca might be carried out temporally, rather than geographically. The Umbria–Marche Basin contains a Jurassic–Paleogene record of cyclic sedimentation which is well-characterised cyclostratigraphically (Cresta et al., 1989; Sprovieri et al., 2013; Laurin et al., 2015; Galeotti et al., 2015; Batenburg et al., 2016), making it the perfect location for a study of changes in 'stratigraphic response' to orbital forcing over time (e.g. are palaeoclimatic 'thresholds', as seen in the Cenomanian, a common mode of climate system to respond to orbital forcing?).

6.2.3 Duration and pacing of CIEs and other proxy records over Mesozoic hyperthermals

Numerous intervals of rapid climate change occurred through the Mesozoic, often recognisable in $\delta^{13}C$ record as carbon-isotope excursions (CIEs), recording both positive shifts due to high burial rates of organic carbon and negative shifts associated with the release of isotopically light carbon to the atmosphere through volcanism or dissociation of gas hydrates (see review of Jenkyns, 2010). Typically, the duration of carbon-isotope excursions (CIEs) is determined using cyclostratigraphic timescales, though ambiguities in recognising and identifying cyclic signals such as, for example, identifying the period of cyclic signals in the rock record, has led in some cases to debate over the duration of CIEs and the rates of change within them. For example, the estimates of the duration of the CIE associated with the Toarcian Oceanic Anoxic Event differ by 2–3×; this variation is significant as the speed and duration of the initial negative isotopic shift has implications as to the nature and origin of the input of isotopically light carbon (Suan et al., 2008; Kemp et al., 2011; Boulila and Hinnov, 2017).

$^{3}He_{ET}$ timescales provide an alternate method of measuring the duration of these events, as has been demonstrated in this thesis, where the new duration estimate of the Bonarelli Level is, in fact, consistent with estimates derived from cyclostratigraphy (Scopelliti et al., 2006; Trabucho-Alexandre et al., 2011; Batenburg et al., 2016). An obvious extension of the work carried out in this thesis would, therefore, be the construction of $^{3}He_{ET}$ timescales for sedimentary records of other Mesozoic climate perturbations. A key next target for study might be the Toarcian OAE (T-OAE), but a more ambitious project constructing $^{3}He_{ET}$ timescales to investigate the pacing of all Mesozoic OAEs (both major events such as the Early Aptian OAE 1a and more minor/localised OAEs) would allow comparison of the timings of climatic drivers and responses recorded by carbon-isotope signals across these various events.

In a similar vein, high-resolution timescales tied to changes in the carbon-isotope record would also provide timing constraints for models of carbon budget across the Mesozoic climatic perturbations (e.g. Kump and Arthur, 1999; Locklair et al., 2011; Owens et al., 2018). In addition, $^{3}He_{ET}$ timescales provide an alternate avenue to cyclostratigraphy for quantifying the speed and duration of weathering response during hyperthermals (as measured through geochemical proxies such as $\delta^{7}Li$, $\delta^{44}Ca$, $^{187}Os/^{188}Os$, and $^{87}Sr/^{86}Sr$ (e.g. Frijia and Parente, 2008; Blättler et al., 2011; Pogge von Strandmann et al., 2013; Du Vivier et al., 2014; Them et al., 2017). In particular, comparing the timing of weathering response to CO_2 input across various Mesozoic hyperthermals might shed light on any characteristic dynamics of "weathering response" generally, where the rapid injections of CO_2 to the atmosphere during Mesozoic hyperthermals, though far slower than Anthropogenic carbon injection, may be a useful, if limited, analogue to the modern situation (in a similar manner to the Paleocene-Eocene Thermal Maximum, see review of McInerney and Wing, 2011).

A major caveat when making comparisons to modern climate change is, of course, that the Cretaceous Earth System was quite different to today's, with different geography, continental configuration and ocean circulation patterns (Poulsen et al., 2001; Robinson et al., 2010; Robinson

and Vance, 2012; Donnadieu et al., 2016), without conclusive evidence of major polar ice caps (see reviews of Hay, 2008; Ray et al., 2019) and with a differing planktonic ecology in which diatoms, a major primary producer in modern oceans, were comparatively rare (Cermeño et al., 2015; Knoll and Follows, 2016). For this reason, the comparison of timings within a suite of Mesozoic through Cenozoic hyperthermal records (such as those expressed, for example, in the long record of the Umbria–Marche Basin) would be particularly interesting as that time spans a move towards more modern geographical and ecological conditions.

6.2.4 Carbonate overshoot

This thesis identified rapid deposition of carbonate sediments after OAE 2, similar to the rapid carbonate deposition identified after the PETM (Farley and Eltgroth, 2003; Zachos et al., 2005; Murphy et al., 2010; Luo et al., 2016; Penman et al., 2016; Boudreau et al., 2018). This overshoot is likely to have been influenced heavily by local factors, both geographical (i.e. position of the sediments relative to the CCD/lysocline) and ecological (i.e. local degree of decrease in carbonate producers); further work might investigate whether carbonate overshoot is as geographically widespread after OAE 2 as after the PETM (Kelly et al., 2010; Leon-Rodriguez and Dickens, 2010; Penman et al., 2016; Luo et al., 2016). This question might be answered through comparisons of carbonate sedimentation rates immediately following OAE 2 with those measured both pre-event and well after its recovery (as determined on a bed-by-bed basis using the $^{3}He_{ET}$ proxy) in other carbonate-dominated Cenomanian-Turonian successions such as Tarfaya, Morocco (Tsikos et al., 2004), or the Vocontian Basin, France (Takashima et al., 2009). The presence of carbonate 'overshoots' after other Mesozoic hyperthermals could be investigated using $^{3}He_{ET}$ timescales constructed over a suite of Mesozoic hyperthermals/OAEs as proposed in Section 6.2.3.

References

Abrajevitch, A., (2020). Diagenetic formation of bedded chert: Implications from a rock magnetic study of siliceous precursor sediments. *Earth and Planetary Science Letters*. **533**, 116039.

Aller, R.C., (1998). Mobile deltaic and continental shelf muds as suboxic, fluidized bed reactors. *Marine Chemistry*. **61**(3-4), 143–155.

Aller, R.C., Blair, N.E., Brunskill, G.J., (2008). Early diagenetic cycling, incineration, and burial of sedimentary organic carbon in the central Gulf of Papua (Papua New Guinea). *Journal of Geophysical Research: Earth Surface*. **113**(F1), F02S09.

Aller, R.C., (2014). Sedimentary diagenesis, depositional environments, and benthic fluxes. In: Holland, H.D., Turekian, K.K., eds. *Treatise on Geochemistry*. 2nd Edition. Oxford: Elsevier. pp. 293–334.

Alvarez, W., (1990). Pattern of extensional faulting in pelagic carbonates of the Umbria-Marche Apennines of central Italy. *Geology*. **18**(5), 407–410.

Amari, S., Ozima, M., (1985). Search for the origin of exotic helium in deep-sea sediments. *Nature*. **317**, 520–522.

Amari, S., Ozima, M., (1988). Extra-terrestrial noble gases in deep sea sediments. *Geochimica et Cosmochimica Acta*. **52**(5), 1087–1095.

Andrews, J.N., (1985). The isotopic composition of radiogenic helium and its use to study groundwater movement in confined aquifers. *Chemical Geology*. **49**, 339–351.

Arthur, M.A., Fischer, A.G., (1977). Upper Cretaceous–Paleocene magnetic stratigraphy at Gubbio, Italy I. Lithostratigraphy and sedimentology. *GSA Bulletin*. **88**(3), 367–371.

Arthur, M.A., Premoli Silva, I., (1982). Development of widespread organic carbon-rich strata in the Mediterranean Tethys. In: Schlanger, S.O., Cita, M.B., eds. *Nature and Origin of Cretaceous Carbon-Rich Facies*. London: Academic Press. pp. 7–54.

Arthur, M.A., Schlanger, S.O., Jenkyns, H.C., (1987). The Cenomanian–Turonian Oceanic Anoxic Event: II. Palaeoceanographic controls on organic-matter production and preservation. *Geological Society, London, Special Publications*. **26**, 401–420.

Arthur, M.A., Dean, W.E., Pratt, L.M., (1988). Geochemical and climatic effects of increased marine organic carbon burial at the Cenomanian/Turonian boundary. *Nature*. **335**, 714–717.

Arthur, M.A., Sageman, B.B., (1994). Marine black shales: depositional mechanisms and environments of ancient deposits. *Annual Review of Earth and Planetary Sciences*. **22**(1), 499–551.

Ballentine, C.J., Barfod, D.N., (2000). The origin of air-like noble gases in MORB and OIB. *Earth and Planetary Science Letters*. **180**(1-2), 39–48.

Ballentine, C.J., Burgess, R., Marty, B., (2002). Tracing fluid origin, transport and interaction in the crust. *Reviews in Mineralogy and Geochemistry*. **47**(1), 539–614.

Ballentine, C.J., Burnard, P.G., (2002). Production, release and transport of noble gases in the continental crust. *Reviews in Mineralogy and Geochemistry*. **47**(1), 481–538.

Barclay, R.S., McElwain, J.C., Sageman, B.B., (2010). Carbon sequestration activated by a volcanic CO2 pulse during Ocean Anoxic Event 2. *Nature Geoscience*. **3**(3), 205–208.

Barron, E.J., Arthur, M.A., Kauffman, E.G., (1985). Cretaceous rhythmic bedding sequences: a plausible link between orbital variations and climate. *Earth and Planetary Science Letters*. **72**(4), 327–340.

Batenburg, S.J., De Vleeschouwer, D., Sprovieri, M., Hilgen, F.J., Gale, A.S., Singer, B.S., Koeberl, C., Coccioni, R., Claeys, P., Montanari, A., (2016). Orbital control on the timing of oceanic anoxia in the Late Cretaceous. *Climate of the Past*. **12**(10), 1995–2009.

Batenburg, S.J., Voigt, S., Friedrich, O., Frank, M. 2014. *Atlantic Ocean circulation during the latest Cretaceous and early Paleogene: progressive deep water exchange*. AGU Fall Meeting, 15 December, San Francisco, USA.

Beaudoin, B., M'Ban, E.P., Montanari, A., Pinault, M., (1996). Lithostratigraphie haute résolution (< 20 ka) dans le Cénomanien du bassin d'Ombrie-Marches (Italie). *Comptes rendus de l'Académie des sciences. Série 2, Sciences de la terre et des planètes*. **323**, 689–696.

Behar, F., Beaumont, V., Penteado, H.L.D.B., (2001). Rock-Eval 6 technology: performances and developments. *Oil & Gas Science and Technology*. **56**(2), 111–134.

Behrenfeld, M.J., Boss, E., Siegel, D.A., Shea, D.M., (2005). Carbon-based ocean productivity and phytoplankton physiology from space. *Global Biogeochemical Cycles*. **19**, GB1006.

Berger, A., Loutre, M.F., Laskar, J., (1992). Stability of the astronomical frequencies over the earth's history for paleoclimate studies. *Science*. **255**, 560–566.

Berger, A., Loutre, M.F., (1994). Astronomical forcing through geological time. In: DeBoer, P.L., Smith, D.G., eds. *Orbital Forcing and Cyclic Sequences*. Oxford: Blackwell Scientific Publications. pp. 15–24.

Berner, R.A., (1982). Burial of organic carbon and pyrite sulfur in the modern ocean: its geochemical and environmental significance. *American Journal of Science*. **282**, 451–473.

Bernoulli, D., Jenkyns, H.C., (1974). Alpine Mediterranean and Central Atlantic Mesozoic facies in relation to the early evolution of the Tethys. *Society of Economic Paleontologists and Mineralogists, Special Publications*. **19**, 129–160.

Bernoulli, D., Jenkyns, H.C., (2009). Ancient oceans and continental margins of the Alpine-Mediterranean Tethys: deciphering clues from Mesozoic pelagic sediments and ophiolites. *Sedimentology*. **56**(1), 149–190.

Blair, N.E., Leithold, E.L., Ford, S.T., Peeler, K.A., Holmes, J.C., Perkey, D.W., (2003). The persistence of memory: the fate of ancient sedimentary organic carbon in a modern sedimentary system. *Geochimica et Cosmochimica Acta*. **67**(1), 63–73.

Blair, N.E., Leithold, E.L., Brackley, H., Trustrum, N., Page, M., Childress, L., (2010). Terrestrial sources and export of particulate organic carbon in the Waipaoa sedimentary system: Problems, progress and processes. *Marine Geology*. **270**(1-4), 108–118.

Blair, N.E., Aller, R.C., (2012). The fate of terrestrial organic carbon in the marine environment. *Annual Review of Marine Science*. **4**, 401–423.

Blakey, R.C., (2020). Paleogeography of Europe, Europe Cretaceous ca. 100 Ma [online]. *Deep Time Maps.* [Viewed 27th August 2021]. Available from https://deeptimemaps.com/europe/

Blättler, C.L., Jenkyns, H.C., Reynard, L.M., Henderson, G.M., (2011). Significant increases in global weathering during Oceanic Anoxic Events 1a and 2 indicated by calcium isotopes. *Earth and Planetary Science Letters*. **309**, 77–88.

Boccaletti, M., Elter, P., Guazzone, G., (1971). Plate tectonic models for the development of the Western Alps and Northern Apennines. *Nature Physical Science*. **234**, 108–111.

Bonarelli, G., (1891). *Il territorio di Gubbio: Notizie geologiche*. Rome.

Bortolotti, V., Passerini, P., Sagri, M., Sestini, G., (1970). Development of the Northern Apennines Geosyncline – The miogeosynclinal sequences. *Sedimentary Geology*. **4**(3/4), 341–444.

Boschi, S., Schmitz, B., Heck, P.R., Cronholm, A., Defouilloy, C., Kita, N.T., Monechi, S., Montanari, A., Rout, S.S., Terfelt, F., (2017). Late Eocene ^{3}He and Ir anomalies associated with ordinary chondritic spinels. *Geochimica et Cosmochimica Acta*. **204**, 205–218.

Bosellini, A., Winterer, E.L., (1975). Pelagic limestone and radiolarite of the Tethyan Mesozoic: A genetic model. *Geology*. **3**(5), 279–282.

Boudreau, B.P., Middelburg, J.J., Meysman, F.J.R., (2010). Carbonate compensation dynamics. *Geophysical Research Letters*. **37**(3), L03603.

Boudreau, B.P., Middelburg, J.J., Luo, Y., (2018). The role of calcification in carbonate compensation. *Nature Geoscience*. **11**(12), 894–900.

Boulila, S., Hinnov, L.A., (2017). A review of tempo and scale of the early Jurassic Toarcian OAE: implications for carbon cycle and sea level variations. *Newsletters on Stratigraphy*. **50**(4), 363–389.

Bouloubassi, I., Rullkötter, J., Meyers, P.A., (1999). Origin and transformation of organic matter in Pliocene–Pleistocene Mediterranean sapropels: organic geochemical evidence reviewed. *Marine Geology*. **153**(1-4), 177–197.

Bradley, J.P., Brownlee, D.E., Fraundorf, P., (1984). Discovery of nuclear tracks in interplanetary dust. *Science*. **226**, 1432–1434.

Bradley, J.P., (1988). Analysis of chondritic interplanetary dust thin-sections. *Geochimica et Cosmochimica Acta*. **52**(4), 889–900.

Bradley, J.P., (2007). Interplanetary Dust Particles. In: Holland, H.D., Turekian, K.K., eds. *Treatise on Geochemistry*. Oxford: Pergamon. pp. 1–24.

Bralower, T.J., Thierstein, H.R., (1984). Low productivity and slow deep-water circulation in mid-Cretaceous oceans. *Geology*. **12**(10), 614–618.

Bralower, T.J., Thierstein, H.R., (1987). Organic carbon and metal accumulation rates in Holocene and mid-Cretaceous sediments: palaeoceanographic significance. *Geological Society, London, Special Publications*. **26**(1), 345–369.

Bromley, R.G., Ekdale, A.A., (1986). Flint and fabric in the European chalk. In: Sieveking, G.D.G., Hart, M.B., eds. *The Scientific Study of Flint and Chert*. Cambridge: Cambridge University Press. pp. 71–82.

Brook, E.J., Kurz, M.D., Curtice, J., (2009). Flux and size fractionation of ^{3}He in interplanetary dust from Antarctic ice core samples. *Earth and Planetary Science Letters*. **286**(3-4), 565–569.

Brownlee, D.E., (1985). Cosmic dust: collection and research. *Annual Review of Earth and Planetary Sciences*. **13**(1), 147–173.

Brumsack, H.-J., (2006). The trace metal content of recent organic carbon-rich sediments: Implications for Cretaceous black shale formation. *Palaeogeography, Palaeoclimatology, Palaeoecology*. **232**(2-4), 344–361.

Calvert, S.E., (1971). Composition and origin of North Atlantic deep sea cherts. *Contributions to Mineralogy and Petrology*. **33**, 273–288.

Canfield, D.E., (1994). Factors influencing organic carbon preservation in marine sediments. *Chemical Geology*. **114**(3-4), 315–329.

Caricchi, C., Aldega, L., Corrado, S., (2015). Reconstruction of maximum burial along the Northern Apennines thrust wedge (Italy) by indicators of thermal exposure and modelling. *GSA Bulletin*. **127**(3-4), 428–442.

Cermeño, P., Falkowski, P.G., Romero, O.E., Schaller, M.F., Vallina, S.M., (2015). Continental erosion and the Cenozoic rise of marine diatoms. *PNAS*. **112**(14), 4239–4244.

Channell, J.E.T., D'Argenio, B., Horváth, F., (1979). Adria, the African promontory, in Mesozoic Mediterranean palaeogeography. *Earth-Science Reviews*. **15**(3), 213–292.

Chavrit, D., Moreira, M.A., Moynier, F., (2016). Estimation of the extraterrestrial ^{3}He and ^{20}Ne fluxes on Earth from He and Ne systematics in marine sediments. *Earth and Planetary Science Letters*. **436**, 10–18.

Claps, M., Masetti, D., (1994). Milankovitch periodicities recorded in Cretaceous deep sea sequences from the southern Alps (Northern Italy). In: DeBoer, P.L., Smith, D.G., eds. *Orbital Forcing and Cyclic Sequences*. Oxford: Blackwell Scientific Publications. pp. 99–107.

Clayton, C.J., (1986). Flint and fabric in the European chalk. In: Sieveking, G. de G., Hart, M.B., eds. *The Scientific Study of Flint and Chert*. Cambridge: Cambridge University Press. pp. 43–54.

Coccioni, R., Erba, E., Premoli-Silva, I., (1992). Barremian-Aptian calcareous plankton biostratigraphy from the Gorgo Cerbara section (Marche, central Italy) and implications for plankton evolution. *Cretaceous Research*. **13**(5-6), 517–537.

Coccioni, R., Galeotti, S., (2003). The mid-Cenomanian Event: prelude to OAE 2. *Palaeogeography, Palaeoclimatology, Palaeoecology*. **190**, 427–440.

Coccioni, R., Luciani, V., (2005). Planktonic foraminifers across the Bonarelli Event (OAE2, latest Cenomanian): The Italian record. *Palaeogeography, Palaeoclimatology, Palaeoecology*. **224**(1-3), 167–185.

Cresta, S., Monechi, S., Parisi, G., (1989). *Mesozoic-Cenozoic stratigraphy in the Umbria-Marche area: Memori e descrittive della carta geologica d'Italia*. Rome: Instituto Poligrafico e Zecca dello Stato.

Cumberland, S.A., Douglas, G., Grice, K., Moreau, J.W., (2016). Uranium mobility in organic matter-rich sediments: A review of geological and geochemical processes. *Earth-Science Reviews*. **159**, 160–185.

Curran, K.J., Hill, P.S., Schell, T.M., Milligan, T.G., Piper, D.J.W., (2004). Inferring the mass fraction of floc-deposited mud: application to fine-grained turbidites. *Sedimentology*. **51**(5), 927–944.

D'Argenio, B., Alvarez, W., (1980). Stratigraphic evidence for crustal thickness changes on the southern Tethyan margin during the Alpine cycle. *GSA Bulletin*. **91**(12), 681–689.

de Boer, P.L., (1982). Cyclicity and the storage of organic matter in Middle Cretaceous pelagic sediments. In: Einsele, G., Seilacher, A., eds. *Cyclic and Event Stratification*. Berlin: Springer-Verlag. pp. 456–475.

de Boer, P.L. de, (1986). Changes in the organic carbon burial during the Early Cretaceous. *Geological Society, London, Special Publications*. **21**, 321–331.

de Boer, P.L., (1991). Pelagic black shale-carbonate rhythms: orbital forcing and oceanographic response. In: Einsele, G., Ricken, W., Seilacher, A., eds. *Cycles and Events in Stratigraphy*. Berlin: Springer-Verlag. pp. 63–78.

Darrah, T.H., Poreda, R.J., (2012). Evaluating the accretion of meteoritic debris and interplanetary dust particles in the GPC-3 sediment core using noble gas and mineralogical tracers. *Geochimica et Cosmochimica Acta*. **84**, 329–352.

Delaney, M.L., (1998). Phosphorus accumulation in marine sediments and the oceanic phosphorus cycle. *Global Biogeochemical Cycles*. **12**(4), 563–572.

Demaison, G.J., Moore, G.T., (1980). Anoxic environments and oil source bed genesis. *AAPG Bulletin*. **64**(8), 1179–1209.

Dermott, S.F., Jayaraman, S., Xu, Y.L., Gustafson, B.Å.S., Liou, J.C., (1994). A circumsolar ring of asteroidal dust in resonant lock with the Earth. *Nature*. **369**, 719–723.

Dermott, S.F., Kehoe, T.J.J., Grogan, K., Durda, D.D., Jayaraman, S., Kortenkamp, S.J., Wyatt, M.C., (2001). Orbital Evolution of Interplanetary Dust. In: Grün, E., Gustafson, B.A., Dermott, S., Fechtig, H., eds. *Interplanetary Dust*. Berlin: Springer. pp. 569–639.

Dewey, J.F., Pitman, W.C., Ryan, W.B.F., Bonnin, J., (1973). Plate tectonics and the evolution of the Alpine System. *GSA Bulletin*. **84**(10), 3137–3180.

Dickson, A.J., Saker-Clark, M., Jenkyns, H.C., Bottini, C., Erba, E., Russo, F., Gorbanenko, O., Naafs, B.D.A., Pancost, R.D., Robinson, S.A., Boorn, S.H.J.M. van den, Idiz, E., (2017). A Southern Hemisphere record of global trace-metal drawdown and orbital modulation of organic-matter burial across the Cenomanian–Turonian boundary (Ocean Drilling Program Site 1138, Kerguelen Plateau). *Sedimentology*. **64**(1), 186–203.

Dohnanyi, J.S., (1978). Particle dynamics. In: McDonnell, J.A.M., ed. *Cosmic Dust*. New York: Wiley. pp. 562–564.

Donatelli, U., Tramontana, M., Venturi, F., (2010). First record of ammonites in the Bonarelli Level (uppermost Cenomanian) of the Umbria-Marche Succession. *Italian Journal of Geosciences*. **129**(1), 69–73.

Donnadieu, Y., Pucéat, E., Moiroud, M., Guillocheau, F., Deconinck, J.-F., (2016). A better-ventilated ocean triggered by Late Cretaceous changes in continental configuration. *Nature Communications*. **7**(1), 10316.

Du Vivier, A.D.C., Selby, D., Sageman, B.B., Jarvis, I., Gröcke, D.R., Voigt, S., (2014). Marine $^{187}Os/^{188}Os$ isotope stratigraphy reveals the interaction of volcanism and ocean circulation during Oceanic Anoxic Event 2. *Earth and Planetary Science Letters*. **389**, 23–33.

Du Vivier, A.D.C., Jacobson, A.D., Lehn, G.O., Selby, D., Hurtgen, M.T., Sageman, B.B., (2015). Ca isotope stratigraphy across the Cenomanian–Turonian OAE 2: Links between volcanism, seawater geochemistry, and the carbonate fractionation factor. *Earth and Planetary Science Letters*. **416**, 121–131.

Ducati, H., Kalbitzer, S., Kiko, J., Kirsten, T., Müller, H.W., (1973). Rare gas diffusion studies in individual lunar soil particles and in artificially implanted glasses. *The Moon*. **8**(1-2), 210–227.

Eberhardt, P., Geiss, J., Graf, H., Grögler, N., Krähenbühl, U., Schwaller, H., Schwarzmüller, J., Stettler, A., (1970). Trapped solar wind noble gases, exposure age and K/Ar-age in Apollo 11 lunar fine material. *Proceedings of the Apollo 11 Lunar Science Conference. Geochimica et Cosmochimica Acta. Supplement*. **1**(2), 1037–1070.

Eberhardt, P., Geiss, J., Graf, H., Groegler, N., Mendia, M.D., Moergeli, M., Schwaller, H., Stettler, A., Kraehenbuehl, U., von Gunten, H.R., (1972). Trapped solar wind noble gases in Apollo 12 lunar fines 12001 and Apollo 11 breccia 10046. *Proceedings Third Lunar Science Conference. Geochimica et Cosmochimica Acta. Supplement.* **3**(2), 1821–1856.

Eggimann, D.W., Manheim, F.T., Betzer, P.R., (1980). Dissolution and analysis of amorphous silica in marine sediments. *Journal of Sedimentary Research*. **50**, 215–225.

Eicher, D.L., Diner, R., (1991). Environmental factors controlling Cretaceous limestone-marlstone rhythms. In: Einsele, G., Ricken, W., Seilacher, A., eds. Cycles and Events in Stratigraphy. Berlin: Springer-Verlag, Berlin. pp. 79–93.

Eldrett, J.S., Ma, C., Bergman, S.C., Lutz, B., Gregory, F.J., Dodsworth, P., Phipps, M., Hardas, P., Minisini, D., Ozkan, A., Ramezani, J., Bowring, S.A., Kamo, S.L., Ferguson, K., Macaulay, C., Kelly, A.E., (2015). An astronomically calibrated stratigraphy of the Cenomanian, Turonian and earliest Coniacian from the Cretaceous Western Interior Seaway, USA: Implications for global chronostratigraphy. *Cretaceous Research*. **56**, 316–344.

Eppley, R.W., Peterson, B.J., (1979). Particulate organic matter flux and planktonic new production in the deep ocean. *Nature*. **282**, 677–680.

Erba, E., (2004). Calcareous nannofossils and Mesozoic oceanic anoxic events. *Marine Micropaleontology*. **52**(1-4), 85–106.

Erba, E., Tremolada, F., (2004). Nannofossil carbonate fluxes during the Early Cretaceous: Phytoplankton response to nutrification episodes, atmospheric CO_2, and anoxia. *Palaeoceanography*. **19**(1), PA1008.

Erbacher, J., Thurow, J., Littke, R., (1996). Evolution patterns of radiolaria and organic matter variations: A new approach to identify sea-level changes in mid-Cretaceous pelagic environments. *Geology*. **24**(6), 499–502.

Erbacher, J., Friedrich, O., Wilson, P.A., Birch, H., Mutterlose, J., (2005). Stable organic carbon isotope stratigraphy across Oceanic Anoxic Event 2 of Demerara Rise, western tropical Atlantic. *Geochemistry, Geophysics, Geosystems*. **6**(6), Q06010.

Espitalié, J., Deroo, G., Marquis, F., (1985). La pyrolyse Rock-Eval et ses applications. Première partie. *Revue de l'Institut Français du Pétrole*. **40**(5), 563–579.

Essington, M.E., (2015). *Soil and Water Chemistry: An Integrative Approach*. 2nd Edition. Boca Raton, FL: CRC Press.

Evans, N.J., Byrne, J.P., Keegan, J.T., Dotter, L.E., (2005). Determination of uranium and thorium in zircon, apatite, and fluorite: application to laser (U-Th)/He Thermochronology. *Journal of Analytical Chemistry*. **60**(12), 1159–1165.

Falkowski, P.G., Barber, R.T., Smetacek, V., (1998). Biogeochemical controls and feedbacks on ocean primary production. *Science*. **281**, 200–206.

Farley, K.A., (1995). Cenozoic variations in the flux of interplanetary dust recorded by ^{3}He in a deep-sea sediment. *Nature*. **376**, 153–156.

Farley, K.A., Patterson, D.B., (1995). A 100-kyr periodicity in the flux of extraterrestrial ^{3}He to the sea floor. *Nature*. **378**, 600–603.

Farley, K.A., Love, S.G., Patterson, D.B., (1997). Atmospheric entry heating and helium retentivity of interplanetary dust particles. *Geochimica et Cosmochimica Acta*. **61**(11), 2309–2316.

Farley, K.A., Montanari, A., Shoemaker, E.M., Shoemaker, C.S., (1998). geochemical evidence for a comet shower in the Late Eocene. *Science*. **280**, 1250–1253.

Farley, K.A., (2001). Extraterrestrial helium in seafloor sediments: identification, characteristics, and accretion rate over geologic time. In: Peucker-Ehrenbrink, B., Schmitz, B., eds. *Accretion of Extraterrestrial Matter Throughout Earth's History*. Boston, MA: Springer US. pp. 179–204.

Farley, K.A., Eltgroth, S.F., (2003). An alternative age model for the Paleocene–Eocene thermal maximum using extraterrestrial ^{3}He. *Earth and Planetary Science Letters*. **208**, 135–148.

Farley, K.A., Vokrouhlický, D., Bottke, W.F., Nesvorný, D., (2006a). A late Miocene dust shower from the break-up of an asteroid in the main belt. *Nature*. **439**, 295–297.

Farley, K.A., Libarkin, J., Mukhopadhyay, S., Amidon, W., (2006b). Cosmogenic and nucleogenic ^{3}He in apatite, titanite, and zircon. *Earth and Planetary Science Letters*. **248**(1-2), 451–461.

Farley, K.A., Montanari, A., Coccioni, R., (2012). A record of the extraterrestrial ^{3}He flux through the Late Cretaceous. *Geochimica et Cosmochimica Acta*. **84**, 314–328.

Farrimond, P., Eglinton, G., Brassell, S.C., Jenkyns, H.C., (1990). The Cenomanian/Turonian anoxic event in Europe: an organic geochemical study. *Marine and Petroleum Geology*. **7**(1), 75–89.

Fiet, N., (1998). Les black shales, un outil chronostratigraphique haute resolution; exemple de l'Albien du bassin de Marches-Ombrie (Italie centrale). *Bulletin de la Société Géologique de France*. **169**, 221–231.

Flynn, G.J., (1996). Sources of 10 micron interplanetary dust: the contribution from the Kuiper Belt. *International Astronomical Union Colloquium*. **150**, 171–175.

Forster, A., Schouten, S., Baas, M., Damsté, J.S.S., (2007a). Mid-Cretaceous (Albian–Santonian) sea surface temperature record of the tropical Atlantic Ocean. *Geology*. **35**(10), 919–922.

Forster, A., Schouten, S., Moriya, K., Wilson, P.A., Sinninghe Damsté, J.S., (2007b). Tropical warming and intermittent cooling during the Cenomanian/Turonian oceanic anoxic event 2: Sea surface temperature records from the equatorial Atlantic. *Paleoceanography*. **22**(1), PA1219.

Forster, A., Kuypers, M.M.M., Turgeon, S.C., Brumsack, H.-J., Petrizzo, M.R., Sinninghe Damsté, J.S., (2008). The Cenomanian/Turonian oceanic anoxic event in the South Atlantic: New insights from a geochemical study of DSDP Site 530A. *Palaeogeography, Palaeoclimatology, Palaeoecology*. **267**(3-4), 256–283.

Fowler, S.W., Knauer, G.A., (1986). Role of large particles in the transport of elements and organic compounds through the oceanic water column. *Progress in Oceanography*. **16**(3), 147–194.

Friedrich, O., Erbacher, J., Mutterlose, J., (2006). Paleoenvironmental changes across the Cenomanian/Turonian Boundary Event (Oceanic Anoxic Event 2) as indicated by benthic foraminifera from the Demerara Rise (ODP Leg 207). *Revue de micropaléontologie*. **49**(3), 121–139.

Friedrich, O., Norris, R.D., Erbacher, J., (2012). Evolution of middle to Late Cretaceous oceans—A 55 m.y. record of Earth's temperature and carbon cycle. *Geology*. **40**(2), 107–110.

Frieling, J., Reichart, G.-J., Middelburg, J.J., Röhl, U., Westerhold, T., Bohaty, S.M., Sluijs, A., (2018). Tropical Atlantic climate and ecosystem regime shifts during the Paleocene–Eocene Thermal Maximum. *Climate of the Past.* **14**(1), 39–55.

Frijia, G., Parente, M., (2008). Strontium isotope stratigraphy in the upper Cenomanian shallow-water carbonates of the southern Apennines: Short-term perturbations of marine $^{87}Sr/^{86}Sr$ during the oceanic anoxic event 2. *Palaeogeography, Palaeoclimatology, Palaeoecology*. **261**(1-2), 15–29.

Fukumoto, H., Nagao, K., Matsuda, J., (1986). Noble gas studies on the host phase of high $^{3}He^{4}He$ ratios in deep-sea sediments. *Geochimica et Cosmochimica Acta*. **50**(10), 2245–2253.

Gale, A.S., (1995). Cyclostratigraphy and correlation of the Cenomanian Stage in Western Europe. *Geological Society, London, Special Publications*. **85**(1), 177–197.

Gale, A.S., Christensen, W.K., (1996). Occurrence of the belemnite Actinocamax plenus in the Cenomanian of SE France and its significance. *Bulletin of the Geological Society of Denmark*. **43**(1), 68–77.

Gale, A.S., Jenkyns, H.C., Tsikos, H., van Breugel, Y., Sinninghe Damsté, J.S., Bottini, C., Erba, E., Russo, F., Falzoni, F., Petrizzo, M.R., Dickson, A.J., Wray, D.S., (2019). High-resolution bio- and chemostratigraphy of an expanded record of Oceanic Anoxic Event 2 (Late Cenomanian–Early Turonian) at Clot Chevalier, near Barrême, SE France (Vocontian Basin). *Newsletters on Stratigraphy*. **52**(1), 97–129.

Galeotti, S., Moretti, M., Cappelli, C., Phillips, J., Lanci, L., Littler, K., Monechi, S., Petrizzo, M.R., Silva, I.P., Zachos, J.C., (2015). The Bottaccione section at Gubbio, central Italy: a classical Paleocene Tethyan setting revisited. *Newsletters on Stratigraphy*. **48**(3), 325–339.

Galy, V., France-Lanord, C., Beyssac, O., Faure, P., Kudrass, H., Palhol, F., (2007). Efficient organic carbon burial in the Bengal fan sustained by the Himalayan erosional system. *Nature*. **450**, 407–410.

Gambacorta, G., Bersezio, R., Erba, E., (2014). Sedimentation in the Tethyan pelagic realm during the Cenomanian: Monotonous settling or active redistribution? *Palaeogeography, Palaeoclimatology, Palaeoecology*. **409**, 301–319.

Gambacorta, G., Jenkyns, H.C., Russo, F., Tsikos, H., Wilson, P.A., Faucher, G., Erba, E., (2015). Carbon- and oxygen-isotope records of mid-Cretaceous Tethyan pelagic sequences from the Umbria – Marche and Belluno Basins (Italy). *Newsletters on Stratigraphy*. **48**(3), 299–323.

Gambacorta, G., Bersezio, R., Weissert, H., Erba, E., (2016). Onset and demise of Cretaceous oceanic anoxic events: The coupling of surface and bottom oceanic processes in two pelagic basins of the western Tethys. *Paleoceanography*. **31**(6), 732–757.

Gambacorta, G., Malinverno, A., Erba, E., (2019). Orbital forcing of carbonate versus siliceous productivity in the late Albian–late Cenomanian (Umbria-Marche Basin, central Italy). *Newsletters on Stratigraphy*. **52**(2), 197–220.

Gebhardt, H., Friedrich, O., Schenk, B., Fox, L., Hart, M., Wagreich, M., (2010). Paleoceanographic changes at the northern Tethyan margin during the Cenomanian–Turonian Oceanic Anoxic Event (OAE-2). *Marine Micropaleontology*. **77**(1-2), 25–45.

Geiss, J., Bühler, F., Cerutti, H., Eberhardt, P., Filleux, C., (1972). Solar wind composition experiment. In: *Apollo 16 Preliminary Science Report*. Washington DC.

Germani, M.S., Bradley, J.P., Brownlee, D.E., (1990). Automated thin-film analyses of hydrated interplanetary dust particles in the analytical electron microscope. *Earth and Planetary Science Letters*. **101**(2-4), 162–179.

Goñi, M.A., Yunker, M.B., Macdonald, R.W., Eglinton, T.I., (2005). The supply and preservation of ancient and modern components of organic carbon in the Canadian Beaufort Shelf of the Arctic Ocean. *Marine Chemistry*. **93**(1), 53–73.

Grachev, A.F., Korchagin, O.A., Tselmovich, V.A., Kollmann, H.A., (2008). Cosmic dust and micrometeorites in the transitional clay layer at the Cretaceous-Paleogene boundary in the gams section (Eastern Alps): Morphology and chemical composition. *Izvestiya, Physics of the Solid Earth*. **44**(7), 555–569.

Hartman-Stroup, C., (1987). The effect of organic matter type and organic carbon content on Rock-Eval hydrogen index in oil shales and source rocks. *Organic Geochemistry*. **11**(5), 351–369.

Hasegawa, T., (1997). Cenomanian-Turonian carbon isotope events recorded in terrestrial organic matter from northern Japan. *Palaeogeography, Palaeoclimatology, Palaeoecology*. **130**(1-4), 251–273.

Hasegawa, T., Pratt, L.M., Maeda, H., Shigeta, Y., Okamoto, T., Kase, T., Uemura, K., (2003). Upper Cretaceous stable carbon isotope stratigraphy of terrestrial organic matter from Sakhalin, Russian Far East: a proxy for the isotopic composition of paleoatmospheric CO_2. *Palaeogeography, Palaeoclimatology, Palaeoecology*. **189**(1-2), 97–115.

Hay, W.W., (2008). Evolving ideas about the Cretaceous climate and ocean circulation. *Cretaceous Research*. **29**(5), 725–753.

Heath, G.R., Moberly, R., (1971). Cherts from the Western Pacific, Leg 7, Deep Sea Drilling Project. In: Winterer, E.L., ed. *Proceedings of the Ocean Drilling Program: Initial Report. Part A*. pp. 991–1007.

Henderson, G.M., Lindsay, F.N., Slowey, N.C., (1999). Variation in bioturbation with water depth on marine slopes: a study on the Little Bahamas Bank. *Marine Geology*. **160**, 105–118.

Henrichs, S.M., Reeburgh, W.S., (1987). Anaerobic mineralization of marine sediment organic matter: Rates and the role of anaerobic processes in the oceanic carbon economy. *Geomicrobiology Journal*. **5**(3-4), 191–237.

Herbert, T.D., (1994). Reading orbital signals distorted by sedimentation: Models and examples. In: DeBoer, P.L., Smith, D.G., eds. *Orbital Forcing and Cyclic Sequences*. Oxford: Blackwell Scientific Publications. pp. 438–507.

Herbert, T.D., Fischer, A.G., (1986). Milankovitch climatic origin of mid-Cretaceous black shale rhythms in central Italy. *Nature*. **321**, 739–743.

Herbert, T.D., Stallard, R.F., Fischer, A.G., (1986). Anoxic events, productivity rhythms, and the orbital signature in a mid-Cretaceous deep-sea sequence from central Italy. *Palaeogeography, Palaeoclimatology, Palaeoecology*. **1**(4), 495–506.

Hesse, R., (1988). Origin of chert: Diagenesis of biogenic siliceous sediments. *Geoscience Canada*. **15**(3), 171–192.

Hesse, R., (1989). Silica diagenesis: origin of inorganic and replacement cherts. *Earth-Science Reviews*. **26**(1-3), 253–284.

Hetzel, A., Böttcher, M.E., Wortmann, U.G., Brumsack, H.-J., (2009). Paleo-redox conditions during OAE 2 reflected in Demerara Rise sediment geochemistry (ODP Leg 207). *Palaeogeography, Palaeoclimatology, Palaeoecology*. **273**(3-4), 302–328.

Hinnov, L.A., (2013). Cyclostratigraphy and its revolutionizing applications in the earth and planetary sciences. *GSA Bulletin*. **125**(11-12), 1703–1734.

Hiyagon, H., (1994). Retention of solar helium and neon in IDPs in deep sea sediment. *Science*. **263**, 1257–1259.

Hochuli, P.A., Menegatti, A.P., Weissert, H., Riva, A., Erba, E., Silva, I.P., (1999). Episodes of high productivity and cooling in the early Aptian Alpine Tethys. *Geology*. **27**(7), 657–660.

Holmden, C., Jacobson, A.D., Sageman, B.B., Hurtgen, M.T., (2016). Response of the Cr isotope proxy to Cretaceous Ocean Anoxic Event 2 in a pelagic carbonate succession from the Western Interior Seaway. *Geochimica et Cosmochimica Acta*. **186**, 277–295.

Hönisch, B., Ridgwell, A., Schmidt, D.N., Thomas, E., Gibbs, S.J., Sluijs, A., Zeebe, R., Kump, L., Martindale, R.C., Greene, S.E., Kiessling, W., Ries, J., Zachos, J.C., Royer, D.L., Barker, S., Marchitto, T.M., Moyer, R., Pelejero, C., Ziveri, P., Foster, G.L., Williams, B., (2012). The geological record of ocean acidification. *Science*. **335**, 1058–1063.

Hori, R.S., Cho, C.-F., Umeda, H., (1993). Origin of cyclicity in Triassic-Jurassic radiolarian bedded cherts of the Mino accretionary complex from Japan. *Island Arc*. **2**, 170–180.

Huber, B.T., Norris, R.D., MacLeod, K.G., (2002). Deep-sea paleotemperature record of extreme warmth during the Cretaceous. *Geology*. **30**(2), 123–126.

Hudson, B., Flynn, G.J., Fraundorf, P., Hohenberg, C.M., Shirck, J., (1981). Noble gases in stratospheric dust particles: confirmation of extraterrestrial origin. *Science*. **211**, 383–386.

Huh, C.-A., Lin, H.-L., Lin, S., Huang, Y.-W., (2009). Modern accumulation rates and a budget of sediment off the Gaoping (Kaoping) River, SW Taiwan: A tidal and flood dominated depositional environment around a submarine canyon. *Journal of Marine Systems*. **76**(4), 405–416.

Huss, G.R., Lewis, R.S., (1995). Presolar diamond, SiC, and graphite in primitive chondrites: Abundances as a function of meteorite class and petrologic type. *Geochimica et Cosmochimica Acta*. **59**(1), 115–160.

Jarvis, I., Carson, G.A., Cooper, M.K.E., Hart, M.B., Leary, P.N., Tocher, B.A., Horne, D., Rosenfeld, A., (1988). Microfossil assemblages and the Cenomanian-Turonian (late Cretaceous) Oceanic Anoxic Event. *Cretaceous Research*. **9**(1), 3–103.

Jarvis, I., Gale, A.S., Jenkyns, H.C., Pearce, M.A., (2006). Secular variation in Late Cretaceous carbon isotopes: a new $\delta^{13}C$ carbonate reference curve for the Cenomanian–Campanian (99.6–70.6 Ma). *Geological Magazine*. **143**(5), 561–608.

Jarvis, I., Lignum, J.S., Groecke, D.R., Jenkyns, H.C., Pearce, M.A., (2011). Black shale deposition, atmospheric CO_2 drawdown, and cooling during the Cenomanian-Turonian Oceanic Anoxic Event. *Paleoceanography*. **26**(3), PA3201.

Jenkyns, H.C., Gale, A.S., Corfield, R.M., (1994). Carbon- and oxygen-isotope stratigraphy of the English Chalk and Italian Scaglia and its palaeoclimatic significance. *Geological Magazine*. **131**(1), 1–34.

Jenkyns, H.C., (2003). Evidence for rapid climate change in the Mesozoic–Palaeogene greenhouse world. *Philosophical Transactions of the Royal Society of London. Series A: Mathematical, Physical and Engineering Sciences*. **361**(1810), 1885–1916.

Jenkyns, H.C., Matthews, A., Tsikos, H., Erel, Y., (2007). Nitrate reduction, sulfate reduction, and sedimentary iron isotope evolution during the Cenomanian-Turonian oceanic anoxic event. *Paleoceanography*. **22**(3), PA3208.

Jenkyns, H.C., (2010). Geochemistry of oceanic anoxic events. *Geochemistry, Geophysics, Geosystems*. **11**(3), Q03004.

Jenkyns, H.C., Dickson, A.J., Ruhl, M., Boorn, S.H.J.M. van den, (2017). Basalt-seawater interaction, the Plenus Cold Event, enhanced weathering and geochemical change: deconstructing Oceanic Anoxic Event 2 (Cenomanian–Turonian, Late Cretaceous). *Sedimentology*. **64**(1), 16–43.

Jiménez Berrocoso, Á., MacLeod, K.G., Martin, E.E., Bourbon, E., Londoño, C.I., Basak, C., (2010). Nutrient trap for Late Cretaceous organic-rich black shales in the tropical North Atlantic. *Geology*. **38**(12), 1111–1114.

Jones, C.E., Jenkyns, H.C., (2001). Seawater strontium isotopes, oceanic anoxic events, and seafloor hydrothermal activity in the Jurassic and Cretaceous. *American Journal of Science*. **301**(2), 112–149.

Kao, S.-J., Shiah, F.-K., Wang, C.-H., Liu, K.-K., (2006). Efficient trapping of organic carbon in sediments on the continental margin with high fluvial sediment input off southwestern Taiwan. *Continental Shelf Research*. **26**(20), 2520–2537.

Kastner, M., Keene, J.B., Gieskes, J.M., (1977). Diagenesis of siliceous oozes – I. Chemical controls on the rate of opal-A to opal-CT transformation – an experimental study. *Geochimica et Cosmochimica Acta.* **41**(8), 1041–1059.

Kehm, K., Flynn, G.J., Sutton, S.R., Hohenberg, C.M., (2002). Combined noble gas and trace element measurements on individual stratospheric interplanetary dust particles. *Meteoritics & Planetary Science*. **37**(10), 1323–1335.

Kehm, K., Flynn, G.J., Hohenberg, C.M., (2006). Noble gas space exposure ages of individual interplanetary dust particles. *Meteoritics & Planetary Science*. **41**(8), 1199–1217.

Keller, G., Adatte, T., Berner, Z., Chellai, E.H., Stueben, D., (2008). Oceanic events and biotic effects of the Cenomanian-Turonian anoxic event, Tarfaya Basin, Morocco. *Cretaceous Research*. **29**(5-6), 976–994.

Kelly, D.C., Zachos, J.C., Bralower, T.J., Schellenberg, S.A., (2005). Enhanced terrestrial weathering/runoff and surface ocean carbonate production during the recovery stages of the Paleocene-Eocene thermal maximum. *Paleoceanography*. **20**(4), PA4023.

Kelly, D.C., Nielsen, T.M.J., McCarren, H.K., Zachos, J.C., Roehl, U., (2010). Spatiotemporal patterns of carbonate sedimentation in the South Atlantic: Implications for carbon cycling during the Paleocene-Eocene thermal maximum. *Palaeogeography Palaeoclimatology Palaeoecology*. **293**(1-2), 30–40.

Kemp, D.B., Coe, A.L., Cohen, A.S., Weedon, G.P., (2011). Astronomical forcing and chronology of the early Toarcian (Early Jurassic) oceanic anoxic event in Yorkshire, UK. *Paleoceanography*. **26**(4), PA4210.

Kerr, A.C., (1998). Oceanic plateau formation: a cause of mass extinction and black shale deposition around the Cenomanian–Turonian boundary? *Journal of the Geological Society*. **155**(4), 619–626.

Knauth, L.P., (1979). A model for the origin of chert in limestone. *Geology*. **7**(6), 274–277.

Knauth, L.P., (1994). Petrogenesis of chert. *Reviews in Mineralogy*. **29**, 233–256.

Knoll, A.H., Follows, M.J., (2016). A bottom-up perspective on ecosystem change in Mesozoic oceans. *Proceedings of the Royal Society B: Biological Sciences*. **283**(1841), 20161755.

Kolonic, S., Wagner, T., Forster, A., Damsté, J.S.S., Walsworth-Bell, B., Erba, E., Turgeon, S., Brumsack, H.-J., Chellai, E.H., Tsikos, H., Kuhnt, W., Kuypers, M.M.M., (2005). Black shale deposition on the northwest African Shelf during the Cenomanian/Turonian oceanic anoxic event: Climate coupling and global organic carbon burial. *Paleoceanography*. **20**(1), PA1006.

Krylov, A.Y., Mamyrin, B.A., Silin, Y.I., Khabarin, L.V., (1973). Helium isotopes in ocean sediments. *Geochemistry International*. **10**, 202–205.

Kuhnt, W., (1990). Agglutinated foraminifera of Western Mediterranean Upper Cretaceous pelagic limestones (Umbrian Apennines, Italy, and Betic Cordillera, Southern Spain). *Micropaleontology*. **36**(4), 297–330.

Kuhnt, W., Luderer, F., Nederbragt, S., Thurow, J., Wagner, T., (2005). Orbital-scale record of the late Cenomanian-Turonian oceanic anoxic event (OAE-2) in the Tarfaya Basin (Morocco). *International Journal of Earth Sciences*. **94**(1), 147–159.

Kuhnt, W., Holbourn, A.E., Beil, S., Aquit, M., Krawczyk, T., Flögel, S., Chellai, E.H., Jabour, H., (2017). Unravelling the onset of Cretaceous Oceanic Anoxic Event 2 in an extended sediment archive from the Tarfaya-Laayoune Basin, Morocco. *Paleoceanography*. **32**(8), 923–946.

Kump, L.R., Arthur, M.A., (1999). Interpreting carbon-isotope excursions: carbonates and organic matter. *Chemical Geology*. **161**(1), 181–198.

Kuroda, J., Ohkouchi, N., Ishii, T., Tokuyama, H., Taira, A., (2005). Lamina-scale analysis of sedimentary components in Cretaceous black shales by chemical compositional mapping: Implications for paleoenvironmental changes during the Oceanic Anoxic Events. *Geochimica et Cosmochimica Acta*. **69**(6), 1479–1494.

Kuroda, J., Ogawa, N.O., Tanimizu, M., Coffin, M.F., Tokuyama, H., Kitazato, H., Ohkouchi, N., (2007). Contemporaneous massive subaerial volcanism and Late Cretaceous Oceanic Anoxic Event 2. *Earth and Planetary Science Letters*. **256**(1-2), 211–223.

Kurz, M.D., Kenna, T.C., Lassiter, J.C., DePaolo, D.J., (1996). Helium isotopic evolution of Mauna Kea Volcano: First results from the 1-km drill core. *Journal of Geophysical Research: Solid Earth*. **101**, 11781–11791.

Kuypers, M.M.M., Pancost, R.D., Damsté, J.S.S., (1999). A large and abrupt fall in atmospheric CO_2 concentration during Cretaceous times. *Nature*. **399**, 342–345.

Kuypers, M.M.M., Pancost, R.D., Nijenhuis, I.A., Damsté, J.S.S., (2002). Enhanced productivity led to increased organic carbon burial in the euxinic North Atlantic basin during the late Cenomanian oceanic anoxic event. *Paleoceanography*. **17**(4), 1051.

Kuypers, M.M.M., Lourens, L.J., Rijpstra, W.I.C., Pancost, R.D., Nijenhuis, I.A., Sinninghe Damsté, J.S., (2004). Orbital forcing of organic carbon burial in the proto-North Atlantic during Oceanic Anoxic Event 2. *Earth and Planetary Science Letters*. **228**(3-4), 465–482.

Lancelot, Y., (1974). Formation of deep-sea chert: role of the sedimentary environment. In: Jenkyns, H.C., Hsü, K.J., eds. *Pelagic Sediments: On Land and Under the Sea*. Oxford: Blackwell Scientific Publications. pp. 349–350.

Lanci, L., Muttoni, G., Erba, E., (2010). Astronomical tuning of the Cenomanian Scaglia Bianca Formation at Furlo, Italy. *Earth and Planetary Science Letters*. **292**(1-2), 231–237.

Langmuir, C.H., Vocke, R.D., Hanson, G.N., Hart, S.R., (1978). A general mixing equation with applications to Icelandic basalts. *Earth and Planetary Science Letters*. **37**(3), 380–392.

Laskar, J., (2020). Astrochronology. In: Gradstein, F.M., Ogg, J.G., Schmitz, M.D., Ogg, G.M., eds. *Geologic Time Scale 2020*. Amsterdam: Elsevier, pp. 139–158.

Laskar, J., Robutel, P., Joutel, F., Gastineau, M., Correia, A.C.M., Levrard, B., (2004). A long-term numerical solution for the insolation quantities of the Earth. *Astronomy & Astrophysics*. **428**(1), 261–285.

Laskar, J., Fienga, A., Gastineau, M., Manche, H., (2011a). La2010: a new orbital solution for the long-term motion of the Earth. *Astronomy & Astrophysics*. **532**, A89.

Laskar, J., Gastineau, M., Delisle, J.-B., Farrés, A., Fienga, A., (2011b). Strong chaos induced by close encounters with Ceres and Vesta. *Astronomy and Astrophysics*. **532**, L4.

Laurin, J., Meyers, S.R., Uličný, D., Jarvis, I., Sageman, B.B., (2015). Axial obliquity control on the greenhouse carbon budget through middle- to high-latitude reservoirs. *Paleoceanography*. **30**(2), 133–149.

Laurin, J., Meyers, S.R., Galeotti, S., Lanci, L., (2016). Frequency modulation reveals the phasing of orbital eccentricity during Cretaceous Oceanic Anoxic Event II and the Eocene hyperthermals. *Earth and Planetary Science Letters*. **442**, 143–156.

Lazarus, D., (2005). A brief review of radiolarian research. *Paläontologische Zeitschrift*. **79**(1), 183–200.

Leckie, R.M., Yuretich, R.F., West, O.L.O., Finkelstein, D., Schmidt, M., (1998). Paleoceanography of the Southwestern Western Interior Sea during the time of the Cenomanian-Turonian Boundary (Late Cretaceous). In: Dean, W.E., Arthur. M.A., eds. *Stratigraphy and Paleoenvironments of the Cretaceous Western Interior Seaway, USA*. Tulsa, OK: SEPM (Society for Sedimentary Geology). pp.101–126.

Leckie, R.M., Bralower, T.J., Cashman, R., (2002). Oceanic anoxic events and plankton evolution: Biotic response to tectonic forcing during the mid-Cretaceous. *Paleoceanography*. **17**(3), 1–23.

Lenniger, M., Nøhr-Hansen, H., Hills, L.V., Bjerrum, C.J., (2014). Arctic black shale formation during Cretaceous Oceanic Anoxic Event 2. *Geology*. **42**(9), 799–802.

Leon-Rodriguez, L., Dickens, G.R., (2010). Constraints on ocean acidification associated with rapid and massive carbon injections: The early Paleogene record at ocean drilling program site 1215, equatorial Pacific Ocean. *Palaeogeography, Palaeoclimatology, Palaeoecology*. **298**(3), 409–420.

Leya, I., Wieler, R., (1999). Nucleogenic production of Ne isotopes in Earth's crust and upper mantle induced by alpha particles from the decay of U and Th. *Journal of Geophysical Research: Solid Earth*. **104**(B7), 15439–15450.

Li, Y.-X., Montañez, I.P., Zhonghui, L., Lifeng, M., (2017). Astronomical constraints on global carbon-cycle perturbation during Oceanic Anoxic Event 2 (OAE2). *Earth and Planetary Science Letters*. **462**, 35–46.

Licciardi, J.M., Kurz, M.D., Clark, P.U., Brook, E.J., (1999). Calibration of cosmogenic ^{3}He production rates from Holocene lava flows in Oregon, USA, and effects of the Earth's magnetic field. *Earth and Planetary Science Letters*. **172**(3-4), 261–271.

Liou, J.-C., Zook, H.A., Dermott, S.F., (1996). Kuiper Belt Dust Grains as a Source of Interplanetary Dust Particles. *Icarus*. **124**(2), 429–440.

Love, S.G., Brownlee, D.E., (1991). Heating and thermal transformation of micrometeoroids entering the Earth's atmosphere. *Icarus*. **89**(1), 26–43.

Love, S.G., Brownlee, D.E., (1993). A direct measurement of the terrestrial mass accretion rate of cosmic dust. *Science*. **262**, 550–553.

Lowery, C.M., Bralower, T.J., Owens, J.D., Rodríguez-Tovar, F.J., Jones, H., Smit, J., Whalen, M.T., Claeys, P., Farley, K., Gulick, S.P.S., Morgan, J.V., Green, S., Chenot, E., Christeson, G.L., Cockell, C.S., Coolen, M.J.L., Ferrière, L., Gebhardt, C., Goto, K., Kring, D.A., Lofi, J., Ocampo-Torres, R., Perez-Cruz, L., Pickersgill, A.E., Poelchau, M.H., Rae, A.S.P., Rasmussen, C., Rebolledo-Vieyra, M., Riller, U., Sato, H., Tikoo, S.M., Tomioka, N., Urrutia-Fucugauchi, J., Vellekoop, J., Wittmann, A., Xiao, L., Yamaguchi, K.E., Zylberman, W., (2018). Rapid recovery of life at ground zero of the end-Cretaceous mass extinction. *Nature*. **558**, 288–291.

Lowrie, W., Alvarez, W., (1981). One hundred million years of geomagnetic polarity history. *Geology*. **9**(9), 392–397.

Luo, Y., Boudreau, B.P., Dickens, G.R., Sluijs, A., Middelburg, J.J., (2016). An alternative model for $CaCO_3$ over-shooting during the PETM: Biological carbonate compensation. *Earth and Planetary Science Letters*. **453**, 223–233.

Ma, C., Meyers, S.R., Sageman, B.B., Singer, B.S., Jicha, B.R., (2014). Testing the astronomical time scale for oceanic anoxic event 2, and its extension into Cenomanian strata of the Western Interior Basin (USA). *GSA Bulletin*. **126**(7-8), 974–989.

MacLeod, K.G., Martin, E.E., Blair, S.W., (2008). Nd isotopic excursion across Cretaceous Ocean Anoxic Event 2 (Cenomanian-Turonian) in the tropical North Atlantic. *Geology*. **36**(10), 811–814.

Madsen, H.B., Stemmerik, L., (2010). Diagenesis of flint and porcellanite in the Maastrichtian Chalk at Stevns Klint, Denmark. *Journal of Sedimentary Research*. **80**(6), 578–588.

Mamyrin, B.A., Tolstikhin, I.N., (1984). *Helium isotopes in nature*. Amsterdam: Elsevier.

Marcantonio, F., Kumar, N., Stute, M., Anderson, R.F., Seidl, M.A., Schlosser, P., Mix, A., (1995). A comparative study of accumulation rates derived by He and Th isotope analysis of marine sediments. *Earth and Planetary Science Letters*. **133**(3-4), 549–555.

Marcantonio, F., Anderson, R.F., Stute, M., Kumar, N., Schlosser, P., Mix, A., (1996). Extraterrestrial ^{3}He as a tracer of marine sediment transport and accumulation. *Nature*. **383**, 705–707.

Marcantonio, F., Higgins, S., Anderson, R.F., Stute, M., Schlosser, P., Rasbury, E.T., (1998). Terrigenous helium in deep-sea sediments. *Geochimica et Cosmochimica Acta*. **62**(9), 1535–1543.

Marcantonio, F., Thomas, D.J., Woodard, S., McGee, D., Winckler, G., (2009). Extraterrestrial He-3 in Paleocene sediments from Shatsky Rise: Constraints on sedimentation rate variability. *Earth and Planetary Science Letters*. **287**(1-2), 24–30.

Margalef, R., (1978). Life-forms of phytoplankton as survival alternatives in an unstable environment. *Oceanologica Acta*. **1**(4), 493–509.

Martin, E.E., MacLeod, K.G., Berrocoso, A.J., Bourbon, E., (2012). Water mass circulation on Demerara Rise during the Late Cretaceous based on Nd isotopes. *Earth and Planetary Science Letters*. **327**, 111–120.

Matsuda, J., Murota, M., Nagao, K., (1990). He and Ne isotopic studies on the extraterrestrial material in deep-sea sediments. *Journal of Geophysical Research: Solid Earth*. **95**, 7111–7117.

McCave, I.N., Gross, T.F., (1991). In-situ measurements of particle settling velocity in the deep sea. *Marine Geology*. **99**(3-4), 403–411.

McCave, I.N., Hall, I.R., (2006). Size sorting in marine muds: Processes, pitfalls, and prospects for paleoflow-speed proxies. *Geochemistry, Geophysics, Geosystems*. **7**(10), Q10N05.

McGee, W.D. (2010). *Reconstructing and interpreting the dust record and probing the plumbing of Mono Lake*. Ph.D. Thesis, Columbia University, United States.

McGee, D., Marcantonio, F., McManus, J.F., Winckler, G., (2010). The response of excess ^{230}Th and extraterrestrial ^{3}He to sediment redistribution at the Blake Ridge, western North Atlantic. *Earth and Planetary Science Letters*. **299**(1-2), 138–149.

McInerney, F.A., Wing, S.L., (2011). The Paleocene-Eocene Thermal Maximum: A perturbation of carbon cycle, climate, and biosphere with implications for the future. *Annual Review of Earth and Planetary Sciences*. **39**, 489–516.

Merrihue, C., (1964). Rare gas evidence for cosmic dust in modern Pacific red clay. *Annals of the New York Academy of Sciences*. **119**, 351–367.

Meyers, S.R., Sageman, B.B., Hinnov, L.A., (2001). Integrated quantitative stratigraphy of the Cenomanian-Turonian Bridge Creek Limestone Member using evolutive harmonic analysis and stratigraphic modelling. *Journal of Sedimentary Research*. **71**, 628–644.

Meyers, P.A., (2006). Paleoceanographic and paleoclimatic similarities between Mediterranean sapropels and Cretaceous black shales. *Palaeogeography, Palaeoclimatology, Palaeoecology*. **235**(1-3), 305–320.

Meyers, S.R., Sageman, B.B., Hinnov, L.A., (2001). Integrated quantitative stratigraphy of the Cenomanian-Turonian Bridge Creek Limestone Member using evolutive harmonic analysis and stratigraphic modelling. *Journal of Sedimentary Research*. **71**(4), 628–644.

Meyers, S.R., Sageman, B.B., Arthur, M.A., (2012). Obliquity forcing of organic matter accumulation during Oceanic Anoxic Event 2. *Paleoceanography*. **27**(3), PA3212.

Miller, K.G., Wright, J.D., Browning, J.V., (2005). Visions of ice sheets in a greenhouse world. *Marine Geology*. **217**(3-4), 215–231.

Mitchell, N.C., Lyle, M.W., (2005). Patchy deposits of Cenozoic pelagic sediments in the central Pacific. *Geology*. **33**(1), 49–52.

Mitchell, R.N., Bice, D.M., Montanari, A., Cleaveland, L.C., Christianson, K.T., Coccioni, R., Hinnov, L.A., (2008). Oceanic anoxic cycles? Orbital prelude to the Bonarelli Level (OAE 2). *Earth and Planetary Science Letters*. **267**(1-2), 1–16.

Monaco, P., Rodríguez-Tovar, F.J., Uchman, A., (2012). Ichnological analysis of lateral environmental heterogeneity within the Bonarelli Level (uppermost Cenomanian) in the classical localities near Gubbio, Central Apennines, Italy. *Palaios*. **27**(1), 48–54.

Moreira, M., (2013). Noble gas constraints on the origin and evolution of earth's volatiles. *Geochemical Perspectives*. **2**(2), 229–230.

Mort, H., Jacquat, O., Adatte, T., Steinmann, P., Föllmi, K., Matera, V., Berner, Z., Stüben, D., (2007). The Cenomanian/Turonian anoxic event at the Bonarelli Level in Italy and Spain: enhanced productivity and/or better preservation? *Cretaceous Research*. **28**(4), 597–612.

Mort, H.P., Adatte, T., Keller, G., Bartels, D., Föllmi, K.B., Steinmann, P., Berner, Z., Chellai, E.H., (2008). Organic carbon deposition and phosphorus accumulation during Oceanic Anoxic Event 2 in Tarfaya, Morocco. *Cretaceous Research*. **29**(5-6), 1008–1023.

Mukhopadhyay, S., Farley, K.A., Montanari, A., (2001a). A 35 Myr record of helium in pelagic limestones from Italy: implications for interplanetary dust accretion from the early Maastrichtian to the middle Eocene. *Geochimica et Cosmochimica Acta*. **65**(4), 653–669.

Mukhopadhyay, S., Farley, K.A., Montanari, A., (2001b). A short duration of the Cretaceous-Tertiary Boundary Event: Evidence from extraterrestrial Helium-3. *Science*. **291**, 1952–1955.

Mukhopadhyay, S., Farley, K.A., (2006). New insights into the carrier phase(s) of extraterrestrial ^{3}He in geologically old sediments. *Geochimica et Cosmochimica Acta*. **70**(19), 5061–5073.

Müller, P.J., Suess, E., (1979). Productivity, sedimentation rate, and sedimentary organic matter in the oceans – I. Organic carbon preservation. *Deep Sea Research Part A. Oceanographic Research Papers*. **26**(12), 1347–1362.

Murphy, B.H., Farley, K.A., Zachos, J.C., (2010). An extraterrestrial ^{3}He-based timescale for the Paleocene–Eocene thermal maximum (PETM) from Walvis Ridge, IODP Site 1266. *Geochimica et Cosmochimica Acta*. **74**(17), 5098–5108.

Murray, R.W., Jones, D.L., Brink, M.R.B., (1992). Diagenetic formation of bedded chert: Evidence from chemistry of the chert-shale couplet. *Geology*. **20**(3), 271–274.

Musavu-Moussavou, B., Danelian, T., Baudin, F., Coccioni, R., Fröhlich, F., (2007). The radiolarian biotic response during OAE2. A high-resolution study across the Bonarelli level at Bottaccione (Gubbio, Italy). *Revue de micropaléontologie*. **50**(3), 253–287.

Muttoni, G., Erba, E., Kent, D.V., Bachtadse, V., (2005). Mesozoic Alpine facies deposition as a result of past latitudinal plate motion. *Nature*. **434**, 59–63.

Nederbragt, A.J., Thurow, Jü., Vonhof, H., Brumsack, H.-J., (2004). Modelling oceanic carbon and phosphorus fluxes: implications for the cause of the late Cenomanian Oceanic Anoxic Event (OAE2). *Journal of the Geological Society*. **161**(4), 721–728.

Negri, A., Cobianchi, M., Luciani, V., Fraboni, R., Milani, A., Claps, M., (2003). Tethyan Cenomanian pelagic rhythmic sedimentation and Pleistocene Mediterranean sapropels: is the biotic signal comparable? *Palaeogeography, Palaeoclimatology, Palaeoecology*. **190**, 373–397.

Negri, A., Ferretti, A., Wagner, T., Meyers, P.A., (2009). Phanerozoic organic-carbon-rich marine sediments: Overview and future research challenges. *Palaeogeography, Palaeoclimatology, Palaeoecology*. **273**, 218–227.

Nemoto, T., Hasegawa, T., (2011). Submillennial resolution carbon isotope stratigraphy across the Oceanic Anoxic Event 2 horizon in the Tappu section, Hokkaido, Japan. *Palaeogeography, Palaeoclimatology, Palaeoecology*. **309**(3-4), 271–280.

Niedermann, S., (2002). Cosmic-ray-produced noble gases in terrestrial rocks: Dating tools for surface processes. *Reviews in Mineralogy and Geochemistry*. **47**(1), 731–784.

Nier, A.O., Schlutter, D.J., (1990). Helium and neon isotopes in stratospheric particles. *Meteoritics*. **25**(4), 263–267.

Nier, A.O., Schlutter, D.J., Brownlee, D.E., (1990). Helium and neon isotopes in deep Pacific ocean sediments. *Geochimica et Cosmochimica Acta*. **54**(1), 173–182.

Nier, A.O., Schlutter, D.J., (1992). Extraction of helium from individual interplanetary dust particles by step-heating. *Meteoritics*. **27**(2), 166–173.

O'Brien, C.L., Robinson, S.A., Pancost, R.D., Sinninghe Damsté, J.S., Schouten, S., Lunt, D.J., Alsenz, H., Bornemann, A., Bottini, C., Brassell, S.C., Farnsworth, A., Forster, A., Huber, B.T., Inglis, G.N., Jenkyns, H.C., Linnert, C., Littler, K., Markwick, P., McAnena, A., Mutterlose, J., Naafs, B.D.A., Püttmann, W., Sluijs, A., van Helmond, N.A.G.M., Vellekoop, J., Wagner, T., Wrobel, N.E., (2017). Cretaceous sea-surface temperature evolution: Constraints from TEX86 and planktonic foraminiferal oxygen isotopes. *Earth-Science Reviews*. **172**, 224–247.

O'Connor, L.K., Jenkyns, H.C., Robinson, S.A., Remmelzwaal, S.R.C., Batenburg, S.J., Parkinson, I.J., Gale, A.S., (2020). A re-evaluation of the Plenus Cold Event, and the links between CO_2, temperature, and seawater chemistry during OAE 2. *Paleoceanography and Paleoclimatology*. **35**(4), e2019PA003631.

Ohkouchi, N., Kawamura, K., Kajiwara, Y., Wada, E., Okada, M., Kanamatsu, T., Taira, A., (1999). Sulfur isotope records around Livello Bonarelli (northern Apennines, Italy) black shale at the Cenomanian-Turonian boundary. *Geology*. **27**(6), 535–538.

Okazaki, R., Noguchi, T., Tsujimoto, S., Tobimatsu, Y., Nakamura, T., Ebihara, M., Itoh, S., Nagahara, H., Tachibana, S., Terada, K., Yabuta, H., (2015). Mineralogy and noble gas isotopes of micrometeorites collected from Antarctic snow. *Earth, Planets and Space*. **67**(1), 90.

Owens, J.D., Gill, B.C., Jenkyns, H.C., Bates, S.M., Severmann, S., Kuypers, M.M.M., Woodfine, R.G., Lyons, T.W., (2013). Sulfur isotopes track the global extent and dynamics of euxinia during Cretaceous Oceanic Anoxic Event 2. *Proceedings of the National Academy of Sciences*. **110**(46), 18407–18412.

Owens, J.D., Lyons, T.W., Hardisty, D.S., Lowery, C.M., Lu, Z., Lee, B., Jenkyns, H.C., (2016). Patterns of local and global redox variability during the Cenomanian–Turonian Boundary Event (Oceanic Anoxic Event 2) recorded in carbonates and shales from central Italy. *Sedimentology*. **64**(1), 168–185.

Owens, J.D., Lyons, T.W., Lowery, C.M., (2018). Quantifying the missing sink for global organic carbon burial during a Cretaceous oceanic anoxic event. *Earth and Planetary Science Letters*. **499**, 83–94.

Oxburgh, E.R., O'nions, R.K., (1987). Helium loss, tectonics, and the terrestrial heat budget. *Science*. **237**, 1583–1588.

Ozima, M., Podosek, F.A., (1983). *Noble Gas Geochemistry*. New York, NY: Cambridge University Press.

Ozima, M., Takayanagi, M., Zashu, S., Amari, S., (1984). High $^{3}He/^{4}He$ ratio in ocean sediments. *Nature*. **311**, 448–450.

Pancost, R.D., Crawford, N., Magness, S., Turner, A., Jenkyns, H.C., Maxwell, J.R., (2004). Further evidence for the development of photic-zone euxinic conditions during Mesozoic oceanic anoxic events. *Journal of the Geological Society*. **161**(3), 353–364.

Parente, M., Frijia, G., Lucia, M.D., Jenkyns, H.C., Woodfine, R.G., Baroncini, F., (2008). Stepwise extinction of larger foraminifers at the Cenomanian-Turonian boundary: A shallow-water perspective on nutrient fluctuations during Oceanic Anoxic Event 2 (Bonarelli Event). *Geology*. **36**(9), 715–718.

Parker, Raymond.L., (1967). Data of geochemistry: composition of the earth's crust. In: Fleischer, M., ed. *Data of Geochemistry, Geological Survey Professional Paper*. Washington: United States Government Printing Office. No. 440-D.

Pastor, L., Cathalot, C., Deflandre, B., Viollier, E., Soetaert, K., Meysman, F.J.R., Ulses, C., Metzger, E., Rabouille, C., (2011a). Modelling biogeochemical processes in sediments from the Rhône River prodelta area (NW Mediterranean Sea). *Biogeosciences*. **8**(5), 1351–1366.

Pastor, L., Deflandre, B., Viollier, E., Cathalot, C., Metzger, E., Rabouille, C., Escoubeyrou, K., Lloret, E., Pruski, A.M., Vétion, G., Desmalades, M., Buscail, R., Grémare, A., (2011b). Influence of the organic matter composition on benthic oxygen demand in the Rhône River prodelta (NW Mediterranean Sea). *Continental Shelf Research*. **31**(9), 1008–1019.

Patterson, D.B., Farley, K.A., (1998). Extraterrestrial ^{3}He in seafloor sediments: evidence for correlated 100 kyr periodicity in the accretion rate of interplanetary dust, orbital parameters, and Quaternary climate. *Geochimica et Cosmochimica Acta*. **62**(23-24), 3669–3682.

Patterson, D.B., Farley, K.A., Schmitz, B., (1998). Preservation of extraterrestrial ^{3}He in 480-Ma-old marine limestones. *Earth and Planetary Science Letters*. **163**(1-4), 315–325.

Patterson, D.B., Farley, K.A., Norman, M.D., (1999). ^{4}He as a tracer of continental dust: a 1.9 million year record of aeolian flux to the west equatorial Pacific Ocean. *Geochimica et Cosmochimica Acta*. **63**(5), 615–625.

Pearce, M.A., Jarvis, I., Tocher, B.A., (2009). The Cenomanian–Turonian boundary event, OAE 2 and palaeoenvironmental change in epicontinental seas: New insights from the dinocyst and geochemical records. *Palaeogeography, Palaeoclimatology, Palaeoecology*. **280**, 207–234.

Pedersen, T.F., Calvert, S.E., (1990). Anoxia vs. productivity: What controls the formation of organic-carbon-rich sediments and sedimentary rocks? *AAPG Bulletin*. **74**, 454–466.

Penman, D.E., Turner, S.K., Sexton, P.F., Norris, R.D., Dickson, A.J., Boulila, S., Ridgwell, A., Zeebe, R.E., Zachos, J.C., Cameron, A., Westerhold, T., Röhl, U., (2016). An abyssal carbonate compensation depth overshoot in the aftermath of the Palaeocene–Eocene Thermal Maximum. *Nature Geoscience*. **9**(8), 575–580.

Pepin, R.O., Palma, R.L., Schlutter, D.J., (2000). Noble gases in interplanetary dust particles, I: The excess helium-3 problem and estimates of the relative fluxes of solar wind and solar energetic particles in interplanetary space. *Meteoritics & Planetary Science*. **35**(3), 495–504.

Percival, L.M.E., Helmond, N.A.G.M. van, Selby, D., Goderis, S., Claeys, P., (2020). Complex interactions between Large Igneous province emplacement and global-temperature changes during the Cenomanian-Turonian Oceanic Anoxic Event (OAE 2). *Paleoceanography and Paleoclimatology*. **35**(10), e2020PA004016.

Pogge von Strandmann, P.A.E., Jenkyns, H.C., Woodfine, R.G., (2013). Lithium isotope evidence for enhanced weathering during Oceanic Anoxic Event 2. *Nature Geoscience*. **6**(8), 668–672.

Porcelli, D., Ballentine, C.J., Wieler, R., (2002). An overview of noble gas geochemistry and cosmochemistry. *Reviews in Mineralogy and Geochemistry*. **47**(1), 1–20.

Poulsen, C.J., Barron, E.J., Arthur, M.A., Peterson, W.H., (2001). Response of the mid-Cretaceous global oceanic circulation to tectonic and CO_2 forcings. *Paleoceanography*. **16**(6), 576–592.

Poulton, S.W., Henkel, S., Maerz, C., Urquhart, H., Floegel, S., Kasten, S., Damste, J.S.S., Wagner, T., (2015). A continental-weathering control on orbitally driven redox-nutrient cycling during Cretaceous Oceanic Anoxic Event 2. *Geology*. **43**(11), 963–966.

Pratt, L.M., King, J.D., (1986). Variable marine productivity and high eolian input recorded by rhythmic black shales in Mid-Cretaceous pelagic deposits from central Italy. *Paleoceanography*. **1**(4), 507–522.

Premoli Silva, I., Paggi, L., Monechi, S., (1977). Cretaceous through Paleocene biostratigraphy of the pelagic sequence at Gubbio. *Memorie della Società Geologica Italiana*. **15**, 21–32.

Premoli Silva, I., Ripepe, M., Tornaghi, M.E., (1989). Planktonic foraminiferal distribution record productivity cycles: evidence from the Aptian-Albian Piobbico core (central Italy). *Terra Nova*. **1**(5), 443–448.

Premoli Silva, I., Erba, E., Salvini, G., Locatelli, C., Verga, D., (1999). Biotic changes in Cretaceous oceanic anoxic events of the Tethys. *The Journal of Foraminiferal Research*. **29**(4), 352–370.

Prokoph, A., Villeneuve, M., Agterberg, F.P., Rachold, V., (2001). Geochronology and calibration of global Milankovitch cyclicity at the Cenomanian-Turonian boundary. *Geology*. **29**(6), 523–526.

Pucéat, E., (2008). A new breath of life for anoxia. *Geology*. **36**(10), 831–832.

Racki, G., Cordey, F., (2000). Radiolarian palaeoecology and radiolarites: is the present the key to the past? *Earth-Science Reviews*. **52**(1-3), 83–120.

Ragueneau, O., Tréguer, P., Leynaert, A., Anderson, R.F., Brzezinski, M.A., DeMaster, D.J., Dugdale, R.C., Dymond, J., Fischer, G., François, R., Heinze, C., Maier-Reimer, E., Martin-Jézéquel, V., Nelson, D.M., Quéguiner, B., (2000). A review of the Si cycle in the modern ocean: recent progress and missing gaps in the application of biogenic opal as a paleoproductivity proxy. *Global and Planetary Change*. **26**(4), 317–365.

Rajan, R.S., Brownlee, D.E., Tomandl, D., Hodge, P.W., Iv, H.F., Britten, R.A., (1977). Detection of ^{4}He in stratospheric particles gives evidence of extraterrestrial origin. *Nature*. **267**, 133–134.

Raquin, A., Moreira, M.A., Guillon, F., (2008). He, Ne and Ar systematics in single vesicles: Mantle isotopic ratios and origin of the air component in basaltic glasses. *Earth and Planetary Science Letters*. **274**(1-2), 142–150.

Raudkivi, A.J., (1990). *Loose boundary hydraulics*. 3rd ed. New York: Pergammon Press.

Ray, D.C., van Buchem, F.S.P., Baines, G., Davies, A., Gréselle, B., Simmons, M.D., Robson, C., (2019). The magnitude and cause of short-term eustatic Cretaceous sea-level change: A synthesis. *Earth-Science Reviews*. **197**, 102901.

Reshma, K., Rudraswami, N.G., Prasad, M.S., (2013). Chondrule-like object from the Indian Ocean cosmic spherules. *Journal of Earth System Science*. **122**(4), 1161–1171.

Robinson, S.A., Murphy, D.P., Vance, D., Thomas, D.J., (2010). Formation of "Southern Component Water" in the Late Cretaceous: Evidence from Nd-isotopes. *Geology*. **38**(10), 871–874.

Robinson, S.A., Vance, D., (2012). Widespread and synchronous change in deep-ocean circulation in the North and South Atlantic during the Late Cretaceous. *Paleoceanography*. **27**(1), PA1102.

Robinson, S.A., Dickson, A.J., Pain, A., Jenkyns, H.C., O'Brien, C.L., Farnsworth, A., Lunt, D.J., (2019). Southern Hemisphere sea-surface temperatures during the Cenomanian–Turonian: Implications for the termination of Oceanic Anoxic Event 2. *Geology*. **47**(2), 131–134.

Röhl, U., Westerhold, T., Bralower, T.J., Zachos, J.C., (2007). On the duration of the Paleocene-Eocene thermal maximum (PETM). *Geochemistry, Geophysics, Geosystems*. **8**(12), Q12002.

Sageman, B.B., Meyers, S.R., Arthur, M.A., (2006). Orbital time scale and new C-isotope record for Cenomanian-Turonian boundary stratotype. *Geology*. **34**(2), 125–128.

Salmon, V., Derenne, S., Lallier-Vergès, E., Largeau, C., Beaudoin, B., (2000). Protection of organic matter by mineral matrix in a Cenomanian black shale. *Organic Geochemistry*. **31**(5), 463–474.

Salmon, V., Derenne, S., Lallier-Vergès, E., Connan, J., Kahn-Harari, A., Largeau, C., (2003). Origin of compositional differences in organic matter abundance and oil potential of cherty and clayey Cenomanian black levels in the Umbria-Marche basin (Italy). *Organic Geochemistry*. **34**(9), 1237–1245.

Sandford, S.A., Walker, R.M., (1985). Laboratory infrared transmission spectra of individual interplanetary dust particles from 2.5 to 25 microns. *The Astrophysical Journal*. **291**, 838–851.

Schlanger, S.O., Jenkyns, H.C., (1976). Cretaceous Oceanic Anoxic Events: Causes and consequences. *Geologie en Mijnbouw*. **55**, 179–184.

Schlanger, S.O., Arthur, M.A., Jenkyns, H.C., Scholle, P.A., (1987). The Cenomanian-Turonian Oceanic Anoxic Event, I. Stratigraphy and distribution of organic carbon-rich beds and the marine $\delta^{13}C$ excursion. *Geological Society, London, Special Publications*. **26**(1), 371–399.

Schmitz, B., Heck, P.R., Alvarez, W., Kita, N.T., Rout, S.S., Cronholm, A., Defouilloy, C., Martin, E., Smit, J., Terfelt, F., (2017). Meteorite flux to Earth in the Early Cretaceous as reconstructed from sediment-dispersed extraterrestrial spinels. *Geology*. **45**(9), 807–810.

Scholle, P.A., Arthur, M.A., (1980). Carbon isotope fluctuations in Cretaceous pelagic limestones: Potential stratigraphic and petroleum exploration tool. *AAPG Bulletin*. **64**(1), 67–87.

Schwarzacher, W., (1994). Cyclostratigraphy of the Cenomanian in the Gubbio District, Italy; a field study. *Special Publication of the International Association of Sedimentologists*. **19**, 87–97.

Scopelliti, G., Bellanca, A., Coccioni, R., Luciani, V., Neri, R., Baudin, F., Chiari, M., Marcucci, M., (2004). High-resolution geochemical and biotic records of the Tethyan 'Bonarelli Level' (OAE2, latest Cenomanian) from the Calabianca–Guidaloca composite section, northwestern Sicily, Italy. *Palaeogeography, Palaeoclimatology, Palaeoecology*. **208**(3-4), 293–317.

Scopelliti, G., Bellanca, A., Neri, R., Baudin, F., Coccioni, R., (2006). Comparative high-resolution chemostratigraphy of the Bonarelli Level from the reference Bottaccione section (Umbria–Marche Apennines) and from an equivalent section in NW Sicily: Consistent and contrasting responses to the OAE2. *Chemical Geology*. **228**(4), 266–285.

Sigurdsson, H., (1990). Assessment of the atmospheric impact of volcanic eruptions. In: Sharpton, V.L., Ward, P.D., eds. *Global Catastrophes in Earth History; An Interdisciplinary Conference on Impacts, Volcanism, and Mass Mortality* (Vol. 247). Geological Society of America. pp. 99–110.

Sinninghe Damsté, J.S., Köster, J., (1998). A euxinic southern North Atlantic Ocean during the Cenomanian/Turonian oceanic anoxic event. *Earth and Planetary Science Letters*. **158**(3-4), 165–173.

Sinninghe Damsté, J.S., van Bentum, E.C., Reichart, G.-J., Pross, J., Schouten, S., (2010). A CO_2 decrease-driven cooling and increased latitudinal temperature gradient during the mid-Cretaceous Oceanic Anoxic Event 2. *Earth and Planetary Science Letters*. **293**(1-2), 97–103.

Sinton, C.W., Duncan, R.A., (1997). Potential links between ocean plateau volcanism and global ocean anoxia at the Cenomanian-Turonian boundary. *Economic Geology*. **92**(7-8), 836–842.

Smith, C.R., A. Levin, L., Hoover, D.J., McMurtry, G., Gage, J.D., (2000). Variations in bioturbation across the oxygen minimum zone in the northwest Arabian Sea. *Deep Sea Research Part II: Topical Studies in Oceanography.* **47**, 227–257.

Snow, L.J., Duncan, R.A., Bralower, T.J., (2005). Trace element abundances in the Rock Canyon Anticline, Pueblo, Colorado, marine sedimentary section and their relationship to Caribbean plateau construction and oxygen anoxic event 2. *Paleoceanography*. **20**(3), PA3005.

Sprovieri, M., Sabatino, N., Pelosi, N., Batenburg, S.J., Coccioni, R., Iavarone, M., Mazzola, S., (2013). Late Cretaceous orbitally paced carbon isotope stratigraphy from the Bottaccione Gorge (Italy). *Palaeogeography, Palaeoclimatology, Palaeoecology*. **379**, 81–94.

Stampfli, G., (2005). Plate tectonic of the Apulia-Adria microcontinents. In: Finetti, I.R., ed. *CROP PROJECT deep seismic explorations of the Mediterranean and Italy.* The Netherlands: Elsevier. pp. 747–766.

Stoll, H.M., Schrag, D.P., (2000). High-resolution stable isotope records from the Upper Cretaceous rocks of Italy and Spain: Glacial episodes in a greenhouse planet? *GSA Bulletin*. **112**(2), 308–319.

Stordal, M.C., Johnson, J.W., Guinasso, N.L., Schink, D.R., (1985). Quantitative evaluation of bioturbation rates in deep ocean sediments. II. Comparison of rates determined by ^{210}Pb and ^{239,240}Pu. *Marine Chemistry.* **17**, 99–114.

Stuart, F.M., Harrop, P.J., Knott, S., Turner, G., (1999). Laser extraction of helium isotopes from Antarctic micrometeorites: source of He and implications for the flux of extraterrestrial ^{3}He to earth. *Geochimica et Cosmochimica Acta*. **63**(17), 2653–2665.

Suan, G., Pittet, B., Bour, I., Mattioli, E., Duarte, L.V., Mailliot, S., (2008). Duration of the Early Toarcian carbon isotope excursion deduced from spectral analysis: Consequence for its possible causes. *Earth and Planetary Science Letters*. **267**, 666–679.

Takashima, R., Nishi, H., Hayashi, K., Okada, H., Kawahata, H., Yamanaka, T., Fernando, A.G., Mampuku, M., (2009). Litho-, bio- and chemostratigraphy across the Cenomanian/Turonian

boundary (OAE 2) in the Vocontian Basin of southeastern France. *Palaeogeography, Palaeoclimatology, Palaeoecology*. **273**(1), 61–74.

Takayanagi, M., Ozima, M., (1987). Temporal variation of $^{3}He/^{4}He$ ratio recorded in deep-sea sediment cores. *Journal of Geophysical Research: Solid Earth*. **92**(B12), 12531–12538.

Tavarnelli, E., (1997). Structural evolution of a foreland fold-and-thrust belt: the Umbria-Marche Apennines, Italy. *Journal of Structural Geology*. **19**(3-4), 523–534.

Taylor, S.R., McLennan, S.M., (1985). *The continental crust: Its composition and evolution*. Palo Alto, CA: Blackwell Scientific Publishing.

Them, T.R., Gill, B.C., Selby, D., Gröcke, D.R., Friedman, R.M., Owens, J.D., (2017). Evidence for rapid weathering response to climatic warming during the Toarcian Oceanic Anoxic Event. *Scientific Reports*. **7**(1), 5003.

Thomas, E., (1990). Late Cretaceous through Neogene deep-sea benthic foraminifers (Maud Rise, Weddell Sea, Antarctica), in: Barker, P.F., Kennett, J.P., eds. *Proceedings of the Ocean Drilling Program, Scientific Results*. ODP, College Station, Texas. Vol. 113. pp. 571–594.

Thomas, K.L., Zolensky, M.E., Kloeck, W., McKay, D.S., (1990). Mineralogical descriptions of eight hydrated interplanetary dust particles and their relationship to chondrite matrix. *Lunar and Planetary Science Conference*. **21**, 1250–1251.

Thompson, C.E., (2009). *Tracking organic matter from source to sink in the Waiapu River watershed: A geochemical perspective*. Ph.D. thesis, NC State University.

Tiraboschi, D., Erba, E., Jenkyns, H.C., (2009). Origin of rhythmic Albian black shales (Piobbico core, central Italy): Calcareous nannofossil quantitative and statistical analyses and paleoceanographic reconstructions. *Paleoceanography*. **24**(2), PA2222.

Torfstein, A., (2012). Size fractionation, reproducibility and provenance of helium isotopes in north-equatorial pacific pelagic clays. *Earth and Planetary Science Letters*. **339**, 151–163.

Trabucho-Alexandre, J., Tuenter, E., Henstra, G.A., van der Zwan, K.J., van de Wal, R.S.W., Dijkstra, H.A., de Boer, P.L., (2010). The mid-Cretaceous North Atlantic nutrient trap: Black shales and OAEs. *Paleoceanography*. **25**(4), PA4201.

Trabucho-Alexandre, J., Negri, A., de Boer, P.L., (2011). Early Turonian pelagic sedimentation at Moria (Umbria-Marche, Italy): Primary and diagenetic controls on lithological oscillations. *Palaeogeography, Palaeoclimatology, Palaeoecology*. **311**(3-4), 200–214.

Tréguer, P.J., De La Rocha, C.L., (2013). The world ocean silica cycle. *Annual Review of Marine Science*. **5**, 477–501.

Trieloff, M., Falter, M., Jessberger, E.K., (2003). The distribution of mantle and atmospheric argon in oceanic basalt glasses. *Geochimica et Cosmochimica Acta.* **67**(6), 1237–1253.

Tsikos, H., Jenkyns, H.C., Walsworth-Bell, B., Petrizzo, M.R., Forster, A., Kolonic, S., Erba, E., Silva, I.P., Baas, M., Wagner, T., DamstÉ, J.S.S., (2004). Carbon-isotope stratigraphy recorded by the Cenomanian–Turonian Oceanic Anoxic Event: correlation and implications based on three key localities. *Journal of the Geological Society*. **161**(4), 711–719.

Turgeon, S., Brumsack, H.-J., (2006). Anoxic vs dysoxic events reflected in sediment geochemistry during the Cenomanian–Turonian Boundary Event (Cretaceous) in the Umbria–Marche Basin of central Italy. *Chemical Geology*. **234**(3-4), 321–339.

Turgeon, S.C., Creaser, R.A., (2008). Cretaceous Oceanic Anoxic Event 2 triggered by a massive magmatic episode. *Nature*. **454**, 323–326.

Turpin, M., Emmanuel, L., Immenhauser, A., Renard, M., (2012). Geochemical and petrographical characterization of fine-grained carbonate particles along proximal to distal transects. *Sedimentary Geology*. **281**, 1–20.

Tyrrell, T., (1999). The relative influences of nitrogen and phosphorus on oceanic primary production. *Nature*. **400**, 525–531.

Uličný, D., Hladíková, J., Attrep Jr, M.J., Čech, S., Hradecká, L., Svobodová, M., (1997). Sea-level changes and geochemical anomalies across the Cenomanian–Turonian boundary: Pecínov quarry, Bohemia. *Palaeogeography, Palaeoclimatology, Palaeoecology*. **132**(1-4), 265–285.

Uramoto, G.-I., Abe, Y., Hirano, H., (2009). Carbon isotope fluctuations of terrestrial organic matter for the Upper Cretaceous (Cenomanian–Santonian) in the Obira area of Hokkaido, Japan. *Geological Magazine*. **146**(5), 761–774.

van Bentum, E.C., Hetzel, A., Brumsack, H.-J., Forster, A., Reichart, G.-J., Sinninghe Damsté, J.S., (2009). Reconstruction of water column anoxia in the equatorial Atlantic during the Cenomanian–Turonian oceanic anoxic event using biomarker and trace metal proxies. *Palaeogeography, Palaeoclimatology, Palaeoecology*. **280**(3-4), 489–498.

van Bentum, E.C., Reichart, G.-J., Forster, A., Damste, J.S.S., (2012). Latitudinal differences in the amplitude of the OAE-2 carbon isotopic excursion: pCO_2 and paleo productivity. *Biogeosciences*. **9**(2), 717–731.

van Graas, G., Viets, T.C., de Leeuw, J.W., Schenck, P.A., (1983). A study of the soluble and insoluble organic matter from the Livello Bonarelli, a Cretaceous black shale deposit in the Central Apennines, Italy. *Geochimica et Cosmochimica Acta*. **47**(6), 1051–1059.

van Helmond, N.A.G.M., Sluijs, A., Reichart, G.-J., Damsté, J.S.S., Slomp, C.P., Brinkhuis, H., (2014). A perturbed hydrological cycle during Oceanic Anoxic Event 2. *Geology*. **42**(2), 123–126.

van Helmond, N.A.G.M., Sluijs, A., Damste, J.S.S., Reichart, G.-J., Voigt, S., Erbacher, J., Pross, J., Brinkhuis, H., (2015). Freshwater discharge controlled deposition of Cenomanian-Turonian black shales on the NW European epicontinental shelf (Wunstorf, northern Germany). *Climate of the Past*. **11**, 495–508.

Vandenberg, J., Klootwijk, C.T., Wonders, A.A.H., (1978). Late Mesozoic and Cenozoic movements of the Italian Peninsula: Further paleomagnetic data from the Umbrian sequence. *GSA Bulletin*. **89**(1), 133–150.

Voigt, S., Gale, A.S., Flögel, S., (2004). Midlatitude shelf seas in the Cenomanian-Turonian greenhouse world: Temperature evolution and North Atlantic circulation. *Paleoceanography*. **19**(4), PA4020.

Voigt, S., Gale, A.S., Voigt, T., (2006). Sea-level change, carbon cycling and palaeoclimate during the Late Cenomanian of northwest Europe; an integrated palaeoenvironmental analysis. *Cretaceous Research*. **27**(6), 836–858.

Voigt, S., Aurag, A., Leis, F., Kaplan, U., (2007). Late Cenomanian to Middle Turonian high-resolution carbon isotope stratigraphy: New data from the Münsterland Cretaceous Basin, Germany. *Earth and Planetary Science Letters*. **253**(1-2), 196–210.

Voigt, S., Erbacher, J., Mutterlose, J., Weiss, W., Westerhold, T., Wiese, F., Wilmsen, M., Wonik, T., (2008). The Cenomanian–Turonian of the Wunstorf section – (North Germany): global stratigraphic reference section and new orbital time scale for Oceanic Anoxic Event 2. *Newsletters on Stratigraphy*. **43**(1), 65–89.

Vollmer, R., (1976). Rb-Sr and U-Th-Pb systematics of alkaline rocks: the alkaline rocks from Italy. *Geochimica et Cosmochimica Acta.* **40**(3), 283–295.

von der Borch, C.C., Galehouse, J., Nesterhoff, W.D., (1971). Silicified limestone-chert sequences cored during leg 8 of the Deep Sea Drilling Project: A petrographic study. In: Tracey, J.I., Jr. and Sutton, G.H., chief scientists. *Initial Reports of the Deep Sea Drilling Project, Volume VIII.* Washington (U.S. Government Printing Office), pp. 819–827.

Waltham, D., (2015). Milankovitch period uncertainties and their impact on cyclostratigraphy. *Journal of Sedimentary Research*. **85**(8), 990–998.

Wedepohl, K.H., (1978). Manganese: abundance in common sediments and sedimentary rocks. In: *Handbook of Geochemistry*. Berlin: Springer. pp. 1–17.

Westerhold, T., Röhl, U., Wilkens, R.H., Gingerich, P.D., Clyde, W.C., Wing, S.L., Bowen, G.J., Kraus, M.J., (2018). Synchronizing early Eocene deep-sea and continental records – cyclostratigraphic age models for the Bighorn Basin Coring Project drill cores. *Climate of the Past*. **14**(3), 303–319.

Westermann, S., Vance, D., Cameron, V., Archer, C., Robinson, S.A., (2014). Heterogeneous oxygenation states in the Atlantic and Tethys oceans during Oceanic Anoxic Event 2. *Earth and Planetary Science Letters*. **404**, 178–189.

Westphal, H., Böhm, F., Bornholdt, S., (2004). Orbital frequencies in the carbonate sedimentary record: distorted by diagenesis? *Facies*. **50**(1), 3–11.

Williams, L.A., Crerar, D.A., (1985). Silica diagenesis; II, General mechanisms. *Journal of Sedimentary Research*. **55**(3), 312–321.

Wise, S., W., Weaver, F., M., (1974). Chertification of oceanic sediments. In: Jenkyns, H.C., Hsü, K.J., eds. *Pelagic Sediments: On Land and Under the Sea*. Oxford: Blackwell Scientific Publications. pp. 301–326.

Zachos, J.C., Röhl, U., Schellenberg, S.A., Sluijs, A., Hodell, D.A., Kelly, D.C., Thomas, E., Nicolo, M., Raffi, I., Lourens, L.J., McCarren, H., Kroon, D., (2005). Rapid acidification of the ocean during the Paleocene-Eocene Thermal Maximum. *Science*. **308**, 1611–1615.

Zeebe, R.E., Zachos, J.C., (2007). Reversed deep-sea carbonate ion basin gradient during Paleocene-Eocene thermal maximum. *Paleoceanography*. **22**(3), PA3201.

Zeebe, R.E., Zachos, J.C., (2013). Long-term legacy of massive carbon input to the Earth system: Anthropocene versus Eocene. *Philosophical Transactions of the Royal Society A: Mathematical, Physical and Engineering Sciences*. **371**(2001), 20120006.

Zeeden, C., Meyers, S.R., Lourens, L.J., Hilgen, F.J., (2015). Testing astronomically tuned age models. *Paleoceanography*. **30**, 369–383.

Zheng, X.-Y., Jenkyns, H.C., Gale, A.S., Ward, D.J., Henderson, G.M., (2013). Changing ocean circulation and hydrothermal inputs during Ocean Anoxic Event 2 (Cenomanian-Turonian): Evidence from Nd-isotopes in the European shelf sea. *Earth and Planetary Science Letters*. **375**, 338–348.

Zheng, X.-Y., Jenkyns, H.C., Gale, A.S., Ward, D.J., Henderson, G.M., (2016). A climatic control on reorganization of ocean circulation during the mid-Cenomanian event and Cenomanian-Turonian oceanic anoxic event (OAE 2): Nd isotope evidence. *Geology*. **44**(2), 151–154.

Zhiyao, S., Tingting, W., Fumin, X., Ruijie, L., (2008). A simple formula for predicting settling velocity of sediment particles. *Water Science and Engineering*. **1**(1), 37–43.

Zolensky, M.E., (1987). Refractory interplanetary dust particles. *Science*. **237**, 1466–1468.

Appendix: Noble Gas data

Contents

Table A.1 (1): Furlo Cycle A – Rock Eval and helium data

Table A.1 (2): Furlo Cycle A – deconvolved helium data, sedimentation rate, organic-carbon mass-accumulation rate and cumulative time

Table A.2 (1): Furlo Cycle B – Rock Eval and helium data

Table A.2 (2): Furlo Cycle B - deconvolved helium data, sedimentation rate, organic-carbon mass-accumulation rate and cumulative time

Table A.3 (1): Furlo Cycle C – Rock Eval and helium data

Table A.3 (2): Furlo Cycle C – deconvolved helium data, sedimentation rate, organic-carbon mass-accumulation rate and cumulative time

Table A.4 (1): Contessa Cycle B – Rock Eval and helium data

Table A.4 (2): Contessa Cycle B – deconvolved helium data, sedimentation rate, organic-carbon mass-accumulation rate and cumulative time

Table A.5 (1): Bonarelli Level – Rock Eval, stable isotope and helium data

Table A.5 (2): Bonarelli Level – deconvolved helium data, sedimentation rate, organic-carbon mass-accumulation rate and cumulative time

Table A.6 (1): Background flux samples – helium data

Table A.6 (2): Background flux samples – deconvolved helium data and background flux

Table A.7: Bottaccione Gorge samples – helium data and deconvolved helium data

Table A.8: Chert transects – helium data

Table A.9: Neon data

TABLE A.1 (1): Furlo Cycle A - Rock Eval and helium data

Cycle Depth [a] (cm)	Sample Name	Lithology	TOC [b] (%)	carbonate [c] (%)	HI [d] (mg HC/g TOC)	3He (cc/g)	3He error [e] (cc/g)	4He (cc/g)	4He error [e] (cc/g)	3He/4He	3He/4He error [e]
0.3	FU 160 B	marl	2.48	59.08	279	6.57E-14	4.66E-15	1.05E-07	2.99E-09	6.23E-07	4.05E-08
0.3	FU 160 C	marl	"	"	"	6.45E-14	4.50E-15	9.20E-08	2.61E-09	7.01E-07	4.48E-08
0.9	FU 159 C	black shale	5.56	60.83	321	1.93E-13	1.02E-14	3.77E-07	1.07E-08	5.12E-07	2.29E-08
0.9	FU 159 A	black shale	"	"	"	2.18E-13	1.28E-14	5.38E-07	1.52E-08	4.05E-07	2.10E-08
1.2	FU 158 A	marl	2.79	30.67	324	3.20E-14	3.92E-15	2.62E-07	7.44E-09	1.22E-07	1.45E-08
1.2	FU 158 B	marl	"	"	"	4.12E-14	8.17E-15	2.92E-07	8.28E-09	1.41E-07	2.77E-08
3.7	FU 157 F	chert	0.43	3.75	277	3.73E-14	6.02E-15	2.52E-07	7.14E-09	1.48E-07	2.35E-08
3.7	FU157 A, B, C	chert	"	"	"	4.50E-14	3.39E-15	4.67E-07	1.44E-08	9.62E-08	6.62E-09
3.7	FU 157 E	chert	"	"	"	2.85E-14	4.76E-15	3.63E-07	1.03E-08	7.84E-08	1.29E-08
3.9	FU 156 D	black shale	1.23	31.92	227	8.63E-14	8.20E-15	2.32E-07	6.58E-09	3.72E-07	3.37E-08
3.9	FU 156 A	black shale	"	"	"	7.81E-14	1.11E-14	2.94E-07	8.33E-09	2.66E-07	3.71E-08
3.9	FU 156 B *	black shale	"	"	"	1.37E-13	8.83E-15	4.61E-07	1.31E-08	2.98E-07	1.72E-08
7.7	FUR/11 22.45 1A	limestone	0.06	91.92	50	3.28E-14	1.84E-15	3.41E-08	9.68E-10	9.62E-07	4.65E-08
7.7	FUR/11 22.45 2	limestone	"	"	"	3.15E-14	1.84E-15	2.37E-08	6.76E-10	1.33E-06	6.79E-08
10.7	FUR/11 22.48 2	limestone	0.02	94.25	50	1.77E-14	8.40E-16	2.31E-08	6.55E-10	7.67E-07	2.92E-08
10.7	FUR/11 22.48	limestone	"	"	"	1.73E-14	1.14E-15	2.51E-08	7.12E-10	6.92E-07	4.12E-08
13.7	FUR/11 22.51 B	limestone	0.01	94.92	300	1.85E-14	8.96E-16	2.10E-08	4.21E-10	8.77E-07	3.88E-08
13.7	FUR/11 22.51 C	limestone	"	"	"	1.45E-14	7.69E-16	1.78E-08	5.05E-10	8.13E-07	3.65E-08
13.7	FUR/11 22.51 *	limestone	"	"	"	3.73E-14	1.86E-15	2.49E-08	4.98E-10	1.50E-06	6.85E-08
16.7	FUR/11 22.54 3	limestone	0.03	94.67	100	2.64E-14	1.93E-15	5.94E-08	1.69E-09	4.44E-07	3.01E-08
16.7	FUR/11 22.54	limestone	"	"	"	1.85E-14	1.11E-15	1.62E-08	4.59E-10	1.15E-06	6.03E-08
20.9	FUR/11 22.57 2	limestone	0.02	93.42	100	1.62E-14	9.64E-16	1.85E-08	5.24E-10	8.75E-07	4.59E-08
20.9	FUR/11 22.57	limestone	"	"	"	1.75E-14	1.14E-15	1.90E-08	5.40E-10	9.19E-07	5.42E-08

[a] Height from base of cycle to top of bed

[b] TOC error = ±0.04 %

[c] carbonate (%) error = ±0.76 %

[d] HI error = ±14 (mg HC/g TOC)

[e] analytical error

* excluded as an outlier

TABLE A.1 (2): Furlo Cycle A - deconvolved helium data, sedimentation rate, organic-carbon mass-accumulation rate and cumulative time

Cycle Depth [a] (cm)	Sample Name	Lithology	3He_ET [f] (cc/g)	3He_ET error [g] (cc/g)	4He_terr [h] (cc/g)	4He_terr error [e] (cc/g)	LSR [i] (cm/kyr)	LSR error [j] (cm/kyr)	OC MAR (g/cm2/kyr)	OC MAR error [j] (g/cm2/kyr)	Cumulative Time [k] (kyr)
0.3	FU 160 B	marl	6.25E-14	1.25E-14	1.05E-07	1.51E-08	0.431	0.144	2.88E-02	8.02E-03	0.7
0.3	FU 160 C	marl	6.17E-14	1.23E-14	9.17E-08	1.31E-08	0.436	0.146	2.92E-02	8.12E-03	"
0.9	FU 159 C	black shale	1.82E-13	3.63E-14	3.76E-07	5.10E-08	0.148	0.049	2.22E-02	6.18E-03	4.9
0.9	FU 159 A	black shale	2.02E-13	4.04E-14	5.37E-07	7.42E-08	0.133	0.045	2.00E-02	5.57E-03	"
1.2	FU 158 A	marl	2.42E-14	4.83E-15	2.62E-07	4.58E-08	1.114	0.372	8.39E-02	2.33E-02	5.2
1.2	FU 158 B	marl	3.25E-14	6.50E-15	2.92E-07	6.84E-08	0.829	0.277	6.25E-02	1.74E-02	"
3.7	FU 157 F	chert	2.97E-14	5.94E-15	2.52E-07	5.14E-08	0.906	0.303	1.05E-02	2.92E-03	7.6
3.7	FU157 A, B, C	chert	3.09E-14	6.19E-15	4.67E-07	6.82E-08	0.870	0.291	1.01E-02	2.81E-03	"
3.7	FU 157 E	chert	1.76E-14	3.52E-15	3.63E-07	7.58E-08	1.531	0.511	1.78E-02	4.94E-03	"
3.9	FU 156 D	black shale	7.93E-14	1.59E-14	2.32E-07	3.64E-08	0.339	0.113	1.13E-02	3.13E-03	8.2
3.9	FU 156 A	black shale	6.93E-14	1.39E-14	2.93E-07	5.56E-08	0.389	0.130	1.29E-02	3.59E-03	"
3.9	FU 156 B *	black shale	1.24E-13	1.88E-14	4.60E-07	6.47E-08					
7.7	FUR/11 22.45 1A	limestone	3.18E-14	6.36E-15	3.40E-08	4.66E-09	0.846	0.283	1.37E-03	3.81E-04	12.5
7.7	FUR/11 22.45 2	limestone	3.08E-14	6.16E-15	2.36E-08	3.25E-09	0.875	0.292	1.42E-03	3.94E-04	"
10.7	FUR/11 22.48 2	limestone	1.70E-14	3.40E-15	2.30E-08	3.08E-09	1.582	0.528	8.54E-04	2.37E-04	14.4
10.7	FUR/11 22.48	limestone	1.66E-14	3.32E-15	2.50E-08	3.53E-09	1.624	0.542	8.77E-04	2.44E-04	"
13.7	FUR/11 22.51 B	limestone	1.78E-14	3.57E-15	2.10E-08	2.81E-09	1.510	0.504	4.08E-04	1.13E-04	16.1
13.7	FUR/11 22.51 C	limestone	1.39E-14	2.79E-15	1.77E-08	2.41E-09	1.930	0.645	5.21E-04	1.45E-04	"
13.7	FUR/11 22.51 *	limestone	3.65E-14	5.19E-15	2.47E-08	3.33E-09					
16.7	FUR/11 22.54 3	limestone	2.46E-14	4.92E-15	5.93E-08	8.59E-09	1.095	0.366	8.87E-04	2.46E-04	18.5
16.7	FUR/11 22.54	limestone	1.80E-14	3.61E-15	1.61E-08	2.23E-09	1.492	0.498	1.21E-03	3.36E-04	"
20.9	FUR/11 22.57 2	limestone	1.56E-14	3.12E-15	1.84E-08	2.55E-09	1.724	0.576	9.31E-04	2.59E-04	21.0
20.9	FUR/11 22.57	limestone	1.69E-14	3.38E-15	1.90E-08	2.67E-09	1.592	0.532	8.60E-04	2.39E-04	"

[a] Height from base of cycle to top of bed

[e] analytical error

[f] calculated using two-component mixing model (Patterson and Farley, 1998): Equation 2.2, Chapter 2

[g] reproducibility error

[h] calculated using two-component mixing model (Patterson and Farley, 1998): Equation 2.3, Chapter 2

i calculated using $\alpha = F / [^3He_{ET}]$ (Takayanagi and Ozima, 1987): Equation 2.1, Chapter 2. Background flux (F) over Furlo Cycle B = $7.05 \pm 1.37 \times 10^{-14}$ ccSTP/cm^2/kyr

[j] dominant source of error is error on the background flux

[k] Cumulative time from the base of the cycle

* excluded as an outlier

TABLE A.2 (1): Furlo Cycle B - Rock Eval and helium data

Cycle Depth [a] (cm)	Sample Name	Lithology	TOC [b] (%)	carbonate [c] (%)	HI [d] (mg HC/g TOC)	3He (cc/g)	3He error [e] (cc/g)	4He (cc/g)	4He error [e] (cc/g)	3He/4He	3He/4He error [e]
0.6	FU 183 A	black shale	10.35	17.33	383	2.71E-13	1.14E-14	6.54E-07	1.85E-08	4.15E-07	1.28E-08
0.6	FU 183 C	black shale	"	"	"	2.96E-13	1.25E-14	3.58E-07	1.02E-08	8.27E-07	2.57E-08
0.6	FU 183 B *	black shale	"	"	"	7.66E-13	2.93E-14	1.67E-07	4.73E-09	4.59E-06	1.18E-07
2.2	FU 184 A	black chert	0.36	2.00	272	1.31E-14	9.54E-16	6.50E-08	1.84E-09	2.02E-07	1.35E-08
2.2	FU 184 B	black chert	"	"	"	6.84E-15	9.03E-16	1.65E-08	4.67E-10	4.15E-07	5.35E-08
2.2	FU 184 C	black chert	"	"	"	1.42E-14	2.76E-15	3.67E-08	1.04E-09	3.87E-07	7.44E-08
2.5	FU 185 A	grey marl	0.13	42.33	77	6.42E-14	4.06E-15	1.91E-07	5.40E-09	3.37E-07	1.91E-08
2.5	FU 185 B	grey marl	"	"	"	1.40E-13	6.22E-15	3.48E-07	9.88E-09	4.03E-07	1.37E-08
10.5	FU B5c A	limestone	0.03	73.50	0	1.89E-14	8.14E-16	1.09E-08	3.09E-10	1.74E-06	5.62E-08
10.5	FU B5c B	limestone	"	"	"	2.08E-14	8.87E-16	8.62E-09	2.45E-10	2.42E-06	7.67E-08
19.5	FU B4 A	limestone	0.02	80.75	0	1.72E-14	8.06E-16	1.92E-08	5.46E-10	8.94E-07	3.34E-08
19.5	FU B4 B	limestone	"	"	"	2.01E-14	1.01E-15	1.74E-08	4.94E-10	1.15E-06	4.82E-08

[a] Height from base of cycle to top of bed

[b] TOC error = ±0.04 %

[c] carbonate (%) error = ±0.76 %

[d] HI error = ±14 (mg HC/g TOC)

[e] analytical error

* excluded as an outlier

TABLE A.2 (2): Furlo Cycle B - deconvolved helium data, sedimentation rate, organic-carbon mass-accumulation rate and cumulative time

Cycle Depth [a] (cm)	Sample Name	Lithology	3He_ET [f] (cc/g)	3He_ET error [g] (cc/g)	4He_terr [h] (cc/g)	4He_terr error [e] (cc/g)	LSR [i] (cm/kyr)	LSR error [j] (cm/kyr)	OC MAR (g/cm2/kyr)	OC MAR error [j] (g/cm2/kyr)	Cumulative Time [k] (kyr)
0.6	FU 183 A	black shale	2.52E-13	5.04E-14	6.53E-07	8.61E-08	0.104	0.035	2.90E-02	8.09E-03	6.2
0.6	FU 183 C	black shale	2.86E-13	5.72E-14	3.57E-07	4.71E-08	0.091	0.031	2.55E-02	7.13E-03	"
0.6	FU 183 B *	black shale	7.61E-13	1.01E-13	1.64E-07	2.14E-08					
2.2	FU 184 A	black chert	1.12E-14	2.23E-15	6.49E-08	9.39E-09	2.338	0.784	2.27E-02	6.35E-03	6.8
2.2	FU 184 B	black chert	6.35E-15	1.27E-15	1.65E-08	2.99E-09	4.111	1.378	4.00E-02	1.12E-02	"
2.2	FU 184 C	black chert	1.31E-14	2.62E-15	3.66E-08	8.47E-09	1.995	0.669	1.94E-02	5.42E-03	"
2.5	FU 185 A	grey marl	5.85E-14	1.17E-14	1.90E-07	2.67E-08	0.446	0.150	1.57E-03	4.37E-04	7.9
2.5	FU 185 B	grey marl	1.30E-13	2.60E-14	3.48E-07	4.61E-08	0.201	0.067	7.05E-04	1.97E-04	"
10.5	FU B5c A	limestone	1.86E-14	3.72E-15	1.08E-08	1.43E-09	1.402	0.470	1.14E-03	3.17E-04	16.1
10.5	FU B5c B	limestone	2.06E-14	4.12E-15	8.53E-09	1.13E-09	1.268	0.425	1.03E-03	2.87E-04	"
19.5	FU B4 A	limestone	1.66E-14	3.33E-15	1.92E-08	2.56E-09	1.570	0.526	8.48E-04	2.37E-04	21.0
19.5	FU B4 B	limestone	1.96E-14	3.91E-15	1.73E-08	2.33E-09	1.335	0.447	7.21E-04	2.01E-04	"

[a] Height from base of cycle to top of bed

[e] analytical error

[f] calculated using two-component mixing model (Patterson and Farley, 1998): Equation 2.2, Chapter 2

[g] reproducibility error

[h] calculated using two-component mixing model (Patterson and Farley, 1998): Equation 2.3, Chapter 2

i calculated using $\alpha = F / [^3He_{ET}]$ (Takayanagi and Ozima, 1987): Equation 2.1, Chapter 2. Background flux (F) over Furlo Cycle B = 7.05±1.37 x 10^{-14} ccSTP/cm^2/kyr

[j] dominant source of error is error on the background flux

[k] Cumulative time from the base of the cycle

* excluded as an outlier

TABLE A.3 (1): Furlo Cycle C - Rock Eval and helium data

Cycle Depth [a] (cm)	Sample Name	Lithology	TOC [b] (%)	carbonate [c] (%)	HI [d] (mg HC/g TOC)	3He (cc/g)	3He error [e] (cc/g)	4He (cc/g)	4He error [e] (cc/g)	3He/4He	3He/4He error [e]
3.0	FU 175 B	grey chert	0.02	31.08	0	1.93E-14	1.55E-15	1.71E-08	4.85E-10	1.13E-06	8.50E-08
3.0	FU 175 C	grey chert	"	"	"	9.82E-15	2.05E-15	1.67E-08	4.73E-10	5.88E-07	1.22E-07
3.0	FU 175 A *	grey chert	"	"	"	1.08E-13	4.58E-15	1.33E-07	3.78E-09	8.10E-07	2.56E-08
8.0	FU 174 B	limestone	0.02	76.33	0	1.21E-14	7.32E-16	3.70E-09	1.05E-10	3.28E-06	1.74E-07
8.0	FU 174 A	limestone	"	"	"	2.06E-14	1.24E-15	1.26E-08	3.57E-10	1.64E-06	8.70E-08
18.0	FU 173 C	limestone	0.05	69.83	0	7.89E-15	4.54E-16	4.86E-09	1.38E-10	1.62E-06	8.12E-08
18.0	FU 173 D	limestone	"	"	"	4.30E-14	2.16E-15	2.72E-08	7.70E-10	1.58E-06	6.55E-08
24.0	FU 170-2 A	limestone	0.05	73.94	0	2.05E-14	1.17E-15	1.33E-08	3.76E-10	1.55E-06	7.64E-08
24.0	FU 170-2 B	limestone	"	"	"	3.37E-14	1.85E-15	3.28E-08	9.29E-10	1.03E-06	4.84E-08
26.0	FU 176 C	laminated limestone	0.13	72.42	0	1.57E-14	8.31E-16	6.36E-09	1.80E-10	2.48E-06	1.10E-07
26.0	FU 176 D	laminated limestone	"	"	"	1.33E-14	9.02E-16	5.66E-09	1.61E-10	2.35E-06	1.45E-07

[a] Height from base of cycle to top of bed

[b] TOC error = ±0.04 %

[c] carbonate (%) error = ±0.76 %

[d] HI error = ±14 (mg HC/g TOC)

[e] analytical error

* excluded as an outlier

TABLE A.3 (2): Furlo Cycle C - deconvolved helium data, sedimentation rate, organic-carbon mass-accumulation rate and cumulative time

Cycle Depth [a] (cm)	Sample Name	Lithology	3He_ET [f] (cc/g)	3He_ET error [g] (cc/g)	4He_terr [h] (cc/g)	4He_terr error [e] (cc/g)	LSR [i] (cm/kyr)	LSR error [j] (cm/kyr)	OC MAR (g/cm2/kyr)	OC MAR error [j] (g/cm2/kyr)	Cumulative Time [k] (kyr)
3.0	FU 175 B	grey chert	1.88E-14	3.76E-15	1.70E-08	2.53E-09	1.419	0.792	7.67E-04	4.03E-04	1.6
3.0	FU 175 C	grey chert	9.32E-15	1.86E-15	1.66E-08	4.05E-09	2.862	1.596	1.55E-03	8.13E-04	"
3.0	FU 175 A *	grey chert	1.04E-13	1.41E-14	1.33E-07	1.75E-08					
8.0	FU 174 B	limestone	1.20E-14	2.41E-15	3.65E-09	5.06E-10	2.216	1.236	1.20E-03	6.30E-04	4.6
8.0	FU 174 A	limestone	2.03E-14	4.05E-15	1.25E-08	1.74E-09	1.316	0.734	7.11E-04	3.74E-04	"
18.0	FU 173 C	limestone	7.75E-15	1.55E-15	4.83E-09	6.65E-10	3.441	1.919	4.64E-03	2.44E-03	14.0
18.0	FU 173 D	limestone	4.22E-14	8.44E-15	2.70E-08	3.64E-09	0.632	0.352	8.53E-04	4.49E-04	"
24.0	FU 170-2 A	limestone	2.01E-14	4.02E-15	1.32E-08	1.81E-09	1.325	0.739	1.64E-03	8.63E-04	19.9
24.0	FU 170-2 B	limestone	3.27E-14	6.55E-15	3.26E-08	4.45E-09	0.815	0.454	1.01E-03	5.30E-04	"
26.0	FU 176 C	laminated limestone	1.56E-14	3.11E-15	6.29E-09	8.54E-10	1.714	0.956	6.02E-03	3.17E-03	21.0
26.0	FU 176 D	laminated limestone	1.31E-14	2.62E-15	5.60E-09	7.97E-10	2.034	1.135	7.14E-03	3.76E-03	"

[a] Height from base of cycle to top of bed

[e] analytical error

[f] calculated using two-component mixing model (Patterson and Farley, 1998): Equation 2.2, Chapter 2

[g] reproducibility error

[h] calculated using two-component mixing model (Patterson and Farley, 1998): Equation 2.3, Chapter 2

i calculated using $\alpha = F / [^3He_{ET}]$ (Takayanagi and Ozima, 1987): Equation 2.1, Chapter 2. Background flux (F) over Furlo Cycle B = 7.05±1.37 x 10^{-14} ccSTP/cm^2/kyr

[j] dominant source of error is error on the background flux

[k] Cumulative time from the base of the cycle

* excluded as an outlier

TABLE A.4 (1): Contessa Cycle B - Rock Eval and helium data

Cycle Depth [a] (cm)	Sample Name	Lithology	TOC [b] (%)	carbonate [c] (%)	HI [d] (mg HC/g TOC)	3He (cc/g)	3He error [e] (cc/g)	4He (cc/g)	4He error [e] (cc/g)	3He/4He	3He/4He error [e]
1.0	CO 161 B	marly limestone	0.24	65.92	117	4.99E-14	3.64E-15	3.60E-08	1.02E-09	1.39E-06	9.31E-08
1.0	CO 161 C	marly limestone	"	"	"	4.50E-14	2.38E-15	2.63E-08	7.45E-10	1.71E-06	7.66E-08
1.0	CO 161 A *	marly limestone	"	"	"	2.59E-14	1.47E-15	2.48E-08	7.03E-10	1.04E-06	5.16E-08
2.5	CO 162 A	black chert	0.07	11.67	86	1.19E-14	1.40E-15	7.02E-09	1.99E-10	1.69E-06	1.94E-07
2.5	CO 162 B	black chert	"	"	"	1.01E-14	1.89E-15	6.11E-09	1.73E-10	1.65E-06	3.06E-07
8.5	CO 163 B	limestone	0.01	61.17	200	8.99E-15	1.26E-15	6.61E-09	1.88E-10	1.36E-06	1.86E-07
8.5	CO 163 C	limestone	"	"	"	9.03E-15	1.66E-15	4.88E-09	1.38E-10	1.85E-06	3.36E-07
8.5	CO 163 A *	limestone	"	"	"	2.18E-14	2.12E-15	6.08E-09	1.72E-10	3.59E-06	3.33E-07
15.5	CO 164 A	limestone	0.00	63.33	0	6.11E-15	8.92E-16	3.06E-09	8.67E-11	2.00E-06	2.86E-07
15.5	CO 164 B	limestone	"	"	"	8.23E-15	1.11E-15	3.71E-09	1.06E-10	2.22E-06	2.93E-07
22.5	CO 165 B	limestone	0.04	69.25	25	1.17E-14	1.43E-15	5.71E-09	1.62E-10	2.04E-06	2.44E-07
22.5	CO 165 E	limestone	"	"	"	2.19E-14	2.54E-15	1.17E-08	3.33E-10	1.86E-06	2.09E-07
22.5	CO 165 A *	limestone	"	"	"	3.25E-13	1.19E-14	8.11E-09	2.30E-10	4.01E-05	9.32E-07
22.5	CO 165 D *	limestone	"	"	"	7.08E-14	4.04E-15	1.41E-08	3.98E-10	5.04E-06	2.50E-07

[a] Height from base of cycle to top of bed

[b] TOC error = ±0.04 %

[c] carbonate (%) error = ±0.76 %

[d] HI error = ±14 (mg HC/g TOC)

[e] analytical error

* excluded as an outlier

TABLE A.4 (2): Contessa Cycle B - deconvolved helium data, sedimentation rate, organic-carbon mass-accumulation rate and cumulative time

Cycle Depth [a] (cm)	Sample Name	Lithology	3He_ET [f] (cc/g)	3He_ET error [g] (cc/g)	4He_terr [h] (cc/g)	4He_terr error [e] (cc/g)	LSR [i] (cm/kyr)	LSR error [j] (cm/kyr)	OC MAR (g/cm2/kyr)	OC MAR error [j] (g/cm2/kyr)	Cumulative Time [k] (kyr)
1.0	CO 161 B	marly limestone	4.88E-14	9.77E-15	3.58E-08	5.18E-09	0.274	0.103	1.77E-03	5.81E-04	3.5
1.0	CO 161 C	marly limestone	4.42E-14	8.84E-15	2.61E-08	3.54E-09	0.302	0.114	1.96E-03	6.41E-04	3.5
1.0	CO 161 A *	marly limestone	2.52E-14	3.67E-15	2.47E-08	3.39E-09					
2.5	CO 162 A	black chert	1.17E-14	2.33E-15	6.97E-09	1.20E-09	1.147	0.431	2.17E-03	7.10E-04	4.7
2.5	CO 162 B	black chert	9.89E-15	1.98E-15	6.06E-09	1.37E-09	1.352	0.508	2.55E-03	8.36E-04	4.7
8.5	CO 163 B	limestone	8.79E-15	1.76E-15	6.58E-09	1.23E-09	1.521	0.572	4.11E-04	1.34E-04	8.7
8.5	CO 163 C	limestone	8.88E-15	1.78E-15	4.84E-09	1.08E-09	1.505	0.566	4.06E-04	1.33E-04	8.7
8.5	CO 163 A *	limestone	2.16E-14	3.97E-15	5.99E-09	9.47E-10					
15.5	CO 164 A	limestone	6.02E-15	1.20E-15	3.03E-09	5.83E-10	2.221	0.835	0.00E+00	0.00E+00	12.4
15.5	CO 164 B	limestone	8.12E-15	1.62E-15	3.68E-09	6.78E-10	1.647	0.619	0.00E+00	0.00E+00	12.4
22.5	CO 165 B	limestone	1.15E-14	2.30E-15	5.66E-09	9.92E-10	1.162	0.437	1.26E-03	4.11E-04	21.0
22.5	CO 165 E	limestone	2.15E-14	4.30E-15	1.17E-08	1.99E-09	0.621	0.234	6.71E-04	2.20E-04	21.0
22.5	CO 165 A *	limestone	3.25E-13	4.30E-14	6.76E-09	8.80E-10					
22.5	CO 165 D *	limestone	7.04E-14	1.03E-14	1.38E-08	1.89E-09					

[a] Height from base of cycle to top of bed

[e] analytical error

[f] calculated using two-component mixing model (Patterson and Farley, 1998): Equation 2.2, Chapter 2

[g] reproducibility error

[h] calculated using two-component mixing model (Patterson and Farley, 1998): Equation 2.3, Chapter 2

i calculated using $\alpha = F / [^3He_{ET}]$ (Takayanagi and Ozima, 1987): Equation 2.1, Chapter 2. Background flux (F) over Furlo Cycle B = 7.05±1.37 x 10^{-14} ccSTP/cm^2/kyr

[j] dominant source of error is error on the background flux

[k] Cumulative time from the base of the cycle

* excluded as an outlier

TABLE A.5 (1): Bonarelli Level - Rock Eval, stable isotope and helium data

Height [a] (cm)	Sample Name	Lithology	TOC [b] (%)	carbonate [c] (%)	HI [d] (mg HC/g TOC)	δ13C_TOC [e] (‰) VPDB	3He (cc/g)	3He error [f] (cc/g)	4He (cc/g)	4He error [f] (cc/g)	3He/4He	3He/4He error [e]
-10.0	FU B1 10	limestone					5.27E-14	5.27E-15	6.73E-08	1.91E-09	7.84E-07	7.51E-08
-9.0	FU B1 09 C	limestone					1.12E-13	1.00E-14	1.32E-07	3.74E-09	8.52E-07	7.21E-08
-9.0	FU B1 09 A	limestone					1.15E-13	7.53E-15	6.43E-08	1.82E-09	1.79E-06	1.06E-07
-8.0	FU B1 08 B	limestone					6.28E-14	8.52E-15	6.82E-08	1.93E-09	9.21E-07	1.22E-07
-8.0	FU B1 08 A *	limestone					2.74E-13	1.76E-14	6.67E-08	1.89E-09	4.10E-06	2.36E-07
-7.0	FU B1 07	limestone					5.18E-14	3.71E-15	5.67E-08	1.61E-09	9.13E-07	6.02E-08
-6.0	FU B1 06	limestone					5.27E-14	4.09E-15	5.20E-08	1.47E-09	1.01E-06	7.33E-08
-5.0	FU B1 05	limestone					3.14E-14	5.38E-15	3.48E-08	9.85E-10	9.05E-07	1.53E-07
-4.0	FU B1 04	limestone					3.36E-14	8.54E-15	4.23E-08	2.79E-09	7.95E-07	1.95E-07
-3.0	FU B1 03	limestone					3.75E-14	5.85E-15	3.30E-08	2.57E-09	1.14E-06	1.54E-07
-2.0	FU B1 02	limestone					5.13E-14	7.82E-15	4.08E-08	2.91E-09	1.26E-06	1.69E-07
-1.0	FU B1 01	limestone					3.97E-14	4.22E-15	3.35E-08	1.96E-09	1.18E-06	1.05E-07
0.5	FU 153	grey shale	0.05	33.75	80	-23.29	2.33E-13	1.11E-14	1.30E-07	3.69E-09	1.79E-06	6.84E-08
1.0	FU 152	grey shale	0.31	21.25	42	-25.34	4.47E-13	1.98E-14	2.75E-07	7.78E-09	1.63E-06	5.56E-08
1.4	FU 151	black shale	4.41	0.83	185	-26.35	1.97E-13	1.00E-14	1.68E-07	4.77E-09	1.17E-06	4.96E-08
1.4	FU 151 B	black shale	"	"	"	"	5.15E-13	3.55E-14	3.69E-07	1.05E-08	1.39E-06	8.76E-08
1.9	FU 150	grey mudstone	0.16	0.42	19		5.66E-13	2.47E-14	3.53E-07	1.00E-08	1.60E-06	5.32E-08
3.0	FU 149	grey shale	0.01	11.17	100		3.05E-13	1.53E-14	1.78E-07	5.04E-09	1.71E-06	7.11E-08
3.5	FU 148	grey mudstone	0.06	0.50	17	-25.40	4.26E-13	2.12E-14	2.63E-07	7.44E-09	1.62E-06	6.66E-08
4.5	FU 147	grey shale	0.06	0.17	0	-29.04	1.50E-13	9.06E-15	1.20E-07	3.39E-09	1.25E-06	6.69E-08
6.8	FU 145/6	black chert	2.33	7.17	326	-26.93	1.27E-13	9.22E-15	1.75E-07	4.96E-09	7.26E-07	4.85E-08
7.3	FU 144	grey shale	0.16	3.83	31	-24.34	1.78E-13	1.23E-14	1.21E-07	3.43E-09	1.47E-06	9.26E-08
8.6	FU 142/3	black shale	2.71	3.50	113	-26.00	1.78E-13	9.97E-15	2.19E-07	6.22E-09	8.11E-07	3.92E-08
9.4	FU 141 B	grey chert	0.11	0.42	9	-22.30	4.05E-13	3.27E-14	9.52E-07	2.70E-08	4.26E-07	3.22E-08
9.4	FU 141 A	grey chert	"	"	"	"	1.20E-13	9.72E-15	3.83E-07	1.08E-08	3.13E-07	2.38E-08
10.4	FU 140	black mudstone	1.12	0.75	79	-26.17	1.04E-13	8.78E-15	6.32E-08	1.79E-09	1.64E-06	1.31E-07
11.4	FU 139	black mudstone	5.97	0.92	425	-26.42	8.24E-14	7.92E-15	7.44E-08	2.11E-09	1.11E-06	1.02E-07
12.4	FU 138	black mudstone	7.05	0.92	380	-26.34	2.77E-13	1.29E-14	4.12E-07	1.17E-08	6.72E-07	2.48E-08
17.4	FU 137	black chert	4.18	0.92	320		1.27E-13	6.55E-15	1.33E-07	3.78E-09	9.54E-07	4.10E-08
19.4	FU 135/6	rad sands	0.01	1.58	250		8.29E-14	5.49E-15	7.75E-08	2.20E-09	1.07E-06	6.40E-08
22.9	FU 131-4 A	rad sands	0.03	0.12	34		2.07E-13	1.14E-14	9.62E-08	2.73E-09	2.15E-06	1.02E-07
22.9	FU 131-4 C	rad sands	"	"	"		2.26E-13	1.96E-14	1.59E-07	4.50E-09	1.42E-06	1.17E-07
23.9	FU 130 A	black shale	1.14	0.75	54	-25.78	2.99E-13	1.53E-14	1.10E-07	3.12E-09	2.72E-06	1.16E-07
23.9	FU 130 C	black shale	"	"	"	-25.78	2.58E-13	2.74E-14	2.75E-07	7.80E-09	9.37E-07	9.60E-08
25.9	FU 128/9	black mudstone	5.48	0.83	382	-26.36	9.06E-14	5.64E-15	8.10E-08	2.30E-09	1.12E-06	6.20E-08
26.4	FU 127	black shale	6.22	0.83	370	-25.94	1.56E-13	9.75E-15	1.15E-07	3.26E-09	1.35E-06	7.56E-08
27.9	FU 125/6	black mudstone	4.13	0.87	321		1.30E-13	8.34E-15	1.49E-07	4.22E-09	8.73E-07	5.04E-08
29.7	FU 123/4	rad sands	0.01	2.35	289		9.73E-14	7.38E-15	7.21E-08	2.05E-09	1.35E-06	9.49E-08

30.9	FU 121/2	rad sands	0.01	0.13	0		6.51E-14	5.02E-15	4.86E-08	1.38E-09	1.34E-06	9.59E-08
32.6	FU 119/20	rad sands	0.01	0.25	47	-25.41	1.33E-13	9.28E-15	1.10E-07	3.12E-09	1.21E-06	7.71E-08
34.3	FU 117/8	black shale	5.13	1.50	267	-26.43	7.50E-14	5.26E-15	8.78E-08	2.49E-09	8.55E-07	5.48E-08
36.9	FU 114-6 A	black mudstone	9.01	1.48	380	-25.60	6.53E-14	6.10E-15	3.47E-07	9.83E-09	1.88E-07	1.68E-08
36.9	FU 114-6 B *	black mudstone	"	"	"	"	3.28E-13	2.66E-14	4.99E-07	1.41E-08	6.58E-07	5.00E-08
39.9	FU 112/3	black shale	6.32	1.54	373	-25.43	3.89E-14	4.89E-15	5.21E-08	1.48E-09	7.47E-07	9.14E-08
42.4	FU 110/1	black shale	3.84	1.67	301	-26.13	9.52E-14	5.88E-15	2.96E-08	8.39E-10	3.21E-06	1.76E-07
43.9	FU 108/9	black shale	2.39	1.17	220	-24.61	4.72E-13	1.93E-14	1.16E-07	3.30E-09	4.06E-06	1.19E-07
44.5	FU 107	black shale	0.62	0.33	65	-23.70	3.31E-13	1.22E-14	3.67E-08	1.04E-09	9.03E-06	2.11E-07
45.3	FU 106	black shale	3.55	1.25	258		3.72E-13	1.58E-14	6.13E-08	1.74E-09	6.08E-06	1.92E-07
46.0	FU 105 B	rad sands	0.03	0.17	0		3.54E-13	1.94E-14	1.57E-07	4.45E-09	2.26E-06	1.06E-07
46.0	FU 105 *	rad sands	"	"	"	"	6.19E-14	7.13E-15	3.32E-08	9.41E-10	1.87E-06	2.08E-07
46.8	FU 104	grey mudstone	0.02	0.33	0		3.25E-13	2.67E-14	1.07E-07	3.04E-09	3.03E-06	2.34E-07
47.6	FU 103	rad sands	0.02	0.08	0	-24.27	4.81E-13	1.84E-14	2.52E-07	7.15E-09	1.91E-06	4.90E-08
48.8	FU 102	grey mudstone	0.15	0.25	0	-22.72	1.68E-13	1.48E-14	1.18E-07	3.35E-09	1.42E-06	1.19E-07
50.0	FU 101 B	black shale	6.92	1.42	343	-24.13	3.01E-13	2.58E-14	2.31E-07	6.56E-09	1.30E-06	1.05E-07
50.0	FU 101 A *	black shale	"	"	"	"	4.54E-14	7.36E-15	5.49E-08	1.56E-09	8.27E-07	1.32E-07
51.7	FU 099 B	grey shale	0.15	0.25	0	-22.91	3.38E-13	2.75E-14	2.21E-07	6.26E-09	1.53E-06	1.17E-07
51.7	FU 099	grey shale	"	"	"	"	1.33E-13	1.48E-14	7.83E-08	2.22E-09	1.70E-06	1.83E-07
52.3	FU 098	black shale	2.28	1.42	99	-23.37	5.01E-14	9.27E-15	2.83E-08	8.03E-10	1.77E-06	3.24E-07
52.5	FU 097	grey shale	0.06	0.58	83	-23.85	4.87E-14	6.76E-15	3.92E-08	1.11E-09	1.24E-06	1.69E-07
53.5	FU 096	black shale	4.22	1.58	220	-23.30	6.04E-14	8.61E-15	4.98E-08	1.41E-09	1.21E-06	1.69E-07
54.3	FU 095	grey shale	0.14	0.58	21	-22.71	2.20E-13	1.50E-14	1.09E-07	3.10E-09	2.02E-06	1.25E-07
58.3	FU 090-3 C	black shale	7.40	1.23	313	-23.23	2.21E-13	1.89E-14	1.70E-07	4.81E-09	1.30E-06	1.05E-07
58.3	FU 090-3 A	black shale	"	"	"	"	3.75E-13	2.15E-14	1.09E-07	3.10E-09	3.43E-06	1.71E-07
58.5	FU 089	grey shale	9.59	5.25	290	-23.55	1.02E-13	9.62E-15	5.74E-08	1.63E-09	1.77E-06	1.60E-07
61.5	FU 086-8	black shale	10.60	1.81	395	-23.13	9.73E-14	1.12E-14	6.73E-08	1.91E-09	1.45E-06	1.61E-07
64.6	FU 083-5	black shale	13.67	1.36	461	-23.34	1.33E-13	1.89E-14	2.00E-07	5.67E-09	6.67E-07	9.25E-08
68.6	FU 078-82 B	black mudstone	10.48	1.28	469	-22.91	1.25E-13	1.07E-14	9.57E-08	2.72E-09	1.30E-06	1.05E-07
68.6	FU 078-82 A *	black mudstone	"	"	"	"	2.92E-14	4.19E-15	4.68E-08	1.33E-09	6.23E-07	8.78E-08
70.8	FU 075-7	black shale	7.04	1.22	345	-23.57	1.05E-13	1.10E-14	8.25E-08	2.34E-09	1.27E-06	1.29E-07
75.3	FU 070-4	grey mudstone	7.86	1.72	323		5.58E-14	7.28E-15	5.22E-08	1.49E-09	1.07E-06	1.36E-07
76.8	FU 069 C	black shale	1.84	1.42	73	-23.36	3.38E-13	2.89E-14	2.60E-07	7.37E-09	1.30E-06	1.05E-07
76.8	FU 069 A *	black shale	"	"	"	"	2.93E-12	9.35E-14	1.75E-07	4.96E-09	1.67E-05	2.46E-07
79.8	FU 066-8	grey shale	3.35	0.92	289	-23.67	8.46E-14	1.10E-14	6.29E-08	1.79E-09	1.35E-06	1.70E-07
80.3	FU 065	black shale	4.28	1.25	218	-23.76	1.59E-13	1.42E-14	1.02E-07	2.95E-09	1.55E-06	1.32E-07
81.8	FU 064	grey shale	0.05	0.50	20	-24.35	1.10E-13	3.83E-15	8.93E-08	2.53E-09	1.23E-06	2.48E-08
83.2	FU 062/3 C	black shale	4.91	1.17	237	-23.78	1.64E-13	1.88E-14	1.69E-07	4.79E-09	9.74E-07	1.08E-07
83.2	FU 062/3 A *	black shale	"	"	"	"	3.77E-13	1.69E-14	1.00E-07	2.84E-09	3.76E-06	1.30E-07
84.2	FU 061	grey shale	0.03	0.25	0		9.84E-14	6.90E-15	8.52E-08	2.42E-09	1.16E-06	7.40E-08
85.2	FU 060	grey shale	0.00	0.08	0		1.56E-13	1.17E-14	9.86E-08	2.80E-09	1.59E-06	1.10E-07
85.9	FU 059	grey shale	0.01	0.08	0		3.73E-13	2.02E-14	2.46E-07	6.96E-09	1.52E-06	7.00E-08
86.6	FU 058 A	grey shale	0.05	0.33	20	-25.34	5.55E-13	2.75E-14	1.98E-07	5.62E-09	2.81E-06	1.14E-07

86.6	FU 058 B	grey shale	"	"	"	"	3.14E-13	1.66E-14	1.51E-07	4.28E-09	2.08E-06	9.31E-08
89.1	FU 056/7	black mudstone	14.70	1.58	522	-22.82	9.60E-14	9.34E-15	1.46E-07	4.14E-09	6.58E-07	6.12E-08
94.1	FU 051-5	black chert	4.19	0.70	424	-23.02	5.93E-14	5.60E-15	9.13E-08	2.59E-09	6.49E-07	5.85E-08
95.1	FU 050	grey shale	0.47	0.58	43	-23.07	1.75E-13	1.21E-14	1.45E-07	4.11E-09	1.21E-06	7.60E-08
95.4	FU 049 B	black shale	5.21	1.17	263	-22.95	1.05E-13	7.00E-15	6.55E-08	1.86E-09	1.60E-06	9.69E-08
95.4	FU 049 A	black shale	"	"	"	"	2.12E-13	1.05E-14	6.33E-08	1.79E-09	3.35E-06	1.37E-07
96.8	FU 048 B	black mudstone	5.50	1.25	348	-23.34	1.46E-13	7.72E-15	1.20E-07	3.41E-09	1.21E-06	5.42E-08
96.8	FU 048	black mudstone	"	"	"	"	5.28E-14	7.96E-15	4.96E-08	1.41E-09	1.06E-06	1.57E-07
97.5	FU 047	black mudstone	4.44	2.08	210	-23.39	1.27E-13	8.30E-15	1.10E-07	3.13E-09	1.15E-06	6.79E-08
97.9	FU 046	black shale	1.70	3.17	59	-23.22	2.77E-13	2.00E-14	2.41E-07	6.82E-09	1.15E-06	7.65E-08
101.9	FU 042-5 A	black mudstone	11.48	1.56	467	-23.14	7.76E-14	1.09E-14	5.12E-07	1.47E-08	1.52E-07	2.09E-08
101.9	FU 042-5 B *	black mudstone	"	"	"	"	7.23E-13	6.19E-14	5.56E-07	1.58E-08	1.30E-06	1.05E-07
103.9	FU 040/1	black shale	5.60	1.67	247	-23.64	5.30E-14	8.58E-15	6.01E-08	1.70E-09	8.82E-07	1.41E-07
104.9	FU 039 B	grey shale	0.77	2.33	56	-23.14	1.25E-13	6.69E-15	1.04E-07	2.95E-09	1.20E-06	5.45E-08
104.9	FU 039 A *	grey shale	"	"	"	"	2.89E-13	1.38E-14	1.85E-07	5.24E-09	1.56E-06	6.02E-08
108.2	FU 036-8	black mudstone	14.44	1.94	380	-23.19	7.62E-14	9.51E-15	5.85E-08	1.66E-09	1.30E-06	1.58E-07
109.7	FU 035	black shale	11.44	2.42	308	-23.30	6.54E-14	6.44E-15	7.07E-08	3.41E-09	9.25E-07	7.94E-08
111.0	FU 034 B	grey shale	0.09	1.58	22	-26.90	6.07E-13	4.21E-14	1.42E-07	4.03E-09	4.27E-06	2.71E-07
111.0	FU 034	grey shale	"	"	"	"	2.75E-13	1.82E-14	2.28E-07	6.95E-09	1.21E-06	7.07E-08
113.0	FU 032-3 B	black shale	9.70	1.54	318		9.98E-14	1.14E-14	1.41E-07	3.99E-09	7.09E-07	7.83E-08
113.0	FU 032/3	black shale	"	"	"		6.26E-14	9.11E-15	6.38E-08	2.92E-09	9.81E-07	1.35E-07
114.0	FU 031	grey shale	0.16	0.50	25	-23.66	3.82E-13	2.43E-14	2.10E-07	6.54E-09	1.82E-06	1.01E-07
114.0	FU 031 B	grey shale	"	"	"	"	1.13E-12	8.79E-14	3.29E-07	9.32E-09	3.43E-06	2.49E-07
114.0	FU 031 C	grey shale	"	"	"	"	3.87E-13	2.08E-14	3.46E-07	9.80E-09	1.12E-06	5.12E-08
115.0	FU 030	grey shale	0.07	0.17	29	-24.55	2.33E-13	2.24E-14	2.36E-07	6.95E-09	9.85E-07	9.02E-08
115.0	FU 030 B	grey shale	"	"	"	"	5.27E-13	4.51E-14	4.05E-07	1.15E-08	1.30E-06	1.05E-07
116.3	FU 029 A	black shale	6.51	1.08	358	-23.79	4.29E-13	2.20E-14	1.16E-07	3.97E-09	3.69E-06	1.41E-07
116.3	FU 029 C *	black shale	"	"	"	"	2.57E-12	1.58E-13	1.89E-07	5.35E-09	1.36E-05	7.40E-07
117.1	FU 027 C	white mudstone	0.02	0.08	0		4.73E-13	4.43E-14	8.37E-08	2.37E-09	5.66E-06	5.05E-07
117.1	FU 027 A	white mudstone	"	"	"		4.18E-13	2.50E-14	1.34E-07	4.54E-09	3.11E-06	1.53E-07
118.6	FU 026 A	grey shale	0.17	0.17	59	-24.23	2.31E-13	1.19E-14	1.50E-07	4.24E-09	1.54E-06	6.67E-08
118.9	FU 025 A	black shale	1.65	0.33	169	-23.46	1.09E-13	5.67E-15	6.22E-08	1.76E-09	1.75E-06	7.64E-08
120.9	FU 022/4 A	white mudstone	0.02	0.23	0		1.67E-13	9.53E-15	4.29E-08	1.22E-09	3.90E-06	1.93E-07
121.1	FU 021 A	grey shale	0.02	0.08	50		1.03E-12	4.16E-14	1.48E-07	4.19E-09	6.97E-06	2.00E-07
121.1	FU 021 B	grey shale	"	"	"		6.16E-13	4.42E-14	4.10E-07	1.16E-08	1.50E-06	9.92E-08
121.1	FU 021 C	grey shale	"	"	"		2.94E-13	2.74E-14	3.89E-07	1.10E-08	7.56E-07	6.69E-08
122.2	FU 020 B	white mudstone	0.01	0.00	0		4.18E-13	1.85E-14	1.64E-07	4.66E-09	2.54E-06	8.65E-08
122.2	FU 020 A	white mudstone	"	"	"		2.51E-13	1.42E-14	1.10E-07	3.11E-09	2.29E-06	1.12E-07
122.2	FU 020 C	white mudstone	"	"	"		1.16E-12	3.99E-14	1.30E-07	3.67E-09	8.92E-06	1.76E-07
123.2	FU 019 A	grey shale	0.00	0.00	0		1.08E-13	7.49E-15	4.90E-08	1.39E-09	2.21E-06	1.40E-07
126.2	FU 017/8 A	white mudstone	0.02	0.58	0		9.10E-14	7.50E-15	7.62E-08	2.16E-09	1.19E-06	9.24E-08
126.7	FU 016 A	grey shale	0.00	0.33	0		1.63E-13	9.82E-15	1.03E-07	2.93E-09	1.58E-06	8.38E-08
127.9	FU 015 A	white mudstone	0.02	1.08	0		7.92E-14	4.02E-15	5.52E-08	1.57E-09	1.43E-06	6.03E-08

128.3	FU 014 C	grey shale	0.01	0.67	100		2.68E-13	1.28E-14	1.39E-07	3.94E-09	1.93E-06	7.42E-08
130.3	FU 012 A	white mudstone	0.00	0.00	0		2.32E-13	1.18E-14	2.17E-07	6.16E-09	1.07E-06	4.51E-08
130.8	FU 011 B	grey shale	0.00	0.58	0		4.11E-13	1.69E-14	8.47E-08	2.40E-09	4.86E-06	1.44E-07
130.8	FU 011 A	grey shale	"	"	"		9.23E-14	4.85E-15	5.55E-08	1.57E-09	1.66E-06	7.36E-08
131.6	FU 010 A	limestone	0.04	10.92	0		1.62E-13	1.03E-14	1.66E-07	4.71E-09	9.72E-07	5.58E-08
131.6	FU 010 B	limestone	"	"	"		5.55E-14	4.45E-15	3.17E-08	8.98E-10	1.75E-06	1.31E-07
132.1	FU 009 A	limestone	0.04	38.67	0		2.78E-14	2.48E-15	1.31E-08	3.72E-10	2.12E-06	1.79E-07
132.1	FU 009 B	limestone	"	"	"		3.05E-14	2.54E-15	1.68E-08	4.77E-10	1.81E-06	1.42E-07
133.1	FU 008 B	limestone	0.05	9.92	0		8.98E-14	6.24E-15	1.29E-07	3.64E-09	6.99E-07	4.43E-08
133.1	FU 008 A	limestone	"	"	"		9.63E-14	6.91E-15	7.03E-08	1.99E-09	1.37E-06	9.02E-08
134.6	FU 007 A	limestone	0.06	26.08	0	-28.09	5.67E-14	1.32E-14	3.25E-08	9.20E-10	1.75E-06	4.03E-07
134.6	FU 007 B	limestone	"	"	"	"	6.65E-14	5.83E-15	3.37E-08	9.57E-10	1.97E-06	1.64E-07
137.1	FU 005/6 A	grey chert	0.05	33.94	0	-29.06	1.18E-13	4.76E-15	1.39E-07	3.94E-09	8.46E-07	2.44E-08
137.1	FU 005/6 B	grey chert	"	"	"	"	6.06E-14	2.99E-15	5.06E-08	1.44E-09	1.20E-06	4.82E-08
139.1	FU 003/4 A	limestone	0.04	28.97	20	-28.81	7.21E-14	4.96E-15	5.03E-08	1.43E-09	1.43E-06	8.99E-08
140.1	FU 002 B	limestone	0.06	4.58	17	-27.71	2.17E-13	1.09E-14	3.65E-07	1.04E-08	5.94E-07	2.46E-08
140.1	FU 002 C	limestone	"	"	"	"	1.62E-13	1.58E-14	2.01E-07	5.69E-09	8.08E-07	7.51E-08
141.6	FU B2 10 B	limestone				-27.49	5.69E-14	4.87E-15	4.38E-08	1.24E-09	1.30E-06	1.05E-07
141.6	FU B2 10 A	limestone				-27.49	9.76E-15	1.54E-15	2.06E-08	5.86E-10	4.74E-07	7.36E-08
142.6	FU B2 09	limestone				-23.44	1.68E-14	2.21E-15	2.24E-08	6.37E-10	7.51E-07	9.64E-08
143.6	FU B2 08	limestone					2.33E-14	4.43E-15	2.94E-08	8.33E-10	7.92E-07	1.49E-07
144.6	FU B2 07 A	limestone					1.57E-14	2.73E-15	3.16E-08	8.95E-10	4.99E-07	8.52E-08
144.6	FU B2 07 B	limestone					7.78E-14	6.66E-15	5.98E-08	1.70E-09	1.30E-06	1.05E-07
145.6	FU B2 06 B	limestone				-24.87	4.80E-14	7.60E-15	7.91E-08	2.24E-09	6.07E-07	9.45E-08
145.6	FU B2 06 A	limestone				-24.87	4.21E-14	4.76E-15	3.51E-08	9.95E-10	1.20E-06	1.31E-07
146.6	FU B2 05	limestone				-21.31	2.30E-14	3.50E-15	3.34E-08	9.47E-10	6.90E-07	1.03E-07
147.6	FU B2 04	limestone				-26.37	3.39E-14	2.74E-15	4.01E-08	1.14E-09	8.45E-07	6.41E-08
148.6	FU B2 03	limestone				-29.91	4.42E-14	6.91E-15	6.42E-08	1.82E-09	6.88E-07	1.06E-07
149.6	FU B2 02	limestone				-31.25	9.04E-14	6.43E-15	1.09E-07	3.08E-09	8.32E-07	5.43E-08
150.6	FU B2 01	limestone				-28.84	1.00E-13	3.72E-15	1.57E-07	4.44E-09	6.41E-07	1.52E-08
151.6	FU 154	limestone					3.87E-14	3.68E-15	4.51E-08	1.28E-09	8.57E-07	7.78E-08

[a] Height from base of Bonarelli Level to top of bed

[b] TOC error = ±0.04 %

[c] carbonate (%) error = ±0.76 %

[d] HI error = ±14 (mg HC/g TOC)

[e] $\delta^{13}C_{TOC}$ error = ±0.15 ‰

[f] analytical error

* excluded as an outlier

TABLE A.5 (2): Bonarelli Level - deconvolved helium data, sedimentation rate, organic-carbon mass-accumulation rate and cumulative time

Height [a] (cm)	Sample Name	Lithology	3He_ET [g] (cc/g)	3He_ET error [h] (cc/g)	4He_terr [i] (cc/g)	4He_terr error [f] (cc/g)	LSR [j] (cm/kyr)	LSR error [k] (cm/kyr)	OC MAR (g/cm2/kyr)	OC MAR error [k] (g/cm2/kyr)	Cumulative Time [l] (kyr)
-10.0	FU B1 10	limestone	5.07E-14	1.01E-14	6.71E-08	1.07E-08	0.835	0.325			-12.1
-9.0	FU B1 09 C	limestone	1.08E-13	2.17E-14	1.31E-07	2.02E-08	0.391	0.152			-10.9
-9.0	FU B1 09 A	limestone	1.13E-13	2.26E-14	6.38E-08	9.01E-09	0.374	0.146			"
-8.0	FU B1 08 B	limestone	6.08E-14	1.22E-14	6.80E-08	1.25E-08	0.697	0.272			-8.3
-8.0	FU B1 08 A *	limestone	2.72E-13	4.13E-14	6.56E-08	9.22E-09					
-7.0	FU B1 07	limestone	5.01E-14	1.00E-14	5.65E-08	8.14E-09	0.846	0.329			-6.8
-6.0	FU B1 06	limestone	5.12E-14	1.02E-14	5.18E-08	7.61E-09	0.827	0.322			-5.6
-5.0	FU B1 05	limestone	3.04E-14	6.08E-15	3.46E-08	7.34E-09	1.393	0.543			-4.4
-4.0	FU B1 04	limestone	3.24E-14	6.48E-15	4.22E-08	1.19E-08	1.308	0.510			-3.7
-3.0	FU B1 03	limestone	3.65E-14	7.30E-15	3.28E-08	6.57E-09	1.160	0.452			-3.0
-2.0	FU B1 02	limestone	5.01E-14	1.00E-14	4.05E-08	7.99E-09	0.845	0.329			-2.1
-1.0	FU B1 01	limestone	3.87E-14	7.73E-15	3.33E-08	5.47E-09	1.096	0.427			-0.9
0.5	FU 153	grey shale	2.30E-13	4.59E-14	1.29E-07	1.73E-08	0.184	0.072	2.49E-04	2.49E-04	2.7
1.0	FU 152	grey shale	4.39E-13	8.78E-14	2.73E-07	3.62E-08	0.096	0.038	8.08E-04	8.08E-04	7.9
1.4	FU 151	black shale	1.92E-13	3.84E-14	1.67E-07	2.26E-08	0.221	0.086	2.63E-02	2.63E-02	10.5
1.4	FU 151 B	black shale	5.04E-13	1.01E-13	3.67E-07	5.24E-08	0.084	0.033	1.00E-02	1.00E-02	"
1.9	FU 150	grey mudstone	5.55E-13	1.11E-13	3.51E-07	4.64E-08	0.076	0.030	3.30E-04	3.30E-04	17.1
3.0	FU 149	grey shale	2.99E-13	5.99E-14	1.77E-07	2.38E-08	0.141	0.055	3.82E-05	3.82E-05	24.8
3.5	FU 148	grey mudstone	4.18E-13	8.36E-14	2.61E-07	3.51E-08	0.101	0.039	1.64E-04	1.64E-04	29.8
4.5	FU 147	grey shale	1.46E-13	2.93E-14	1.19E-07	1.65E-08	0.289	0.113	4.69E-04	4.69E-04	33.2
6.8	FU 145/6	black chert	1.22E-13	2.44E-14	1.75E-07	2.52E-08	0.348	0.135	2.18E-02	2.18E-02	39.9
7.3	FU 144	grey shale	1.75E-13	3.49E-14	1.20E-07	1.72E-08	0.243	0.094	1.05E-03	1.05E-03	41.9
8.6	FU 142/3	black shale	1.71E-13	3.43E-14	2.19E-07	3.00E-08	0.247	0.096	1.81E-02	1.81E-02	47.2
9.4	FU 141 B	grey chert	3.77E-13	7.53E-14	9.50E-07	1.41E-07	0.112	0.044	3.34E-04	3.34E-04	50.4
9.4	FU 141 A	grey chert	1.08E-13	2.16E-14	3.82E-07	5.70E-08	0.391	0.152	1.16E-03	1.16E-03	"
10.4	FU 140	black mudstone	1.02E-13	2.04E-14	6.28E-08	9.48E-09	0.415	0.162	1.26E-02	1.26E-02	52.8
11.4	FU 139	black mudstone	8.01E-14	1.60E-14	7.40E-08	1.17E-08	0.528	0.206	8.52E-02	8.52E-02	54.7
12.4	FU 138	black mudstone	2.65E-13	5.29E-14	4.11E-07	5.49E-08	0.160	0.062	3.05E-02	3.05E-02	60.9
17.4	FU 137	black chert	1.23E-13	2.46E-14	1.33E-07	1.79E-08	0.344	0.134	3.88E-02	3.88E-02	75.4
19.4	FU 135/6	rad sands	8.06E-14	1.61E-14	7.71E-08	1.09E-08	0.525	0.205	1.42E-04	1.42E-04	79.3
22.9	FU 131-4 A	rad sands	2.04E-13	4.08E-14	9.54E-08	1.30E-08	0.207	0.081	1.42E-04	1.42E-04	96.8
22.9	FU 131-4 C	rad sands	2.21E-13	4.42E-14	1.58E-07	2.40E-08	0.192	0.075	1.32E-04	1.32E-04	"
23.9	FU 130 A	black shale	2.95E-13	5.91E-14	1.09E-07	1.47E-08	0.143	0.056	4.41E-03	4.41E-03	103.2
23.9	FU 130 C	black shale	2.49E-13	4.99E-14	2.74E-07	4.50E-08	0.170	0.066	5.23E-03	5.23E-03	"
25.9	FU 128/9	black mudstone	8.82E-14	1.76E-14	8.07E-08	1.13E-08	0.480	0.187	7.11E-02	7.11E-02	107.3
26.4	FU 127	black shale	1.52E-13	3.04E-14	1.14E-07	1.60E-08	0.278	0.108	4.68E-02	4.68E-02	109.1
27.9	FU 125/6	black mudstone	1.25E-13	2.51E-14	1.48E-07	2.08E-08	0.338	0.132	3.77E-02	3.77E-02	113.6
29.7	FU 123/4	rad sands	9.52E-14	1.90E-14	7.17E-08	1.05E-08	0.445	0.173	1.74E-04	1.74E-04	117.6

30.9	FU 121/2	rad sands	6.37E-14	1.27E-14	4.84E-08	7.10E-09	0.665	0.259	8.98E-05	8.98E-05	119.4
32.6	FU 119/20	rad sands	1.30E-13	2.60E-14	1.09E-07	1.57E-08	0.326	0.127	8.81E-05	8.81E-05	124.6
34.3	FU 117/8	black shale	7.24E-14	1.45E-14	8.75E-08	1.25E-08	0.585	0.228	8.09E-02	8.09E-02	127.5
36.9	FU 114-6 A	black mudstone	5.49E-14	1.10E-14	3.47E-07	5.41E-08	0.772	0.301	1.88E-01	1.88E-01	130.9
36.9	FU 114-6 B *	black mudstone	3.14E-13	5.24E-14	4.98E-07	7.41E-08					
39.9	FU 112/3	black shale	3.74E-14	7.48E-15	5.20E-08	9.21E-09	1.133	0.441	1.93E-01	1.93E-01	133.6
42.4	FU 110/1	black shale	9.43E-14	1.89E-14	2.92E-08	4.07E-09	0.449	0.175	4.66E-02	4.66E-02	139.1
43.9	FU 108/9	black shale	4.69E-13	9.37E-14	1.14E-07	1.50E-08	0.090	0.035	5.84E-03	5.84E-03	155.7
44.5	FU 107	black shale	3.30E-13	6.60E-14	3.53E-08	4.60E-09	0.128	0.050	2.15E-03	2.15E-03	160.4
45.3	FU 106	black shale	3.71E-13	7.41E-14	5.98E-08	7.89E-09	0.114	0.045	1.09E-02	1.09E-02	167.4
46.0	FU 105 B	rad sands	3.50E-13	6.99E-14	1.55E-07	2.12E-08	0.121	0.047	9.81E-05	9.81E-05	173.2
46.0	FU 105 *	rad sands	6.09E-14	1.24E-14	3.29E-08	5.60E-09					
46.8	FU 104	grey mudstone	3.22E-13	6.44E-14	1.06E-07	1.58E-08	0.131	0.051	7.10E-05	7.10E-05	179.3
47.6	FU 103	rad sands	4.74E-13	9.48E-14	2.50E-07	3.27E-08	0.089	0.035	4.82E-05	4.82E-05	188.2
48.8	FU 102	grey mudstone	1.64E-13	3.29E-14	1.17E-07	1.80E-08	0.258	0.100	1.04E-03	1.04E-03	192.9
50.0	FU 101 B	black shale	2.94E-13	5.88E-14	2.30E-07	3.49E-08	0.144	0.056	2.69E-02	2.69E-02	201.2
50.0	FU 101 A *	black shale	4.38E-14	1.14E-14	5.47E-08	1.12E-08					
51.7	FU 099 B	grey shale	3.31E-13	6.62E-14	2.20E-07	3.28E-08	0.128	0.050	5.18E-04	5.18E-04	208.8
51.7	FU 099	grey shale	1.31E-13	2.62E-14	7.78E-08	1.30E-08	0.323	0.126	1.31E-03	1.31E-03	"
52.3	FU 098	black shale	4.92E-14	9.84E-15	2.81E-08	6.28E-09	0.861	0.335	5.30E-02	5.30E-02	209.5
52.5	FU 097	grey shale	4.75E-14	9.50E-15	3.90E-08	7.29E-09	0.892	0.347	1.44E-03	1.44E-03	209.7
53.5	FU 096	black shale	5.89E-14	1.18E-14	4.95E-08	9.39E-09	0.719	0.280	8.19E-02	8.19E-02	211.1
54.3	FU 095	grey shale	2.17E-13	4.34E-14	1.08E-07	1.54E-08	0.195	0.076	7.37E-04	7.37E-04	215.2
58.3	FU 090-3 C	black shale	2.16E-13	4.31E-14	1.69E-07	2.56E-08	0.196	0.077	3.93E-02	3.93E-02	240.9
58.3	FU 090-3 A	black shale	3.71E-13	7.43E-14	1.08E-07	1.48E-08	0.114	0.044	2.28E-02	2.28E-02	"
58.5	FU 089	grey shale	1.00E-13	2.00E-14	5.70E-08	8.93E-09	0.424	0.165	1.10E-01	1.10E-01	241.4
61.5	FU 086-8	black shale	9.53E-14	1.91E-14	6.69E-08	1.14E-08	0.444	0.173	1.27E-01	1.27E-01	248.2
64.6	FU 083-5	black shale	1.27E-13	2.55E-14	1.99E-07	3.76E-08	0.333	0.130	1.23E-01	1.23E-01	257.5
68.6	FU 078-82 B	black mudstone	1.22E-13	2.43E-14	9.52E-08	1.44E-08	0.348	0.136	9.84E-02	9.84E-02	269.0
68.6	FU 078-82 A *	black mudstone	2.78E-14	6.58E-15	4.67E-08	8.90E-09					
70.8	FU 075-7	black shale	1.03E-13	2.05E-14	8.21E-08	1.34E-08	0.412	0.161	7.84E-02	7.84E-02	274.3
75.3	FU 070-4	grey mudstone	5.42E-14	1.08E-14	5.19E-08	9.39E-09	0.781	0.304	1.66E-01	1.66E-01	280.1
76.8	FU 069 C	black shale	3.30E-13	6.60E-14	2.58E-07	3.91E-08	0.128	0.050	6.37E-03	6.37E-03	291.8
76.8	FU 069 A *	black shale	2.92E-12	3.79E-13	1.63E-07	2.10E-08					
79.8	FU 066-8	grey shale	8.28E-14	1.66E-14	6.25E-08	1.13E-08	0.512	0.199	4.63E-02	4.63E-02	297.6
80.3	FU 065	black shale	1.56E-13	3.12E-14	1.02E-07	1.56E-08	0.272	0.106	3.14E-02	3.14E-02	299.5
81.8	FU 064	grey shale	1.07E-13	2.15E-14	8.89E-08	1.15E-08	0.394	0.154	5.32E-04	5.32E-04	303.3
83.2	FU 062/3 C	black shale	1.59E-13	3.19E-14	1.68E-07	2.85E-08	0.266	0.103	3.52E-02	3.52E-02	308.5
83.2	FU 062/3 A *	black shale	3.74E-13	5.13E-14	9.87E-08	1.31E-08					
84.2	FU 061	grey shale	9.59E-14	1.92E-14	8.48E-08	1.22E-08	0.442	0.172	3.58E-04	3.58E-04	310.8
85.2	FU 060	grey shale	1.53E-13	3.07E-14	9.80E-08	1.43E-08	0.276	0.107	0.00E+00	0.00E+00	314.4
85.9	FU 059	grey shale	3.66E-13	7.31E-14	2.44E-07	3.32E-08	0.116	0.045	3.13E-05	3.13E-05	320.5
86.6	FU 058 A	grey shale	5.49E-13	1.10E-13	1.96E-07	2.63E-08	0.077	0.030	1.04E-04	1.04E-04	327.0

86.6	FU 058 B	grey shale	3.10E-13	6.19E-14	1.50E-07	2.03E-08	0.137	0.053	1.85E-04	1.85E-04	"
89.1	FU 056/7	black mudstone	9.17E-14	1.83E-14	1.46E-07	2.31E-08	0.462	0.180	1.83E-01	1.83E-01	332.4
94.1	FU 051-5	black chert	5.65E-14	1.13E-14	9.11E-08	1.43E-08	0.749	0.292	8.48E-02	8.48E-02	339.1
95.1	FU 050	grey shale	1.71E-13	3.41E-14	1.44E-07	2.06E-08	0.248	0.097	3.15E-03	3.15E-03	343.1
95.4	FU 049 B	black shale	1.03E-13	2.06E-14	6.50E-08	9.22E-09	0.412	0.160	5.79E-02	5.79E-02	344.1
95.4	FU 049 A	black shale	2.10E-13	4.20E-14	6.24E-08	8.39E-09	0.202	0.079	2.84E-02	2.84E-02	"
96.8	FU 048 B	black mudstone	1.42E-13	2.85E-14	1.20E-07	1.63E-08	0.297	0.116	4.42E-02	4.42E-02	346.6
96.8	FU 048	black mudstone	5.13E-14	1.03E-14	4.94E-08	9.67E-09	0.825	0.321	1.23E-01	1.23E-01	"
97.5	FU 047	black mudstone	1.23E-13	2.47E-14	1.10E-07	1.55E-08	0.343	0.134	4.11E-02	4.11E-02	348.7
97.9	FU 046	black shale	2.70E-13	5.40E-14	2.39E-07	3.46E-08	0.157	0.061	7.20E-03	7.20E-03	351.2
101.9	FU 042-5 A	black mudstone	6.23E-14	1.25E-14	5.11E-07	9.62E-08	0.680	0.265	2.11E-01	2.11E-01	357.1
101.9	FU 042-5 B *	black mudstone	7.07E-13	1.21E-13	5.53E-07	8.38E-08					
103.9	FU 040/1	black shale	5.12E-14	1.02E-14	5.99E-08	1.22E-08	0.827	0.322	1.25E-01	1.25E-01	359.5
104.9	FU 039 B	grey shale	1.22E-13	2.44E-14	1.04E-07	1.41E-08	0.347	0.135	7.22E-03	7.22E-03	362.4
104.9	FU 039 A *	grey shale	2.83E-13	3.94E-14	1.84E-07	2.46E-08					
108.2	FU 036-8	black mudstone	7.44E-14	1.49E-14	5.82E-08	1.03E-08	0.569	0.222	2.22E-01	2.22E-01	368.2
109.7	FU 035	black shale	6.33E-14	1.27E-14	7.04E-08	1.12E-08	0.669	0.261	2.07E-01	2.07E-01	370.4
111.0	FU 034 B	grey shale	6.03E-13	1.21E-13	1.40E-07	1.99E-08	0.070	0.027	1.71E-04	1.71E-04	381.8
111.0	FU 034	grey shale	2.69E-13	5.37E-14	2.27E-07	3.21E-08	0.158	0.061	3.83E-04	3.83E-04	"
113.0	FU 032-3 B	black shale	9.56E-14	1.91E-14	1.40E-07	2.37E-08	0.443	0.172	1.16E-01	1.16E-01	385.3
113.0	FU 032/3	black shale	6.07E-14	1.21E-14	6.36E-08	1.22E-08	0.698	0.272	1.83E-01	1.83E-01	"
114.0	FU 031	grey shale	3.76E-13	7.52E-14	2.08E-07	2.92E-08	0.113	0.044	4.87E-04	4.87E-04	396.7
114.0	FU 031 B	grey shale	1.12E-12	2.24E-13	3.24E-07	4.77E-08	0.038	0.015	1.64E-04	1.64E-04	"
114.0	FU 031 C	grey shale	3.76E-13	7.53E-14	3.44E-07	4.68E-08	0.113	0.044	4.86E-04	4.86E-04	"
115.0	FU 030	grey shale	2.26E-13	4.51E-14	2.35E-07	3.71E-08	0.188	0.073	3.55E-04	3.55E-04	404.2
115.0	FU 030 B	grey shale	5.15E-13	1.03E-13	4.03E-07	6.11E-08	0.082	0.032	1.55E-04	1.55E-04	"
116.3	FU 029 A	black shale	4.26E-13	8.52E-14	1.15E-07	1.55E-08	0.099	0.039	1.75E-02	1.75E-02	417.2
116.3	FU 029 C *	black shale	2.57E-12	3.84E-13	1.78E-07	2.48E-08					
117.1	FU 027 C	white mudstone	4.71E-13	9.42E-14	8.17E-08	1.28E-08	0.090	0.035	4.85E-05	4.85E-05	425.6
117.1	FU 027 A	white mudstone	4.14E-13	8.28E-14	1.33E-07	1.84E-08	0.102	0.040	5.52E-05	5.52E-05	"
118.6	FU 026 A	grey shale	2.27E-13	4.53E-14	1.49E-07	2.01E-08	0.187	0.073	8.58E-04	8.58E-04	433.6
118.9	FU 025 A	black shale	1.07E-13	2.14E-14	6.18E-08	8.36E-09	0.396	0.154	1.77E-02	1.77E-02	434.3
120.9	FU 022/4 A	white mudstone	1.66E-13	3.32E-14	4.22E-08	5.79E-09	0.255	0.100	1.07E-04	1.07E-04	442.2
121.1	FU 021 A	grey shale	1.02E-12	2.05E-13	1.43E-07	1.88E-08	0.041	0.016	2.23E-05	2.23E-05	444.5
121.1	FU 021 B	grey shale	6.04E-13	1.21E-13	4.07E-07	5.87E-08	0.070	0.027	3.79E-05	3.79E-05	"
121.1	FU 021 C	grey shale	2.83E-13	5.65E-14	3.88E-07	6.05E-08	0.150	0.058	8.09E-05	8.09E-05	"
122.2	FU 020 B	white mudstone	4.13E-13	8.26E-14	1.63E-07	2.16E-08	0.103	0.040	2.77E-05	2.77E-05	455.1
122.2	FU 020 A	white mudstone	2.48E-13	4.96E-14	1.08E-07	1.49E-08	0.171	0.067	4.61E-05	4.61E-05	"
122.2	FU 020 C	white mudstone	1.15E-12	2.30E-13	1.25E-07	1.62E-08	0.037	0.014	9.93E-06	9.93E-06	"
123.2	FU 019 A	grey shale	1.07E-13	2.14E-14	4.85E-08	6.93E-09	0.396	0.154	0.00E+00	0.00E+00	457.6
126.2	FU 017/8 A	white mudstone	8.87E-14	1.77E-14	7.59E-08	1.14E-08	0.477	0.186	1.93E-04	1.93E-04	463.9
126.7	FU 016 A	grey shale	1.60E-13	3.21E-14	1.03E-07	1.43E-08	0.264	0.103	0.00E+00	0.00E+00	465.8
127.9	FU 015 A	white mudstone	7.76E-14	1.55E-14	5.49E-08	7.41E-09	0.546	0.213	2.95E-04	2.95E-04	468.0

128.3	FU 014 C	grey shale	2.64E-13	5.28E-14	1.38E-07	1.84E-08	0.160	0.063	4.33E-05	4.33E-05	470.5
130.3	FU 012 A	white mudstone	2.25E-13	4.50E-14	2.16E-07	2.92E-08	0.188	0.073	0.00E+00	0.00E+00	475.8
130.8	FU 011 B	grey shale	4.09E-13	8.18E-14	8.30E-08	1.09E-08	0.104	0.040	0.00E+00	0.00E+00	477.6
130.8	FU 011 A	grey shale	9.06E-14	1.81E-14	5.51E-08	7.47E-09	0.467	0.182	0.00E+00	0.00E+00	"
131.6	FU 010 A	limestone	1.57E-13	3.13E-14	1.66E-07	2.33E-08	0.270	0.105	2.92E-04	2.92E-04	479.1
131.6	FU 010 B	limestone	5.46E-14	1.09E-14	3.14E-08	4.67E-09	0.776	0.302	8.38E-04	8.38E-04	"
132.1	FU 009 A	limestone	2.74E-14	5.49E-15	1.30E-08	1.99E-09	1.543	0.601	1.67E-03	1.67E-03	479.4
132.1	FU 009 B	limestone	3.00E-14	6.00E-15	1.67E-08	2.51E-09	1.413	0.550	1.53E-03	1.53E-03	"
133.1	FU 008 B	limestone	8.60E-14	1.72E-14	1.28E-07	1.83E-08	0.493	0.192	6.65E-04	6.65E-04	481.6
133.1	FU 008 A	limestone	9.42E-14	1.88E-14	6.99E-08	1.01E-08	0.449	0.175	6.07E-04	6.07E-04	"
134.6	FU 007 A	limestone	5.58E-14	1.12E-14	3.22E-08	8.50E-09	0.759	0.296	1.23E-03	1.23E-03	483.7
134.6	FU 007 B	limestone	6.55E-14	1.31E-14	3.35E-08	5.11E-09	0.646	0.252	1.05E-03	1.05E-03	"
137.1	FU 005/6 A	grey chert	1.13E-13	2.27E-14	1.38E-07	1.82E-08	0.373	0.145	4.68E-04	4.68E-04	488.3
137.1	FU 005/6 B	grey chert	5.91E-14	1.18E-14	5.04E-08	6.77E-09	0.716	0.279	8.97E-04	8.97E-04	"
139.1	FU 003/4 A	limestone	7.06E-14	1.41E-14	5.00E-08	7.13E-09	0.600	0.234	6.16E-04	6.16E-04	491.6
140.1	FU 002 B	limestone	2.06E-13	4.12E-14	3.64E-07	4.91E-08	0.206	0.080	3.33E-04	3.33E-04	495.8
140.1	FU 002 C	limestone	1.56E-13	3.12E-14	2.00E-07	3.17E-08	0.271	0.106	4.39E-04	4.39E-04	"
141.6	FU B2 10 B	limestone	5.56E-14	1.11E-14	4.36E-08	6.60E-09	0.761	0.296			496.2
141.6	FU B2 10 A	limestone	9.15E-15	1.83E-15	2.06E-08	4.14E-09	4.630	1.804			"
142.6	FU B2 09	limestone	1.62E-14	3.23E-15	2.23E-08	4.05E-09	2.622	1.021			496.6
143.6	FU B2 08	limestone	2.24E-14	4.48E-15	2.93E-08	6.67E-09	1.891	0.737			497.1
144.6	FU B2 07 A	limestone	1.48E-14	2.96E-15	3.15E-08	6.73E-09	2.863	1.115			497.7
144.6	FU B2 07 B	limestone	7.60E-14	1.52E-14	5.95E-08	9.01E-09	0.557	0.217			"
145.6	FU B2 06 B	limestone	4.56E-14	9.13E-15	7.89E-08	1.59E-08	0.928	0.361			498.7
145.6	FU B2 06 A	limestone	4.10E-14	8.20E-15	3.49E-08	5.88E-09	1.032	0.402			"
146.6	FU B2 05	limestone	2.20E-14	4.41E-15	3.33E-08	6.55E-09	1.922	0.749			499.2
147.6	FU B2 04	limestone	3.27E-14	6.53E-15	3.99E-08	5.95E-09	1.296	0.505			500.0
148.6	FU B2 03	limestone	4.23E-14	8.46E-15	6.41E-08	1.28E-08	1.001	0.390			501.0
149.6	FU B2 02	limestone	8.72E-14	1.74E-14	1.08E-07	1.56E-08	0.486	0.189			503.0
150.6	FU B2 01	limestone	9.58E-14	1.92E-14	1.56E-07	2.04E-08	0.442	0.172			505.3
151.6	FU 154	limestone	3.73E-14	7.47E-15	4.50E-08	7.06E-09	1.134	0.442			506.2

[a] Height from base of Bonarelli Level to top of bed

[f] analytical error

[g] calculated using two-component mixing model (Patterson and Farley, 1998): Equation 2.2, Chapter 2

[h] reproducibility error

[i] calculated using two-component mixing model (Patterson and Farley, 1998): Equation 2.3, Chapter 2

[j] calculated using $\alpha = F / [^3He_{ET}]$ (Takayanagi and Ozima, 1987): Equation 2.1, Chapter 2. Background flux (F) over the Bonarelli Level = 1.14±0.38 x 10^{-13} ccSTP/cm^2/kyr

[k] dominant source of error is error on the background flux

[l] Cumulative time from the base of the Bonarelli Level, not including any potential hiatuses

* excluded as an outlier

TABLE A.6 (1): Background flux samples - helium data

Depth [a] (m)	Sample Name	Sample Type	Outcrop	3He (cc/g)	3He error [b] (cc/g)	4He (cc/g)	4He error [b] (cc/g)	3He/4He	3He/4He error [b]
-1.65	FUR/11 24.90	spot sample	Furlo	3.25E-14	1.77E-15	2.65E-08	5.30E-10	1.23E-06	6.22E-08
-1.86	FUR/11 24.69	spot sample	Furlo	1.03E-13	2.91E-15	8.99E-08	1.80E-09	1.14E-06	2.30E-08
-2.04	FUR/11 24.51	spot sample	Furlo	1.28E-13	4.33E-15	1.23E-07	2.47E-09	1.04E-06	2.82E-08
-2.04	FUR/11 24.51 B	spot sample	Furlo	1.37E-13	4.90E-15	1.33E-07	2.68E-09	1.03E-06	3.04E-08
-2.25	FUR/11 24.30 B	spot sample	Furlo	2.90E-14	1.92E-15	2.51E-08	5.02E-10	1.16E-06	7.29E-08
-2.25	FUR/11 24.30 *	spot sample	Furlo	1.59E-13	4.10E-15	1.78E-08	3.56E-10	8.95E-06	1.45E-07
-2.43	FUR/11 24.12	spot sample	Furlo	1.98E-14	9.71E-16	2.34E-08	4.68E-10	8.49E-07	3.79E-08
-2.68	FUR/11 23.87	spot sample	Furlo	2.44E-14	1.03E-15	2.78E-08	5.56E-10	8.78E-07	3.27E-08
-2.68	FUR/11 23.87 B	spot sample	Furlo	2.97E-14	1.32E-15	4.00E-08	8.02E-10	7.42E-07	2.94E-08
-2.80	FUR/11 23.75	spot sample	Furlo	8.87E-15	4.30E-16	8.29E-09	1.66E-10	1.07E-06	4.73E-08
-2.80	FUR/11 23.75 B	spot sample	Furlo	4.21E-14	1.89E-15	3.90E-08	7.80E-10	1.08E-06	4.33E-08
-3.07	FUR/11 23.48	spot sample	Furlo	4.00E-15	1.86E-16	5.38E-09	1.08E-10	7.43E-07	3.11E-08
-3.43	FUR/11 23.12	spot sample	Furlo	2.70E-14	1.18E-15	2.44E-08	4.88E-10	1.11E-06	4.29E-08
-3.43	FUR/11 23.12 B	spot sample	Furlo	2.08E-14	1.07E-15	1.80E-08	3.61E-10	1.15E-06	5.44E-08
-3.62	FUR/11 22.93	spot sample	Furlo	2.25E-14	1.01E-15	1.86E-08	3.72E-10	1.21E-06	4.84E-08
-3.86	FUR/11 22.69	spot sample	Furlo	3.44E-14	1.04E-15	1.43E-08	2.87E-10	2.40E-06	5.44E-08
-3.86	FUR/11 22.69 B	spot sample	Furlo	3.98E-14	1.28E-15	1.49E-08	2.99E-10	2.67E-06	6.69E-08
2.21	FU FM SR 81 D	homogenised precession cycle	Furlo	1.52E-13	9.50E-15	3.78E-07	1.07E-08	4.02E-07	2.24E-08
2.21	FU FM SR 81 A	homogenised precession cycle	Furlo	1.77E-14	2.40E-15	4.77E-09	1.35E-10	3.71E-06	4.91E-07
2.21	FU FM SR 81 B	homogenised precession cycle	Furlo	9.24E-14	4.16E-15	1.19E-07	3.38E-09	7.75E-07	2.71E-08
-1.85	FU FM 332 B	homogenised precession cycle	Furlo	3.23E-14	2.44E-15	2.96E-08	8.39E-10	1.09E-06	7.64E-08
-1.85	FU FM 332 A	homogenised precession cycle	Furlo	3.14E-14	2.13E-15	4.25E-09	1.20E-10	7.40E-06	4.56E-07
-1.85	FU FM 332 C	homogenised precession cycle	Furlo	3.09E-14	1.41E-15	2.71E-08	7.68E-10	1.14E-06	4.09E-08
-3.17	FU FM 200 B	homogenised precession cycle	Furlo	2.35E-14	1.77E-15	8.02E-09	2.28E-10	2.92E-06	2.05E-07
-3.17	FU FM 200 A	homogenised precession cycle	Furlo	1.65E-14	1.52E-15	4.82E-09	1.37E-10	3.43E-06	2.99E-07
-3.17	FU FM 200 D	homogenised precession cycle	Furlo	2.59E-14	1.32E-15	1.39E-08	3.95E-10	1.87E-06	7.88E-08
-4.14	Cycle Mix 1A	homogenised precession cycle	Furlo	2.60E-14	1.92E-15	4.30E-08	1.22E-09	6.06E-07	4.12E-08

-4.14	Cycle Mix 1C	homogenised precession cycle	Furlo	2.84E-14	3.18E-15	4.77E-08	1.35E-09	5.96E-07	6.46E-08
-4.14	Cycle Mix 1D	homogenised precession cycle	Furlo	2.68E-14	2.63E-15	4.30E-08	1.22E-09	6.22E-07	5.86E-08
-4.14	Cycle Mix 3A	homogenised precession cycle	Furlo	1.77E-14	1.87E-15	3.85E-08	1.09E-09	4.59E-07	4.69E-08
-4.14	Cycle Mix 3B	homogenised precession cycle	Furlo	2.13E-14	1.93E-15	3.91E-08	1.11E-09	5.46E-07	4.70E-08
	CO 50 FM C	homogenised precession cycle	Contessa	1.25E-14	1.03E-15	9.46E-09	2.68E-10	1.32E-06	1.03E-07
	CO 50 FM B	homogenised precession cycle	Contessa	1.05E-14	2.17E-15	1.24E-08	3.51E-10	8.52E-07	1.73E-07
	CO FM A 2	homogenised precession cycle	Contessa	2.03E-14	2.31E-15	1.11E-08	3.14E-10	1.83E-06	2.02E-07
	CO 50 FM A *	homogenised precession cycle	Contessa	4.03E-14	5.74E-15	1.96E-08	5.57E-10	2.05E-06	2.87E-07

[a] Height above base of Bonarelli Level at Furlo

[b] analytical error

* excluded as an outlier

TABLE A.6 (2): Background flux samples - deconvolved helium data and background flux

Depth [a] (m)	Sample Name	Sample Type	Outcrop	3He_ET [c] (cc/g)	3He_ET error [d] (cc/g)	4He_terr [e] (cc/g)	4He_terr error [b] (cc/g)	background flux [f] (cc/kyr/cm2)	background flux error [d] (cc/kyr/cm2)
-1.65	FUR/11 24.90	spot sample	Furlo	3.17E-14	6.34E-15	2.63E-08	3.59E-09	9.42E-14	1.88E-14
-1.86	FUR/11 24.69	spot sample	Furlo	9.99E-14	2.00E-14	8.94E-08	1.15E-08	2.97E-13	5.93E-14
-2.04	FUR/11 24.51	spot sample	Furlo	1.24E-13	2.49E-14	1.23E-07	1.59E-08	3.69E-13	7.39E-14
-2.04	FUR/11 24.51 B	spot sample	Furlo	1.33E-13	2.66E-14	1.33E-07	1.73E-08	3.95E-13	7.90E-14
-2.25	FUR/11 24.30 B	spot sample	Furlo	2.82E-14	5.65E-15	2.50E-08	3.53E-09	8.39E-14	1.68E-14
-2.25	FUR/11 24.30 *	spot sample	Furlo	1.59E-13	2.04E-14	1.71E-08	2.19E-09		
-2.43	FUR/11 24.12	spot sample	Furlo	1.91E-14	3.82E-15	2.33E-08	3.13E-09	5.68E-14	1.14E-14
-2.68	FUR/11 23.87	spot sample	Furlo	2.36E-14	4.72E-15	2.77E-08	3.65E-09	7.00E-14	1.40E-14
-2.68	FUR/11 23.87 B	spot sample	Furlo	2.85E-14	5.70E-15	3.99E-08	5.30E-09	8.47E-14	1.69E-14
-2.80	FUR/11 23.75	spot sample	Furlo	8.62E-15	1.72E-15	8.25E-09	1.11E-09	2.56E-14	5.12E-15
-2.80	FUR/11 23.75 B	spot sample	Furlo	4.10E-14	8.19E-15	3.88E-08	5.15E-09	1.22E-13	2.43E-14
-3.07	FUR/11 23.48	spot sample	Furlo	3.84E-15	7.68E-16	5.36E-09	7.15E-10	1.14E-14	2.28E-15
-3.43	FUR/11 23.12	spot sample	Furlo	2.63E-14	5.26E-15	2.43E-08	3.21E-09	7.81E-14	1.56E-14
-3.43	FUR/11 23.12 B	spot sample	Furlo	2.03E-14	4.06E-15	1.80E-08	2.43E-09	6.03E-14	1.21E-14
-3.62	FUR/11 22.93	spot sample	Furlo	2.20E-14	4.39E-15	1.85E-08	2.45E-09	6.53E-14	1.31E-14
-3.86	FUR/11 22.69	spot sample	Furlo	3.39E-14	6.79E-15	1.42E-08	1.82E-09	1.01E-13	2.02E-14
-3.86	FUR/11 22.69 B	spot sample	Furlo	3.94E-14	7.88E-15	1.48E-08	1.91E-09	1.17E-13	2.34E-14
2.21	FU FM SR 81 D	homogenised precession cycle	Furlo	1.41E-13	2.81E-14	3.77E-07	5.28E-08	4.18E-13	8.35E-14
2.21	FU FM SR 81 A	homogenised precession cycle	Furlo	1.76E-14	3.51E-15	4.70E-09	8.65E-10	5.21E-14	1.04E-14
2.21	FU FM SR 81 B	homogenised precession cycle	Furlo	8.89E-14	1.78E-14	1.19E-07	1.58E-08	2.64E-13	5.28E-14
-1.85	FU FM 332 B	homogenised precession cycle	Furlo	3.15E-14	6.29E-15	2.95E-08	4.30E-09	9.34E-14	1.87E-14
-1.85	FU FM 332 A	homogenised precession cycle	Furlo	3.13E-14	6.26E-15	4.12E-09	5.86E-10	9.30E-14	1.86E-14
-1.85	FU FM 332 C	homogenised precession cycle	Furlo	3.01E-14	6.02E-15	2.70E-08	3.59E-09	8.94E-14	1.79E-14
-3.17	FU FM 200 B	homogenised precession cycle	Furlo	2.32E-14	4.64E-15	7.93E-09	1.16E-09	6.89E-14	1.38E-14
-3.17	FU FM 200 A	homogenised precession cycle	Furlo	1.64E-14	3.28E-15	4.75E-09	7.37E-10	4.87E-14	9.74E-15
-3.17	FU FM 200 D	homogenised precession cycle	Furlo	2.55E-14	5.11E-15	1.38E-08	1.86E-09	7.58E-14	1.52E-14
-4.14	Cycle Mix 1A	homogenised precession cycle	Furlo	2.48E-14	4.95E-15	4.29E-08	6.23E-09	7.35E-14	1.47E-14

-4.14	Cycle Mix 1C	homogenised precession cycle	Furlo	2.70E-14	5.40E-15	4.76E-08	7.99E-09	8.02E-14	1.60E-14
-4.14	Cycle Mix 1D	homogenised precession cycle	Furlo	2.55E-14	5.09E-15	4.29E-08	6.82E-09	7.57E-14	1.51E-14
-4.14	Cycle Mix 3A	homogenised precession cycle	Furlo	1.65E-14	3.30E-15	3.84E-08	6.30E-09	4.90E-14	9.80E-15
-4.14	Cycle Mix 3B	homogenised precession cycle	Furlo	2.02E-14	4.03E-15	3.90E-08	6.02E-09	5.99E-14	1.20E-14
	CO 50 FM C	homogenised precession cycle	Contessa	1.22E-14	2.44E-15	9.41E-09	1.41E-09	3.62E-14	7.23E-15
	CO 50 FM B	homogenised precession cycle	Contessa	1.02E-14	2.03E-15	1.23E-08	2.97E-09	3.02E-14	6.04E-15
	CO FM A 2	homogenised precession cycle	Contessa	2.00E-14	3.99E-15	1.10E-08	1.86E-09	5.93E-14	1.19E-14
	CO 50 FM A *	homogenised precession cycle	Contessa	3.97E-14	9.35E-15	1.95E-08	3.69E-09		

[a] Height above base of Bonarelli Level at Furlo

[b] analytical error

[c] calculated using two-component mixing model (Patterson and Farley, 1998): Equation 2.2, Chapter 2

[d] reproducibility error

[e] calculated using two-component mixing model (Patterson and Farley, 1998): Equation 2.3, Chapter 2

[f] calculated using $F = \alpha \times [^3He_{ET}]$ (Takayanagi and Ozima, 1987): Equation 2.1, Chapter 2. Sedimentation rate (α) = 1.1 cm/kyr (Batenburg et al, 2016)

* excluded as an outlier

TABLE A.7: Bottaccione Gorge samples - helium data and deconvolved helium data

Depth [a] (m)	Sample Name	3He (cc/g)	3He error [b] (cc/g)	4He (cc/g)	4He error [b] (cc/g)	3He/4He	3He/4He error [b]	3He_ET [c] (cc/g)	3He_ET error [d] (cc/g)	4He_terr [e] (cc/g)	4He_terr error [b] (cc/g)
2.25	Samples 59 1 1-6	1.30E-14	5.66E-15	5.88E-09	1.13E-10	2.21E-06	9.61E-07	1.28E-14	2.56E-15	5.83E-09	2.64E-09
1.25	Samples 58 1 1-6	5.19E-14	4.25E-15	1.32E-08	2.50E-10	3.92E-06	3.12E-07	5.15E-14	1.03E-14	1.30E-08	1.95E-09
-0.5	Samples 5625 1 4-9	3.87E-14	6.69E-15	1.80E-08	3.41E-10	2.15E-06	3.69E-07	3.82E-14	7.64E-15	1.79E-08	3.81E-09
-0.5	Sample 5625 3C 11-15	4.93E-14	2.49E-15	2.40E-08	4.54E-10	2.05E-06	9.59E-08	4.86E-14	9.72E-15	2.38E-08	3.21E-09
-0.5	Sample 5625 3D B	6.71E-15	3.90E-16	2.64E-08	5.29E-10	2.54E-07	1.39E-08	5.91E-15	1.18E-15	2.64E-08	3.64E-09
-0.5	Sample 5625 3D A	1.84E-14	8.55E-16	2.48E-08	4.96E-10	7.44E-07	3.11E-08	1.77E-14	3.54E-15	2.47E-08	3.29E-09
-0.5	Sample 5625 3C 26-30	4.56E-14	2.94E-15	1.92E-08	3.64E-10	2.37E-06	1.35E-07	4.51E-14	9.01E-15	1.90E-08	2.64E-09
-0.5	Sample 5625 3C 21-25	4.40E-14	2.45E-15	2.02E-08	3.82E-10	2.18E-06	1.14E-07	4.34E-14	8.68E-15	2.00E-08	2.74E-09
-0.5	Sample 5625 3C 16-20	3.98E-14	1.96E-15	1.81E-08	3.43E-10	2.19E-06	1.00E-07	3.92E-14	7.84E-15	1.80E-08	2.41E-09
-0.5	Sample 5625 3C 1-5	3.84E-14	2.42E-15	2.11E-08	3.99E-10	1.82E-06	1.10E-07	3.78E-14	7.56E-15	2.09E-08	2.93E-09
-0.5	Sample 5625 3C 6-10	4.20E-14	2.53E-15	2.19E-08	4.14E-10	1.92E-06	1.09E-07	4.13E-14	8.27E-15	2.17E-08	3.01E-09
-0.5	Samples 5625 1 1-3	5.51E-15	2.70E-15	6.09E-09	1.15E-10	9.05E-07	4.43E-07	5.33E-15	1.07E-15	6.07E-09	3.07E-09
-0.5	Samples 5625 2B1	3.12E-14	1.48E-14	2.22E-08	4.19E-10	1.41E-06	6.65E-07	3.05E-14	6.11E-15	2.20E-08	1.08E-08
-0.5	Samples 5625 1 16-21	2.27E-14	3.77E-15	1.96E-08	3.71E-10	1.16E-06	1.91E-07	2.22E-14	4.43E-15	1.95E-08	4.05E-09
-0.5	Samples 5625 3A15	4.47E-14	7.96E-15	1.95E-08	3.68E-10	2.29E-06	4.06E-07	4.41E-14	8.83E-15	1.93E-08	4.20E-09
-0.5	Samples 5625 1 10-15	3.19E-14	6.30E-15	2.28E-08	4.30E-10	1.40E-06	2.75E-07	3.13E-14	6.25E-15	2.26E-08	5.29E-09
-0.5	FU 2625 3D 2	3.17E-14	3.51E-13	2.41E-08	6.82E-10	1.32E-06	1.24E-07	3.10E-14	6.20E-15	2.39E-08	3.80E-09
-3.5	Samples 5325 2 1-6	7.82E-15	1.45E-15	8.00E-09	1.51E-10	9.78E-07	1.80E-07	7.58E-15	1.52E-15	7.97E-09	1.78E-09

[a] Height above base of Bonarelli Level at Bottaccione Gorge

[b] analytical error

[c] calculated using two-component mixing model (Patterson and Farley, 1998): Equation 2.2, Chapter 2

[d] reproducibility error

[e] calculated using two-component mixing model (Patterson and Farley, 1998): Equation 2.3, Chapter 2

TABLE A.8: Chert transects - helium data

Scaglia Bianca Formation, Furlo, Italy

Sample Name	Distance [a] (cm)	carbonate (%)	3He (cc/g)	3He error [b] (cc/g)	4He (cc/g)	4He error [b] (cc/g)	3He/4He	3He/4He error [b]
FU CT D1	0.60	50	3.17E-14	1.61E-15	1.87E-08	5.32E-10	1.69E-06	7.10E-08
FU CT D2	0.60	50	3.23E-14	2.85E-15	2.40E-08	6.80E-10	1.35E-06	1.13E-07
FU CT C1	1.55	65	3.56E-14	2.77E-15	2.73E-08	7.75E-10	1.30E-06	9.45E-08
FU CT C2	1.55	65	2.12E-14	2.51E-15	2.36E-08	6.69E-10	8.99E-07	1.03E-07
FU CT C3	1.55	65	2.24E-14	2.41E-15	2.08E-08	5.89E-10	1.08E-06	1.12E-07
FU CT B1	2.30	74	2.15E-14	2.67E-15	1.88E-08	5.32E-10	1.15E-06	1.39E-07
FU CT B2	2.30	74	1.83E-14	1.65E-15	1.45E-08	4.11E-10	1.26E-06	1.08E-07
FU CT A1	3.20	76	1.78E-14	1.50E-15	7.03E-08	1.99E-09	2.53E-07	2.01E-08
FU CT A2	3.20	76	1.26E-14	1.17E-15	1.69E-08	4.80E-10	7.44E-07	6.60E-08
FU CT A3	3.20	76	2.73E-14	2.87E-15	2.18E-08	6.19E-10	1.25E-06	1.27E-07

Newhaven Chalk, Peacehaven, UK

Sample Name	Distance [a] (cm)	carbonate (%)	3He (cc/g)	3He error [b] (cc/g)	4He (cc/g)	4He error [b] (cc/g)	3He/4He	3He/4He error [b]	Stratigraphic height [c] (m)
PH NT 07	-3.75	99	1.08E-14	7.99E-16	4.05E-09	1.15E-10	2.66E-06	1.82E-07	-1.65
PH NT 00 B	0.00	2	1.87E-14	3.39E-15	7.98E-09	2.26E-10	2.34E-06	4.19E-07	-1.65
PH NT 00 A	0.00	2	1.10E-14	4.13E-16	5.31E-09	1.51E-10	2.07E-06	5.10E-08	-1.65
PH NT 01	3.75	99	5.34E-15	2.97E-16	2.47E-09	7.06E-11	2.16E-06	1.03E-07	-1.65
PH NT 02	7.50	99	1.76E-14	1.20E-15	4.94E-09	1.40E-10	3.57E-06	2.21E-07	-1.65
PH NT 03	13.00	100	1.18E-14	7.43E-16	3.00E-09	8.50E-11	3.94E-06	2.21E-07	-1.65
PH NT 04	18.00	99	1.88E-14	1.09E-15	6.78E-09	1.92E-10	2.77E-06	1.40E-07	-1.65
PH NT 05	22.50	99	1.82E-14	1.14E-15	4.81E-09	1.37E-10	3.77E-06	2.11E-07	-1.65
PH NT 06	27.50	99	1.33E-14	4.87E-16	4.35E-09	1.23E-10	3.06E-06	7.08E-08	-1.65
PH 11		99	2.34E-14	1.05E-15	4.45E-09	1.26E-10	5.25E-06	1.83E-07	-0.2
PH 10		99	1.51E-14	7.01E-16	4.82E-09	1.37E-10	3.13E-06	1.15E-07	-0.65
PH 09		99	2.17E-14	1.12E-15	7.62E-09	2.16E-10	2.85E-06	1.23E-07	-1.15
PH 08		99	2.45E-14	1.11E-15	6.93E-09	1.97E-10	3.53E-06	1.25E-07	-2.2

[a] Distance from (approximate) centre of chert nodule

[b] analytical error

[c] Height measured from Telscome Marl 3, *Offaster pilula* Zone, Lower Campanian

TABLE A.9: Neon data

Sample Name	20Ne (cc/g)	20Ne error [a] (cc/g)	22Ne (cc/g)	22Ne error [a] (cc/g)	21Ne (cc/g)	21Ne error [a] (cc/g)	20Ne/22Ne	20Ne/22Ne error [a]	21Ne/22Ne	21Ne/22Ne error [a]	3He/4He	3He/4He error [a]
FU 002 B	1.23E-06	1.86E-08	1.25E-07	2.24E-09	3.79E-09	7.83E-11	9.94	0.08	0.0303	0.0003	5.94E-07	2.46E-08
FU 003/4 A	5.28E-07	8.04E-09	5.15E-08	9.22E-10	1.58E-09	3.27E-11	11.02	0.09	0.0303	0.0003	1.43E-06	8.99E-08
FU 005/6 A	5.69E-04	8.65E-06	5.55E-05	9.94E-07	1.71E-06	3.54E-08	11.09	0.09	0.0305	0.0003	8.46E-07	2.44E-08
FU 005/6 B	4.15E-07	6.31E-09	4.02E-08	7.20E-10	1.23E-09	2.55E-11	11.16	0.09	0.0303	0.0003	1.20E-06	4.82E-08
FU 007 A	1.82E-07	2.77E-09	1.74E-08	3.12E-10	5.33E-10	1.10E-11	11.30	0.09	0.0303	0.0003	1.75E-06	4.03E-07
FU 007 B	1.72E-07	2.61E-09	1.66E-08	2.97E-10	5.09E-10	1.05E-11	11.22	0.09	0.0303	0.0003	1.97E-06	1.64E-07
FU 008 A	3.05E-07	4.63E-09	2.93E-08	5.24E-10	9.01E-10	1.86E-11	11.27	0.09	0.0304	0.0003	1.37E-06	9.02E-08
FU 008 B	1.11E-06	1.68E-08	1.08E-07	1.93E-09	3.29E-09	6.80E-11	11.12	0.09	0.0302	0.0003	6.99E-07	4.43E-08
FU 009 A	2.91E-07	4.43E-09	2.82E-08	5.05E-10	8.69E-10	1.80E-11	11.20	0.09	0.0304	0.0003	2.12E-06	1.79E-07
FU 009 B	2.71E-07	4.12E-09	2.62E-08	4.69E-10	8.12E-10	1.68E-11	11.20	0.09	0.0306	0.0003	1.81E-06	1.42E-07
FU 011 A	1.47E-07	2.24E-09	1.44E-08	2.57E-10	4.40E-10	9.11E-12	11.12	0.09	0.0303	0.0003	1.66E-06	7.36E-08
FU 011 B	1.87E-07	2.84E-09	1.81E-08	3.25E-10	5.61E-10	1.16E-11	11.14	0.09	0.0305	0.0003	4.86E-06	1.44E-07
FU 012 A	6.26E-07	9.52E-09	6.13E-08	1.10E-09	1.89E-09	3.90E-11	11.03	0.09	0.0304	0.0003	1.07E-06	4.51E-08
FU 014 C	4.24E-07	6.45E-09	4.14E-08	7.40E-10	1.27E-09	2.64E-11	11.02	0.09	0.0304	0.0003	1.93E-06	7.42E-08
FU 015 A	1.87E-07	2.85E-09	1.82E-08	3.26E-10	5.40E-10	1.12E-11	11.02	0.09	0.0297	0.0003	1.43E-06	6.03E-08
FU 016 A	2.98E-07	4.53E-09	2.90E-08	5.19E-10	8.90E-10	1.84E-11	11.02	0.09	0.0303	0.0003	1.58E-06	8.38E-08
FU 017/8 A	2.80E-07	4.26E-09	2.74E-08	4.89E-10	8.37E-10	1.73E-11	11.01	0.09	0.0302	0.0003	1.19E-06	9.24E-08
FU 019 A	2.21E-07	3.37E-09	2.16E-08	3.86E-10	6.64E-10	1.37E-11	11.03	0.09	0.0304	0.0003	2.21E-06	1.40E-07
FU 020 A	2.31E-07	3.51E-09	2.23E-08	3.99E-10	6.82E-10	1.41E-11	11.05	0.09	0.0302	0.0003	2.29E-06	1.12E-07
FU 020 B	3.26E-07	3.83E-08	3.16E-08	3.64E-09	9.05E-10	4.91E-11	10.64	0.09	0.0295	0.0018	2.54E-06	8.65E-08
FU 020 C	1.59E-07	1.87E-08	1.54E-08	1.78E-09	4.51E-10	2.44E-11	10.83	0.09	0.0308	0.0019	8.92E-06	1.76E-07
FU 021 A	3.52E-07	5.35E-09	3.43E-08	6.13E-10	1.04E-09	2.14E-11	11.03	0.09	0.0300	0.0003	6.97E-06	2.00E-07
FU 025 A	3.45E-07	5.25E-09	3.34E-08	5.97E-10	1.02E-09	2.11E-11	11.32	0.09	0.0302	0.0003	1.75E-06	7.64E-08
FU 026 A	2.70E-07	4.10E-09	2.61E-08	4.67E-10	7.91E-10	1.64E-11	11.06	0.09	0.0300	0.0003	1.54E-06	6.67E-08
FU 027 A	3.25E-06	1.45E-09	3.20E-07	1.42E-10	9.25E-09	4.12E-12	10.57	0.09	0.0290	0.0003	3.11E-06	1.53E-07
FU 029 A	2.60E-06	1.13E-09	2.55E-07	1.11E-10	7.49E-09	3.25E-12	10.65	0.09	0.0294	0.0003	3.69E-06	1.41E-07
FU 030	2.43E-06	7.78E-10	2.39E-07	7.65E-11	6.83E-09	2.18E-12	10.63	0.09	0.0286	0.0003	9.85E-07	9.02E-08
FU 031	3.15E-06	1.43E-09	3.07E-07	1.40E-10	9.01E-09	4.10E-12	10.77	0.09	0.0294	0.0003	1.82E-06	1.01E-07
FU 032/3	3.08E-06	9.04E-10	3.02E-07	8.87E-11	8.67E-09	2.54E-12	10.69	0.09	0.0287	0.0003	9.81E-07	1.35E-07
FU 034	4.90E-07	2.21E-10	4.85E-08	2.19E-11	1.42E-09	6.43E-13	10.12	0.09	0.0295	0.0003	1.21E-06	7.07E-08
FU 035	5.47E-07	1.62E-10	5.40E-08	1.60E-11	1.59E-09	4.73E-13	10.15	0.09	0.0297	0.0003	9.25E-07	7.94E-08
FU 036-8	1.95E-07	1.42E-10	1.92E-08	1.40E-11	5.70E-10	4.15E-13	10.25	0.09	0.0298	0.0003	1.30E-06	1.58E-07
FU 039 A	2.88E-07	1.34E-10	2.83E-08	1.32E-11	8.45E-10	3.93E-13	10.29	0.09	0.0299	0.0003	1.56E-06	6.02E-08
FU 040/1	2.09E-07	1.24E-10	2.06E-08	1.22E-11	6.02E-10	3.57E-13	10.31	0.09	0.0294	0.0003	8.82E-07	1.41E-07
FU 046	4.63E-07	1.48E-10	4.59E-08	1.47E-11	1.36E-09	4.34E-13	10.11	0.09	0.0296	0.0003	1.15E-06	7.65E-08
FU 047	5.09E-07	1.77E-10	5.05E-08	1.76E-11	1.47E-09	5.12E-13	10.09	0.09	0.0292	0.0003	1.15E-06	6.79E-08
FU 048	4.12E-07	1.45E-10	4.09E-08	1.44E-11	1.19E-09	4.20E-13	10.11	0.09	0.0293	0.0003	1.06E-06	1.57E-07

FU 049 A	4.29E-07	1.47E-10	4.25E-08	1.46E-11	1.26E-09	4.31E-13	10.10	0.09	0.0296	0.0003	3.35E-06	1.37E-07
FU 050	3.65E-07	1.64E-10	3.63E-08	1.63E-11	1.07E-09	4.80E-13	10.10	0.09	0.0296	0.0003	1.21E-06	7.60E-08
FU 051-5	6.47E-07	1.38E-10	6.41E-08	1.37E-11	1.89E-09	4.04E-13	10.09	0.09	0.0295	0.0003	6.49E-07	5.85E-08
FU 056/7	2.21E-07	1.54E-10	2.18E-08	1.52E-11	6.38E-10	4.45E-13	10.23	0.09	0.0296	0.0003	6.58E-07	6.12E-08
FU 058 A	4.41E-07	1.36E-10	4.36E-08	1.34E-11	1.27E-09	3.90E-13	10.14	0.09	0.0293	0.0003	2.81E-06	1.14E-07
FU 059	2.98E-07	1.70E-10	2.95E-08	1.69E-11	8.51E-10	4.87E-13	10.16	0.09	0.0292	0.0003	1.52E-06	7.00E-08
FU 060	2.89E-07	1.79E-10	2.88E-08	1.78E-11	8.34E-10	5.15E-13	10.13	0.09	0.0293	0.0003	1.59E-06	1.10E-07
FU 061	4.27E-07	1.75E-10	4.26E-08	1.74E-11	1.26E-09	5.15E-13	10.09	0.09	0.0297	0.0003	1.16E-06	7.40E-08
FU 062/3 A	6.18E-07	2.22E-10	6.15E-08	2.20E-11	1.78E-09	6.37E-13	10.11	0.09	0.0290	0.0003	3.76E-06	1.30E-07
FU 064	5.77E-07	2.02E-10	5.75E-08	2.01E-11	1.67E-09	5.86E-13	10.08	0.09	0.0292	0.0003	1.23E-06	2.48E-08
FU 065	5.36E-07	1.72E-10	5.33E-08	1.71E-11	1.55E-09	4.99E-13	10.10	0.09	0.0293	0.0003	1.55E-06	1.32E-07
FU 066-8	6.20E-07	8.41E-10	6.16E-08	8.36E-11	1.81E-09	2.46E-12	10.13	0.09	0.0295	0.0003	1.35E-06	1.70E-07
FU 069 A	5.69E-07	1.82E-10	5.65E-08	1.81E-11	1.67E-09	5.34E-13	10.12	0.09	0.0297	0.0003	1.67E-05	2.46E-07
FU 070-4	5.60E-07	1.51E-10	5.56E-08	1.50E-11	1.63E-09	4.40E-13	10.09	0.09	0.0295	0.0003	1.07E-06	1.36E-07
FU 086-8	3.83E-08	1.44E-10	3.81E-09	1.43E-11	1.18E-10	4.44E-13	10.93	0.09	0.0301	0.0003	1.45E-06	1.61E-07
FU 089	3.65E-08	2.48E-10	3.62E-09	2.46E-11	1.03E-10	7.03E-13	11.22	0.10	0.0294	0.0003	1.77E-06	1.60E-07
FU 106	3.49E-07	4.09E-08	3.40E-08	3.93E-09	1.00E-09	5.42E-11	10.78	0.09	0.0302	0.0018	6.08E-06	1.92E-07
FU 125/6	7.71E-07	9.06E-08	7.67E-08	8.86E-09	2.27E-09	1.23E-10	10.47	0.09	0.0296	0.0018	8.73E-07	5.04E-08
FU 127	4.01E-07	4.71E-08	3.95E-08	4.56E-09	1.15E-09	6.26E-11	10.48	0.09	0.0295	0.0018	1.35E-06	7.56E-08
FU 128/9	4.72E-07	5.55E-08	4.66E-08	5.38E-09	1.36E-09	7.38E-11	10.34	0.08	0.0295	0.0018	1.12E-06	6.20E-08
FU 131-4 A	2.68E-07	3.14E-08	2.64E-08	3.05E-09	7.69E-10	4.17E-11	10.19	0.08	0.0295	0.0018	2.15E-06	1.02E-07
FU 135/6	6.68E-07	7.85E-08	6.53E-08	7.53E-09	1.91E-09	1.03E-10	10.21	0.08	0.0293	0.0018	1.07E-06	6.40E-08
FU 137	4.62E-07	5.43E-08	4.56E-08	5.26E-09	1.34E-09	7.29E-11	10.40	0.09	0.0297	0.0018	9.54E-07	4.10E-08
FU 138	2.24E-07	2.63E-08	2.21E-08	2.55E-09	6.53E-10	3.56E-11	10.76	0.09	0.0299	0.0018	6.72E-07	2.48E-08
FU 139	1.69E-07	1.99E-08	1.68E-08	1.94E-09	4.94E-10	2.69E-11	10.69	0.09	0.0299	0.0018	1.11E-06	1.02E-07
FU 140	5.37E-07	6.30E-08	5.26E-08	6.07E-09	1.53E-09	8.30E-11	10.23	0.08	0.0293	0.0018	1.64E-06	1.31E-07
FU 142/3	2.36E-07	2.78E-08	2.30E-08	2.65E-09	6.57E-10	3.56E-11	10.37	0.08	0.0297	0.0018	8.11E-07	3.92E-08
FU 145/6	2.15E-07	2.52E-08	2.06E-08	2.38E-09	6.14E-10	3.34E-11	10.62	0.09	0.0306	0.0019	7.26E-07	4.85E-08
FU 147	2.86E-07	3.36E-08	2.81E-08	3.24E-09	8.28E-10	4.49E-11	10.20	0.08	0.0302	0.0018	1.25E-06	6.69E-08
FU 148	6.05E-07	7.11E-08	5.91E-08	6.82E-09	1.72E-09	9.32E-11	10.23	0.08	0.0294	0.0018	1.62E-06	6.66E-08
FU 149	4.75E-07	5.58E-08	5.87E-08	6.78E-09	1.69E-09	9.18E-11	8.31	0.07	0.0292	0.0018	1.71E-06	7.11E-08
FU 150	5.96E-07	7.00E-08	5.84E-08	6.74E-09	1.68E-09	9.10E-11	10.20	0.08	0.0292	0.0018	1.60E-06	5.32E-08
FU 151	4.44E-07	5.22E-08	4.35E-08	5.02E-09	1.28E-09	6.93E-11	10.49	0.09	0.0297	0.0018	1.17E-06	4.96E-08
FU 152	8.22E-07	9.66E-08	8.10E-08	9.35E-09	2.37E-09	1.29E-10	10.18	0.08	0.0295	0.0018	1.63E-06	5.56E-08
FU 153	5.76E-07	6.76E-08	5.66E-08	6.53E-09	1.63E-09	8.81E-11	10.16	0.08	0.0289	0.0018	1.79E-06	6.84E-08
FU 154	9.48E-07	3.51E-10	9.43E-08	3.50E-11	2.81E-09	1.04E-12	10.39	0.09	0.0297	0.0003	8.57E-07	7.78E-08
FU 170-2 A	8.16E-08	9.59E-09	8.00E-09	9.23E-10	2.31E-10	1.25E-11	10.18	0.08	0.0292	0.0018	1.55E-06	7.64E-08
FU 170-2 B	6.28E-08	7.38E-09	6.13E-09	7.08E-10	1.78E-10	9.67E-12	10.21	0.08	0.0295	0.0018	1.03E-06	4.84E-08
FU 173 C	6.77E-08	1.03E-09	6.62E-09	1.18E-10	2.03E-10	4.20E-12	10.98	0.09	0.0301	0.0003	1.62E-06	8.12E-08
FU 173 D	6.81E-08	8.00E-09	6.61E-09	7.62E-10	1.94E-10	1.05E-11	10.62	0.09	0.0298	0.0018	1.58E-06	6.55E-08
FU 174 A	6.43E-08	9.78E-10	6.47E-09	1.16E-10	1.97E-10	4.08E-12	10.06	0.08	0.0305	0.0003	1.64E-06	8.70E-08
FU 175 A	4.80E-07	7.30E-09	4.81E-08	8.60E-10	1.45E-09	3.00E-11	10.02	0.08	0.0301	0.0003	8.10E-07	2.56E-08
FU 175 B	1.61E-07	2.45E-09	1.61E-08	2.88E-10	4.89E-10	1.01E-11	10.11	0.08	0.0304	0.0003	1.13E-06	8.50E-08

FU 175 C	1.91E-07	2.24E-08	1.84E-08	2.12E-09	5.31E-10	2.88E-11	10.77	0.09	0.0300	0.0018	5.88E-07	1.22E-07
FU 183 A	7.74E-07	2.69E-08	7.58E-08	2.59E-09	2.30E-09	7.06E-11	10.21	0.08	0.0303	0.0003	4.15E-07	1.28E-08
FU 183 C	2.19E-07	2.57E-08	2.15E-08	2.48E-09	6.33E-10	3.44E-11	12.24	0.10	0.0305	0.0018	8.27E-07	2.57E-08
FU 184 A	3.05E-07	1.06E-08	2.96E-08	1.01E-09	9.02E-10	2.77E-11	10.29	0.08	0.0304	0.0003	2.02E-07	1.35E-08
FU 184 B	3.75E-07	1.31E-08	3.67E-08	1.25E-09	1.11E-09	3.41E-11	10.23	0.08	0.0303	0.0003	4.15E-07	5.35E-08
FU 184 C	1.93E-07	2.27E-08	1.86E-08	2.15E-09	5.44E-10	2.95E-11	10.96	0.09	0.0306	0.0019	3.87E-07	7.44E-08
FU 185 A	3.58E-07	1.25E-08	3.52E-08	1.20E-09	1.07E-09	3.29E-11	10.20	0.08	0.0304	0.0003	3.37E-07	1.91E-08
FU B1 01	2.94E-07	1.10E-10	2.92E-08	1.09E-11	8.50E-10	3.17E-13	10.12	0.09	0.0293	0.0003	1.18E-06	1.05E-07
FU B1 02	3.43E-07	1.59E-10	3.41E-08	1.58E-11	1.01E-09	4.68E-13	10.11	0.09	0.0298	0.0003	1.26E-06	1.69E-07
FU B1 03	2.49E-07	1.19E-10	2.49E-08	1.19E-11	7.31E-10	3.51E-13	10.07	0.09	0.0296	0.0003	1.14E-06	1.54E-07
FU B1 04	3.83E-07	1.62E-10	3.82E-08	1.62E-11	1.12E-09	4.75E-13	10.06	0.09	0.0296	0.0003	7.95E-07	1.95E-07
FU B1 05	2.00E-06	6.06E-10	1.99E-07	6.01E-11	5.79E-09	1.75E-12	10.43	0.09	0.0291	0.0003	9.05E-07	1.53E-07
FU B1 06	1.63E-06	8.74E-10	1.62E-07	8.70E-11	4.79E-09	2.57E-12	10.50	0.09	0.0295	0.0003	1.01E-06	7.33E-08
FU B1 07	1.68E-06	8.10E-10	1.68E-07	8.09E-11	4.89E-09	2.36E-12	10.41	0.09	0.0291	0.0003	9.13E-07	6.02E-08
FU B1 08 A	1.99E-06	6.36E-10	1.98E-07	6.34E-11	5.85E-09	1.87E-12	10.34	0.09	0.0295	0.0003	4.10E-06	2.36E-07
FU B1 09 A	1.17E-06	5.26E-10	1.16E-07	5.23E-11	3.46E-09	1.56E-12	10.49	0.09	0.0298	0.0003	1.79E-06	1.06E-07
FU B1 10	1.14E-06	3.87E-10	1.14E-07	3.86E-11	3.34E-09	1.13E-12	10.42	0.09	0.0293	0.0003	7.84E-07	7.51E-08
FU B2 01	2.24E-06	7.24E-10	2.24E-07	7.22E-11	6.60E-09	2.13E-12	10.40	0.09	0.0295	0.0003	6.41E-07	1.52E-08
FU B2 02	1.31E-06	4.93E-10	1.31E-07	4.93E-11	3.78E-09	1.42E-12	10.48	0.09	0.0288	0.0003	8.32E-07	5.43E-08
FU B2 03	1.04E-06	5.74E-10	1.04E-07	5.75E-11	3.08E-09	1.70E-12	10.53	0.09	0.0295	0.0003	6.88E-07	1.06E-07
FU B2 04	1.12E-06	5.46E-10	1.11E-07	5.43E-11	3.19E-09	1.56E-12	10.58	0.09	0.0286	0.0003	8.45E-07	6.41E-08
FU B2 05	1.01E-06	5.89E-10	1.01E-07	5.88E-11	2.97E-09	1.74E-12	10.66	0.09	0.0295	0.0003	6.90E-07	1.03E-07
FU B2 06 A	5.95E-07	3.92E-10	5.92E-08	3.90E-11	1.73E-09	1.14E-12	10.65	0.09	0.0292	0.0003	1.20E-06	1.31E-07
FU B2 07 A	1.19E-06	7.34E-10	1.18E-07	7.29E-11	3.52E-09	2.17E-12	10.48	0.09	0.0297	0.0003	4.99E-07	8.52E-08
FU B2 08	9.09E-07	4.69E-10	9.05E-08	4.67E-11	2.72E-09	1.40E-12	10.46	0.09	0.0299	0.0003	7.92E-07	1.49E-07
FU B2 09	9.76E-07	4.11E-10	9.70E-08	4.08E-11	2.90E-09	1.22E-12	10.41	0.09	0.0298	0.0003	7.51E-07	9.64E-08
FU B2 10 A	7.01E-07	3.14E-10	6.98E-08	3.12E-11	2.03E-09	9.10E-13	10.32	0.09	0.0291	0.0003	4.74E-07	7.36E-08
FU FM 200 D	8.05E-08	1.22E-09	7.84E-09	1.40E-10	2.42E-10	5.00E-12	11.10	0.09	0.0304	0.0003	1.87E-06	7.88E-08
FU FM 332 C	1.73E-07	6.01E-09	1.69E-08	5.78E-10	5.13E-10	1.57E-11	10.19	0.08	0.0302	0.0003	1.14E-06	4.09E-08
FU FM SR 81 B	1.39E-07	4.82E-09	1.35E-08	4.62E-10	4.12E-10	1.26E-11	10.24	0.08	0.0304	0.0003	7.75E-07	2.71E-08

[a] analytical error